A Measurement of Multijet Production in Low-x_{Bj} Neutral Current Deep Inelastic Scattering with ZEUS at HERA

by

Thomas Erik Danielson

A dissertation submitted in partial fulfillment of the

requirements for the degree of

Doctor of Philosophy

(Physics)

at the

University of Wisconsin – Madison

2007

Abstract

Inclusive dijet and trijet production in deep inelastic ep scattering has been measured for $10 < Q^2 < 100$ GeV^2 and low Bjorken x, $10^{-4} < x_{\mathrm{Bj}} < 10^{-2}$. The data were taken at the HERA ep collider with center-of-mass energy $\sqrt{s} = 318$ GeV using the ZEUS detector and correspond to an integrated luminosity of 82 pb^{-1}. Jets were identified in the hadronic center-of-mass (HCM) frame using the k_T cluster algorithm in the longitudinally invariant inclusive mode. Measurements of dijet and trijet differential cross sections are presented as functions of Q^2, x_{Bj}, jet transverse energy, and jet pseudorapidity. As a further examination of low-x_{Bj} dynamics, multi-differential cross sections as functions of the jet correlations in transverse momenta, azimuthal angles, and pseudorapidity are also presented. Calculations at $\mathcal{O}(\alpha_s^3)$ generally describe the trijet data well and improve the description of the dijet data compared to the calculation at $\mathcal{O}(\alpha_s^2)$.

Acknowledgements

I would like first to thank the University of Wisconsin Physics Department for providing me the opportunity to pursue my degree and for the financial support during my graduate career. I'd especially like to thank Professors Wesley Smith and Don Reeder for their insight, support, and guidance. They've both been excellent advisors.

I would like to thank the members of the ZEUS collaboration, who kept the experiment running and who coordinated all the analyses of the data. Special mention goes to Tim Gosau, Sascha Savin, Dorian Kçira, without whom this analysis would not have happened. I'd also like to thank Juan Terron and Claudia Glasman for providing additional insight into the analysis.

I'd like to thank all of my friends from Hamburg and Madison for making my grad school experience some of the best years of my life.

The acknowledgments would not be complete without mention of two sources of guidance growing up: Jeff Forrest and Mike Thomas.

Above all, I'd like to thank my Mom, Dad, and the rest of my family. Their love and support have helped me throughout and have allowed me to pursue my interests. To them I dedicate this thesis.

Contents

List of Tables

List of Figures

Chapter 1

Introduction

The aim of the natural sciences is to observe, classify, measure and explain natural phenomena. Physics is the branch of the natural sciences that deals with matter, time, energy, and space, the understanding of which is important to all natural sciences, as all phenomena are subject to the laws of physics. The history of human efforts towards understanding fundamental natural processes is, of course, long and far too detailed to encapsulate here, but one issue would eventually (after a few millennia) give rise to the discipline of particle physics: what forms matter and what are the physical laws which govern the formation and properties thereof?[1] Among the studies of the properties of matter is the study of the internal structure of the nucleons (protons and neutrons), which are comprised of quarks and gluons, collectively known as partons. The interactions of quarks and gluons is characterized by the theory of Quantum Chromodynamics (QCD), which can be used in conjunction with perturbation theory to predict the partonic content of a nucleon. Measurements of the energies and positions of the final-state particles in Deep Inelastic Scattering (DIS) interactions, in which a lepton and proton collide, provide a good testing ground for predictions from

[1]Sources [1] and [2] were referenced for compiling this chapter.

the most commonly used pQCD (perturbative QCD) approach to characterize the proton's partonic content. This analysis examines the applicability of this approach in a kinematic range relatively near the non-perturbative limit.

1.1 An Introduction to Particle Physics

The origins of particle physics can be traced to Democritus (born ca. 460 BC), who postulated that everything in the universe falls into one of two categories: matter comprised of fundamental, indivisible particles or atoms ("atomas" is Greek for "indivisible units"), and void. However, this theory of atoms was a philosophical construct rather than a mathematically rigorous theory and at the time was not accepted as the primary explanation for the fundamental constituents of matter. By 1758, when Boscovich founded the basis of modern atomic theory, physics had evolved from a philosophy to an empirical science with a mathematical formalism upon which predictions could be made, thanks to the contributions from people such as Galileo and Newton. As early as 1829, scientists arranging the elements by their atomic weight noticed a periodicity in the properties of the elements, and studies of this periodic behavior ultimately led to Mendeleev's formulation of the Periodic Table in 1869. That the elements could be classified in groups according to their similar properties was an indication that the atoms themselves were comprised of smaller particles.

The modern origin of particle physics begins with Joseph Thompson's discovery of the electron in 1898, which confirmed that atoms themselves are comprised of smaller particles and gave rise to the "plum pudding" model of the atom, which described an atom as a positively charged extended object with negatively charged electrons as points within the atom. This model was quickly supplanted in 1909, when

Rutherford's scattering experiment demonstrated that atoms contain small, dense, positively charged nuclei at their center. This experiment led to the Bohr model of the atom in 1913, which was soon followed the first evidence of the proton found by Rutherford in 1919. In 1931, James Chadwick's discovery of the neutron completed the representation of the atomic nucleus used today, with the protons and neutrons known collectively as nucleons.

With the discovery of the neutron, however, the mechanisms for nuclear binding and nuclear decay remained unexplained. Subsequent experiments with observation of cosmic particles and experiments using particle accelerators designed to probe the structure of the atomic nuclei led to the discovery of both a particle with the same properties as the electron, but 200 times heavier (the muon), and a proliferation of new, briefly stable particles that interact via the strong nuclear force, collectively known as hadrons. Early collider experiments also provided the first indications that the nucleons themselves contain a charge structure. In 1964 Gell-Mann and Zweig put forth the idea that hadrons are made from combinations of quarks. The strong interaction theory of quarks from Fritzsch and Gell-Mann, which explains nuclear binding, and the electroweak theory [3], which explains nuclear decay, form the Standard Model used in particle physics today.

1.2 The Standard Model

The Standard Model is currently the most complete theoretical framework to describe the fundamental particles and their interactions. Within the Standard Model, there are 3 types of particle: quarks, leptons, and force mediators (bosons). In addition to the three types of particles, the Standard Model also describes three different forces

acting on these particles: the electromagnetic force, the weak nuclear force, and the strong nuclear force.

Quarks are spin-$\frac{1}{2}$ particles that have both a fractional electric charge and a color charge of either red, green, or blue. Quarks are not observed as free particles (see section 1.2.1 for an explanation of quark confinement). The six flavors of quarks are divided into three generations, with each generation consisting of two quarks and differing from the other generations only in flavor and mass. Quarks combine to form colorless hadrons, which consist of baryons (e.g. protons), which are combinations of three quarks or antiquarks, each with a different color charge (red, green, blue or anti-red, anti-green, anti-blue), and mesons (e.g. pions, consisting of π^0 and $\pi^{\pm}$), which are bound states of a quark and an antiquark of opposite color charge (e.g. a red and an anti-red quark combination). Baryons and mesons are the only types of hadrons observed[2] and can be formed from all types of quarks except the top quark, which decays before hadron formation can occur.

Leptons are spin-$\frac{1}{2}$ particles with a neutral color charge, which allows them to be observed as free particles. As with the quarks, there are three known lepton generations which differ from each other only in mass and flavor. Each generation consists of a particle with a negative charge of one unit–the electron (e), the muon (μ), and the tau (τ)–and a corresponding neutrino (ν) with a very small mass and no electric charge. The generations of quarks and leptons and their important properties are given in Table 1.1.

The interactions of the particles described above are mediated by a third class

[2]Five-quark bound states, or pentaquarks consisting of a baryonic and mesonic combination of quarks have been posited, but conclusive evidence of these particles has not yet been found.

Quarks			Leptons		
Flavor	**Mass(Gev)**	**Charge**	**Flavor**	**Mass(GeV/c^2)**	**Charge**
u	0.003	2/3	ν_e	$< 10^{-8}$	0
d	0.006	-1/3	e	0.000511	-1
c	1.3	2/3	ν_μ	< 0.0002	0
s	0.1	-1/3	μ	0.106	-1
t	175	2/3	ν_τ	< 0.02	0
b	4.3	-1/3	τ	1.7771	-1

Table 1.1: The properties of the three generations of quarks and leptons. Each generation differs from other generations in mass and flavor only. The basic unit of charge is -1, the charge of the electron. The antiparticle partners of these quarks and leptons (not included in this table) have the same mass and opposite electric charge.

Boson	**Mass(GeV)**	**Charge**	**Force**
γ (photon)	0	0	Electromagnetic
$W^\pm$	80.4	± 1	Weak
Z^0	91.187	0	Weak
g (gluon)	0	0	Strong

Table 1.2: Properties of the bosons in the Standard Model. The standard unit of charge is that of the electron, also used in Table 1.1

.

of particle in the Standard Model: bosons, which are spin-1 particles that allow for force and quantum number exchange. Each force described by the Standard Model is mediated by a distinct boson or set of bosons. The types of interactions in which a particle can participate is governed by the types of bosons it can exchange with other particles. Neutrinos, for example, have neither a color charge nor an electric charge, and therefore do not emit or absorb the bosons associated with the strong or the electromagnetic force, and therefore interact with matter only via the weak interaction.

Table 1.2 lists the properties of the bosons responsible for mediating the forces in the Standard Model. The electromagnetic force is mediated by the photon, which has no mass or electric charge. The weak force is mediated by three particles: the electrically charged W^+ and W^- particles, and the electrically neutral Z^0 particle. As mentioned previously, the electromagnetic and weak interactions are unified in the Standard Model to form the electroweak interaction. The strong force is mediated by gluons, which like the quarks carry a color charge that also prevents the observation of gluons as free particles (see again the discussion of confinement in section 1.2.1). Quarks interacting with each other through gluon exchange undergo a change in color charge, which means that a gluon has both a color charge and an anti-color charge, as color is a conserved quantum number. The three color charges and three anti-color can form eight different combinations for the overall color charge of the gluon. The Higgs boson, which has not yet been observed experimentally, is the final predicted boson of the Standard Model and is needed for the breaking of the electroweak gauge symmetry that results in the generation of particle mass.

Although the ability of the Standard Model to describe experimental result has been exhaustively tested and verified, it fails to encompass all natural phenomena and is therefore not regarded as a fundamental theory of physics. The most obvious omission from the Standard Model is the fourth fundamental force: gravity. Additionally, the theory does not incorporate neutrino mass or oscillation. The theory also has many input parameters, such as the masses of the particles and the units of charge, all of which have been determined experimentally but not derived from first principles. Addressing these issues and incorporating gravity into a fundamental model (a grand

unified theory, or GUT) is one of the major goals of current physics research.

1.2.1 The Standard Model as a Field Theory

Quantum field theory, upon which the Standard Model is based, represents the quantized particles as dynamical fields. The quantized treatment of the fields accounts for multiparticle states, causality issues, transition between states with different numbers of particles, antiparticles, and the relation between spin and statistics. The Standard Model is also an example of a gauge theory, which describes a system that is invariant under local transformations (i.e. a phase rotation of $\phi(x) \rightarrow e^{i\alpha(x)}\phi(x)$ applied in a certain space-time region, where $\phi(x)$ is an arbitrary field) as well as global transformations. Gauge theories like the Standard Model can be described mathematically using a group theory approach.

The field theory of Quantum Electrodynamics (QED) is described by the mathematical group U(1). The designation U(1) denotes that the generator matrix M for the group is one-dimensional and is unitary ($M^{\dagger}M = 1$). As mentioned earlier, electroweak theory is a combined description of electromagnetism and the weak interaction, the latter of which is described by the SU(2) mathematical group. In addition to being unitary, a generator matrix for a special unitary group (like SU(2)) has a determinant of 1. The SU(2) group is described by three two-dimensional generator matrices, giving the combined electroweak theory 4 generator matrices, which correspond to two neutral boson fields (γ and Z^0) and two charged boson fields ($W^{\pm}$).

The field theory of Quantum Chromodynamics (QCD) is described by the SU(3) gauge group, which requires eight generators, corresponding to the eight types of gluon described above. Unlike the electroweak portion of the Standard Model, QCD is non-

Abelian, which means that the group generators are non-commutative and that the gauge bosons associated with the group, the gluons, can interact with other gluons.

1.3 Quantum Chromodynamics

That QCD is based on a non-Abelian gauge theory gives rise the two most important properties of QCD, which are confinement and asymptotic freedom.

1.3.1 QCD Confinement and Asymptotic Freedom

Unlike the other forces in the Standard Model, the potential describing the strong interaction exhibits an approximately linear dependence on the distance between the interacting particles. As a consequence of this property, known as QCD Confinement, free quarks and gluons have not been experimentally observed. Conversely, partons[3] that are close together behave, from the standpoint of the strong interaction, as free particles, a property known as Asymptotic Freedom.

An analogy with the more familiar Abelian QED interactions, where the photons do not interact with other photons, can give insight into these seemingly counter-intuitive properties of QCD. A basic example of how these two theories differ can be illustrated by describing a simple measurement of the charge of a lepton as opposed to a measurement of the color charge of a quark. The measurement of the charge of an electron in a vacuum is sensitive to charge screening, where the electron radiates photons which then split into electron-positron pairs (see Fig. 1.1). Due to the charge of the initial electron, the resulting electron-positron pairs will polarize, with the positrons attracted to the original electron. The measured charge of the electron will

[3]Particles participating in the strong interaction. This term was coined by Feynman in 1969 to describe the particles within the proton

therefore be dependent on where in the "screening cloud" the probe measures, with the measured charge increasing as the probe approaches the electron. The electric field strength in the case of QED exhibits a well-known $1/r^2$ dependence.

In a similar manner, the measurement of a quark's color charge will be affected by gluons emitted by the quark, which can subsequently form both quark-antiquark pairs, or, unlike in the case of QED, gluon-gluon pairs (see Fig. 1.2). The overall gluon color charge is twice that of the quark, so the gluon production effectively spreads out the measured color charge. Also unlike QED, the measured quark will be preferentially surrounded by partons of like color charge. As the probe approaches the quark through the like-color screen, the measured charge of the quark will be reduced, rather than enhanced as in the case of QED screening. The anti-screening effect of QCD yields a color field strength that increases approximately linearly with distance.

1.3.2 Perturbative Quantum Chromodynamics

The property of asymptotic freedom allows for a perturbative treatment for calculations of QCD when the separation between partons is small, corresponding to a high-energy probe. Perturbative QCD (pQCD) allows for the prediction of an observable to be expressed in terms of a finite expansion power series in a coupling constant α_s, in which a simple system is "perturbed" by higher-order corrections:

$$f(\alpha_s) = f_1 + f_2\alpha_s + f_3\alpha_s^2 + \ldots \tag{1.1}$$

The pQCD calculation of an observable associated with a given scattering process is determined by a summation over the amplitudes of all Feynman diagrams associated with the scattering. The power of the coupling parameter for a given Feynman dia-

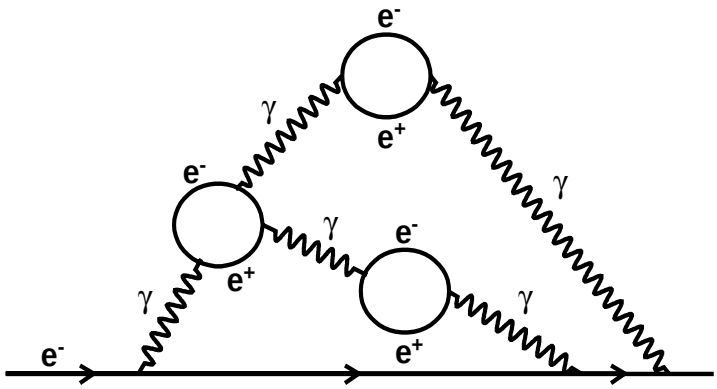

Figure 1.1: Electric charge screening in QED. The initial electron radiates a photon which then produces subsequent electron-positron and further QED radiation. The positrons are attracted to the initial electron, and creates a screening effect that reduces the measured charge of the electron.

gram, and therefore the term within the expansion to which the diagram contributes, is determined by the number of vertices associated with quark-gluon or gluon-gluon interactions, with each quark-gluon or gluon-gluon vertex contributing a factor of α_s. A Leading-Order (LO) prediction sums over only the lowest-order contributions to the observable, which are Feynman diagrams for processes with a single gluon emission. A Next-to-Leading order (NLO) calculation includes terms with an additional power of the coupling constant, which corresponds to either the emission of a second gluon or a virtual gluon loop (see Fig. 1.3).

Calculation of the virtual loop diagrams involve integration over the loop momenta, and leads to divergences when the loop momenta are integrated to infinity (the ultraviolet divergence). Because of this divergent behavior, it is necessary to introduce

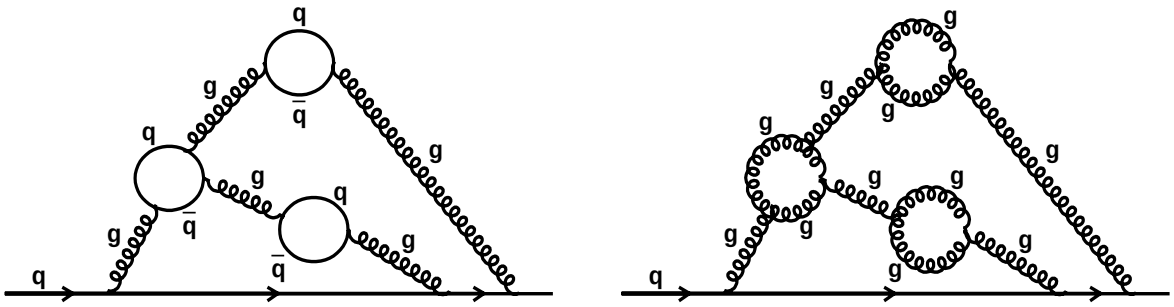

Figure 1.2: Color charge screening in QCD. Similar to the photon emission in QED, the initial quark radiates a gluon. The gluon then splits either into a $q\overline{q}$ pair, as shown at left, or a gg pair, as shown at right.

a renormalization scale μ_R [4] which is a cutoff on the loop momenta. The strength of the QCD interaction, which is given by the QCD coupling constant α_s, then becomes dependent on the renormalization scale μ_R:

$$\alpha_s(\mu_R^2) = \frac{12\pi}{(11N_C - 2N_F)\ln(\mu_R^2/\Lambda_{QCD}^2)} \tag{1.2}$$

where N_C is the number of colors ($N_C = 3$ in the Standard Model) and N_F is the number of quark flavors ($N_F = 6$ in the Standard Model). Equation 1.2 also introduces

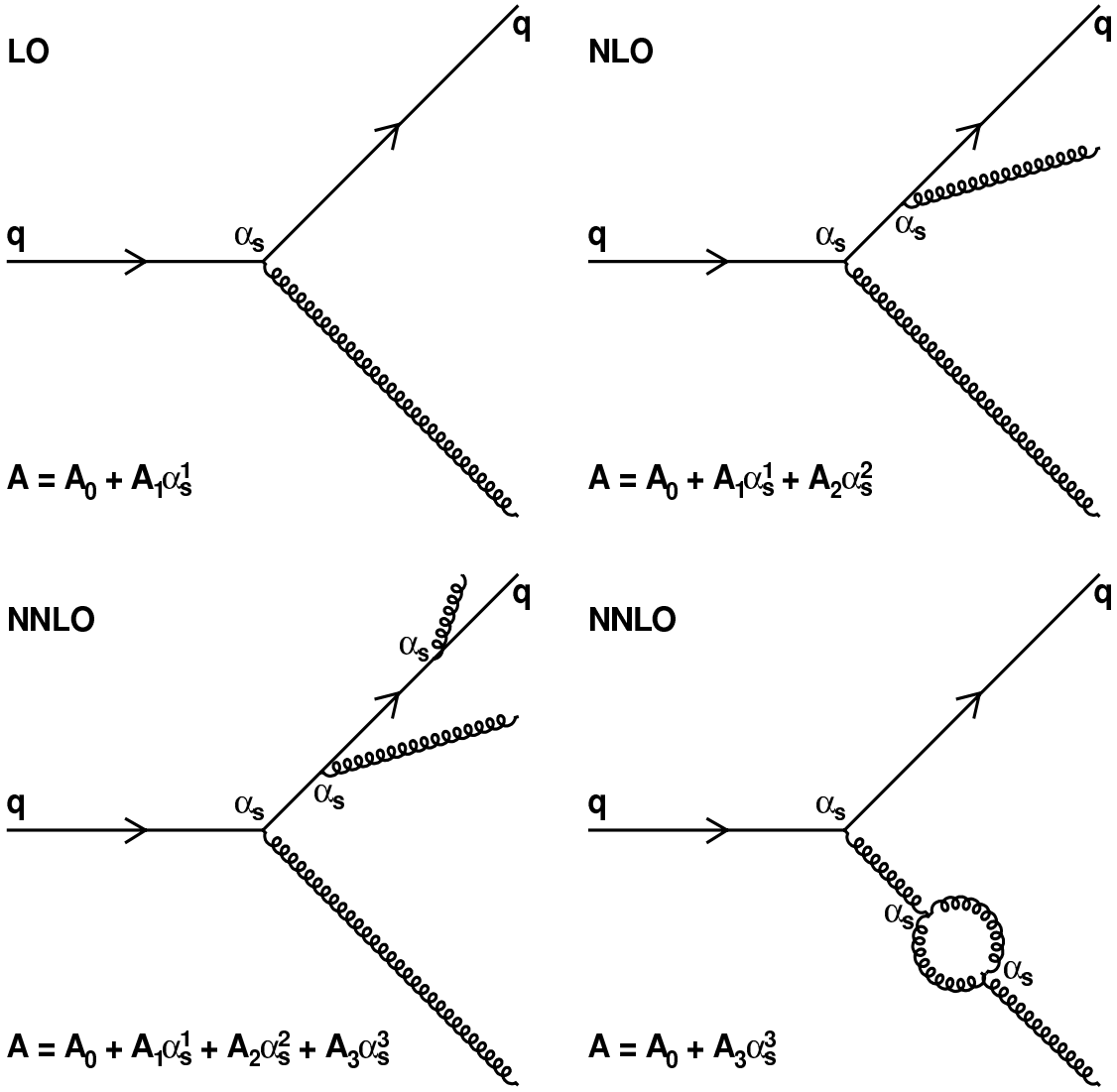

Figure 1.3: Diagrams for LO, NLO, and NNLO processes in QCD, where each successive step in the perturbation series adds the emission of an additional gluon or, in the case of the NNLO process shown at lower right, an internal gluon loop correction.

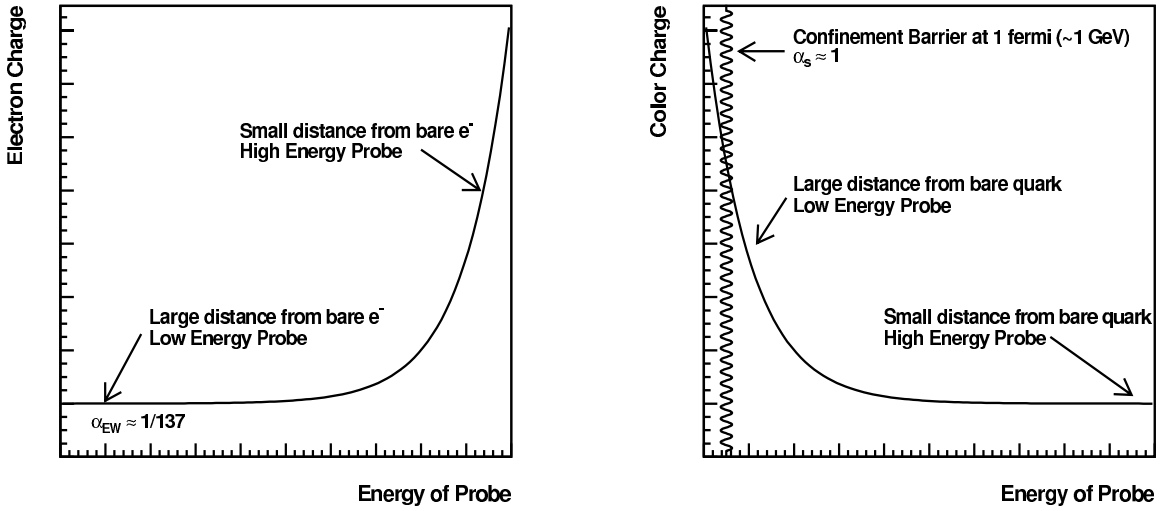

Figure 1.4: The behavior of the QED coupling constant α_{EM} (left) and the QCD coupling constant α_s (right) as a function of the energy of the energy transferred between two interacting particles. At low energy, α_s is large enough such that pQCD techniques cannot be applied, which illustrates confinement. The coupling constant α_s decreases as the energy of the probe increases, which demonstrates asymptotic freedom. Diagrams are based on those in [1].

the parameter Λ_{QCD}, which is a cutoff scale that corresponds to the energy at which the value of α_s becomes too large for the pQCD expansions, and the treatment of quarks and gluons as free particles rather than as bound states in hadrons is not applicable. The variable Λ_{QCD} has been determined from experimental results to be approximately $0.1 - 0.5$ GeV. Diagrams of the the behavior of the QED coupling constant α_{EM} and α_s are shown in Figure 1.4.

Indications that nucleons themselves contain charge structure came from early collider experiments, as mentioned previously. Subsequent experiments have characterized the quark and gluon content of the proton for an extensive kinematic range; however these experiments have an inherently limited kinematic coverage, which means that pQCD techniques are needed to predict the content of the proton in a more gen-

eralized kinematic range.

Chapter 2

Parton Evolution in Deep Inelastic Scattering

Many of the properties of the Standard Model were realized through scattering experiments at colliders. In a scattering experiment, a beam of high energy particles bombards a target, particles emerging from the interaction are measured and their distributions compared to theoretical predictions, which provides an understanding of the physics behind the interactions. Scattering experiments are divided into three categories: elastic scattering, where both the target is left intact and in a non-excited state; inelastic scattering, where the interaction disturbs or breaks up the target particle; and deep inelastic scattering (DIS), where the target particle is annihilated and new particles are formed. In the case of elastic scattering, the distribution of the deflection angles of the incident particles is described by the scattering cross section described in section 2.1.2. For inelastic scattering and deep inelastic scattering, the cross section and scattering amplitude also must take into account the structure of the target, which is characterized by form factors.

2.1 Deep Inelastic Scattering

Deep Inelastic Scattering experiments use high-energy leptons scattered off hadrons to determine the structure of the hadronic targets. As mentioned in Chapter 1, interactions between particles are mediated by bosons. Because leptons do not contain a color charge, DIS interactions do not involve gluon exchange between the lepton and hadron. The electroweak bosons therefore mediate DIS interactions, and the types of DIS interactions fall into two categories: neutral-current DIS, which is mediated by γ and Z^0 exchange; and charged-current DIS, which is mediated by $W^{\pm}$ exchange. A signature of a charged current DIS event is the incoming lepton changing flavor to form a neutrino, which is not detected experimentally.

The wavelength of the boson exchanged between the lepton and hadronic target is

$$\lambda = \frac{\hbar}{Q} \tag{2.1}$$

where $\hbar$ is Planck's constant and Q is related to the 4-momentum of the exchange boson. Equation 2.1 shows that the wavelength of the probe is inversely proportional to the momentum of the probe. As shown in Figures 2.1 and 2.2, a probe in an electron-proton (ep) interaction with a long wavelength "sees" the proton as a point particle. At higher Q^2, the probe resolves the valence quarks of the proton, and at even higher Q^2 the probe resolves the "sea" quarks and gluons within the proton.

Due to the Uncertainty Principle, the exchange boson itself does not obey the law of conservation of energy and momentum, and instead, the lifetime of the boson is related to its energy via $\Delta t < \hbar/\Delta E$. A boson that does not conserve energy and

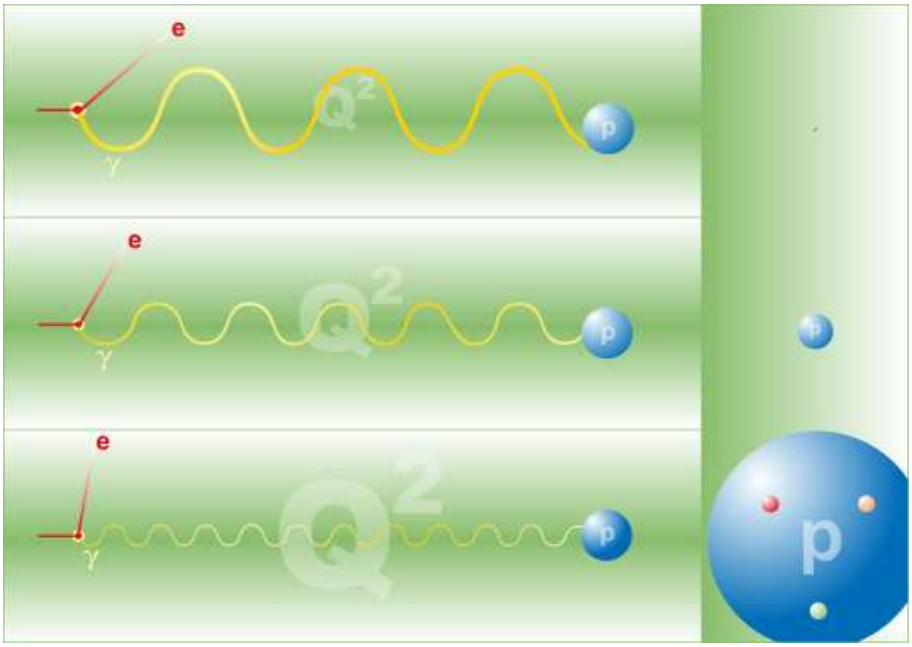

Figure 2.1: An illustration of the relation between energy and wavelength of the probe. A low-energy probe with a long wavelength resolves the proton as a point particle, whereas a higher energy probe resolves the valence quarks of the proton.

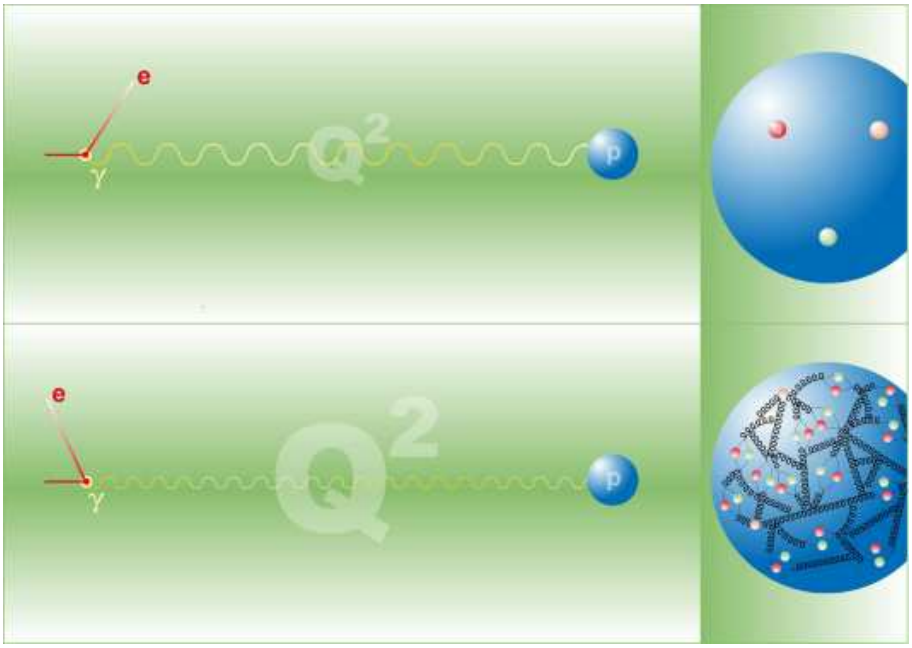

Figure 2.2: As the energy of the probe becomes very large, the probe can resolve a "sea" of quarks and gluons within the proton. The two illustrations used here are courtesy of [5]

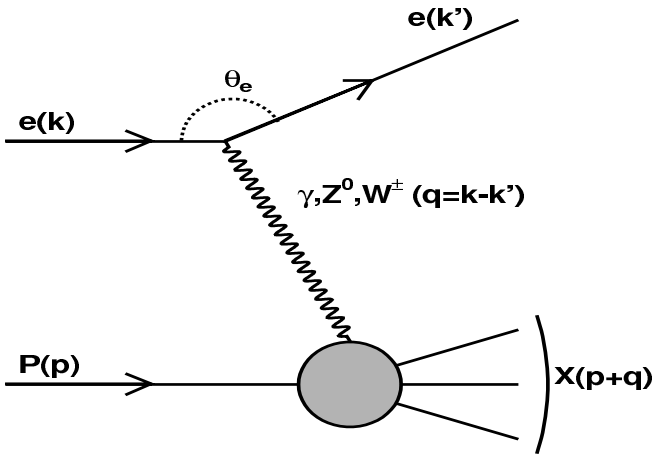

Figure 2.3: A general diagram of a DIS interaction with a lepton with momentum k scattering off a hadron with momentum p and exchanging a boson with momentum $q = k - k'$.

momentum is termed a virtual boson. The virtuality of the boson, which is a measure of how far off mass-shell the virtual boson is, is given by Q^2.

2.1.1 DIS Kinematics

A DIS interaction illustrated in Figure 2.3 consists of a lepton with a momentum vector k interacting with a proton with momentum p and scattering with a momentum of k'. The center-of-mass energy of the system is denoted as $\sqrt{s}$ and is given by

$$s^2 = (p + k)^2 \tag{2.2}$$

In the massless approximation used in high energy accelerators where $p \gg m_p$ and $k \gg m_e$, the proton mass and lepton mass are taken to be zero, and $s = 2p \cdot k$. The 4-momentum of the exchange boson is given by $q = k - k'$. The virtuality of the exchange boson is defined kinematically as

$$Q^2 \equiv -q^2 = -(k - k')^2 \tag{2.3}$$

In addition to the center-of-mass energy and boson virtuality, the kinematic description of a DIS event uses the scaling variable introduced by Bjorken in 1969 [6], which describes to lowest order the fraction of the proton momentum carried by the struck parton:

$$x_{\mathrm{Bj}} = \frac{Q^2}{2p \cdot q} \tag{2.4}$$

Also introduced by Bjorken was the inelasticity y, which is a measure of the lepton momentum transferred to the proton:

$$y = \frac{p \cdot q}{p \cdot k} \tag{2.5}$$

Combining the DIS kinematic variables listed above, one obtains the relation

$$Q^2 = s x_{\mathrm{Bj}} y \tag{2.6}$$

2.1.2 DIS Cross Section and Structure Functions

In a scattering experiment, the differential cross section $d\sigma$ is the probability of observing a scattered particle in a given state per unit of solid angle

$$\frac{d\sigma}{d\Omega} = \frac{\text{Scattered flux / Unit of solid angle}}{\text{Incident flux / Unit of surface}} \tag{2.7}$$

which can be integrated over the solid angle to obtain the total cross section σ. For a generic interaction $A + B \rightarrow C + D$ with a transition rate per unit volume of W_{fi},

the cross section can also be expressed as

$$\sigma = \frac{W_{fi}}{\text{Initial flux}}(\text{Number of final states}) \tag{2.8}$$

The cross section for lepton-lepton scattering can be written in terms of a product of two leptonic tensors, which characterize the interaction with a summation over initial and final state spins, for two arbitrary scattering leptons, A and B:

$$\begin{aligned} \overline{|\mathcal{M}|^2} &= \frac{e^4}{q^4} \\ d\sigma &\sim L^A_{\mu\nu}(L^{\mu\nu})^B \end{aligned} \tag{2.9}$$

where $\overline{|\mathcal{M}|}$ is identified as the spin-averaged scattering amplitude. As a similar treatment for DIS interactions, a hadronic tensor $W^{\mu\nu}$ is used to characterize the structure of the proton, which yields an expression of the cross section in the form of:

$$d\sigma \sim L^A_{\mu\nu}(W^{\mu\nu})^B \tag{2.10}$$

The proton structure functions more commonly used in the expression of the DIS cross section, $F_i(x, Q^2)$, are obtained from the hadronic tensor in the kinematic range where the exchange boson resolves the proton's partonic constituents:

$$\begin{aligned} \nu W_2(\nu, Q^2) &\rightarrow F_2(x, Q^2) \\ M W_1(\nu, Q^2) &\rightarrow F_1(x, Q^2) \end{aligned} \tag{2.11}$$

where M is the proton mass and

$$x = \frac{Q^2}{2M\nu} \tag{2.12}$$

The proton structure functions $F_i(x, Q^2)$ are expressed in terms of parton density functions (PDFs) $f_i(x, Q^2)$, which represent the probability of finding a parton with a momentum fraction in the interval $[x, x + dx]$ for an exchange boson with virtuality Q^2. The parton density functions themselves cannot be calculated from first principles and must therefore be extracted from fits to structure function measurements. The proton structure functions expressed in terms of the PDFs and parton charge e_i are as follows:

$$F_1(x, Q^2) = \sum_i \frac{1}{2} e_i^2 f_i(x, Q^2) \tag{2.13}$$

$$F_2(x, Q^2) = \sum_i e_i^2 x f_i(x, Q^2) \tag{2.14}$$

$$F_L(x, Q^2) = F_2 - 2xF_1 \tag{2.15}$$

The structure function F_2 is the contribution to the cross section from transversely polarized virtual bosons, while F_L is the contribution from longitudinally polarized bosons, and is relatively small compared to F_2. The DIS cross section as a function of x and Q^2 expressed in terms of these structure functions and an additional structure function F_3, which comes from the parity violation from Z^0 boson exchange and only becomes important at $Q^2 \sim M_Z^2$ (see also Table 1.1):

$$\frac{d^2\sigma(e^{\pm}p)}{dxdQ^2} = \frac{4\pi\alpha_{EM}^2}{xQ^4}[Y_+ F_2(x, Q^2) - y^2 F_L(x, Q^2) \mp Y_- xF_3(x, Q^2)] \tag{2.16}$$

where $Y_{\pm} = 1 \pm (1 - y)^2$.

2.1.3 Factorization and Parton Density Functions

The DIS cross section, as expressed in 2.16, is useful for the measurement of the proton structure functions, from which the PDFs can be extracted. However, the cross section is not calculable using pQCD techniques alone due to long-range (soft) contributions where α_s is sufficiently large such that these contributions are non-perturbative and non-calculable. To separate the long-range (soft) processes from the short-range (hard) processes that are calculable by pQCD methods requires the introduction of a factorization scale μ_F, which represents an energy cutoff below which pQCD is not applicable. The soft terms below the factorization scale are absorbed into the PDFs, while the terms above the factorization scale are included in the calculation of the partonic cross section. The factorization scale is therefore the scale at which the PDFs are evaluated. The overall cross section can also be expressed both in terms of 2.16 and as a convolution of the PDFs and hard processes.

$$d\sigma = \sum_{a=q\bar{q}g} \int dx f_a(x, \mu_F^2) d\hat{\sigma}_a(x, \alpha_s(\mu_R^2), \mu_R^2, \mu_F^2) \tag{2.17}$$

2.1.4 Splitting Functions and Parton Evolution

Gluon radiation (QCD radiation) comes from a quark emitting a gluon, which can subsequently form either a quark-antiquark pair or a gluon-gluon pair. The probabilities of these processes are given by splitting functions, which are expressed perturbatively in $z = x/y$, and to first order are

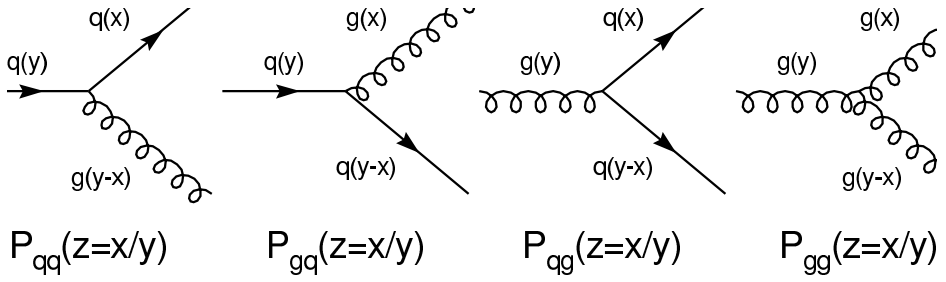

Figure 2.4: The leading order diagrams for the parton splitting functions representing a quark radiating a gluon, and a gluon splitting into $q\overline{q}$ and gg pairs.

$$\begin{aligned} P_{qq}(z) &= \frac{4}{3}\left(\frac{1+z^2}{1-z}\right) \\ P_{gq}(z) &= \frac{4}{3}\left(\frac{1+(1-z)^2}{z}\right) \\ P_{qg}(z) &= \frac{1}{2}\left(z^2+(1-z)^2\right) \\ P_{gg}(z) &= 6\left(\frac{1-z}{z}+\frac{z}{1-z}+z(1-z)\right) \end{aligned} \tag{2.18}$$

These splitting functions are illustrated in Figure 2.4.

As PDFs are typically written as functions of x and Q^2 and must be extracted from experimental structure function measurements that cover only a restricted kinematic phase space, PDFs are extrapolated to a general phase space via the DGLAP equations describing parton evolution [7]:

$$\begin{aligned} \frac{\partial g(x,Q^2)}{\partial \ln Q^2} &= \frac{\alpha_s(Q^2)}{2\pi}\int_x^1 \frac{dz}{z}\left[P_{gg}\left(\frac{x}{z}\right)g(z,Q^2)+P_{gq}\left(\frac{x}{z}\right)q(z,Q^2)\right] \\ \frac{\partial q(x,Q^2)}{\partial \ln Q^2} &= \frac{\alpha_s(Q^2)}{2\pi}\int_x^1 \frac{dz}{z}\left[P_{qg}\left(\frac{x}{z}\right)g(z,Q^2)+P_{qq}\left(\frac{x}{z}\right)q(z,Q^2)\right] \end{aligned} \tag{2.19}$$

For a PDF extracted at a given value of x and Q^2, the x-dependence is parameterized at the scale at which the PDF was extracted, Q_0^2, and evolved in Q^2 using these

equations.

2.2 Parton Evolution Schemes at low x_{Bj}

The DGLAP equations cannot be analytically solved to all orders of α_s. Therefore, certain approximations are made to obtain solutions to these equations. These approximations to the DGLAP equations are generally applicable only to limited kinematic regions. In addition to the two approaches for DGLAP resummation that will subsequently be discussed (the Leading Log and Double-Leading Log approximations), two alternative methods of parton evolution, BFKL and CCFM are based on different treatments of the parton evolution equations or splitting functions and have different regions of expected applicability. The focus of this analysis is testing the applicability of the DGLAP approach at low x_{Bj} in DIS, and to determine if other forms of resummation need to be introduced.[1]

2.2.1 DGLAP Leading Log Approximation

The Leading Log Approximation for resumming the DGLAP equations involves the treatment of the soft divergences where $z \to 1$, which ultimately leads to a resummation of terms contributing factors of $\ln Q^2$, while neglecting terms containing factors of $\ln(1/x)$. Noting that $z = x/y$, this treatment is expected to apply to scattering with sufficiently large Q^2 and x such that the terms contributing $\ln(1/x)$ are negligible.

Mathematically, the leading log approach involves the use of a Sudakov Form Factor [9] expressed with the Mandelstam variable t, which for DIS is Q^2:

[1] Reference [8] was useful in compiling this section.

$$\Delta_s = \exp\left(-\overline{\alpha_s}\int\frac{dz}{z}\int_{t_0}^{t}\frac{dt^{'}}{t^{'}}\tilde{P}(z)\right) \tag{2.20}$$

where $\overline{\alpha}_s$ is the running coupling constant and $\tilde{P}(z)$ is the gluon splitting function $g \rightarrow gg$ to all orders. By using the plus prescription defined by

$$\int_0^1 \frac{f(z)}{(1-z)_+} = \int_0^1 \frac{f(z)-f(1)}{1-z} \tag{2.21}$$

to treat the soft divergences and including the Sudakov Form Factor, one can obtain the integral equation

$$f(x,t) = f(x,t_0)\Delta_s(t) + \int\frac{dz}{z}\int\frac{dt^{'}}{t^{'}}\cdot\frac{\Delta_s(t)}{\Delta_s(t^{'})}f\left(\frac{x}{z},t^{'}\right) \tag{2.22}$$

Physically, the Sudakov Form Factors represent non-branching probabilities. In Equation 2.22, the factor $\Delta_s(t)$ in the term $f(x,t_0)\Delta_s(t)$ represents the probability that no branching (gluon emission) occurs between the initial scale t_0 and the evaluated scale t, while the fraction $\Delta_s(t)/\Delta_s(t^{'})$ in the integral represents the probability that no branching occurs from $t^{'}$ to t. The integral in z of $\tilde{P}(z)$ gives the branching probability at scale t. Equation 2.22 has the functional form of a Fredholf type integral

$$\phi(x) = f(x) = \lambda\int_a^b K(x,y)\phi(y)dy \tag{2.23}$$

which is solved iteratively by a Neumann series of the form

$$\phi(x) = \lim_{n\rightarrow\infty}\sum_{i=0}^{\infty}\lambda^i u_i(x) \tag{2.24}$$

Using this form, equation 2.22 becomes

$$f(x,t) = \lim_{n\to\infty} f_n(x,t) = \lim_{n\to\infty} \sum_n \frac{1}{n!} \ln^n \left(\frac{t}{t_0}\right) A^n \otimes \Delta_s(t) f\left(\frac{x}{z}, t_0\right) \tag{2.25}$$

with $A = \int dz/z\tilde{P}$.

Setting $t = Q^2$ for DIS gives the result that the leading log approximation to the DGLAP equations resums to all orders in $\ln Q^2$. A diagram of parton emission in DIS interactions is illustrated in Figure 2.5. The leading log resummation of the DGLAP equations, as seen in Equation 2.25, imposes a strong ordering in virtuality, which also gives rise to a strong ordering in transverse momenta: $Q^2 \gg k^2_{T,n} \gg k^2_{T,n-1} \gg \ldots \gg k^2_{T,1}$, and an ordering in the fractional momenta of the proton momenta carried by the partons: $x_1 > x_2 > \ldots > x_{\mathrm{Bj}}$.

2.2.2 Double Leading Log Approximation

At low x_{Bj}, approximations used in solving the DGLAP equations must take into account the divergent behavior of the gluon splitting function P_{gg} from equation 2.18, which contains a $1/z$ divergence as $z = x/y \to 0$. In the low-x region, the gluon contribution to the proton structure dominates (see Figure 2.6), which means terms contributing factors of $\ln(1/x)$ corresponding to gluon emission are non-negligible. The double-leading log (DLL) approach, which includes resummations of terms contributing factors of $\ln Q^2 \ln(1/x)$, allows more phase space for gluon emission than the leading log approach, and is expected to be more accurate than the leading log approximation at low x_{Bj}. However, because the DLL approach does not include the terms contributing factors of the single logarithm $\ln(1/x)$, the DLL approach might not be applicable at sufficiently low x_{Bj} (see Figure 2.7).

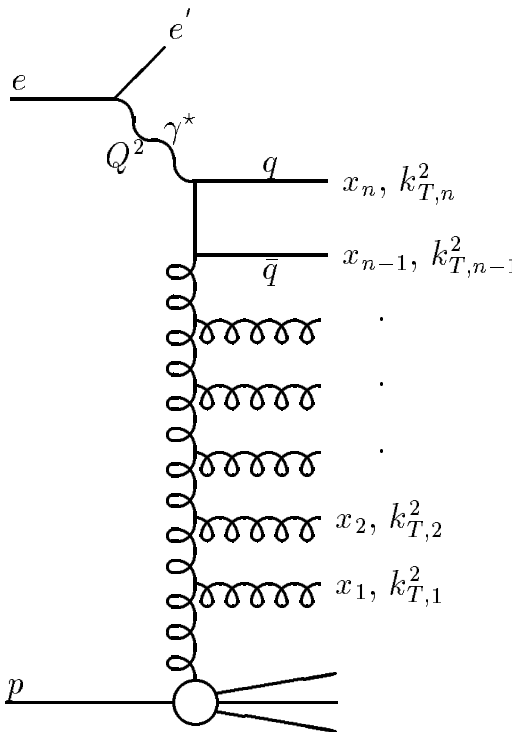

Figure 2.5: A "gluon ladder" diagram with a gluon cascade leading to the hard scatter. The ordering of the transverse momenta of the gluons, $k_\perp$, and the fractional momentum of the proton carried by the gluons, x, depends on the evolution scheme used.

The mathematical treatment of the DLL approach to the DGLAP equations focuses on the gluon PDF, with a low-x approximation to its evolution of

$$\frac{dg(x,Q^2)}{d\ln Q^2} = \frac{\alpha_s}{2\pi}\int_x^1 \frac{dz}{z} g(z,Q^2) P_{gg}\left(\frac{x}{z}\right) \tag{2.26}$$

Setting $P_{gg} \to 6/z$ from 2.18 for the case of $z \to 0$, one can rewrite this equation as

$$xg(x,t) = \frac{3\alpha_s}{2\pi}\int_{t_0}^{t} d\ln t' \int_x^1 \frac{dz}{z} z g(z,t') \tag{2.27}$$

An iterative technique for solving equation 2.27 is approximating the integral as an infinite sum beginning with an initial constant gluon distribution at small t

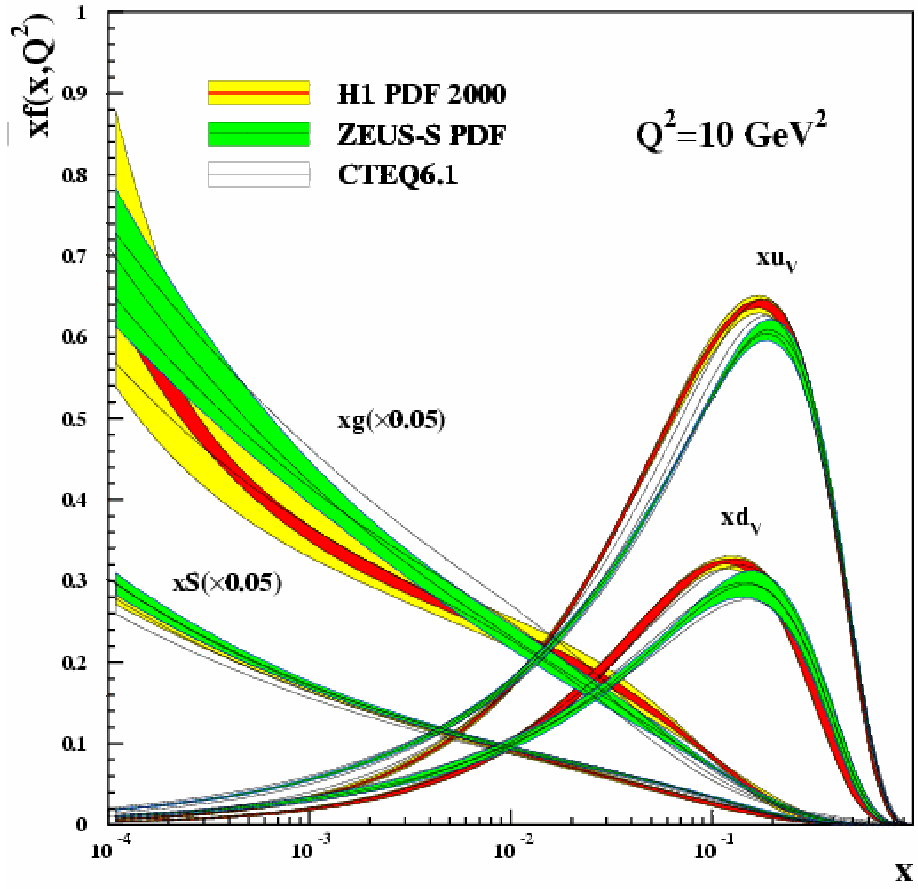

Figure 2.6: Proton PDF fits from CTEQ6, H1, and ZEUS as a function of x. Towards low x the contributions from the sea, in particular the gluons become dominant as gluon emission increases. Image courtesy of [8].

designated as $C = xg_0(x)$, which represents the initial gluon from the "bottom rung" of the ladder diagram shown in Figure 2.5. As an infinite sum 2.27 is written as [8]

$$\begin{aligned} xg(x,t) &= \sum_n \frac{1}{n!}\frac{1}{n!}\left(\frac{3\alpha_s}{2\pi}\frac{1}{2}\ln\frac{t}{t_0}\ln\frac{1}{x}\right)^n C \\ xg(x,t) &\sim C\exp\left(2\sqrt{\frac{3\alpha_s}{\pi}\ln\frac{t}{t_0}\ln\frac{1}{x}}\right) \end{aligned} \tag{2.28}$$

Equation 2.28 is a resummation of terms contributing factors of $\ln Q^2 \ln(1/x)$. Like

the leading log approximation, the DLL resummation imposes a strong ordering in virtuality, but the DLL also imposes a strong ordering in the fraction of the proton momentum x carried by each parton: $x_1 \gg x_2 \gg \ldots \gg x_{\mathrm{Bj}}$.

The approximations to the DGLAP equations, in particular, the DLL approach, have been tested extensively in DIS experiments at HERA and were found to describe the inclusive cross sections [10, 11] and jet production [12–15]. At low x_{Bj}, where the phase space for parton emissions increases, terms proportional to $\alpha_s \ln(1/x)$ may become large and spoil the accuracy of the DGLAP approach.

2.2.3 BFKL

At low x_{Bj}, a better approximation might be provided by the BFKL formalism [16] in which the evolution equations resum over terms contributing factors of $\ln(1/x)^2$. Unlike the DGLAP evolution, the BFKL treatment incorporates unintegrated parton densities defined by

$$\mathcal{F}(x, k_\perp^2) = x\frac{dg(x, Q^2)}{dQ^2} \tag{2.29}$$

which yields a parton evolution equation of

$$\frac{\partial \mathcal{F}(x, k_\perp^2)}{\partial \ln(1/x)} = \int dk^2 K(k_\perp^2, k^2) f(x, k^2) \tag{2.30}$$

where the term $K(k_\perp^2, k^2)$ is the BFKL kernel, given as

$$K(k_\perp^2, k^2) = \frac{3\alpha_s}{\pi}\left(\frac{1}{|\boldsymbol{k}_\perp - \boldsymbol{k}|^{\boldsymbol{2}}} - \delta(k^2 - k_\perp^2)\int^k \frac{d^2q}{\pi q}\right) \tag{2.31}$$

[2]For the BFKL section, [17] was also referenced

which accounts for gluon emission (in the first term of the kernel) and virtual corrections (in the second term).

As in the case of the DGLAP approximations described above, resummation techniques are applied to the BFKL evolution equation, but in the case of BFKL non-Sudakov Regge Form Factors are used [18]. Resummation techniques ultimately yield an unintegrated gluon density at low x of

$$\mathcal{F}(x, k_\perp^2) \sim \left(\frac{1}{x}\right)^{4\overline{\alpha}_s \ln 2} \tag{2.32}$$

Because the resummation for BFKL is done for terms contributing factors of $\ln(1/x)$, the BFKL approach imposes strong ordering in x, as is the case of the DGLAP DLL approximation; but unlike the DLL approximation, an ordering in $k_\perp$ is not applied to the parton cascade.

2.2.4 CCFM

The CCFM approach [19], like BFKL, incorporates unintegrated parton densities evaluated at the scale of $k_\perp$. The k_t factorization approach used by CCFM, which allows for coupling of gluons to the photon and reproduces the collinear limit used by the DGLAP factorization, interpolates between BFKL and DGLAP to describe a larger range in x and Q^2. A discussion of k_t factorization can be found in [20].

The CCFM approach includes the aforementioned non-Sudakov form factors into the splitting function itself:

$$\tilde{P}(z, q, k_\perp) = \frac{\overline{\alpha}_s}{1-z} + \frac{\overline{\alpha}_s}{z}\Delta_{ns}(z, q, k_\perp) \tag{2.33}$$

with the non-Sudakov form factor given as

$$\Delta_{ns} = \exp\left[-\overline{\alpha}_s(k_\perp^2)\int_0^1 \frac{dz'}{z'}\int \frac{dq^2}{q^2}\Theta(k_\perp - q)\Theta(q - z'q_\perp)\right] \tag{2.34}$$

The CCFM approach applies color coherence via angular ordering: $\overline{q} > z_n q_n,\ z_n > z_{n-1}q_{n-1}, \ldots q_1 > Q_0$ with $z_i = E_i/E_{i-1}$, but like BFKL does not impose an ordering in $k_\perp$ for the parton cascade.

2.3 Jet Physics and QCD Evolution

The property of QCD confinement ensures that the individual partons from a DIS interaction are not observed. Instead, the emitted partons form colorless hadrons, which can result in collimated showers of particles, or jets. Studies of jets in DIS are a useful means of testing the predictions of parton evolution schemes. In the case of the DGLAP approximations, the strong ordering in transverse momentum, $k_\perp$ of the emitted partons means that the partons with the highest transverse momentum will be the partons emitted from the hard scatter and will be emitted at a relatively large polar angle from the proton beam. For events with more than one jet, the two leading jets in transverse momentum should also be strongly correlated in azimuthal angle due to energy and momentum conservation.

Unlike DGLAP, neither the BFKL nor the CCFM scheme imposes a strong ordering in $k_\perp$ of the emitted partons. Because the emitted partons are not necessarily ordered in $k_\perp$, it is possible for partons with a large fraction of the proton momentum also to have a significant $k_\perp$, an effect that gives rise to jets emitted at a low polar angle. The experimental signature of non-DGLAP effects and the onset of BFKL or CCFM effects is an excess of forward jets compared to predictions from either the leading

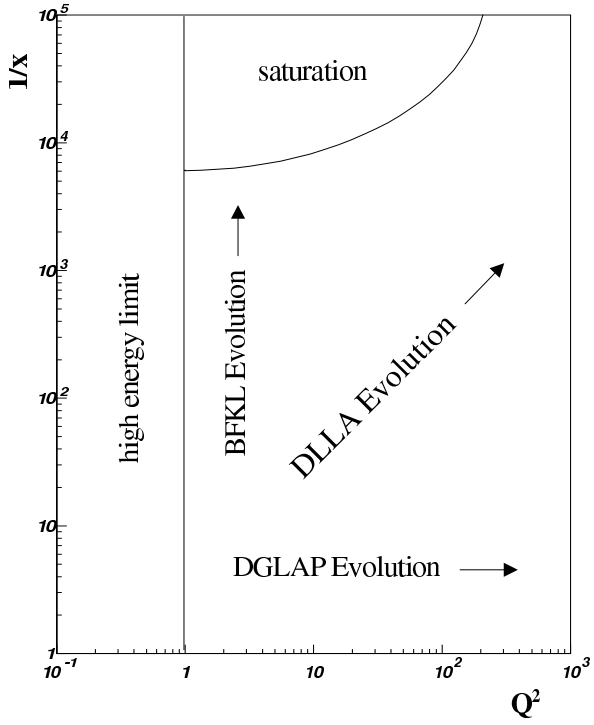

Figure 2.7: An illustration of the kinematic ranges for which the parton evolution schemes discussed are expected to be applicable. Towards very low x the gluon density gets sufficiently large such that saturation from gluon overlap and multiple interactions makes the pQCD approach non-applicable to this kinematic region.

log or DLL approximations. This also manifests itself in the form of jets produced in the hard scatter that are not strongly correlated in transverse momentum. Figure 2.7 gives a rough indication of the kinematic range in which the DGLAP approximations and the BFKL treatment are expected to be applicable, with low-x_{Bj} effects raising the question of the accuracy of the DGLAP approximations at sufficiently low-x_{Bj}.

An understanding of this regime is of particular relevance in view of the startup of the LHC, where many of the Standard Model processes such as the production of electroweak gauge bosons or the Higgs particle involve the collision of partons with a low fraction of the proton momentum. The information about cross sections,

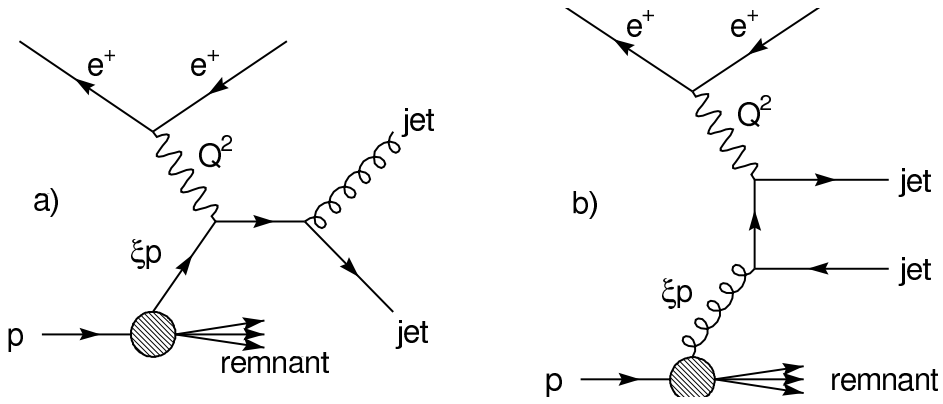

Figure 2.8: Leading order diagrams for QCD Compton (a) and Boson-Gluon Fusion (b) processes.

transverse energy, E_T, and angular correlations between the two leading jets in multijet production therefore provides an important testing ground for studying the parton dynamics in the region of small x_{Bj}.

In this analysis, correlations for both azimuthal and polar angles, and correlations in jet transverse energy and momenta for dijet and trijet production in the hadronic ($\gamma^* p$) center-of-mass (HCM) frame are measured in the kinematic region restricted to $10 < Q^2 < 100\,\mathrm{GeV}^2$ and $10^{-4} < x_{\mathrm{Bj}} < 10^{-2}$. The results are compared with DGLAP-based NLO pQCD calculations (described in chapter 5) at next-to-leading order (NLO).[3]

2.3.1 Hadronic Center of Mass Frame

Jet production in DIS originates with the hard scatter, with the struck quark evolving into a single jet in a quark-parton model (QPM) event. Dijet production in DIS proceeds via two mechanisms, both illustrated in Figure 2.8: Boson-Gluon Fusion

[3]BFKL-based pQCD calculations, which would allow for a similar analysis of BFKL predictions of the jet correlations, are currently unavailable.

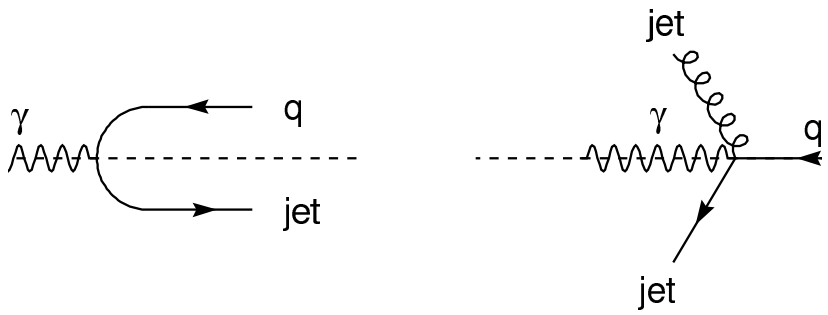

Figure 2.9: An illustration of the HCM frame for a QPM event (left) and a QCDC event (right). The $+z$ direction is taken to be the direction of the incoming photon.

(BGF) processes, where the exchange boson and a gluon within the proton interact to produce a $q\overline{q}$ pair, and QCD Compton (QCDC) processes, where the boson interacts with a quark within the photon, and the struck quark subsequently radiates a gluon, which forms its own jet.

For this analysis, which examines the correlations between the two hardest jets in a multijet event, it is desirable to suppress single jet events, which is accomplished by selecting a frame such that the proton and the virtual photon on the same axis. The Hadronic Center-of-Mass (HCM) frame is defined by $\vec{p}+\vec{q}=0$, where $\vec{p}$ and $\vec{q}$ are the 3-momenta of the incoming proton and virtual photon, respectively, with the $+z$ axis taken to be in the direction of $\vec{q}$. For the purposes of jet finding, this reference frame is equivalent to the Breit frame [21] defined by $2x\vec{p}+\vec{q}=0$ apart from a longitudinal boost. A common feature of both frames is that for a QPM event, which is an event with only a single jet coming from the interaction between the virtual boson and the struck quark, the struck quark recoils along the $+z$ direction and therefore has a negligible E_T in that frame. For BGF and QCDC dijet events at leading order, the final state partons have equal and opposite transverse momenta (see Figure 2.9). By

requiring a non-zero $E_{T,\mathrm{HCM}}^{\mathrm{jet}}$, events with at least two jets are selected, while QPM events are rejected. This analysis therefore uses the HCM frame for jet finding.

Chapter 3

Experimental Setup

The examination of QCD evolution in deep inelastic scattering using jet correlations in transverse momenta and azimuthal angle requires experimental measurements to test the predictions from the aforementioned evolution schemes. To examine multijet physics at low-x_{Bj} DIS, measurements were taken at the Deutsches Elektronen Synchrotron (DESY) laboratory using the ZEUS detector (described in Section 3.3) at the HERA *ep* collider (described in Section 3.2).

3.1 The DESY Laboratory

The DESY laboratory, founded in 1959, is part of the Helmholz Association, which is the largest scientific research organization in Germany, with a total of 15 research centers covering six different fields of research. DESY is a publicly funded research center with two campuses–one in Hamburg, and one in Zeuthen (Brandenburg)–dedicated to fundamental research in particle physics and to the study of synchrotron radiation. DESY's Hamburg campus is home to several particle accelerators: the DESY accelerator, the linear accelerator (LINAC) the Positron-Elektron Tandem Ring Anlage (PETRA), the Doppel Ring Speicher (DORIS), and the Hadron-Elektron Ring

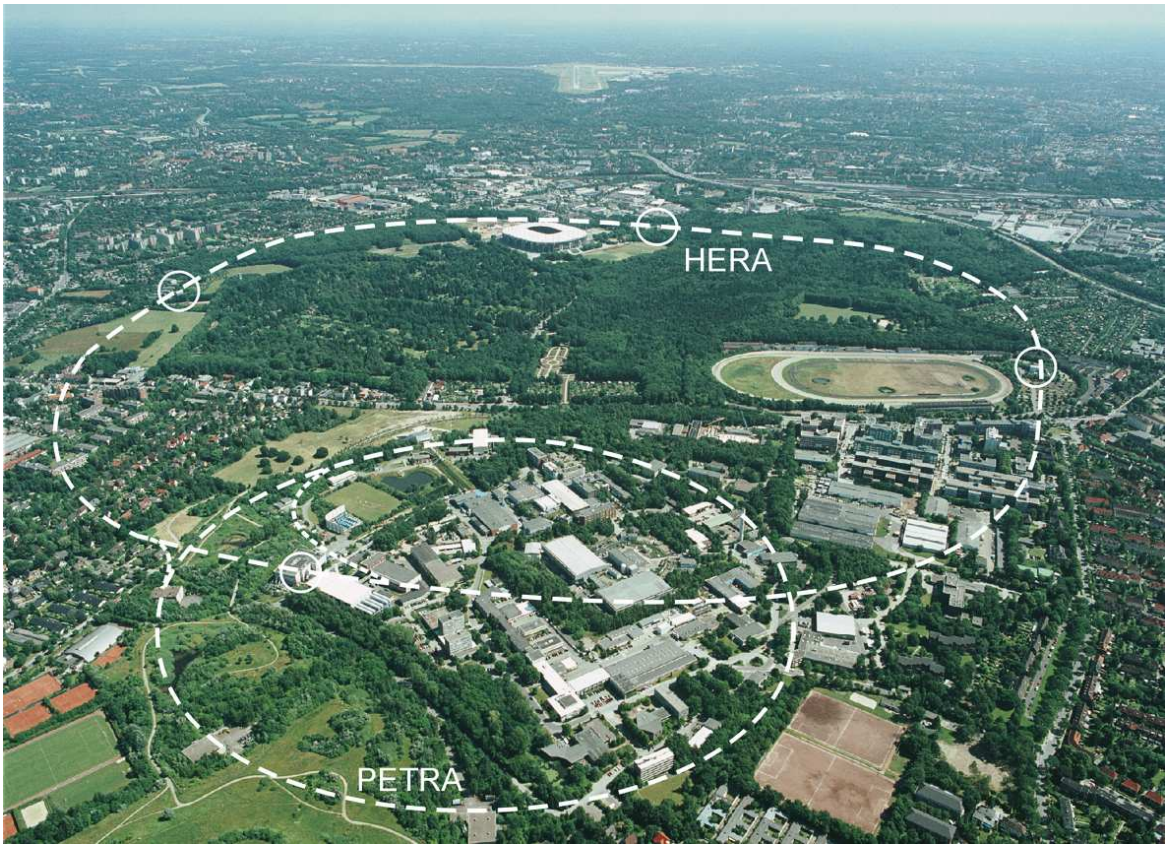

Figure 3.1: An aerial view of the DESY-Hamburg research center. Shown in the white dashed lines are the accelerators PETRA and HERA, with the white circles showing the locations of the HERA experiments.

Anglage (HERA). Synchrotron radiation studies are conducted at the Hamburg Synchrotron Radiation Laboratory (HASYLAB), which uses the DORIS ring. The other accelerators acted primarily for injection into the HERA ring (see Figure 3.2 for a schematic view). In addition to these accelerators, the DESY Hamburg site is scheduled to house the European Free Electron Laser (XFEL). A research and development program for the International Linear Collider (ILC) and a theory institute are also located at DESY.

In total, the DESY facility has 1560 employees, including 365 scientists. DESY

also hosts approximately 3000 scientists from 33 different countries, who perform research with the HERA-based experiments or HASYLAB.

3.2 The HERA Accelerator

The HERA accelerator was the only lepton-nucleon beam collider with electron and positron beams colliding with proton beams. The HERA ring is 6.336 kilometers in circumference and at a depth underground of between 10 and 25 meters. The ring has four 90° curves and four straight sections, where the experiments were located. HERA was approved in 1984, and construction was completed on schedule in November 1990. Luminosity operations at HERA began in 1992 and concluded on June 30, 2007. The north and south halls housed the general purpose detectors H1 and ZEUS, which studied lepton-proton interactions. Both ZEUS and H1 started operation in 1992 and took data through 2007. The HERA-B experiment, which studied the interaction between particles in the proton beam halo and a fixed wire grid, was proposed to measured CP violation in the $b\bar{b}$ system and took data from 1999 to 2003. The HERMES experiment, which operated from 1995 to 2007, studied the spin structure of the proton using the electron beam on a polarized gas target.

3.2.1 Proton Injection and Acceleration

The protons used in the HERA accelerator were obtained from negatively charged Hydrogen (H^-) ions, which are accelerated to 50 MeV in the LINAC. The ions were then passed through a thin foil to strip the electrons from the ions, and then were accelerated to 7.5 GeV in the DESY III ring. From the DESY III ring the protons were fed into the PETRA ring and accelerated to 39 GeV before being injected into

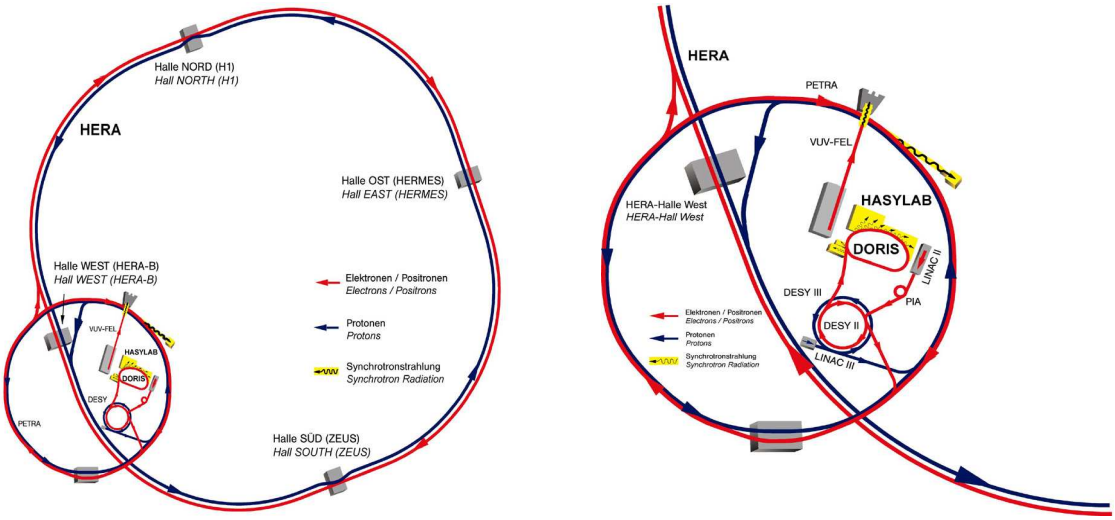

Figure 3.2: A schematic diagram of the accelerators at DESY-Hamburg. The figure on the right is a closeup view of the HERA injection system.

the HERA ring. In the HERA ring, a series of superconducting dipole magnets with a field strength of 4.65 T accelerated the protons further to their final interaction energy. Up to 1997, the proton energy was 820 GeV. Beginning in 1998 the proton energy was increased to 920 GeV. During the final months of operation, HERA also used proton energies of 460 GeV and 575 GeV, which facilitated measurements of the proton longitudinal structure function F_L.

3.2.2 Lepton Injection and Acceleration

HERA used electrons and positrons for the lepton beam during operations (see Section 3.2.3). The electrons were obtained from a hot filament, while the positrons

were obtained from e^+e^- pair production from bremsstrahlung ("braking") radiation emitted by electrons passing through a tungsten sheet. The electrons[1] were then injected into DESY II, where they were accelerated to an energy of 7 GeV before being fed into the PETRA II ring, where they were accelerated to 14 GeV. From the PETRA II ring, the electrons were injected to the HERA ring and accelerated using conventional dipole magnets with a field strength of 0.165 T to a final interaction energy of 27.5 GeV.

3.2.3 Beam Circulation and Collisions

The proton and electron beams in HERA were circulated in opposite directions in separate rings with two interaction points. Quadrupole magnets were used to focus both beams, with sextupole magnets also used on the electron beam. During injection, the electron and proton beams were separated into bunches with a 96 ns spacing between bunches. HERA could hold up to 220 bunches each of protons and electrons, but not all bunch positions were filled during HERA operations. Approximately 15 consecutive bunches in both the proton and electron beams were left unfilled to allow time for the kicker magnets responsible for dumping the beams to energize. In addition to these "abort" gaps, both the proton and electron beam contained bunches intentionally left empty such that each beam contained pilot bunches, bunches of electrons or protons paired with an empty counterpart. The pilot bunches were used for studies of beam-gas interactions, background caused by protons or electrons interacting with residual gas in the 3×10^{-11} Torr vacuum.

---

[1]From this point, the term "electron" is used interchangeably for both positrons and electrons, unless stated otherwise.

Near the interaction regions, guiding magnets directed the proton beam into the electron beam path to allow for *ep* interactions. For a proton beam energy of 920 GeV and an electron beam energy of 27.5 GeV, the center-of-mass energy is approximately $318\,\mathrm{GeV}^2$.

3.2.4 HERA Luminosity

Between 2000 and 2002, HERA underwent an upgrade in luminosity (number of interactions per unit area per unit time), where additional focusing magnets were installed to reduce the cross-sectional area of the beam profiles in the interaction regions. Prior to the luminosity upgrade (the "HERA I" running period), the peak luminosity was approximately $2\times10^{31}\mathrm{cm}^{-2}\mathrm{s}^{-1}$. After the luminosity upgrade, the peak luminosity delivered was $5.1\times10^{31}\mathrm{cm}^{-2}\mathrm{s}^{-1}$. Figure 3.3 shows the integrated luminosity for each year of HERA I and HERA II, while Figure 3.4 shows the complete integrated luminosity delivered to the ZEUS experiment by HERA.

3.3 Detection of Particle Interactions

As particles pass through matter, they deposit energy through radiation, particle production, or reactions with the medium through which they pass. The amount and pattern of energy deposited by the particles depends on the particles and the medium, which helps in the identification of the particles.

3.3.1 Electromagnetic Showers

High energy electrons passing through a medium lose their energy primarily through bremsstrahlung radiation, while high energy photons lose their energy primar-

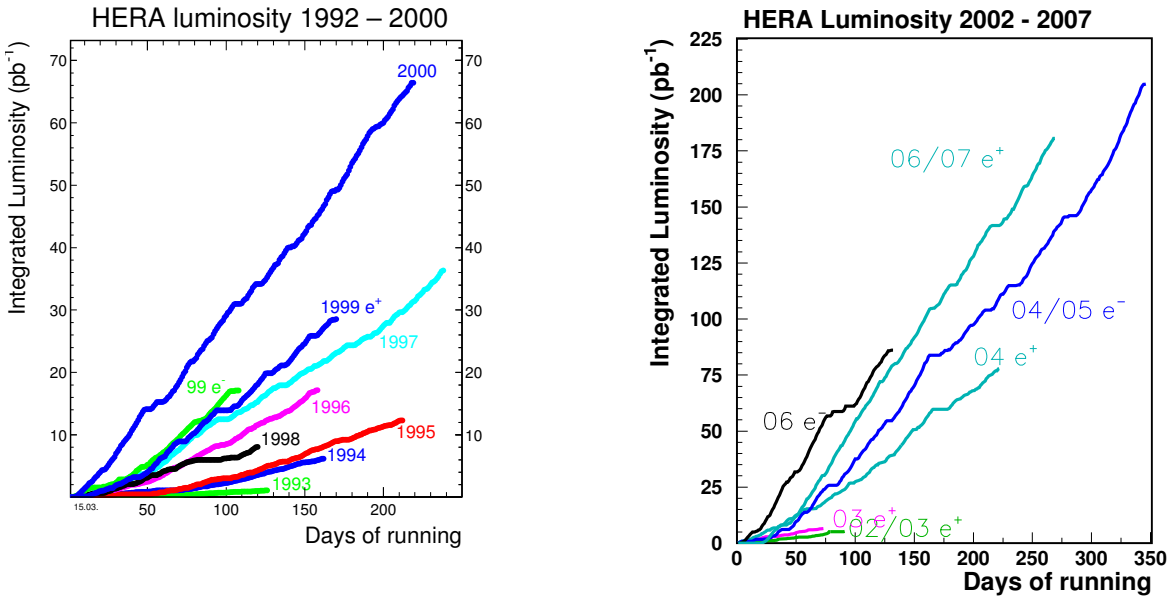

Figure 3.3: The integrated luminosity delivered by HERA for each year of its operation. The figure on the left is the delivered luminosity from HERA I, and the figure on the right is the delivered luminosity from HERAII.

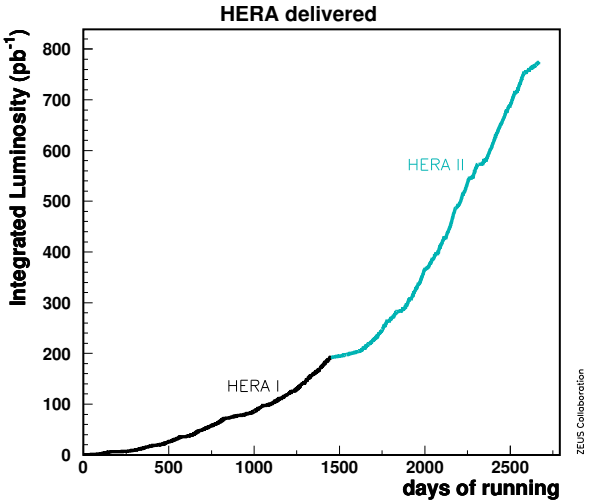

Figure 3.4: The combined integrated luminosity delivered by HERA over its entire operation.

ily through e^+e^- pair production, with the e^+e^- pairs then undergoing the bremsstrahlung process. Subsequent energy deposits from bremsstrahlung and pair production result in an electromagnetic shower. The depth of an electromagnetic shower in a medium is a function of the energy of the incident particle and the properties of the medium, and is usually expressed in terms of the Radiation Length, X_0. For a high-energy electron, X_0 is defined as the average length it takes the electron to lose all but $1/e$ of its original energy. For a high-energy photon, it is 7/9 of the mean free path for pair production. Like the shower depth, X_0 is a characteristic property of the medium and depends on its atomic number and atomic weight. Quantitatively, the characteristic depth for the electromagnetic shower maximum is given by

$$t_{max} \approx \log(E/\epsilon) - a \tag{3.1}$$

where t_{max} is expressed in terms of X_0, $a = 0.5$ for photons and 1.0 for electrons, ϵ is the critical energy of the medium–the point at which energy loss from bremsstrahlung is equal to the energy loss from ionization of the medium–and E is the energy of the incident particle. The depth at which 95 % of the shower is contained is

$$t_{95\%} \approx t_{max} + 0.08Z + 9.6 \tag{3.2}$$

The width of the electromagnetic shower is given as

$$R_{95\%} \approx 14A/Z \tag{3.3}$$

where A and Z are the atomic mass and atomic number of material, respectively.

3.3.2 Hadronic Showers

Whereas the electromagnetic showers proceed via the electromagnetic force, hadronic showers proceed via the strong interaction, where an incoming hadron, such as a proton, pion, or neutron, undergoes an inelastic interaction with the medium. Because π^0 particles are often produced in these interactions, hadronic showers generally have an electromagnetic component as well. The characteristic length of a hadronic shower is expressed in terms of the nuclear interaction length λ, which is the mean free path of a particle before undergoing a non-elastic nuclear interaction. Like the radiation length X_0, λ is also a property of the medium traversed by the particle.

The shower maximum for a hadronic shower is

$$l_{max} \approx 0.6 \log(E) - 0.2\lambda \tag{3.4}$$

Like the characteristic depth t_{max} for the electromagnetic shower, which is expressed in terms of X_0, l_{max} is expressed in terms of λ. The depth of 95% containment is

$$l_{95\%} \approx l_{max} + 4E^a\lambda \tag{3.5}$$

where $a = 0.15$ and E is the energy of the incident hadron. For most materials used for particle detectors, $\lambda \sim 20X_0$, which means that hadronic showers are broader and occur further into the medium than do the electromagnetic showers.

3.3.3 A Generic Particle Detector

Figure 3.5 shows a general template for a particle detector for an experiment studying the interactions of colliding beams. The interaction point of the colliding

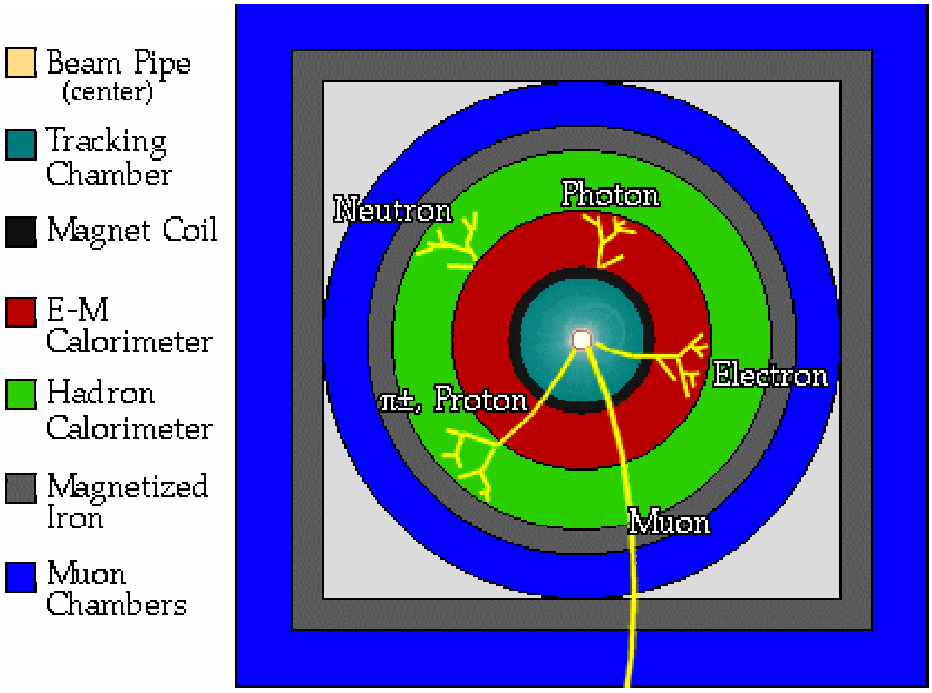

Figure 3.5: A an $x - y$ view of a generic particle detector shown with the most important components and diagrams of the behavior of different types of particles in the detector.

beams is usually at the center of the detector. The detector layer closest to the interaction point is usually a tracking chamber and/or vertex detector. A tracking chamber measures the path of a charged particle traveling through a magnetic field by detecting the slight ionization created by the particle traveling through the chamber. The transverse momenta of the particles can be measured from the deflection of the particles by the magnetic field according to the cyclotron equation, $p_T = qBr$. The charge of the particle can be determined from the direction of curvature of the track it leaves. Particles without electric charge, such as neutrons and photons do not leave tracks.

The next layer in the detector is the calorimeter, which measures the energy and

position of incident particles by absorbing the particles. Whereas the design goal of the tracking chamber is to cause minimal disturbance to the particles, the calorimeter is designed to contain the particle and its resulting shower (electromagnetic or hadronic) completely. Also unlike the tracking detectors, calorimeters detect neutrally charged particles. The accuracy of a calorimeter increases with the energy of the incident particles, as the shower fluctuations decrease as the number of particles in an electromagnetic or hadronic shower increases.

Calorimeters are usually segmented such that the maximum amount of information about the the incident particle can be obtained. The first level of segmentation is the separation of the calorimeter into two longitudinal components: the electromagnetic calorimeter and the hadronic calorimeter. The depth of the electromagnetic and portion of the calorimeter are chosen such that electromagnetic showers are contained entirely within the electromagnetic portion of the calorimeter, and is therefore determined from the radiation length X_0, while the depth of the hadronic calorimeter is determined from the interaction length, λ. To ensure that incident hadrons deposit the minimum amount of energy in the electromagnetic portion of the calorimeter, the parameter λ/X_0 should be maximized. Figure 3.5 shows different types of showers in the calorimeter initiated by different types of particles. The next level of segmentation for calorimeters is the transverse subdivision into cells, in which radially projected towers are created within the calorimeter, allowing for the measurement of latitudinal and longitudinal shower profiles.

Unlike hadrons and electromagnetic particles, muons interact with the detector components by leaving an ionizing track in all components. Muon chambers allow for

identification of muons, as muons leave a track in the chambers that can matched to the muon track through the tracking chamber and calorimeter.

3.4 The ZEUS Detector

The ZEUS collaboration, which is made up of approximately 350 physicists, technicians, and staff from 37 institutes in 15 countries, performed studies of *ep* interactions using the ZEUS detector, which was located 30 m underground in the southern HERA experimental hall with dimensions of 12m $\times$ 10m $\times$ 19m and a weight of 3600 tonnes. It was one of the two general purpose detectors at HERA used to make precision physics studies of interactions by measuring the energies, direction of travel, and momentum of particles produced in *ep* interactions. A schematic diagram of the ZEUS detector is shown in Figure 3.7. The forward direction in the ZEUS coordinate system is defined as the direction of the proton beam. ZEUS was a asymmetric hermetic detector, covering the entire solid angle with the exception of the beam pipe. Because of the imbalance in the energy of the protons and the electrons in HERA *ep* collisions, most hadronic particles were emitted in the forward direction[2]. To account for this effect, the sub-detector components in the forward region were larger and deeper than their counterparts in the rear region.

The ZEUS detector was comprised of sub-detectors used for tracking, calorimetry, and muon detection. The tracking measurements and vertex determination were handled by the wire chambers comprising the Central, Rear, and Forward Tracking Detectors (CTD, RTD, and FTD) [22]. For the HERA II running period beginning in

[2]The ZEUS coordinate system is a right-handed Cartesian system, with the Z axis pointing in the proton beam direction, referred to as the "forward direction", and the X axis pointing left towards the center of HERA. The coordinate origin is at the nominal interaction point.

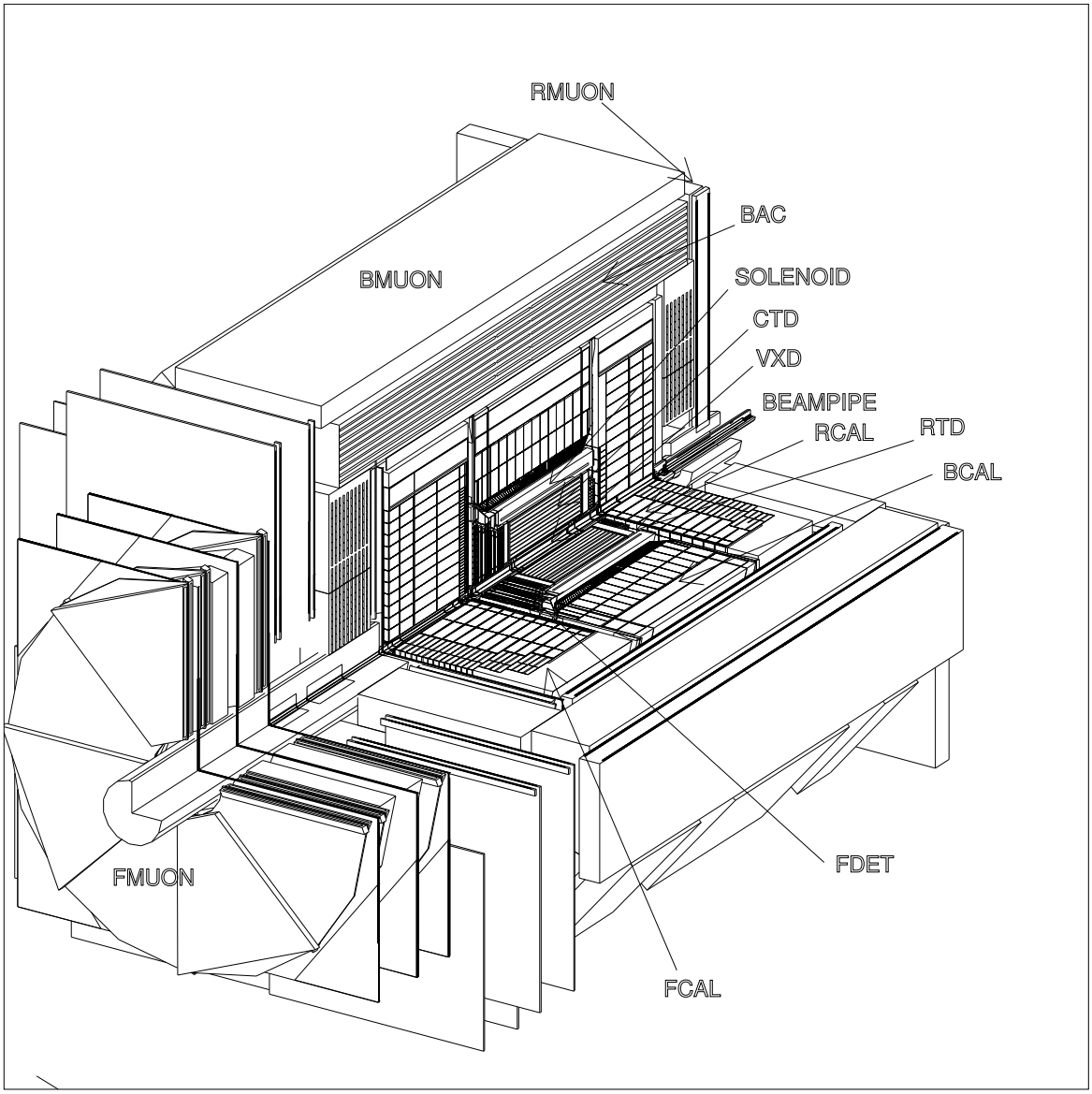

Figure 3.6: A 3-dimensional cutout view of the ZEUS detector.

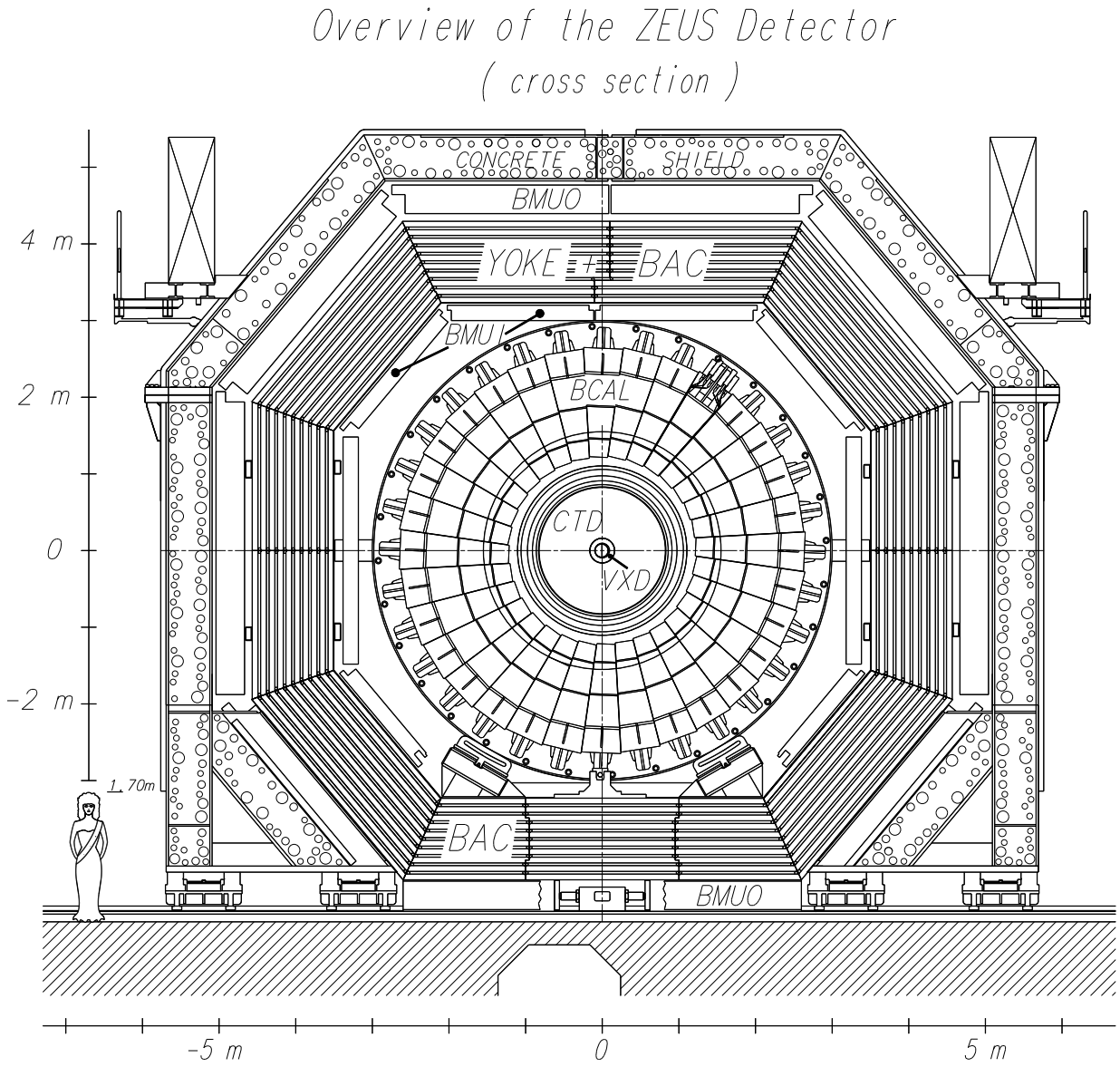

Figure 3.7: A 2-dimensional $x - y$ view of the ZEUS detector.

2002, the silicon-based ZEUS Micro Vertex Detector (MVD) was installed to replace the malfunctioning Vertex Detector (VXD, shown in the Figure 3.7), which was removed in 1996. During the 1998 - 2000 running period, the tracking detectors were the innermost subcomponents from the beam pipe. The tracking detectors were surrounded by a solenoid that provided a magnetic field of 1.43 T, which allowed for determinations of transverse momenta of and charge of charged particles by measurements of the direction and radius of curvature of their deflections in the field.

The tracking detectors were encompassed by the hermetic depleted Uranium-scintillator Calorimeter (CAL) [23]. Between the electromagnetic and hadronic portions of the front and rear sections of the CAL was the Hadron-Electron Separator (HES), which helped distinguish between electromagnetic and hadronic showers in the RCAL, where most electrons from DIS interactions would deposit their energy. Hadronic showers not fully contained by the CAL deposited their remaining energy in the Backing Calorimeter (BAC), which consisted of proportional tube chambers used with the magnetized iron yoke to record energy deposits in the yoke. The outer layer of the ZEUS detector consisted of the limited streamer tube chambers used to identify tracks from muons. The muon transverse momenta were measured both from the information from the tracking chambers and from the deflection of the muon traversing the toroidally magnetized iron yoke, which had a magnetic field strength of up to 1.6 T. The forward muon (FMUON) chambers could measure highly energetic muons with energy up to 150 GeV/c.

A thorough description of the ZEUS detector is found in the ZEUS bluebook [24]. The components most important to this analysis are detailed in the subsequent sec-

tions.

3.4.1 ZEUS Tracking Detectors

The ZEUS tracking system was designed to measure the momentum and charge of particles and to determine the event vertex from the tracking information provided by the CTD. During the 1998-2000 data taking period, the innermost components of the tracking system were the CTD, RTD, and FTD.

The CTD was a cylindrical wire drift chamber filled with a gas mixture of $Ar:CO_2:C_2H_6$ of 85:13:2. A wire drift chamber contains multiple positively charged signal, or *sense*, wires and negatively charged potential, or *field*, wires in a gas medium. A charged particle passing through the gas ionizes the molecules. The electrons released by the ionization drift at a known speed towards the sense wires, while the ions drift slowly towards the field wires. As the freed electrons travel towards the sense wire, they further ionize the gas, which results in an shower of electrons reaching the sense wire and producing a measurable current pulse in the sense wire (an example of this process is shown in Figure 3.8). The position of the track in the cell is determined by measuring the time of arrival of the electron shower.

The active length of the CTD was 205 cm and its active radius was $18.2 - 79.4$ cm. It was centered on the nominal interaction point. The 205 cm active length allowed for a polar angle coverage of $15° < \theta < 164°$, with θ defined with respect to the $+z$-axis, which corresponds to a coverage in pseudorapidity of $-1.96 < \eta < 2.03$.

The structure of the CTD is shown in the $x - y$ view of the CTD shown in Figure 3.9. The CTD consisted of 9 concentric superlayers, with each superlayer comprised of 32 - 96 drift cells, each cell containing 8 tungsten sense wires. In total,

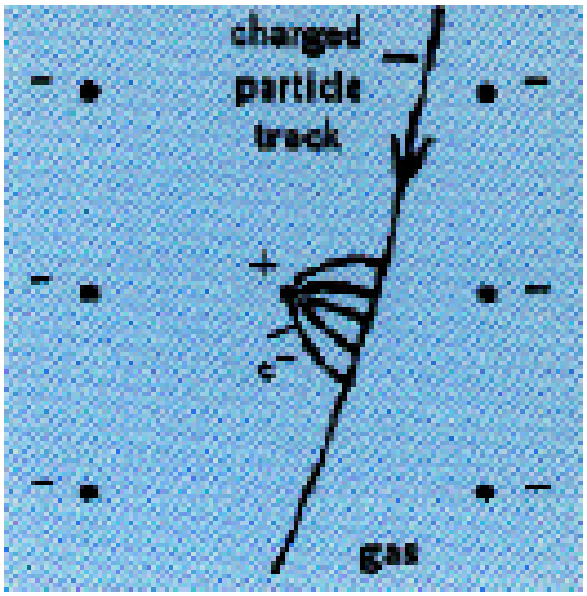

Figure 3.8: An example of a charged particle traversing a wire drift chamber. The electron shower produced by the gas ionization is shown arriving at the sense wire at center.

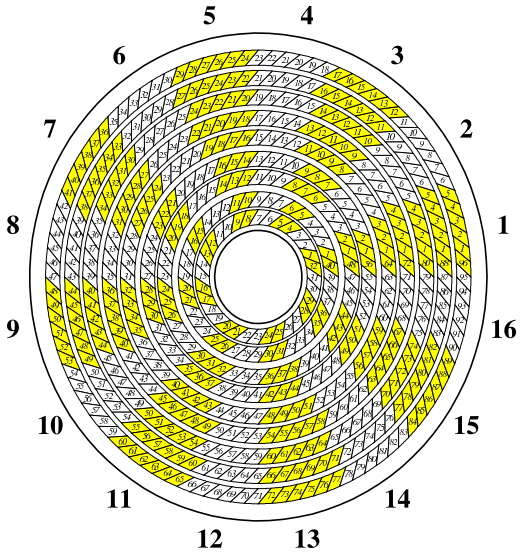

Figure 3.9: An $x - y$ view of the ZEUS CTD. Shown are the 9 superlayers and 16 sectors. The cells in the CTD are numbered according to their superlayer position (with superlayer 1 being the innermost) and their sector.

the CTD contained 4608 sense wires. As shown in Figure 3.9, the drift cells were rotated by a 45° Lorentz angle to the electric field. In 5 of the superlayers, the wires were parallel to the chamber axis, while in the other 4 superlayers, the wires were set at a stereo angle (angle from the $+z$ axis) of approximately $\pm 5°$ to ensure the resolution in azimuthal and polar angles was roughly equal and to provide a good accuracy in measuring the polar angle of tracks.

The transverse momentum resolution for tracks with $p_T > 150$ MeV that have passed through all superlayers is $\sigma(p_T)/p_T = 0.0058 p_T \oplus 0.0065 \oplus 0.0014/p_T$ [25], with p_T in GeV. The spatial resolution of a track passing through all superlayers is 180 μm in the $r - \phi$ direction and 2mm in the z-direction. The first three axial superlayers (superlayers 1, 3, and 5) were also equipped with a z-by-timing system [26], which used the difference in the pulse arrival times at either end of the detector for a quick determination of the z-position of a track within $\sim$ 3cm. The information from the z-by-timing system was used in the first and second level trigger information (see Section 3.4.7). The tracking system was also used to measure the interaction vertex with a typical resolution along (transverse to) the beam direction of 0.4 (0.1) cm and also to cross-check the energy scale of the calorimeter.

3.4.2 The ZEUS Calorimeter

As discussed in Section 3.3.3, a calorimeter is designed to provide accurate measurements of the energy and position of incident particles and to distinguish hadronic showers from electromagnetic showers. For measurements of the energy of incident particles, the ZEUS CAL, shown in Figure 3.10, used alternating layers of depleted Uranium absorber, encased in a thin foil of stainless steel, and plastic scintillator,

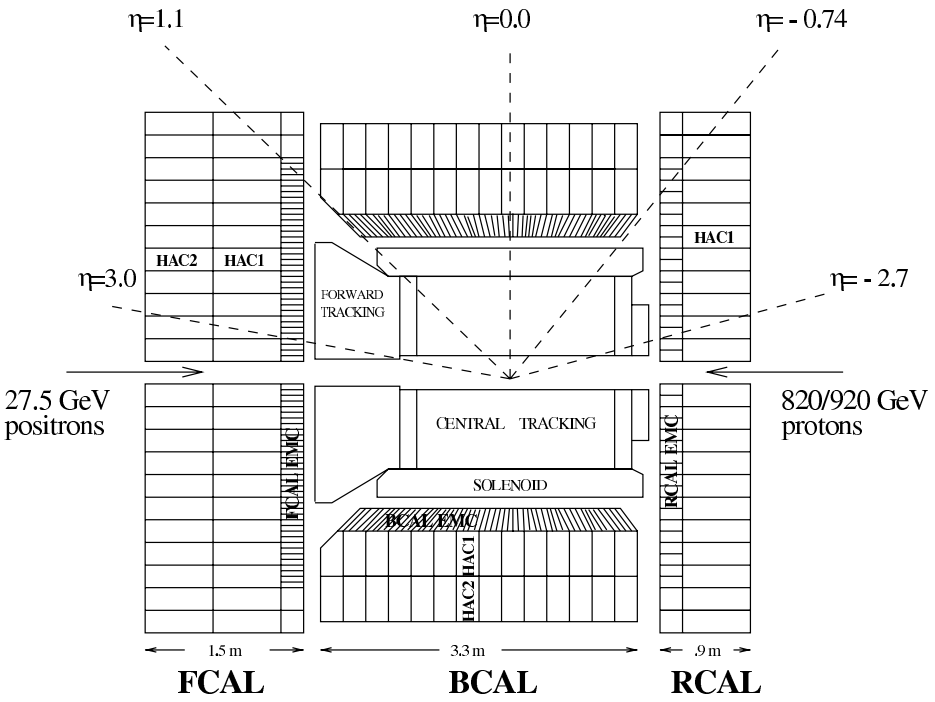

Figure 3.10: An $x - y$ view of the ZEUS CAL. The boundaries between the CAL sections are indicated by their approximate pseudorapidities from the nominal interaction point.

which converted a fraction of the deposited energy into light, which was then converted into a signal by photomultiplier tubes (PMTs). The uranium-scintillator sandwiches were stacked repeatedly to form the individual cells of the calorimeter. Calorimeters that use different materials for absorption and detection are known as sampling calorimeters, since only a fraction of the deposited energy is converted into a signal. The ZEUS CAL, which used alternating layers of Uranium and scintillator, was also termed as a sandwich-type sampling calorimeter.

Because hadronic and electromagnetic showers proceed via different processes, the signal response from an electromagnetic shower differs from that of a hadronic shower. Because hadronic showers proceed via nuclear interactions, some energy is

lost in overcoming the nuclear binding potential, a process with a non-detectable energy dissipation. As a result of this effect, the ratio of the average signal response from an electromagnetic shower to that from a hadronic shower, e/h, is typically between 1.1 and 1.35, depending on the absorber material used. A non-unity e/h ratio is problematic because the average electromagnetic component of a hadronic shower increases logarithmically with the energy of the initializing particle. A non-unity e/h ratio therefore produces a non-linear overall response to a hadronic shower and a resolution worse than that of a detector with an e/h ratio of 1.

To make the ZEUS CAL a compensating calorimeter (a sampling calorimeter for which $e/h = 1$), detailed theoretical calculations and test measurements were employed [24]. The energy from the fission of the ^{238}U in the ZEUS CAL, primarily in the form of neutrons and soft photons, compensated for the energy loss from the nuclear binding energy [27]. The steel cladding of the ^{238}U plates provided a small signal attenuation from soft photons in the electromagnetic showers and from the ^{238}U fission (thereby selectively boosting the signal of the hadronic component of the hadronic showers[3]). The thickness of the scintillator was chosen based on the neutron response of the scintillator–a thicker scintillator layer captures a larger portion of the neutron energy from the ^{238}U fission. For Uranium plates with a thickness of 1 X_0, which for ^{238}U is 3.3 mm, a scintillator thickness of 2.6 mm was chosen based on test measurements. The ZEUS CAL e/h ratio was 1.00 ± 0.05, thus making it a compensating calorimeter.

Aside from its use in achieving a compensating calorimeter, Uranium has a

[3]For the ZEUS CAL, the effect of the steel cladding was a reduction in e/h of 0.03 [24]

very high Z number, which means that particle showers form after traveling a short distance through it. This allows for a compact calorimeter. The natural radioactivity of ^{238}U also provides a small constant uniform background radiation, which was used for calibrating the CAL. The steel foil encasing the ^{238}U plates served to adjust the signal from the background radiation. Because of the well-understood background, it was possible to calibrate the absolute energy scale of the CAL to a level of 1%.

As shown in Figure 3.10, the CAL was divided into three sections: a forward segment (FCAL), a barrel segment (BCAL), and a rear segment (RCAL). These segments were divided into modules, which were further segmented into towers with a front surface dimension of 20 cm $\times$ 20 cm. The towers were longitudinally segmented into an electromagnetic (EMC) section and either one (RCAL) or two (FCAL, BCAL) hadronic sections (HAC). A diagram of a BCAL tower is shown in Figure 3.11. The EMC section of a tower was comprised of 4 EMC cells in the FCAL and BCAL and 2 EMC cells in the RCAL. Each HAC section constituted a HAC cell. All EMC cells had a depth of 1 interaction length, λ, which for ^{238}U is equal to 25 radiation lengths X_0. The HAC cells of the FCAL and RCAL had a depth of 3λ, while the HAC cells of the BCAL had a depth of 2λ. This asymmetric arrangement reflects the difference in energy between the proton and electron beams, with final state particles in the forward direction being greater in number and energy than particles in the rearward direction. The depth of the CAL ensured 95% containment of 90% of the jets in all parts of the CAL. Table 3.1 summarizes the characteristics of the CAL sections.

The light produced by the particles traveling through the scintillator was fed through wavelength shifters into the PMTs, which in turn digitized the signal received

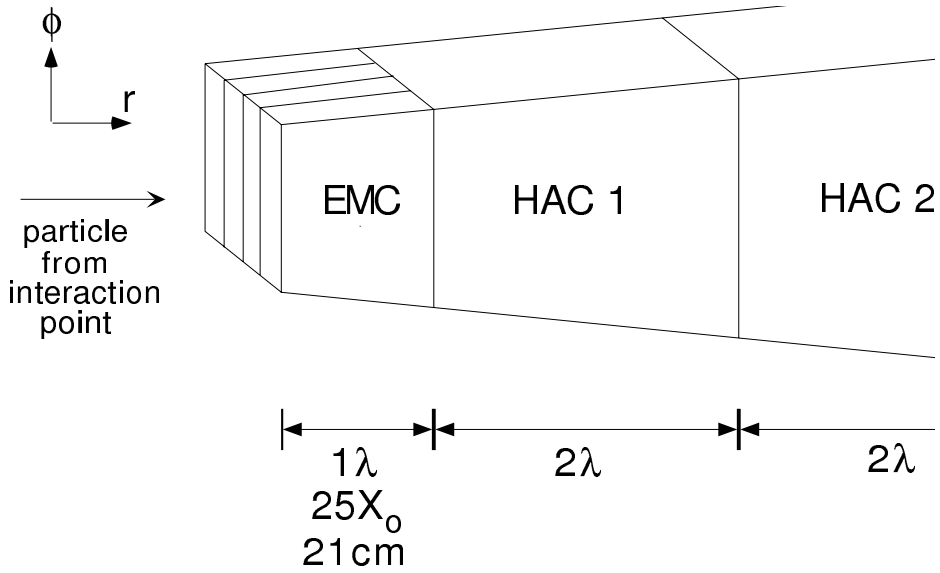

Figure 3.11: A diagram of a BCAL tower. 4 EMC cells are stacked horizontally and backed by 2 HAC cells. Unlike the cells in the FCAL and RCAL, the BCAL towers were projective in η and ϕ.

	FCAL	BCAL	RCAL
Angular Coverage (θ)	$2.2° - 39.9°$	$36.7° - 129.1°$	$128.1° - 176.5°$
Angular Coverage (η)	$1.01 - 3.95$	$-0.74 - 1.10$	$-3.49 - -0.72$
Number of Modules	24	32	24
Towers/Module	$11 - 23$	16	$11 - 23$
Number of Cells	2172	2592	1668
Depth (m)	1.5	1.07	0.84
Depth (λ)	7.1	5.1	4.0
Depth (X_0)	181.0	129.0	103.0
EMC Front Face Dimensions (cm)	5×20	5×20	10×20

Table 3.1: Properties of the ZEUS CAL listed by section.

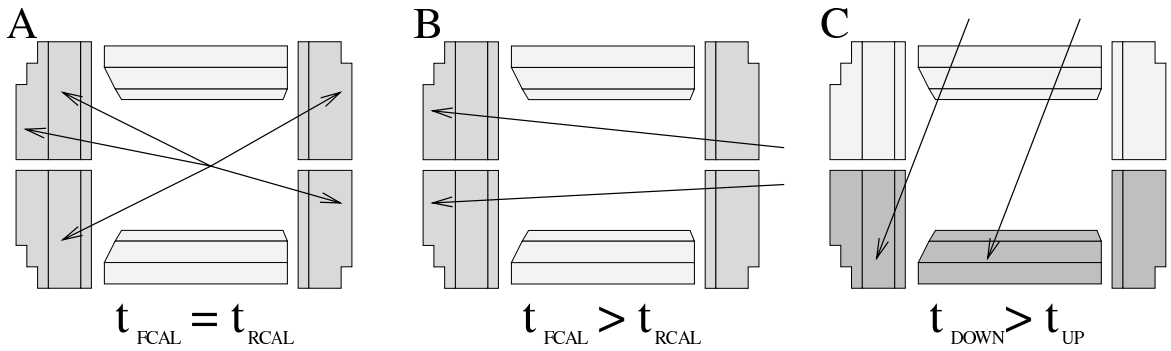

Figure 3.12: The timing of various events in the ZEUS detector. Figure A shows the timing for an event consistent with an *ep* interaction. Figure B shows the timing for an event initiated by beam-gas interactions. Figure C shows the timing for a cosmic muon event.

from the shifters and passed the information to the readout electronics. Each cell had two PMTs, which allowed for averaging the signal in each cell for a more uniform detector response. Having two PMTs per cell also provided a degree of redundancy, as a single dead PMT would not create a dead cell. The use of scintillator and PMTs for readout is suited to experiments with a high interaction rate. The pulses from the PMTs were kept shorter than the 96 ns crossing rate to avoid pile-up effects, and the quick rise time of the PMTs allowed for measurements of pulse timing to within a nanosecond, which was important for suppression of background from beam-gas interactions and cosmic rays (see Figure 3.12 and Section 3.4.5).

The CAL energy resolutions were measured under test-beam conditions to be $\sigma(E)/E = 0.18/\sqrt{E}$ for electromagnetic showers and $\sigma(E)/E = 0.35/\sqrt{E}$, with E in GeVin both cases, for hadronic showers [24].

There were several other components which were, at some point during the ZEUS operation period, part of the calorimeter system. These included the small-angle rear tracking detector (SRTD), the beam-pipe calorimeter (BNC), the forward and rear

presamplers (RPES) and barrel presampler (BPRES), the forward plug calorimeter (FPC), the backing calorimeter (BAC), which surrounded the CAL and served to correct or reject showers that leaked from the CAL and help identify muons, and the hadron-electron separator (HES).

3.4.3 Luminosity Monitor

A measured cross section is the number of events per luminosity: $\sigma = N/\mathcal{L}$. For the absolute normalization of these cross sections to be accurate, an accurate measurement of the luminosity is essential. To obtain a precise measurement of the luminosity, HERA measured the rate of the well-understood Bethe-Heitler process ($ep \rightarrow e^{'}\gamma p$), in which lepton-proton bremsstrahlung produces a lepton and photon at small scattering angles [28]. Because the Bethe-Heitler cross section is well known for photons emitted at a fixed angle and energy, measuring the rate of photon production (N_γ) at a fixed angle and energy provides an accurate measurement of the luminosity: $\mathcal{L} = N_\gamma/\sigma_{BH}$.

The ZEUS luminosity system, shown in Figure 3.13, used a lead-scintillator photon calorimeter located at $z = -107$ m and an electron calorimeter at $z = -35$ m. To filter out soft (0.01 MeV) photons produced from the synchrotron radiation, a carbon-lead filter was placed in front of the photon calorimeter. The energy resolution of the photon calorimeter with the filter was measured in a test beam to be $\sigma(E) = 25\%\sqrt{E}$, while the resolution of the electron calorimeter was $\sigma(E) = 18\%\sqrt{E}$, with E in GeV. Events with coincident deposits in the photon and electron calorimeters were used to calibrate the energy scale of the photon calorimeter, as the combined energies of the detected photon and electron were equal to the initial electron energy.

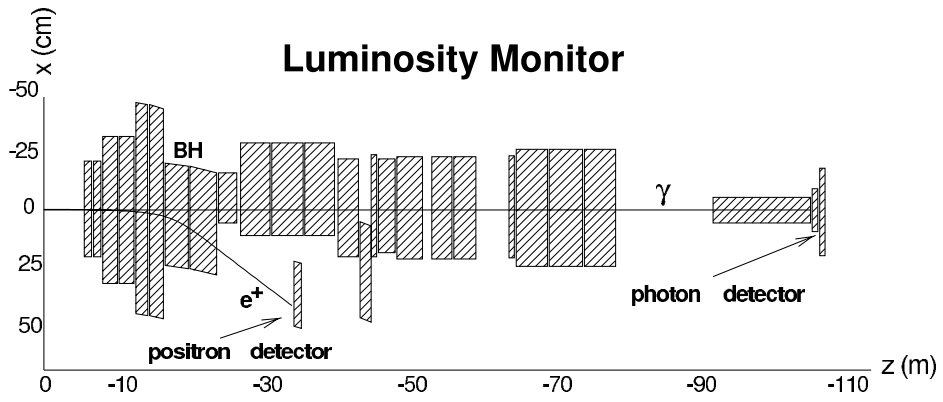

Figure 3.13: The layout of the ZEUS luminosity system.

3.4.4 Veto Wall and C5 Counter

The Veto Wall was an iron slab covered with scintillator on both sides. It was located at $z = -7$m and measured $8 \times 7.6 \times 0.86$m with square holes with a width of 0.95m to accommodate the beam pipe and magnets. The Veto Wall shielded the detector from particles produced in the proton beam halo, provided information used to reject events with halo particles that passed the Veto Wall, and provided timing information to reject beam-gas interactions. The C5 counter was a scintillator attached to the C5 collimator at $z = -3.15$m that provided timing information used to synchronize the HERA and ZEUS clocks and to reject events originating from beam-gas interactions.

3.4.5 Trigger and Data Acquisition

During typical HERA operations, proton and electron bunches crossed every 96 ns, which gave a bunch crossing frequency of 10.4 MHz, with actual ep interactions occurring at a frequency of about 10 Hz. The total background rate was roughly 100

kHz, which due to bandwidth and storage limitations was not written to tape. The primary sources of background were from beam-gas interactions (the largest contribution to the overall background), halo muon events, and cosmic rays. The signature of a beam-gas event is a shower of particles entering the detector from upstream or downstream, depending on which beam interacts with the gas, and leaving energy deposits in the calorimeter and tracking detectors. Halo muon events were a byproduct of the proton beam-gas interactions and beam scraping, where the proton beam would occasionally hit the quadrupole magnets, which produced muons via pion decay that traveled approximately parallel to the proton beam and left energy deposits in the calorimeter and muon chambers. Cosmic events, which were the smallest source of background, came from cosmic rays, primarily protons and alpha particles, interacting with the earth's atmosphere and producing particle showers. The signature of a cosmic event at ZEUS was muons entering the detector roughly perpendicular to the z-axis.

To work within the storage and bandwidth limits of the Data Acquisition (DAQ) system, ZEUS employed a 3-level real-time online trigger system to reduce the rate from the 10.4 MHz crossing rate to a rate of 10 Hz written to tape. The goal of the trigger system was to reject as much background as possible while keeping events consistent with ep interactions that could contribute to a physics measurement. The ZEUS trigger system was tiered such that the output rate of each level was lower than the maximum possible input rate for the subsequent trigger level. Each subsequent trigger level therefore increased the complexity of the triggering requirements because of the larger amount of information and calculation time available per event.

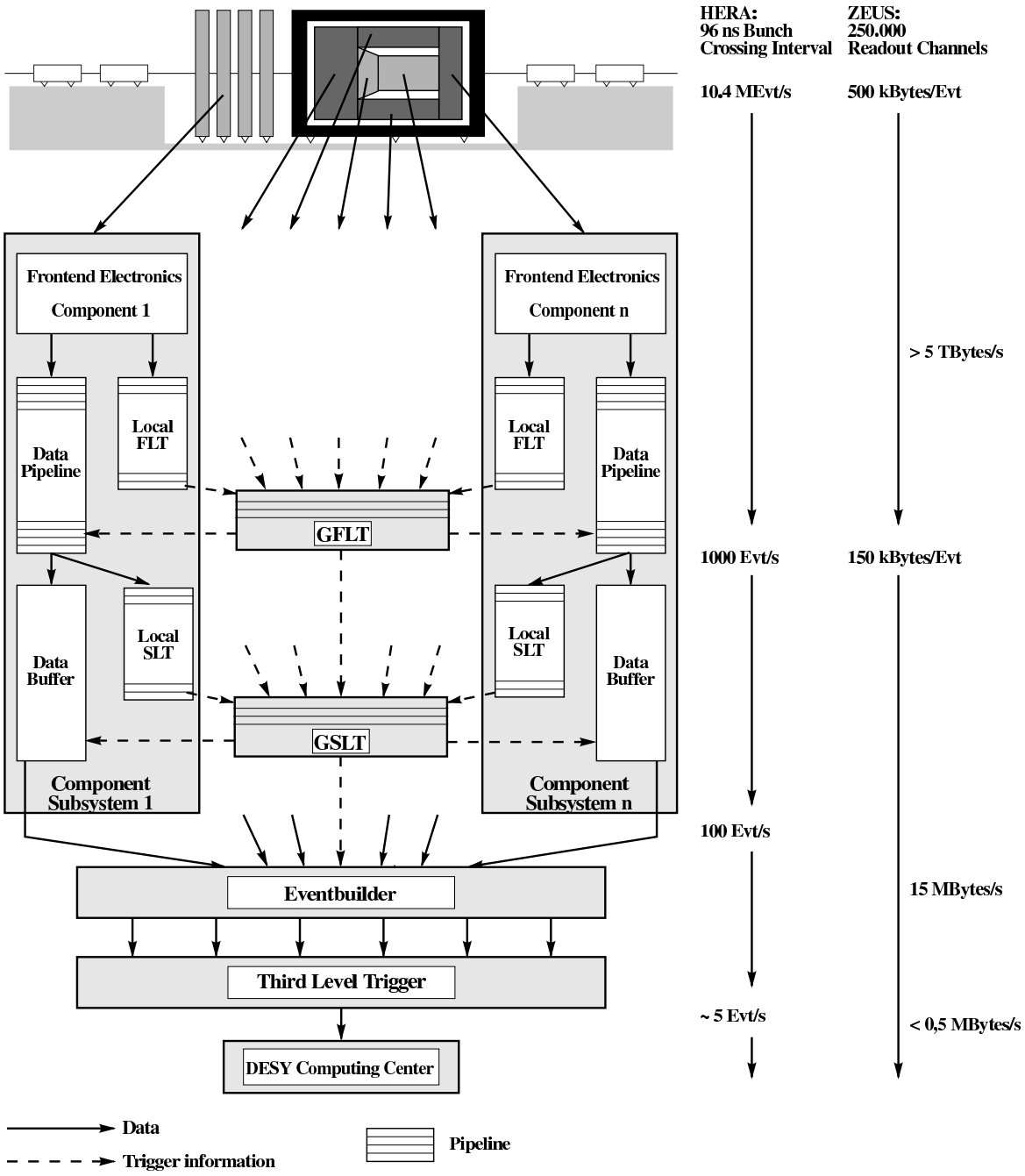

Figure 3.14: A diagram of the ZEUS trigger and DAQ system.

3.4.5.1 First Level Trigger

Because the First-Level Trigger (FLT) could not make a decision within the 96 ns bunch crossing time, each component had a 5 μs pipeline, which stored the complete information from that component and was synchronized with the HERA clock on a 96 ns cycle. Most components also had their own FLTs, which used a subset of the complete event information to perform triggering calculations and then send their triggering information to the Global First Level Trigger (GFLT) within 1.0 - 2.5 μs after the bunch crossing. The GFLT combined the trigger information from the components and sent the trigger decision to the front-end electronics of the components. The GFLT reported a first level trigger decision every 4.4 μs. Because of the 5 μs pipeline, the GFLT operated with minimal deadtime, instances where event information was discarded rather than processed, which was normally 1 - 2% during data taking.

3.4.5.2 Second Level Trigger

When an event was triggered at the first level, the full component information was passed to each component's Second-Level Trigger (SLT). Component SLTs were transputer-based networks which sent their information to the transputer-based Global Second Level Trigger (GSLT). Because of the larger computation time available at the second level (10 ms), the SLT made more complex calculations, such as basic vertex finding from the CTD SLT (later changed to the Global Tracking Trigger (GTT) during the HERAII running period), and $E - p_z$ calculations from the information from the CAL PMT timing and energy information. The GSLT further reduced the

event rate to 30 - 85 Hz.

3.4.5.3 Third Level Trigger

Events triggered by the GSLT were sent to the Event Builder (EVB), which formatted the data and sent the complete event information to the Third-Level Trigger (TLT). The TLT had about 100 ms to make a triggering decision, which allowed it to use a reduced version of the full reconstruction software on a processor farm to increase the accuracy of the tracking information and vertex finding as well as perform more sophisticated electron finding and jet finding. Events were classified according to the type of interaction (i.e. charged current DIS, photoproduction, neutral current DIS) using software-based TLT filters. The typical TLT output rate was approximately 10 Hz.

Information from events accepted by the online ZEUS trigger system were passed to offline reconstruction software (described in more detail in Chapter 6) and written to data storage tapes. Each event was labeled with trigger bits according to the manner in which the event was accepted, and with additional information calculated during offline reconstruction. The combined online trigger information and offline quantities were used to label events by Data Storage Tape (DST) bits, which provide a means of selecting certain categories of events from the storage tapes for analysis. The overall event section is discussed further in Chapter 7.

Chapter 4

Event Simulation

For an experimental measurement to be useful, it should be compared to theoretical predictions. To be comparable to experimental measurements, any theoretical prediction of partonic final states should therefore include a hadronization step in which the partons convert to colorless hadrons, and a step for simulating the detector response and acceptance in order to remove any detector effects from the final result. Both of these steps are handled by means of the Monte Carlo method of event simulation.

4.1 Monte Carlo Simulations

For pQCD calculations, the theoretical predictions are not analytically calculable to all orders in α_s, which requires the simulation of higher-order effects. A method employed extensively in HEP is the Monte Carlo (MC) method, which uses pseudo-random numbers weighted in accordance with the underlying process being modeled. Using the probability distributions as input, the MC programs use the random numbers to sample over the distributions to simulate events. This technique is applicable when the probability distributions are well-understood and can be simulated accurately, and is useful for probabilistic calculations based on pQCD.

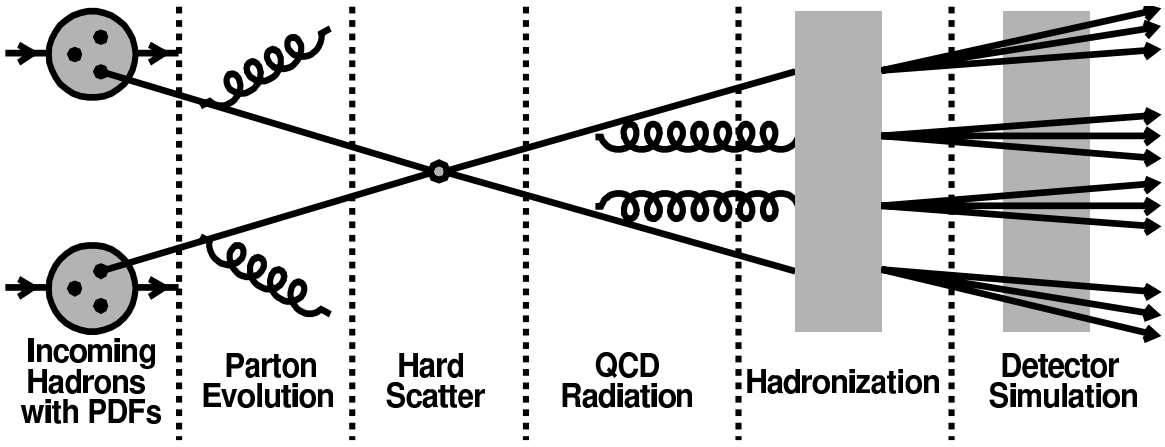

Figure 4.1: An illustration of the stages in the simulation of a HEP event.

A complete simulation of an event in ep collisions proceeds in several stages. The first stage is the input of initial probability densities, which for this analysis are the proton parton density functions (PDFs) introduced in section 2.1.3. The PDFs in the initial state are then evolved according to the underlying model. The next stage is a calculation the perturbative hard scatter, followed by a simulation of radiative effects. The hadronization process then converts the final state partons into hadrons. The simulated final state is then put through a simulation of the detector.

4.1.1 PDF and Hard Scatter

As discussed in section 2.1.3, the hard and soft terms in a scattering process are separated by factorization, which absorbs the soft terms into the PDFs. The overall PDF comes from a global fit of Leading-Order (LO) and Next-to-Leading-Order (NLO) calculations at a given value of Q_0^2. The quark and gluon distributions are parameterized and predict the evolution of the partons as a function of x and Q^2 (see Section 2.2). Commonly used proton PDF fits come from several groups, among

which are the Coordinated Theoretical-Experimental Project on QCD (CTEQ) [29] and Martin Roberts Stirling Thorne (MRST) [30]. The complete system after the parton cascade has proceeded defines the "parton level" of a simulation.

Calculations from pQCD are used to calculate the *ep* DIS hard process to order $\mathcal{O}(\alpha^2\alpha_s)$. Using the probability distribution and the available phase space the event generator creates a partonic final state according to the model's treatment of the parton cascade.

4.1.2 Parton Cascade

Because the calculations from the hard scatter are only to a fixed order in α_s, the higher order terms are approximated by means of a parton cascade, which also serves to connect the hard scattering process with the hadronic final state. The manner in which the parton cascade is generated allows for the examination of the model used to generate the parton shower. Examining the treatment of the parton shower is important for multijet analyses at low x_{Bj} for two reasons: multijet measurements are sensitive to terms beyond $\mathcal{O}(\alpha_s)$ and the sensitivity to low-x_{Bj} effects of the parton evolution scheme used in the parton cascade should be understood.

4.1.2.1 Matrix Element Plus Parton Shower Approach

QCD radiation can occur in DIS both before and after the hard scattering, as is shown in Figure 4.2. The Matrix-Elements plus Parton Shower (MEPS) [31] approach treats the showers originating from QCD radiation before and after the hard scatter separately. In both cases, however, the parton showers proceed via splitting functions described by the DGLAP equations. The splitting process continues, with

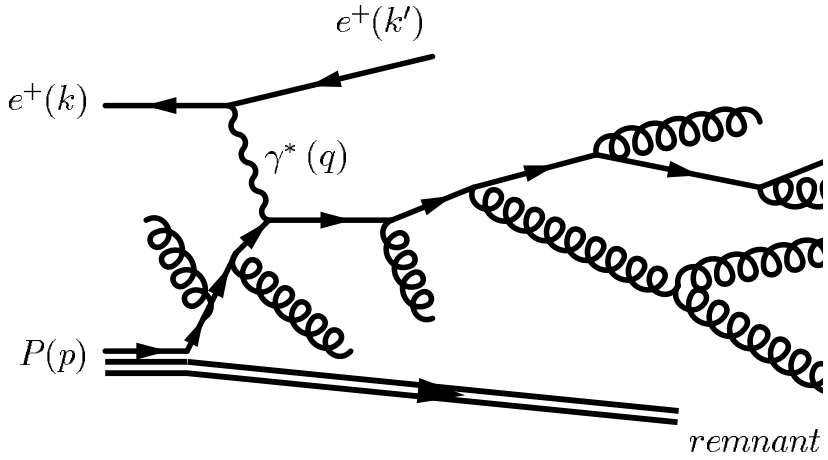

Figure 4.2: A diagram of the MEPS treatment of the parton cascade. As seen in the figure, the MEPS approach accounts for initial-state and final-state QCD radiation.

each emitted parton having a lower virtuality than its parent, until an arbitrary parton virtuality cutoff, typically on the order of $q \sim 1$ GeV^2, is reached. Because the parton shower evolves using the DGLAP evolution equations, the emitted partons are strongly ordered in transverse momentum, k_T, and ordered in the fractional proton momentum carried by the parton, x, with the parton in the hard scatter having the highest k_T and lowest x.

4.1.2.2 Color Dipole Model

The Color-Dipole Model (CDM) [32] treats the proton remnant and the struck quark as a color dipole from which a gluon radiates, which is equivalent to a QCD-Compton (QCDC, see Section 2.3) process. Each radiated gluon forms a color dipole with the struck quark and the proton remnant, which allows for further gluon radiation. In contrast to the MEPS approach, which handles initial state and final state QCD radiation separately, all radiation in the CDM approach comes from the initial dipole between the struck quark and the proton remnant. Unlike the MEPS approach,

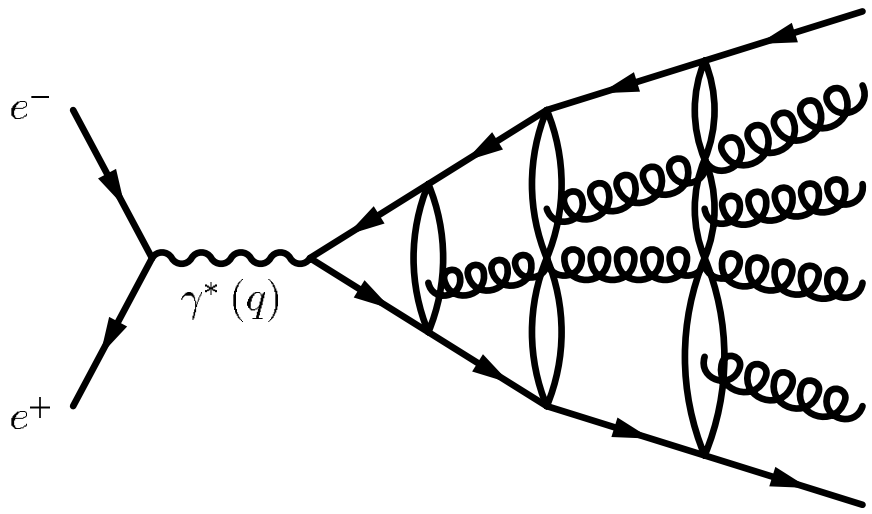

Figure 4.3: A diagram of the CDM treatment of the parton cascade. For *ep* DIS interactions, this model is modified to account for the extended proton remnant and to include BGF processes.

the radiated gluons are not necessarily ordered in k_T.

Because the CDM approach was originally developed for e^+e^- interactions, as Figure 4.3 illustrates, two important adaptations have been applied to the model for use in *ep* interactions. The first modification places a restriction on the fraction of the proton remnant momentum used to generate the dipole, which reduces the available phase space relative to e^+e^- interactions. The second modification is the addition of the matrix elements of the boson-gluon fusion (BGF) processes, which do not occur in e^+e^- interactions. To simulate BGF processes, the struck quark emits its antiquark partner, which forms a separate color dipole with the proton remnant. These two separate color dipoles then proceed via the process described above.

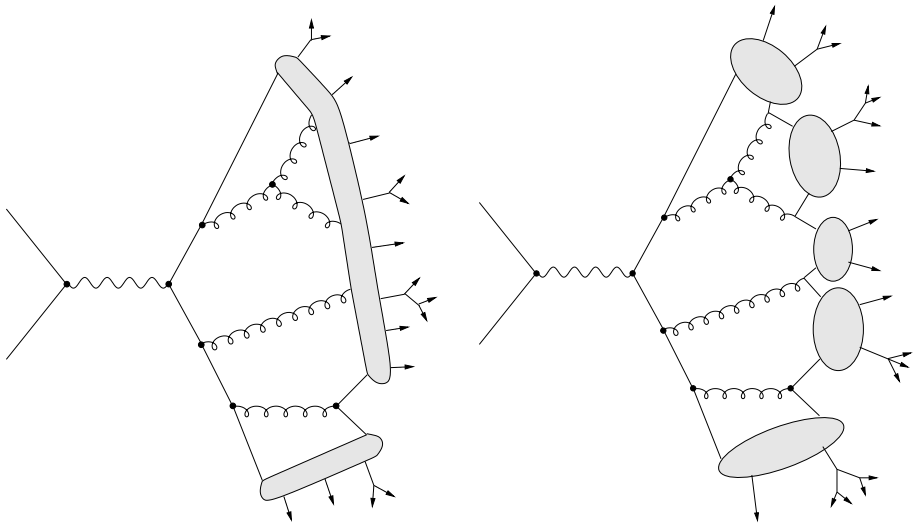

Figure 4.4: Two commonly used hadronization schemes. The Lund string model (left) is shown with $q\overline{q}$ pairs connected via color strings, which are modified by gluons, while the Cluster model (right) shows the gluons separating into $q\overline{q}$ pairs, which are then combined into clusters.

4.1.3 Hadronization

Because QCD confinement (see Section 1.2.1) prevents free colored partons in the final state of an event, the partons produced in the simulations must evolve into colorless stable hadronization that can be observed in a detector, a process known as hadronization. Because hadronization is a non-perturbative effect, it is described instead by phenomenological models. Two commonly used models are the Lund String Model and the Cluster model, illustrated in Figure 4.4. The complete system after the hadronization effects is referred to as the "hadron level."

4.1.3.1 Lund String Model

In the Lund String Model [33] illustrated in Figures 4.4 and 4.5, the color field between a $q\overline{q}$ pair is represented as a one-dimensional string with an energy per unit

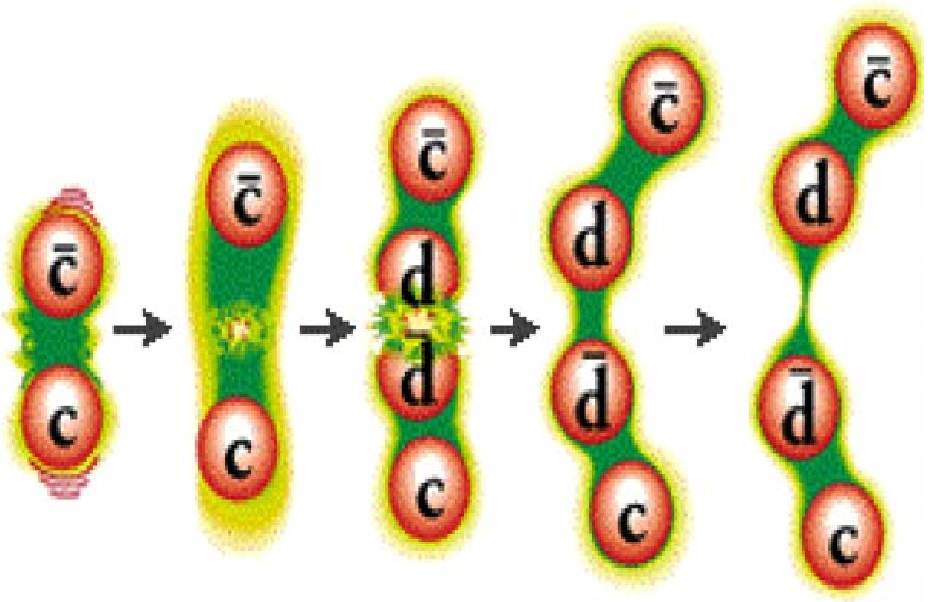

Figure 4.5: An illustration one possible string separation in the Lund String Model which generates new $q\overline{q}$ pairs.

length determined by phenomenological methods to be $\kappa \sim 1$ GeV$/fm$, with gluons treated as "kinks" in the string. As the partons move apart, the potential energy stored in the string increases until it is sufficient to create a new $q\overline{q}$ pair from the color field between the initial $q\overline{q}$ pair, at which point the string is separated into two new strings, as illustrated in Figure 4.5. The two strings formed by the splitting evolve independently and continue the process of iterative splitting until only on-mass-shell hadrons remain.

4.1.4 QED Effects

Any stand-alone simulation of ep interactions does not include in the simulation QED effects from the incoming electron radiating a photon before the hard scatter (initial-state radiation, or ISR) or after the hard scatter (final-state radiation, or

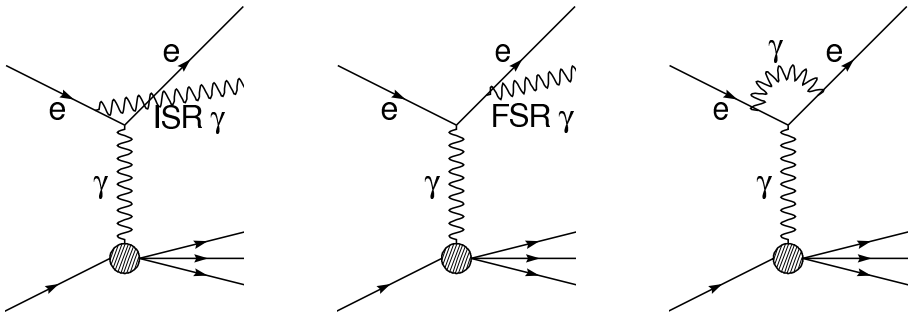

Figure 4.6: An illustration of QED effects that can affect the result of an experimental measurement. These effects include ISR(left), FSR(center), and a virtual photon loop (right).

FSR). For this analysis, the MC programs used for event simulation are interfaced to HERACLES 4.5.2 [34] via DJANGO 6.2.4 [35]. The HERACLES program includes QED effects up to $\mathcal{O}(\alpha_{\mathrm{EM}}^2)$.

4.1.5 Detector Simulation and Reconstruction

In order to be compared to the experimental measurements, the hadron level system must undergo a full detector simulation. The simulation of particles passing through the ZEUS detector is simulated by the Monte Carlo for ZEUS Analysis, Reconstruction, and Trigger (MOZART), which uses the GEANT [36] package. The GEANT package takes as input from MOZART the geometry and material of the detector components, and simulates the passage of particles through the components and the dead material in the detector. The information for these simulations comes from test beam studies of the components, which determine the energy resolutions and component responses, and from dead material and geometry studies of the detector. After the detector simulation, the event is processed by the Complete ZGANA Analysis Routine (CZAR), which simulates the ZEUS online trigger (described in Section 3.4.5)

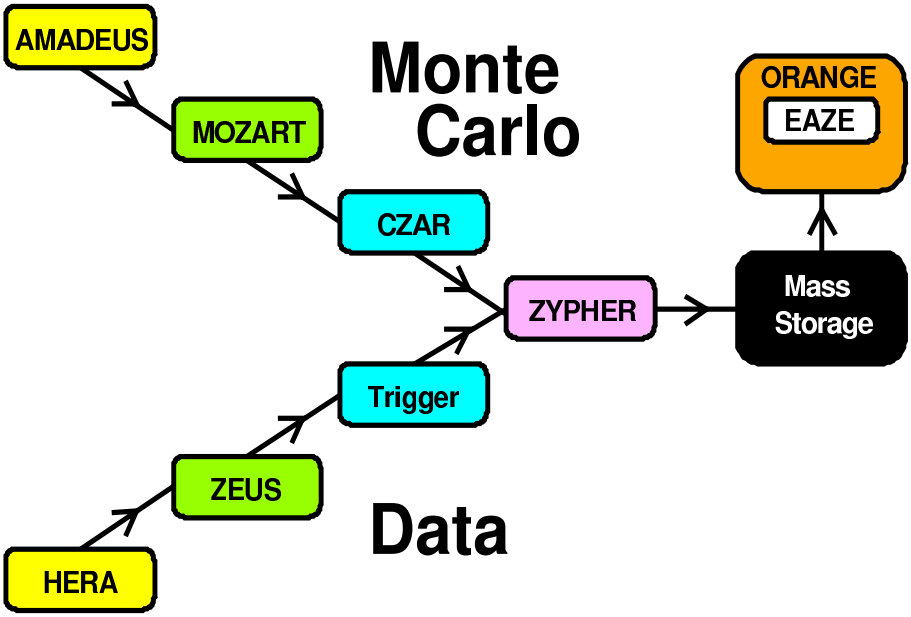

Figure 4.7: An illustration of the processing of ZEUS data and MC events.

acting on the event.

After the detector and trigger information is simulated, the event is passed through the ZEUS Physics Reconstruction (ZEPHYR) program, which is also used for the data reconstruction described in Chapter 6. This program applies the reconstruction code, including calibration constants to the event. The simulation of the detector and trigger and the offline reconstruction yields the "detector level" event. The event is then stored to tape and made available for offline analysis. The EAZE (Easy Analysis of ZEUS Events) package is the standard ZEUS offline analysis package and produces Ntuples containing the event information. Figure 4.7 shows the processing of ZEUS data and MC events.

4.2 Monte Carlo Programs

For this analysis, neutral current DIS events were generated using the ARIADNE 4.10 program [37] and the LEPTO 6.5 program [38]. In the case of ARIADNE, events were generated using CDM whereas for LEPTO, the MEPS method was used. The CTEQ5L parameterizations of the proton parton density functions (PDFs) [39] were used in the generation of DIS events for ARIADNE, and the CTEQ4D PDFs [39] were used for LEPTO. For hadronization the Lund string model, as implemented in JETSET 7.4 [40, 41] was used for both models.

Chapter 5

Next-to-Leading Order pQCD Calculations

In addition to Monte Carlo simulations, which are based on phenomenological models which simulate higher-order processes beyond $\mathcal{O}(\alpha_s)$, next-to-leading order (NLO) calculations are obtained from a class of programs that calculate the partonic jet cross section in DIS. One such program, NLOJET [42], is capable of providing calculations in perturbative QCD (see section 1.2.2) up to $\mathcal{O}(\alpha_s^3)$. Unlike MC simulations, the calculations from the NLO programs are not dependent on any phenomenological model and are exact to the order in $\mathcal{O}(\alpha_s)$ calculated.

As mentioned in section 2.1.2, the general form of the DIS cross section is given as

$$d\sigma = \sum_{a=q\bar{q}g} \int dx \; f_a(x, \mu_F^2) \; d\hat{\sigma}_a(x, \alpha_s(\mu_R), \mu_R^2, \mu_F^2) \tag{5.1}$$

which is a sum of a convolution of the partonic cross section, $d\hat{\sigma}$, and the PDFs, $f_a(x, \mu_F^2)$. The inclusive trijet cross section has contributions from both 4-parton final states and from virtual loop corrections to the 3-parton final states, examples

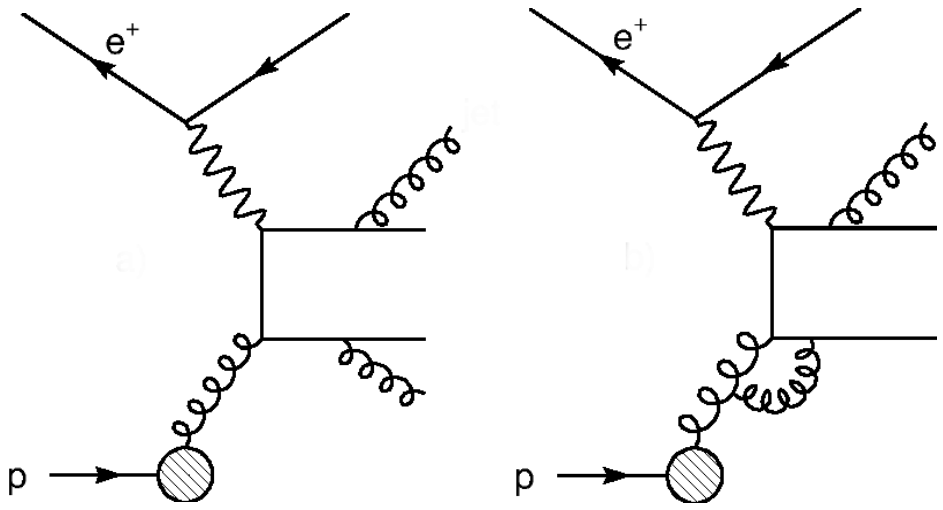

Figure 5.1: An example of two types of corrections to a 3-parton final state, with a real parton emission shown at left and a virtual loop correction shown at right.

of which are illustrated in Figure 5.1. Both types of contribution, however, lead to divergent terms in the calculation. The contributions from the virtual loops are negative and diverge as the 4-momentum of the virtual gluon loop is integrated to infinity (ultraviolet divergence). On the other hand, the contributions from 4-parton final state corrections are positive and diverge as the energy of the radiated gluon approaches zero (soft divergences) or as the angle of the radiated gluon from its parent parton approaches zero (collinear divergence; collectively soft and collinear divergences are known as infrared divergence). To obtain a finite cross section, divergences from the initial-state gluon radiation is factorized at scale μ_F into the PDFs, and the remaining soft and collinear divergences are canceled with the virtual loop corrections [43]. The two most common methods used to cancel the divergences are the phase space splicing method [44] and the subtraction method [45].

5.1 NLOJET Program

The NLO calculations were carried out in the $\overline{\text{MS}}$ scheme [4] for five massless quark flavors with the program NLOJET. The NLOJET program allows a computation of the dijet (trijet) production cross sections to next-to-leading order, i.e. including all terms up to $\mathcal{O}(\alpha_s^2)$ ($\mathcal{O}(\alpha_s^3)$). In certain regions of the jet phase space, where the two hardest jets are not balanced in transverse momentum, NLOJET can be used to calculate the cross sections for dijet production at $\mathcal{O}(\alpha_s^3)$. It was checked that the LO and NLO calculations from NLOJET agree at the 1-2% level for the dijet cross sections with those of DISENT [46], another program for NLO calculations that has been used extensively for HERA analyses [47, 48]. This agreement was achieved by using a fixed electromagnetic coupling constant $\alpha_{EM} = 1/137$ for NLOJET, rather than using a Q^2-dependent α_{EM}. The strong coupling constant was set to the value used for the CTEQ6 PDFs, $\alpha_s(M_Z) = 0.118$, and evolved according to the two-loop solution of the renormalization group equation.

5.1.1 Subtraction Method

Divergences in the subtraction method are handled by introducing a counterterm of $d\hat{\sigma}^{local}$, which serves to make the real and virtual emission cross sections separately integrable. The partonic cross section $d\hat{\sigma}$ can be expressed as a Born-level cross section with higher order corrections, i.e.

$$d\hat{\sigma} = d\sigma^{\hat{LO}} + d\sigma^{\hat{NLO}} \tag{5.2}$$

The term $d\hat{\sigma}^{NLO}$ is comprised of terms for real and virtual emission, $d\hat{\sigma}^{real}$ and $d\hat{\sigma}^{virtual}$, respectively. For a final state of m partons for which the NLO correction is

being calculated, the counterterm $d\hat{\sigma}^{local}$ is included in the NLO cross section in the following manner:

$$d\hat{\sigma}^{NLO} = \int_{m+1} [d\hat{\sigma}^{real} - d\hat{\sigma}^{local}] + \int_{m} d\hat{\sigma}^{virtual} + \int_{m+1} d\hat{\sigma}^{local} \tag{5.3}$$

The term $d\hat{\sigma}^{local}$ is an approximation of $d\hat{\sigma}^{real}$ that exhibits the same singular behavior, thus allowing the first term on the right in equation 5.3 to be integrated numerically in four dimensions. The other requirement of $d\hat{\sigma}^{local}$ is that it should be analytically integrable over the one-parton phase space containing the virtual loop divergences. The poles associated with this integration can be combined with those in the virtual term to yield a finite sum for all terms in 5.3. Combining all of these terms yields a finite result of the NLO partonic cross section.

5.1.2 $\overline{MS}$ Renormalization scheme

The type of subtraction method used by NLOJET for the renormalization scheme is the modified minimal subtraction, or $\overline{MS}$ scheme, which uses a dimensional regularization approach to reduce the dimension of the logarithmically divergent momentum integrals from $d = 4$ to $d = 4 - 2\epsilon$ and to subtract the resulting poles. The renormalization scale μ_R introduced in section 1.2.2 is used to keep the coupling constant α_s dimensionless. Taking the limit as $\epsilon \to 0$ separates the momentum integrals into singular and finite terms. The singular terms are attributed to a renormalized charge, while the finite terms modify the coupling constant, which gives the coupling constant a dependence on μ_R. The renormalization scale μ_R is therefore the scale at which α_S is evaluated.

5.2 Scale Dependence and Uncertainty

Calculations from pQCD to all orders in α_S would yield results entirely independent of μ_R; however, the results from fixed order calculations like the ones used in this analysis do depend on μ_R, resulting in an uncertainty in the predicted cross sections. The choice of μ_R is arbitrary, and is often chosen as either Q^2 or the average transverse energy, E_T, of the two (three) highest E_T jets in a given dijet (trijet) event, $\overline{E}_T^2$. Similarly, the choice of the factorization scale μ_F is arbitrary, and it is usually set to the same value of μ_R. For this analysis the renormalization and factorization scales were both chosen to be $(\bar{E}_T^2 + Q^2)/4$, which the previous ZEUS multijet analysis [12] determined to be suitable for a multijet analysis in DIS, as it takes into account the energies of the exchange photon and of the emitted partons in the evaluation of α_s.

To estimate the theoretical uncertainty due to the choice of the renormalization and factorization scales, the scales were varied simultaneously up and down by a factor of two, which is the usual convention within HERA analyses. The magnitude of variation in the predicted cross section arising from the variation of μ_R provides an estimate of the higher order contributions to the calculated cross sections. As seen in the previous ZEUS forward jet analysis [49], the renormalization scale uncertainty of the fixed-order pQCD predictions increases dramatically at low x_{Bj} as the calculations are generally performed near the non-perturbative limit, which therefore makes the renormalization scale uncertainty the dominant contribution to the overall theoretical uncertainty at low x_{Bj}.

5.3 PDFs and PDF Uncertainty

The PDFs convoluted with the partonic cross section are obtained from fits to data using the DGLAP parameterization. For the calculations used in this analysis, the CTEQ6M [50] proton PDFs were used. Because the predicted cross sections are convolutions of the partonic cross sections and PDFs, the uncertainty in the PDFs also contributes to the overall theoretical uncertainty. The uncertainties in the proton PDFs were estimated in the previous ZEUS multijets analysis [12] by repeating NLO calculations using 40 additional sets from CTEQ6M, which resulted in a 2.5% contribution to the theoretical uncertainty and was therefore neglected in this analysis, where the contribution to the theoretical uncertainty from the PDF uncertainty is expected to be far smaller than the renormalization scale uncertainty. Because the PDF uncertainly is insignificant relative to the renormalization scale uncertainty, its effect was neglected in this analysis.

5.4 Asymmetric Jet Cut

Along with the divergences arising from soft, collinear, and virtual loop corrections, which are treated by the renormalization scheme, the NLOJET calculations are sensitive to the defined jet phase space. Without any gluon radiation, a dijet event in the HCM frame (see Section 2.3) consists of two jets with identical transverse energy, $E_{T,\mathrm{HCM}}^{\mathrm{jet}}$, by conservation of energy and momentum. The additional gluon radiation included in the NLO calculations results in an imbalance in $E_{T,\mathrm{HCM}}^{\mathrm{jet}}$ of the two leading jets in $E_{T,\mathrm{HCM}}^{\mathrm{jet}}$. Therefore a symmetric cut on $E_{T,\mathrm{HCM}}$, where the requirement on $E_{T,\mathrm{HCM}}$ is the same for both jets, allows for unphysical behavior near the cut bound-

aries by artificially restricting the phase space for gluon emission while still allowing virtual loop corrections.

The unphysical behavior of a symmetric cut can be avoided either by using an asymmetric cut on jet $E_{T,\mathrm{HCM}}$, in which the cut on the jet with the highest $E_{T,\mathrm{HCM}}$ is higher than the cut on the $E_{T,\mathrm{HCM}}$ of the second jet, or by placing a requirement on the invariant mass of the di(tri)jet system. To compare experimental measurements to the NLOJET calculations, the jet selection used in selecting the data sample matches that used in the calculations. The previous ZEUS multijets analysis [12] used a cut on the invariant mass of the di(tri)jet system to avoid depleting the statistics of the trijet sample, which was crucial for a precision measurement of the trijet cross section needed for extracting α_s. This analysis, on the other hand, examines the $\mathcal{O}(\alpha_s^3)$ correction to the dijet cross section in the jet phase space where the jets are not strongly correlated in transverse momentum. For the measurement of these cross sections, this analysis uses an asymmetric cut on $E_{T,\mathrm{HCM}}^{\mathrm{jet}}$ to avoid depleting the statistics of the dijet sample. The cuts on $E_{T,\mathrm{HCM}}^{\mathrm{jet}}$ are selected to match those used in the event selection described in Chapter 7.

Chapter 6

Event Reconstruction

Events that trigger are written to tape and undergo a precise reconstruction of the event information. In the reconstruction process, the raw data are processed and corrected to ensure that the fundamental information (e.g. CAL energies, tracking information) is correct and accurate. The processed information from the ZEUS components determines the kinematics of the event and the properties of any jets in the event.

6.1 Track and Vertex Reconstruction

The information from the hits on the sense wires in the tracking detectors (see Section 3.4.1) is used to reconstruct the tracks of individual charged particles and to determine the event vertex where the *ep* interaction took place within the detector. For the reconstruction of the tracks, and for the reconstruction of the primary and any secondary vertices from particle decays or interactions with the beam pipe, ZEUS uses the VCTRACK [51] program.

For offline reconstruction, the VCTRACK package incorporates tracking information from all tracking detectors, with the primary tracking information coming from

CTD. Track finding begins with CTD seeds, each of which is comprised of a hit in each of the three outermost axial superlayers of the CTD. Each seed is extrapolated iteratively towards the inner superlayers, with the longest tracks extrapolated first. The trajectory parameters of each track are recalculated with each iteration, as the information from the inner superlayers is added to the track. Tracks with more than 15% shared hits with other tracks are removed. This process continues until all tracks that pass through the innermost superlayer are identified and included. The next iteration covers tracks that do not reach the innermost superlayer. The z position of the track is found initially from the z-by-timing information and then refined from the information from the stereo superlayers.

The next stage in the track reconstruction is finding the trajectory of the tracks using a 5-parameter helix model, illustrated in Figure 6.1. The fittings begin with the hits in the innermost superlayer and work outwards. During this procedure, the information about the beam location, z-by-timing information, information from the stereo hits, and other details are incorporated into the fitting.

To find the primary vertex from the ep interaction and any secondary vertices, the fitted tracks are used as the input. The vertex finding routine loops over the input tracks, identifying the tracks consistent with a primary or secondary vertex. The vertex is then determined by a χ^2 minimization routine. Tracks assigned to the primary vertex by the minimization routine are refitted using the primary vertex as the point of origin for the track, which improves the accuracy of the reconstruction of the track.

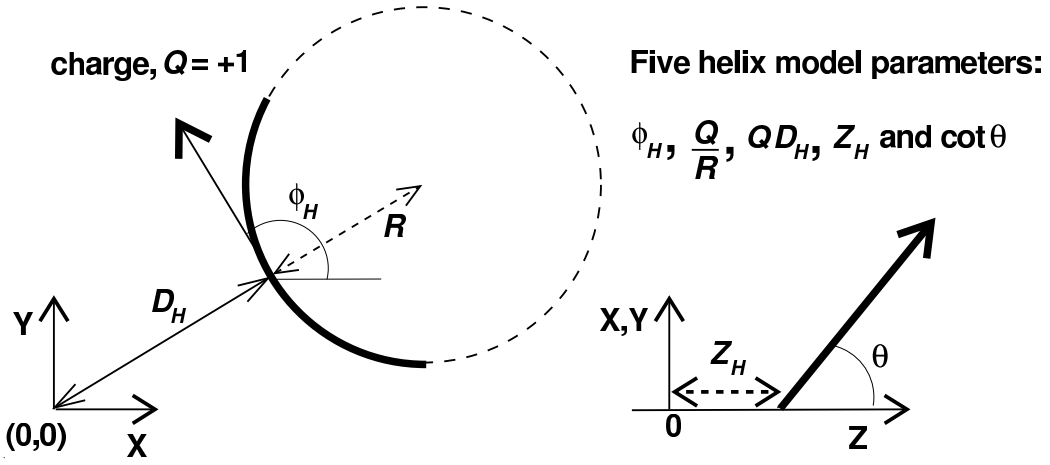

Figure 6.1: An illustration of the five parameters used in the helix fitting of CTD tracks.

6.2 Calorimeter Reconstruction

The information from the CAL used for the reconstruction of the position and energy of a particle comes from the cell positions, from the pulse amplitude from the two PMTs associated with each cell, and from the timing difference between the two PMT pulses. To ensure that the information from the CAL is accurate, noise in the CAL is suppressed and the energy scale of the CAL is corrected. The cells are then grouped into clusters.

6.2.1 Calorimeter Cell Removal

As mentioned in Section 3.4.2, the use of ^{238}U for the absorbing material in the CAL creates a small background signal that is treated as noise. To suppress the noise from the ^{238}U background, non-isolated EMC cells with $E < 60$ MeV and HAC cells with $E < 110$ MeV are not considered in the reconstruction. Isolated EMC cells with $E < 80$ MeV and HAC cells with $E < 140$ MeV are also removed.

Other calorimeter noise is identified by two features: a large imbalance, I_{cell}, between the pulses of the PMTs associated with a cell and higher than average cell activity. A large imbalance between the PMT signals in a cell usually indicate that a spark has traveled between a PMT housing and the PMT itself, which creates a false signal. To remove noise created from sparks, cells with an energy imbalance of $I_{cell} > 0.49E + 0.03$, where E is the overall cell energy, are removed. The noise from the ^{238}U noise and PMT sparks are handled by the Noise96s routine [52]. Higher than average cell activity (so-called "hot" cells) are often caused by a hardware failure. The list of hot cells for a given event are used for corrections for offline analysis at the EAZE level (see section 4.1.5).

6.2.2 Island Formation

Due to the segmentation of the CAL into cells, particles would often deposit energy in more than one cell. To account for this granularity effect, adjacent cells with energy deposits are combined using a clustering algorithm run separately over the EMC and HAC cells. The resulting 2-dimensional cell islands are then combined to form 3-dimensional cone islands using a probability function based on the angular separation between the EMC cell-islands and HAC cell-islands. These islands are used

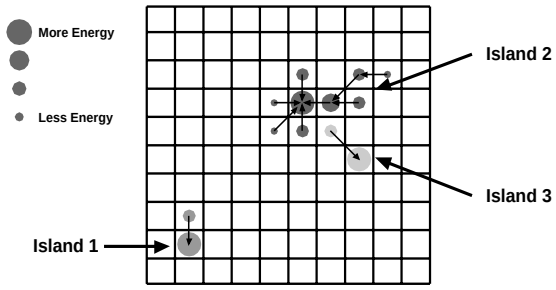

Figure 6.2: An illustration of the clustering process used in finding CAL islands.

for both electron reconstruction and reconstruction of the hadronic system (sections 3.3 and 3.4).

6.3 Electron Reconstruction

The primary feature of a neutral current DIS event is a scattered electron that deposits most of its energy in the electromagnetic portion of the calorimeter. Electromagnetic showers are first located in the calorimeter using the ELECPO routine [53], which calculates the position of the particle initiating the shower by using an energy weighted sum over the imbalance-corrected position of the deposits in the cells associated with the shower. Electromagnetic showers are initiated by both the scattered electron from a DIS event and by other particles (e.g. a π^0 decaying into two photons). The difference between the shower profile coming from a scattered electron and the shower profiles coming from other particles is used to identify the scattered electron. Any algorithm used for electron identification must therefore maximize both the acceptance of true DIS electrons (efficiency) and rejection of non-electron mimic

particles (purity).

The electron finding program used in this analysis is the SINISTRA [54] program, which uses a neural network to identify and classify electron candidates. The input parameters of the SINISTRA program are the transverse and longitudinal profiles of islands associated with electromagnetic showers. Islands within the CTD acceptance region must have a corresponding track to be considered. Using these parameters, SINISTRA outputs a list of electron candidates with their associated probabilities, which are based on how consistent their shower profiles are with that of a scattered DIS electron. Candidates with a probability greater than 90% are considered viable electron candidates. For a scattered electron candidate with a 90% probability and energy greater than 10 GeV, SINISTRA has an 80% purity and an efficiency of nearly 100% in electron finding [55]. For this analysis the electron candidate with the highest probability of being the scattered DIS electron in the event is considered the scattered electron.

The energy of the scattered electron is calculated initially from summing the energy of the cells of the electron island. This energy is subsequently corrected for calorimeter response and inactive material in the detector. The calculation of the electron scattering angle depends on the location of the electron in the detector. For electrons within the CTD acceptance region, the electron angle is given by the angle of the corresponding CTD track. If an electron is outside the CTD acceptance region, but has an SRTD hit, then the angle is reconstructed based on the vertex and SRTD hit position. Outside the SRTD coverage, if the position of the electron in the HES is available and the electron position given by ELECPO is further than 2 cm from a

cell edge, then the HES position of the electron is used in the angle reconstruction. Otherwise, the electron scattering angle is calculated using the ELECPO position of the electron and the event vertex.

6.4 Energy Flow Objects (EFOs)

The reconstruction of the hadronic final state is obtained by combining the calorimeter and CTD information, which provides a better description of the hadronic final state than each component individually. The CTD has a better overall angular resolution than the CAL and is less sensitive to dead material losses than the CAL. The CAL, on the other hand, covers more of the solid angle and can detect neutral particles. The combined information from the CAL and CTD is used to form ZEUS Unidentified Flow Objects (ZUFOs) [56], as they are known within the ZEUS collaboration, and are referred to as Energy Flow Objects (EFOs) in ZEUS publications.

The formation of ZUFOs, illustrated in Figure 6.3 begins with island formation in the CAL, with the position of the island determined by means of a logarithmic center of gravity of the hadronic shower. These islands are then matched to "good" CTD tracks, with the criteria for a good track being a track associated with the primary vertex with a transverse momenta of $0.1 < p_T < 20$ GeV and hits in at least 4 superlayers. The upper cut on track p_T is raised to 25 GeV for tracks passing through 7 or more CTD superlayers. A track is matched to an island if the distance of closest approach between the track and the island is less than 20 cm. In circumstances where an island has no matching track, the particle is treated as a neutral particle, and the energy is calculated from the CAL information. The CAL information is also used when an island is associated with more than 3 tracks. In circumstances where a

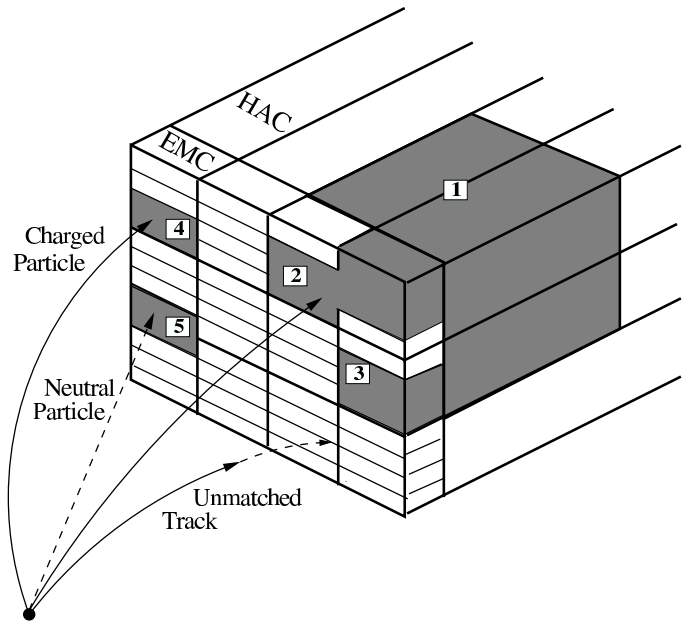

Figure 6.3: The formation of ZUFOs from CAL islands and tracks. The EMC cell islands 2 and 3 are combined with HAC cell island 1 to form a tower island, which is matched to the corresponding track to form a ZUFO. Also shown are EMC cell islands for a charged particle (4) and a neutral particle (5).

track is not matched to an island, the particle is treated as a charged pion, and the tracking information is used for determining the energy. In the case where there is a 1-to-1 track-island match, the CTD information is used if the momentum resolution of the track is better than the energy resolution of the CAL island, and if the information deposit in the island is associated with the track alone: $\frac{E_{CAL}}{p_{track}} < 1.0 + 1.2 \times \delta(\frac{E_{CAL}}{p_{track}})$.

ZUFOs are sensitive to backsplash, which is energy deposited from showering particles scattering into the opposite side of the detector, or by material scattering off the dead material. At the EAZE level, the information from the uncorrected ZUFOs and the ZUFOs corrected for backsplash effects are available for the description of the hadronic system used for the jet finding. Because the backsplash is not well-modeled

by the Monte Carlo, the uncorrected ZUFOs were used. Instead, to help account for the effects of backsplash on the hadronic system, in particular the jets, the jet energy was corrected using a procedure outlined in Section 8.2.

6.5 Hadronic Quantities

The reconstructed electron and the hadronic system obtained from ZUFOs are used for the reconstruction of

$$\delta = E - p_z = \sum_i E_i(1 - \cos\theta_i) \tag{6.1}$$

where the sum runs over all energy deposits and is reconstructed as

$$\delta = E - p_z = E_e^{'}(1 - \cos\theta_e^{'}) \sum_i E_i(1 - \cos\theta_i) \tag{6.2}$$

where the sum runs over all hadronic ZUFOs, and $E_e^{'}$ and $\theta_e^{'}$ are the corrected energy and scattering angle, respectively, of the electron. The quantity δ is conserved and is not sensitive to the proton remnant, as particles associated with the proton remnant have similar energy and longitudinal momentum and therefore make a negligible contribution to δ. The constraint on δ is twice the incoming electron energy: $\delta = 2E_e \approx 55\,\text{GeV}$. Because δ is a conserved quantity, the final state δ should also be $\approx 55\,\text{GeV}$. Experimentally, limitations in detector resolution and energy losses due to dead material lead to a large range of reconstructed δ. In the case of photoproduction, however, where the electron escapes through the rear beampipe, or charged current DIS, where the electron is converted to a neutrino, the reconstructed δ is significantly less than 55 GeV. This experimental signature provides a means of differentiating

between neutral current DIS and charged current or photoproduction events.[1]

Another important quantity in reconstructing the hadronic final state is the polar angle of the hadronic system, which in the QPM model is the polar angle of the struck quark. In reconstructing the hadronic angle, a ratio of ZUFO information is used in order to minimize the systematic differences in energy scales between the MC and data. The reconstructed hadronic angle γ_h is

$$\cos\gamma_h = \frac{(\sum P_x)^2 + (\sum P_y)^2 - (\sum E - P_z)^2}{(\sum P_x)^2 + (\sum P_y)^2 + (\sum E - P_z)^2} \tag{6.3}$$

where the sum runs over all ZUFOs associated with the hadronic system.

6.6 Kinematic Reconstruction

For a full description of a DIS event, eight variables are needed: the 4-momentum components of the scattered electron and the 4-momentum components of the hadronic system. Energy and momentum conservation provides 4 constraints, while the fixed electron mass provides a fifth constraint. With these five constraints, only three independent variables are needed to provide a description of the final state in a DIS interaction, which are typically chosen to be the Lorentz-invariant quantities Q^2, x_{Bj}, and y. The fixed center-of-mass energy s in HERA operations provides one more constraint and reduces the number of variables needed to describe the system to two.

For reconstructing Q^2, x_{Bj} and y, there are four quantities available: the energy and polar angle of the scattered electron, and the $E - p_z$ and polar angle γ_h of the hadronic system. Because only two are necessary, it is possible to choose which pair

[1]For the kinematic range used in this analysis (outlined in Chapter 7), charged current DIS events are not a consideration.

provide the best reconstruction of these variables for the kinematic range considered. MC samples were used to test the reconstruction of Q^2 and x using the various methods outlined below [57].

6.6.1 Electron Method

The electron method uses the scattered electron's energy, $E_e^{'}$, and polar angle, θ_e, for the reconstruction of the kinematic variables Q^2 and y:

$$Q^2_{el} = 2E_e E_e^{'}(1-\cos\theta_e) \tag{6.4}$$

$$y_{el} = 1-\frac{E_e^{'}}{2E_e}(1+\cos\theta_e) \tag{6.5}$$

$$x_{el} = \frac{Q^2_{el}}{sy_{el}} \tag{6.6}$$

where E_e is the energy of the electron beam. The electron method produces a good reconstruction of x_{Bj} and Q^2 over the entire kinematic range, but underestimates the generated Q^2 and x_{Bj} at higher values of Q^2 and x_{Bj}.

6.6.2 Double-Angle Method

The double-angle method [58] measures the kinematic variables using the polar angles of the scattered electron and hadronic system, θ_e and γ_h:

$$Q^2_{\mathrm{DA}} = 4E_e^2\frac{\sin\gamma_h(1+\cos\theta_e)}{\sin\gamma_h+\sin\theta_e-\sin\gamma_h+\theta_e} \tag{6.7}$$

$$x_{\mathrm{DA}} = \frac{E_e}{E_p}\cdot\frac{\sin\gamma_h+\sin\theta_e+\sin\gamma_h+\theta_e}{\sin\gamma_h+\sin\theta_e-\sin\gamma_h+\theta_e} \tag{6.8}$$

$$y_{\mathrm{DA}} = \frac{\sin\theta_e(1+\cos\gamma_h)}{\sin\gamma_h+\sin\theta_e-\sin\gamma_h+\theta_e} \tag{6.9}$$

The double-angle method has been shown to provide a good reconstruction of Q^2 and x_{Bj} at higher x_{Bj} and Q^2 but has a worse resolution than the electron method at lower x_{Bj} and Q^2 [57]. Because this analysis examines QCD dynamics at low x_{Bj} with a consequent restriction of Q^2 to lower vales, the electron method was chosen for reconstructing x_{Bj} and Q^2.

6.6.3 Calorimeter Energy Scale Corrections

To provide the most accurate measurement possible, differences between the simulated calorimeter response and the real calorimeter response have to be taken into account [59]. This is done by recalibrating the calorimeter response for the data such that it matches the simulation. For the data, the cell energies in the FCAL are unmodified, the BCAL cell energies are scaled by a factor of +5%, and the RCAL cell energies are scaled by a factor of +2.2% unless more detailed calibration information exists for an individual RCAL cell. RCAL cells closer to the beam pipe have detailed calibration information and are scaled individually by factors that are typically $\pm 2-3\%$ [60].

The calibration factors are obtained by using the kinematic-peak method and the double-angle method. The kinematic peak method was used for events in which the electron is scattered close to the RCAL beam pipe. These events are characterized by a very low inelasticity, y, and a scattered electron energy to the electron beam energy: $E_e^{'} \sim 27.5$ GeV. The electron energy distributions for the data and MC are therefore expected to peak near 27.5 GeV. The recalibration factor is obtained from the ratio of the peak positions of the data and MC distributions. The double angle method, which is used otherwise, calculates the electron energy using the angles of

the scattered electron and the angle of the hadronic system. The recalibration factor is obtained from the average difference between the measured electron energy and the electron energy calculated from the DA method.

6.6.4 Jacquet-Blondel Method

The Jacquet-Blondel method [61] uses the reconstructed hadronic system exclusively in reconstructing the kinematic variables:

$$y_{\mathrm{JB}} = \frac{\sum_i E_i(1-\cos\theta_i)}{2E_e} \tag{6.10}$$

$$Q^2_{\mathrm{JB}} = \frac{(\sum_i p_{x,i})^2 + (\sum_i p_{y,i})^2}{1-y_{\mathrm{JB}}} \tag{6.11}$$

where the sums run over the ZUFOs associated with the hadronic system. Placing a minimum requirement on y_{JB} ensures a good reconstruction of the hadronic system (see also Section 7.2.2) as it requires a minimum hadronic $E - p_z$, which in turn requires a minimal hadronic energy not associated with the proton remnant and helps to remove events from beam-gas interactions.

6.7 Jet Reconstruction

As described earlier, partons emitted in the hard scatter form showers through QCD radiation. The partons then combine via hadronization to form colorless hadrons. As the energy of QCD radiation is on the order of 1 GeV, the particles associated with a parton emitted from the hard scatter are roughly collimated into an object known as a jet. The 4-momentum of a jet is calculated, which is then used to calculate the jet transverse energy (E_T^{jet}), pseudorapidity (η^{jet}), and azimuthal angle (ϕ^{jet}):

$$\begin{aligned} E_T^{\rm jet} &= \sqrt{p_x^2 + p_y^2} \\ \eta^{\rm jet} &= -\ln\tan(\theta/2) \\ \phi^{\rm jet} &= \tan^{-1}(p_y/p_x) \end{aligned} \tag{6.12}$$

where $\theta = \tan^{-1}(E_T^{\rm jet}/p_z)$.

6.7.1 Jet Algorithms

Jets can be reconstructed from partons, hadrons, calorimeter cells, or ZUFOs; but ultimately, the jet should reflect the properties of the hard scatter regardless of the objects used as input. A jet finding algorithm applied to the partons, hadrons, and ZUFOs from an event should therefore produce jets with comparable energies and angles. In addition to this consideration, the jet finding algorithm should be insensitive to soft or collinear particles, otherwise known as infrared and collinear safety. The energy of a jet reconstructed by an algorithm that is not infrared safe changes as a number of infinitely soft particles with an arbitrary directions are added, which in turn can lead to soft divergences in pQCD calculations.

6.7.1.1 Cone Algorithm

The EUCELL [62] cone algorithm, which is used in some of the ZEUS third-level-trigger logic, defines jets by the Snowmass Convention [63]. In the Snowmass Convention, objects with an E_T above a specified minimum value are treated as seeds, which are treated as the center points for cones with a radius R_{cone} in $\eta - phi$ space. Objects within the cone radius are added to the jet, and the jet variables for the candidate are reconstructed as follows:

$$
\begin{aligned}
E_T^{\text{jet}} &= \sum_i E_{T,i} \\
\eta^{\text{jet}} &= \frac{1}{E_T^{\text{jet}}} \sum_i E_{T,i}\eta_i \\
\phi^{\text{jet}} &= \frac{1}{E_T^{\text{jet}}} \sum_i E_{T,i}\phi_i
\end{aligned}
\tag{6.13}
$$

The process is repeated iteratively with each successive jet candidate treated as the center of the cone until the distance between the input position and recalculated position is less than a specified value, or until a maximum number of iterations (15 in the case of the ZEUS implementation) is reached.

With the cone algorithm, some of the input objects might not be included in any jet. For this reason, cone algorithms have been used extensively at hadron colliders, where pp collisions typically produce more particles not associated with any jet. The primary drawback to the cone algorithm is that soft radiation between two jets can make the algorithm incorrectly merge them into one jet, which therefore makes the cone algorithm infrared unsafe. Another problem with the cone algorithm is the lack of a standardized treatment of overlapping jets, which means that two cone jet finders with the same R_{cone} parameter can find different jets for the same event, depending on the treatment of jet overlap.

The advantages of the cone algorithm are that it is conceptually simple and computationally fast, which makes it suitable for fast jet finding in the ZEUS third-level trigger. The ZEUS implementation of EUCELL has a seed threshold of $E_T^{seed} > 1\,\text{GeV}$ and associates energy shared by overlapping jets with the jet with highest E_T^{jet}

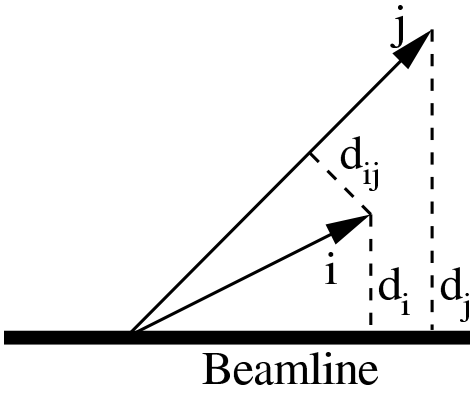

Figure 6.4: An illustration of the variables used by the k_T algorithm. The distances d_i and d_{ij} are in momentum space.

6.7.1.2 k_T Cluster Algorithm

The k_T algorithm, which was originally used in e^+e^- collisions, has been adapted for use in ep collisions. With an input set of partons, hadrons, or ZUFOs, the KT-CLUS [64] algorithm calculates the distance of each particle to the proton beam line in momentum space (see Figure 6.4),

$$d_i = E_{T,i}^2 \tag{6.14}$$

and the distance between two objects as

$$d_{ij} = \min(E_{T,i}^2, E_{T,j}^2)[(\eta_i - \eta_j)^2 + (\phi_i - \phi_j)^2] \tag{6.15}$$

The quantities d_i and d_{ij} are calculated for all input particles, and the algorithm finds the minimum value of all d_i and d_{ij}. If the minimum value in the set is a value of d_{ij}, the algorithm then combines objects i and j into a new object k with

$$\begin{aligned} E_{T,k}^2 &= E_{T,i}^2 + E_{T,j}^2 \\ \eta_k &= \frac{E_{T,i}\eta_i + E_{T,j}\eta_j}{E_{T,i} + E_{T,j}} \\ \phi_k &= \frac{E_{T,i}\phi_i + E_{T,j}\phi_j}{E_{T,i} + E_{T,j}} \end{aligned} \tag{6.16}$$

If the minimum value in the set is instead a value of d_i, then the associated object is classified as a jet and no longer merged. This process continues until all input objects are merged into jets.

Unlike the cone algorithm, the k_T algorithm is infrared and collinear safe. The k_T algorithm also does not have any ambiguity arising from overlapping jets, as each input object is assigned to one jet during the merging process. This analysis therefore uses the k_T finder for jet finding.

6.7.2 Jet Energy Scale Uncertainties

As mentioned in section 6.2.2, the calorimeter response is recalibrated to match Monte Carlo simulations. However, the methods for estimating the CAL energy scale corrections used electrons to estimate the difference between the actual and simulated CAL response. Because jets are multiparticle showers that are primarily hadronic and therefore deposit energy in both the electromagnetic and hadronic sections of the CAL, the energy response of a jet does not exactly match the energy response of an electron.

The jet energy scale uncertainty has been estimated using an exclusive single jet DIS sample [65], where the jet energy and the energy of the scattered electron are expected to balance. The scattered electron energy was corrected for the calorimeter

energy response, and the energy of the jet was predicted. The average difference between the measured and predicted jet energy provides an estimate of the difference in detector response for jets between data and MC samples. It was found that for jets with $E_{T,LAB}^{\text{jet}} > 10\,\text{GeV}$, the uncertainty in the calorimeter energy scale was reduced from 3% to 1%.

Chapter 7

Event Selection

The experimental measurements that are compared to both the Leading-Order MC and Next-to-Leading Order pQCD calculations come from events that have triggered and undergone the full event reconstruction described in Chapter 6. The final sample used for the measurements must be selected online by the ZEUS trigger to ensure that the event is well-reconstructed by all the components, and must also be selected offline by more stringent criteria that make use of the full ZEUS reconstruction. The two samples used for this analysis come from the 1998-2000 HERA running period corresponding to an integrated luminosity of 82 pb^{-1} and are selected for low-x_{Bj} inclusive dijet and trijet events, with the trijet sample as a subset of the dijet sample.

7.1 Online Event Selection

The dijet and trijet samples were selected online by requiring that events meet the requirements of at least one of three trigger "chains" with requirements at all three trigger levels. Each trigger chain consists of a third-level trigger (TLT) filter (see also section 3.4.5), at least one second level trigger (SLT) filter required by the TLT filter, and at least one first-level trigger (FLT) filter required by the SLT filter. The

trigger chains used for this analysis are for both low-Q^2 and medium-Q^2 inclusive DIS events (called "DIS01" and "DIS03", respectively), and for inclusive dijet production ("HPP14"). A total of 1271045 events passed the online event selection.

7.1.1 First Level Trigger

Events consistent with DIS physics are selected at this level primarily by the CTD first-level trigger (CTD FLT), which indicates if a good track is present, and the Calorimeter First Level Trigger (CFLT). The CFLT takes 5% of the signal from the PMTs in the calorimeter, shapes and digitizes the analog signal from the PMTs, and computes global energy sums. The CFLT also performs basic pattern recognition for isolated electrons and muons. The GFLT trigger decision is based on the coarse energy and tracking information from the component FLTs, as well as information from the SRTD, VETO, and C5, which provide timing information that helps reject beam-gas interactions and halo muon events. As mentioned previously, the GFLT reduces the event rate from 10.4 MHz to a few hundred Hz.

For this analysis, the following criteria from the FLT were used to select events:

- The total electromagnetic energy in the calorimeter exceeds 15 GeV (FLT40).
- The total transverse energy in the calorimeter exceeds 30 GeV (FLT41).
- The total energy in the calorimeter exceeds 15 GeV, the total electromagnetic energy in the calorimeter exceeds 10 GeV, the electromagnetic energy in the barrel calorimeter exceeds 3.4 GeV, or the electromagnetic energy in the rear calorimeter exceeds 2.0 GeV. In addition to one of these calorimeter requirements, a good track must also be found (FLT42).

- The total transverse energy in the calorimeter exceeds 11.5 GeV and a good track is found (FLT43).
- The electromagnetic energy in the barrel calorimeter exceeds 4.8 GeV and a good track is found, or if the electromagnetic energy in the rear calorimeter exceeds 3.4 GeV (FLT44).
- The CFLT locates an electron in the rear calorimeter and one of the following requirements is satisfied (FLT46):
  - The electromagnetic energy in the rear calorimeter exceeds 2.0 GeV.
  - There is SRTD data for the event good track is found.
  - There is a good track and the total transverse energy in the calorimeter exceeds 18 GeV.

The inclusive low-Q^2 and medium-Q^2 trigger chains DIS01 and DIS03 require that the event passes one of the FLT bits listed above, while the inclusive dijet trigger chain HPP14 requires the event satisfies one of the slots FLT40-43.

7.1.2 Second Level Trigger

The SLT filter (DIS06) used for the two inclusive DIS trigger chain requires $E - p_z + (2 * E_{\gamma}^{lumi}) > 29$ GeV, and also requires one of the following to increase the likelihood of finding an event with both a well-reconstructed electron and a well-reconstructed hadronic final state:

- The electromagnetic energy in the rear calorimeter exceeds 2.5 GeV.

- The electromagnetic energy in the barrel calorimeter exceeds 2.5 GeV.
- The hadronic energy in the forward calorimeter exceeds 10 GeV.
- The electromagnetic energy in the forward calorimeter exceeds 10 GeV.

The SLT filter (HPP01) used for the inclusive dijet trigger chain takes the event if the following criteria are met:

- The CTD-SLT reconstructs a vertex with $|Z_{vtx}| < 60$ cm, or if the CTD-SLT cannot reconstruct a vertex.
- A good track is found.
- $E - p_z < 8$ GeV
- The sum of the transverse energy in all the calorimeter cells excluding those within the first ring around the forward calorimeter beam pipe exceeds 8 GeV.
- $E - p_z > 12$ GeV or $p_z/E < 0.95$.

7.1.3 Third Level Trigger

The TLT event selection for this analysis is based on the reconstruction of electrons and jets online in the TLT filters used. The filter HPP14 is a dijet photoproduction trigger that requires two jets found in the lab frame using the EUCELL jet finding algorithm with $E_{T,\mathrm{LAB}}^{\mathrm{jet}} > 4$ GeV or 4.5 GeV, depending on the running period, and $|\eta_{\mathrm{LAB}}^{\mathrm{jet}}| < 2.5$.

The medium-Q^2 trigger bit DIS03 requires an electron found with an energy exceeding 4 GeV found outside a circle centered on the beampipe with a radius of 35 cm. It also requires $E - p_z + (2 * E_\gamma^{lumi}) > 30$ GeV and $E - p_z < 100$ GeV.

The low-Q^2 trigger bit DIS01 also requires an found with an energy exceeding 4 GeV, but unlike the filter DIS03, it requires that the electron be outside a 12 x 6 cm box around the beam pipe. Due to rate considerations, this filter was prescaled by a factor of 1, 10, or 100 during the HERA I running period. Because of this prescale, the events passing this filter have an overall luminosity of 11.35 pb^{-1}. To account for the prescaling, events passing DIS01 only are given a weight of $1/11.35\text{pb}^{-1}$, while events that are taken by DIS03 or HPP14 are given a weight of $1/81.7\text{pb}^{-1}$ regardless of whether they are taken by DIS01.

7.2 Offline Event Selection

In addition to the online trigger requirements, the *Data Summary Tape* bit DST9 was required. Like the DIS01 and DIS03 trigger chains, DST bit 9 requires an electron found with energy greater than 4 GeV; however unlike the online trigger chains used, the bit DST 9 uses the fully reconstructed event information rather than the TLT information.

Events passing the online selection are reconstructed offline using the methods described in Chapter 6. Additional offline cuts are placed on the sample to reject any remaining background and photoproduction events and to avoid regions in which the detector performance is limited.

7.2.1 Background Rejection

- $|Z_{vtx}| < 50$ cm, which selects events consistent with an ep interaction within a well-understood acceptance region of the calorimeter and central tracking detector. Of the events selected by the trigger chain used in this analysis, 1218891 events pass this selection requirement.

- $p_T/\sqrt{E_T} < 3\sqrt{\text{GeV}}$, where p_T is the sum of the vector transverse momentum of the final state particles, and E_T is the sum of their scalar transverse energy. In a neutral current DIS interaction, momentum conservation requires that $p_T = 0$; however, due to the finite resolution of the calorimeter, which roughly scales with the transverse energy, p_T is often nonzero. Placing the restriction $p_T/\sqrt{E_T} < 3\sqrt{\text{GeV}}$ eliminates mainly cosmic events. Of the remaining events, 1218795 events pass this requirement.

- In order to ensure a well-constructed electron consistent with a DIS interaction, a scattered electron reconstructed by the Sinistra95 program with the following criteria is required:

  - $|X| > 13$ cm or $|Y| > 7$ cm where X and Y are the x and y coordinates in the rear calorimeter of the scattered electron. This cut ensures that the scattered electron falls outside the low-acceptance region around the RCAL beam pipe. 1204825 events remain after this requirement is applied.

  - $E_{cone}/E_e^{'} < 0.1$, where E_{cone} is the energy of deposits not associated with the scattered electron within a cone with a radius of 1 in $\eta - \phi$ space centered around the scattered electron. This cut selects electrons well-separated

from the hadronic deposits. 1042772 events remain after this requirement is applied.

- $E_e^{'} > 10$ GeV and $E_{prob} > 0.9$, where $E_e^{'}$ is the corrected energy of the scattered electron and E_{prob} is the probability of finding the electron. 856122 events remain after this requirement is applied.
- $(E - p_z)_{elec} < 54$ GeV, where $(E - p_z)_{elec}$ is the $E - p_z$ of the scattered electron. This cut eliminates electrons scattered at a low angle, which are inaccurately reconstructed with a higher $E - p_z$ than is kinematically allowed. Such electrons spoil the accuracy of the boost to the HCM frame. 828619 events remain after this requirement is applied.

- $40 < \sum_i (E - p_z)_i < 60$ GeV, where E_i and $P_{Z,i}$ are the energy and z-momentum of each final-state object. The lower cut removed background from photoproduction and events with large initial-state QED radiation, while the upper cut removed cosmic-ray background. 789571 events remain after this requirement is applied.

7.2.2 Kinematic Selection

The kinematic range of the analysis is

$$10 < Q^2 < 100 \text{ GeV}^2,\ 10^{-4} < x_{\text{Bj}} < 10^{-2}, \text{ and } 0.1 < y < 0.6.$$

The cuts on Q^2 and x_{Bj} ensure events with good acceptance in the ZEUS detector in the low-x_{Bj} kinematic region. For the kinematic selection, the cuts were placed on Q^2 and x_{Bj} reconstructed by the electron method described in section 6.4.1.

The requirements on y were as follows:

- $y_{el} < 0.6$, where y_{el} is y reconstructed by the electron method. This cut is used to remove photoproduction background, mostly from energetic pions in the FCAL decaying into photon pairs. 747688 events remain after this requirement is applied.

- $y_{jb} > 0.1$, where y_{jb} is y reconstructed by the Jacquet-Blondel method described in section 6.4.2. This cut requires a minimum hadronic energy in the calorimeter and helps ensure an accurate hadronic reconstruction. 532596 events remain after this requirement is applied.

After the kinematic selection, the sample consists of 308196 events.

7.2.3 Jet Selection

During the 1998-2000 running period the cut on $E^{\text{jet}}_{T,\text{LAB}}$ by the TLT slot HPP14 trigger chain was raised from 4 to 4.5 GeV. In order to address this inconsistency and to ensure well-defined jets in the final samples, the uncorrected $E^{\text{jet}}_{T,\text{LAB}}$ is required to be larger than 5 GeV for the jet to be included in the sample. The jet phase space for the dijet(trijet) sample is defined by two(three) jets satisfying the following criteria:

- $-1 < \eta^{\text{jet}}_{\text{LAB}} < 2.5$, where $\eta^{\text{jet}}_{\text{LAB}}$ is pseudorapidity of the jets found in the HCM frame after a boost back to the LAB frame. This cut ensures the jets are contained within in a well-understood region of the detector with good acceptance.

- An asymmetric cut on the corrected $E^{\text{jet}}_{T,\text{HCM}}$ is applied to meet the requirements on the jet phase space imposed by the NLOJET calculations (see section

5.4), with the jet with highest transverse energy required to have $E_{T,\mathrm{HCM}}^{\mathrm{jet1}} > 7$ GeV, and the other jet(s) comprising the dijet(trijet) sample required to have $E_{T,\mathrm{HCM}}^{\mathrm{jet2(,3)}} > 5$ GeV. This requirement eliminates jets with low $E_{T,\mathrm{HCM}}^{\mathrm{jet}}$, which are likely the result of soft partonic radiation, and ensures that the dijet(trijet) system is comprised of jets from the hard *ep* scatter that are measured with reasonable precision. These requirements result in a dijet sample consisting of 81645 events, and a trijet sample of 9734 events.

Chapter 8

Analysis Method

The cross sections, which are the probabilities of certain types of interactions to occur for an incident flux, are measured using the sample obtained by the selection methods described in Chapter 7. The measured distributions of the sample were corrected for dependencies on the performance and limitations of the ZEUS detector and then used to produce the cross sections. Such corrections account for inactive material in the detector, triggering efficiency, geometric acceptance, and limitations in the tracking and calorimetry. Simulated Monte Carlo events were used to account for these effects by obtaining and comparing dijet and trijet samples at the detector level (Section 4.5), and at hadron and parton levels. The detector-level samples were obtained by applying the event selection criteria to the reconstructed kinematic and jet variables, while the hadron and parton level samples were obtained by applying the selection criteria to the generated kinematic values and the hadron-level and parton-level jets, respectively.

8.1 Comparison of Monte Carlo and Data

In order to measure the cross sections reliably the detector-level distributions from the MC models must provide a reasonable description of the data. Too large a disagreement between data and MC can result in a large systematic uncertainty, which prevents a reliable measurement. The detector-level distributions from both ARIADNE and LEPTO were therefore compared to the measured distributions for the variables used to define the dijet and trijet samples, and with variables measured in the cross sections used in the analysis. The agreement between the data and the Monte Carlo distributions was examined both within the phase space used for the analysis and in the regions just outside the phase space, where a large discrepancy between the measured distributions and the Monte Carlo predictions can provide large contributions to the systematic uncertainty.

8.1.1 Reweighting in Q^2

In order to improve the Q^2 dependence of the simulations for acceptance corrections, the weight assigned to the events from the Monte Carlo samples were adjusted as a function of Q^2. To obtain the reweighting factor, the Q^2 distribution from the dijet sample was divided by the detector-level Q^2 distribution from the Monte Carlo dijet samples. The ratio was plotted as a function of Q^2 and a linear fit was applied. Each event in the Monte Carlo was then reweighted based on the generated Q^2 of the event according to the obtained linear fit. The reweighting for the LEPTO and ARIADNE programs are as follows:

$$f_{\textsc{Ariadne}} = 0.874 + (0.00302 \cdot (Q^2/GeV^2))$$
$$f_{\textsc{Lepto}} = 1.146 - (0.00378 \cdot (Q^2/GeV^2)) \quad (8.1)$$

Figures 8.1 and 8.2 show the comparisons between the dijet data and the predictions from ARIADNE and LEPTO before and after the reweighting in Q^2 was applied to the Monte Carlo samples. In both cases, the agreement between the measured distribution and the predictions from ARIADNE or LEPTO improved after the reweighting was applied.

8.1.2 Detector-level Comparisons

The distributions in the reconstructed kinematic variables Q^2_{el}, x_{el}, y_{el}, and $y_{\rm jb}$ compared to the predictions from ARIADNE are shown in Figures 8.3 and 8.5, respectively. The ARIADNE predictions match the measured dijet distributions well for the kinematic variables (Figure 8.3), especially the variables reconstructed with the electron method, while providing a reasonable description of the trijet kinematic distributions (Figure 8.4). The jet transverse energies in the HCM frame (Section 6.5.4), $E^{\rm jet1}_{T,\rm HCM}$, $E^{\rm jet2(,3)}_{T,\rm HCM}$, and the azimuthal separation of the two jets with the largest $E^{\rm jet}_{T,\rm HCM}$, $|\Delta\phi^{\rm jet1,2}_{\rm HCM}|$, are shown in Figures 8.4 and 8.6 for the dijet and trijet samples, respectively. The level of agreement between the dijet and trijet samples and the ARIADNE predictions is similar to that seen in the previous ZEUS multijet analysis [47], where the ARIADNE distributions agree with the data at lower $E^{\rm jet}_{T,\rm HCM}$, but overestimate the data slightly at higher $E^{\rm jet}_{T,HCM}$. $|\Delta\phi^{\rm jet1,2}_{\rm HCM}|$ is better described at low $|\Delta\phi^{\rm jet1,2}_{\rm HCM}|$ by the ARIADNE predictions, which use the Color-Dipole Model (CDM) than by the LEPTO predictions, which use the DGLAP-based Matrix-Elements plus Par-

ton Shower (MEPS) approach. Because the region of low $|\Delta\phi^{\mathrm{jet1,2}}_{\mathrm{HCM}}|$ is expected to be sensitive to parton evolution scheme at low x_{Bj}, which is of primary interest to this analysis, the ARIADNE sample was used for correcting the data to the hadron level.

Before reweighting in Q^2

LEPTO ARIADNE

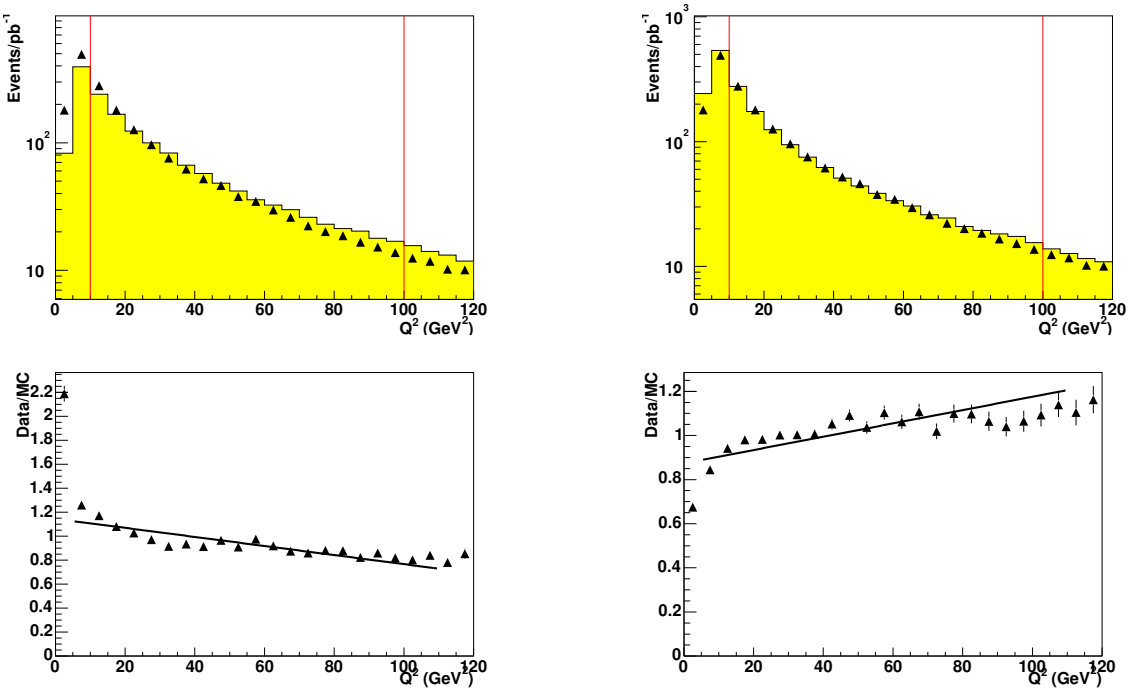

Figure 8.1: Detector-level comparisons of Q^2_{el} between the dijet sample, represented by the points in the figure and the predictions from ARIADNE and LEPTO, represented by the histograms in the figure, before the MC samples were reweighted in Q^2.

After reweighting in Q^2

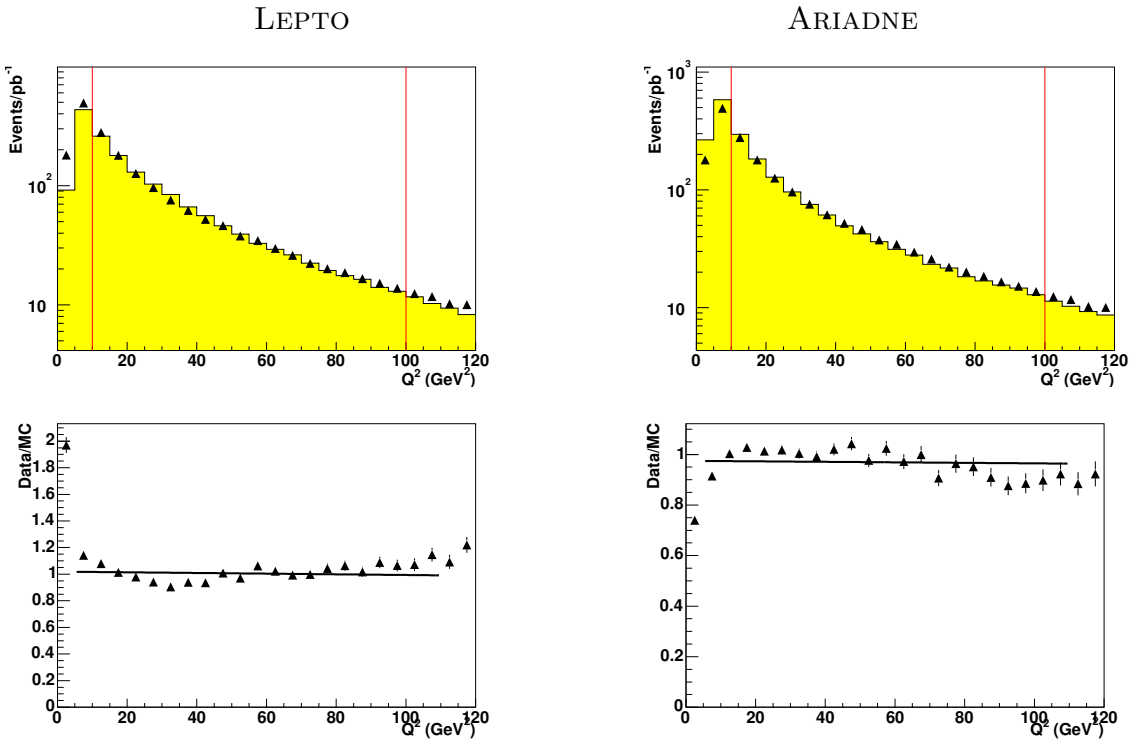

Figure 8.2: Detector-level comparisons of Q^2_{el} between the dijet sample, represented by the points in the figure and the predictions from ARIADNE and LEPTO, represented by the histograms in the figure, after the MC samples were reweighted in Q^2.

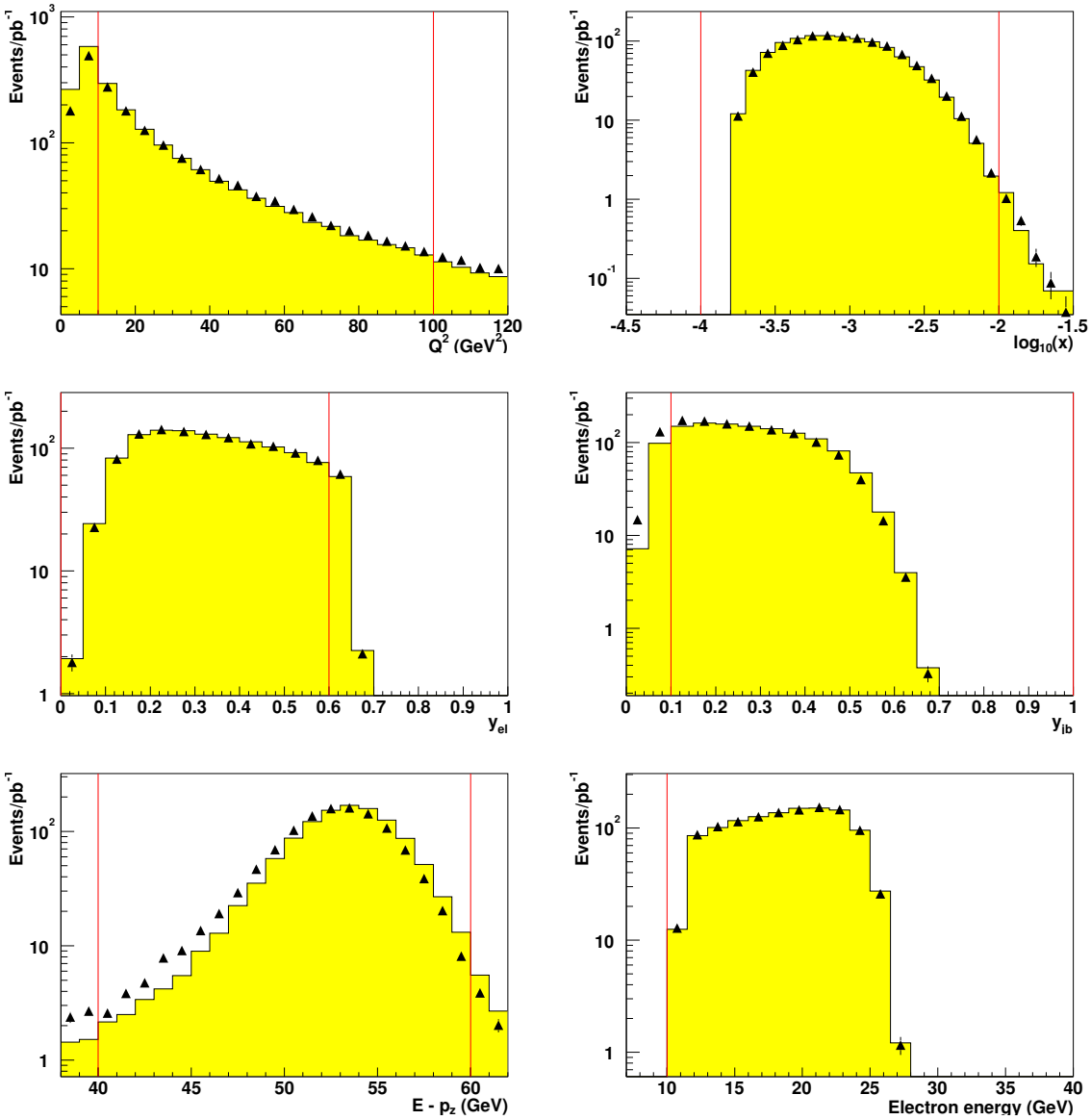

Figure 8.3: Distributions in the kinematic variables Q^2_{el}, x_{el}, y_{jb}, y_{el}, $E - p_z$, and scattered electron energy from the dijet sample, appearing in the figures as points, compared to those from ARIADNE, appearing in the figures as histograms. The distributions from ARIADNE are area-normalized to the data within the cut boundaries (indicated by the lines) in order to compare shapes.

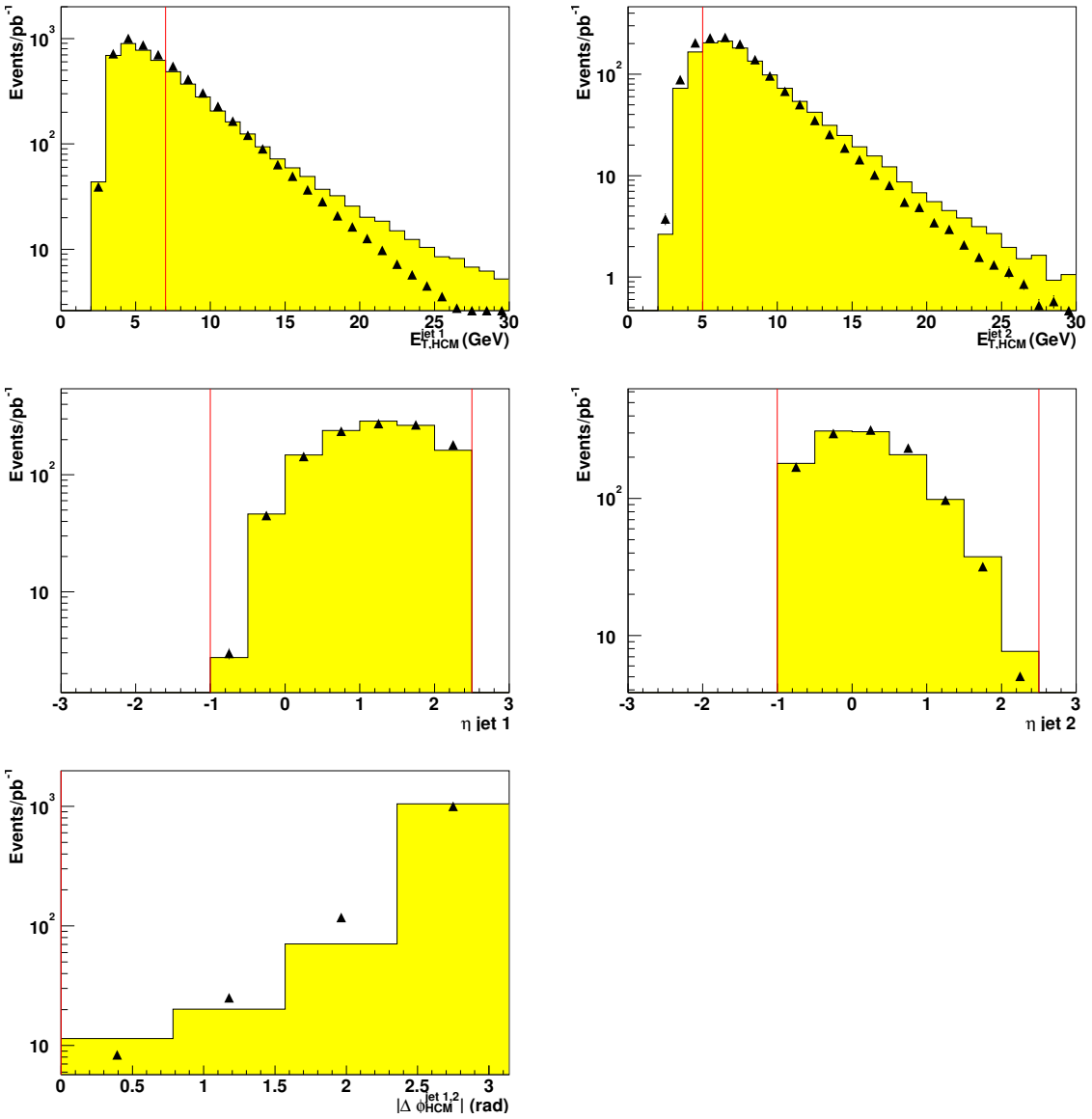

Figure 8.4: Distributions in the jet variables $E_{T,\mathrm{HCM}}^{\mathrm{jet1}}$, $E_{T,\mathrm{HCM}}^{\mathrm{jet2}}$, $\eta_{\mathrm{LAB}}^{\mathrm{jet1}}$, $\eta_{\mathrm{LAB}}^{\mathrm{jet2}}$, and $|\Delta\phi_{\mathrm{HCM}}^{\mathrm{jet1,2}}|$ from the dijet sample compared to those from ARIADNE. Other details as in the caption to Figure 8.3.

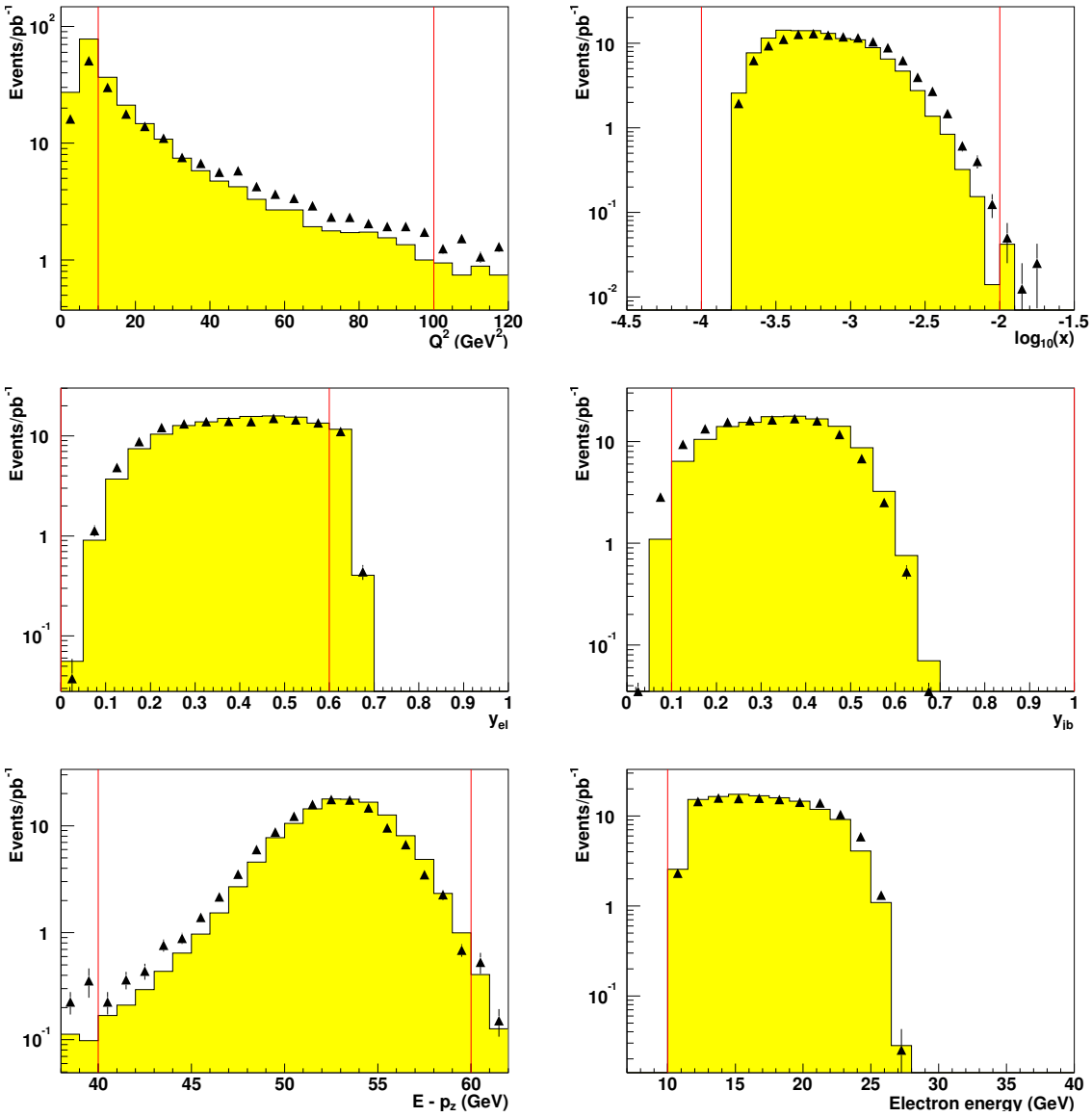

Figure 8.5: Distributions in the kinematic variables Q^2_{el}, x_{el}, y_{jb}, y_{el}, $E - p_z$, and scattered electron energy from the trijet sample compared to those from ARIADNE. Other details as in the caption to Figure 8.3.

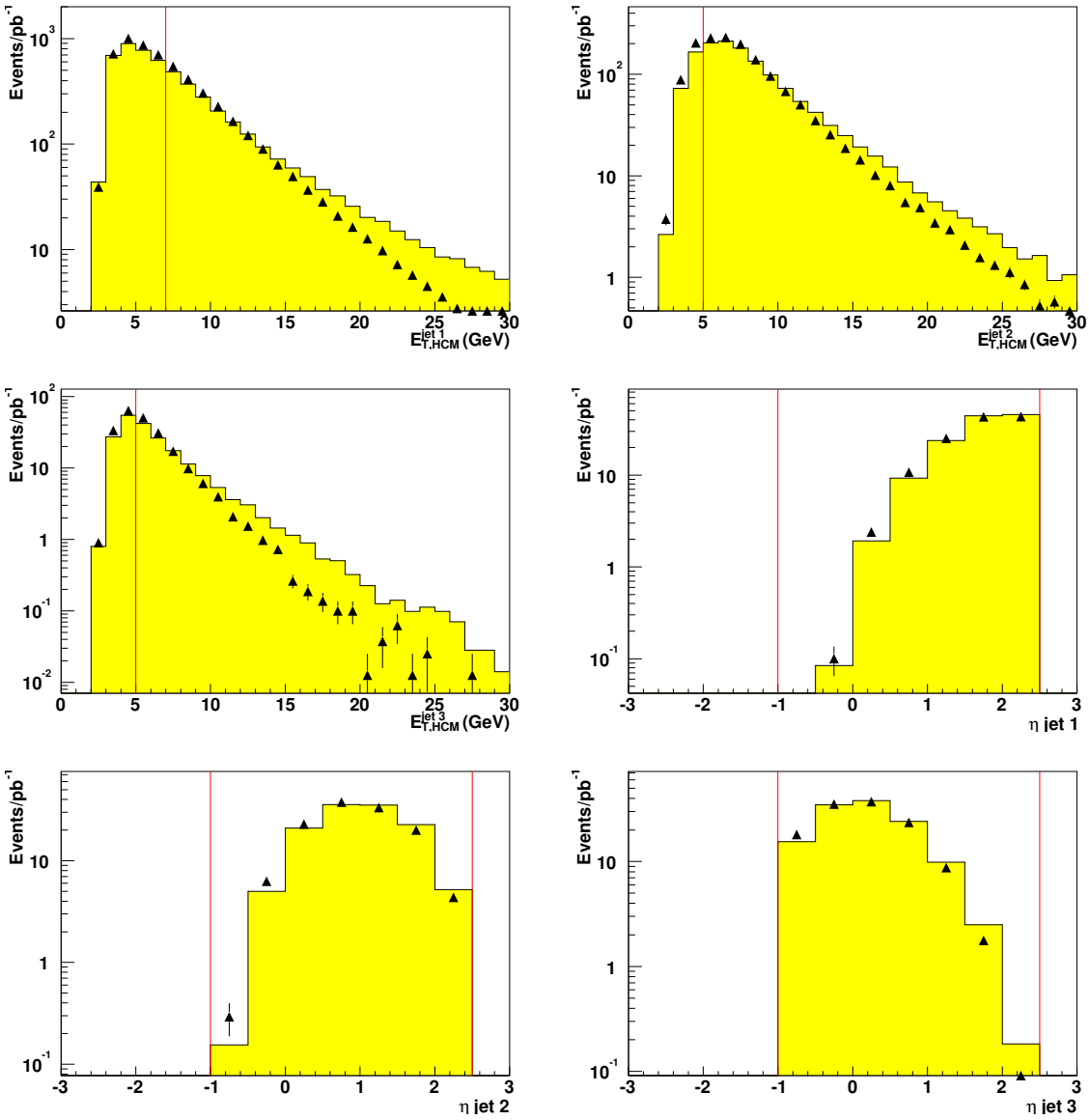

Figure 8.6: $E_{T,\mathrm{HCM}}^{\mathrm{jet3}}$, $\eta_{\mathrm{LAB}}^{\mathrm{jet1}}$, $\eta_{\mathrm{LAB}}^{\mathrm{jet2}}$, and $\eta_{\mathrm{LAB}}^{\mathrm{jet3}}$ from the trijet sample compared to those from ARIADNE. Other details as in the caption to Figure 8.3.

8.2 Jet Energy Corrections

The jet energies were corrected for energy losses from inactive material in the detector by using the Monte Carlo to estimate the average fraction of jet energy lost by a hadron-level jet due to the inactive material in the detector. Because the fractional energy loss depends on the thickness of the material the jet passes through, it depends on the polar angle of the jet in the detector. The measured range in pseudorapidity, $-1 < \eta_{\rm LAB} < 2.5$, was therefore divided into sectors with a width in η of 0.2, with one sector, $2.2 < \eta_{\rm LAB} < 2.5$, having a width of 0.3.

To estimate the fractional energy loss in each segment of the detector, the hadron-level jets were matched to their corresponding detector-level jets. To ensure that the detector-level jets were highly correlated to their matching hadron-level jets, each detector-level jet was matched to the hadron-level jet closest in $\eta - \phi$ space to it, with the minimal requirement that the separation in $\eta - \phi$ space between a detector-level jet and its corresponding hadron-level jet be less than 1 unit in $\eta - \phi$ space. A profile histogram of detector-level $E_{T,\rm LAB}^{\rm jet}$ vs. hadron-level $E_{T,\rm LAB}^{\rm jet}$ was made for each region in pseudorapidity, and bins with insufficient statistics were removed. The estimated fractional jet energy lost by a jet in each region in η was then obtained by performing a quadratic fit to that region's profile histogram. The quadratic term accounts for deviations from a linear correlation between the detector-level jet $E_{T,\rm LAB}^{\rm jet}$ and the hadron-level jet $E_{T,\rm LAB}^{\rm jet}$ and provides a more accurate correction factor over the entire range of $E_{T,\rm HCM}^{\rm jet}$ than does a linear fit (see Fig. 8.7). Measurements of correlations in jet transverse energy and momenta require a good level of agreement

between the corrected detector-level jet energy and the hadron-level jet energy, as a systematic difference between the hadron level and detector level distributions of these correlations will result in a poor reconstruction of these events due to increased smearing between bins. The corrected transverse energy of a reconstructed jet is then parameterized as

$$E_{T,\mathrm{HCM}}^{\mathrm{corr}} = \frac{-A_1 + \sqrt{A_1^2 - 4 \cdot A_2 \cdot (A_0 - E_{T,\mathrm{HCM}}^{\mathrm{jet}})}}{2 \cdot A_2} \tag{8.2}$$

where the factors A_0, A_1, and A_2 are the intercept, slope, and quadratic correction terms, respectively, obtained from the fit in the region corresponding to the reconstructed jet's measured pseudorapidity. A correction factor based on the ratio of the corrected to uncorrected jet transverse energy was also applied to the jet 4-momenta:

$$Corr = \frac{E_{T,\mathrm{HCM}}^{\mathrm{corr}}}{E_{T,\mathrm{HCM}}^{\mathrm{jet}}} \tag{8.3}$$

Typical jet energy correction factors were $1 - 1.2$, depending on the transverse energy of the detector-level jet and the location of the jet within the detector.

8.3 Cross Sections and Corrections

With a measurement made with a specific binning, the "raw" cross section for each bin is the number of data events divided by the measured luminosity, $\mathcal{L}$:

$$\sigma_{raw,i} = \frac{N_{\mathrm{events},i}^{\mathrm{data}}}{\mathcal{L}} \tag{8.4}$$

To account for the limitations of the detector, a correction factor is applied to each bin of the "raw" cross sections, giving the following definition of the cross section:

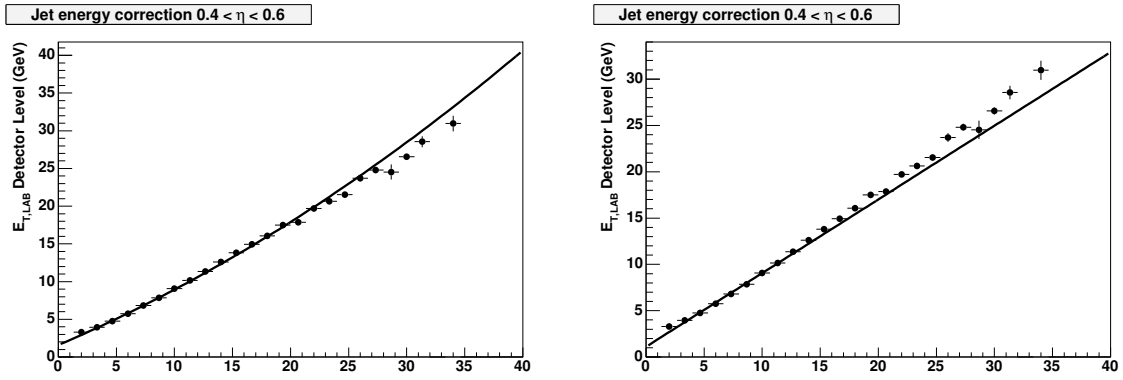

Figure 8.7: A comparison of a quadratic fit (left) to a linear fit (right) of one of the detector-level vs. hadron-level profile histograms of $E^{\text{jet}}_{T,\text{LAB}}$. The better overall description of the profile by the quadratic fit is important for measurements of correlations in jet transverse momenta.

$$\sigma_i = c_i \cdot \frac{N^{\text{data}}_{\text{events},i}}{\mathcal{L}} \tag{8.5}$$

The correction factor c_i for each bin is obtained from the Monte Carlo by using the events passing the detector-level selection and events passing the hadron-level selection:

$$c = \frac{\text{Number of events generated}}{\text{Number of events reconstructed}} \tag{8.6}$$

The correction factors can be factorized into terms of the purity and efficiency: $c_i = pur_i/eff_i$. The purity for each bin is defined as the number of events generated *and* reconstructed at the detector level divided by the number of events reconstructed at the detector level:

$$pur = \frac{\text{Number of events generated AND reconstructed}}{\text{Number of events reconstructed}} \tag{8.7}$$

The efficiency is defined as the number of events generated *and* reconstructed at

the detector level divided by the number of events generated.

$$eff = \frac{\text{Number of events generated AND reconstructed}}{\text{Number of events generated}} \tag{8.8}$$

Typical efficiencies and purities were about 50% for the differential cross sections, with correction factors typically between 1 and 1.5. For the double-differential cross sections, the efficiencies and purities were typically $20 - 50\%$, with correction factors between 1 and 2. Examples of typical purities, efficiencies, and correction factors are shown in Figures 8.8 and 8.9; and all purities, efficiencies and correction factors are included in Appendix B.

8.3.1 Calculation of the Statistical Error

Because the correction factor, c, as expressed in equation 8.6 is a ratio of correlated quantities, the correlations must be treated in the correct manner. For the calculation of the correction factor for each bin, the quantities are broken up into their uncorrelated components. Events in the correction factor fall into three uncorrelated categories: those generated and reconstructed, those generated and not reconstructed, and those reconstructed but not generated. Expressing 8.6 in these categories yields

$$c = \frac{gen \oplus det + gen \oplus \overline{det}}{gen \oplus det + \overline{gen} \oplus det} \tag{8.9}$$

Expressing c in this manner allows for the usage of the standard error propagation treatment for a measurement x that can be expressed as a function of a number of uncorrelated values, x_i:

$$x = f(x_1, x_2, x_3, \ldots) \tag{8.10}$$

The error of the quantity x is given by the formula for error propagation:

$$\Delta x = \sqrt{(\Delta x_1 \cdot \frac{\partial f}{\partial x_1})^2 + (\Delta x_2 \cdot \frac{\partial f}{\partial x_2})^2 + (\Delta x_3 \cdot \frac{\partial f}{\partial x_3})^2 + \ldots} \tag{8.11}$$

The calculation of the uncertainty of c was handled in this manner by use of an algorithm using the above procedure. To obtain the overall statistical error of the cross sections, the uncertainty of the correction factor was then added in quadrature to the uncertainty in the following manner:

$$\Delta\sigma = \sqrt{(\Delta c \cdot \sigma_{raw})^2 + (\Delta\sigma_{raw} \cdot c)^2} \tag{8.12}$$

Bins in which $gen \oplus det = 0$ from 8.9 were excluded, as the purities and the efficiencies for such bins are zero, resulting in unreliable measurements.

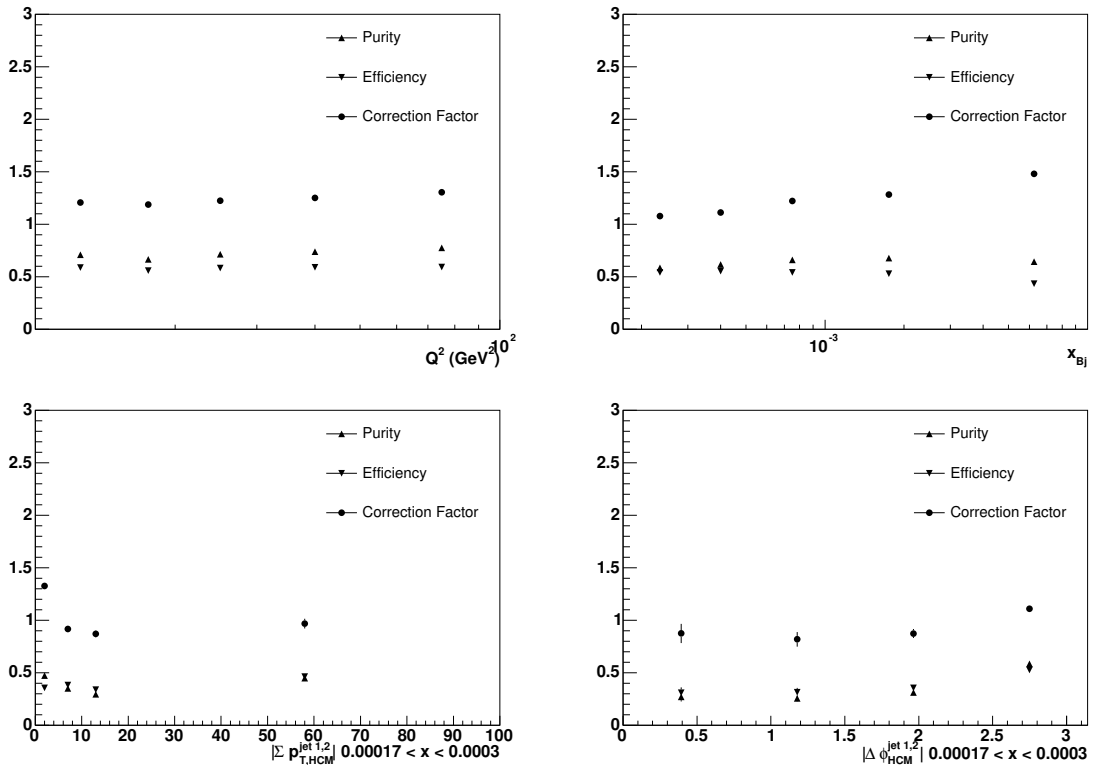

Figure 8.8: Purities, efficiencies, and correction factors for dijet sample as functions of Q^2, x_{Bj}, and $|\Sigma p_{T,\mathrm{HCM}}^{\mathrm{jet1,2}}|$ and $|\Delta\phi_{\mathrm{HCM}}^{\mathrm{jet1,2}}|$ for the lowest bin in x_{Bj}. The correction factors were obtained using ARIADNE.

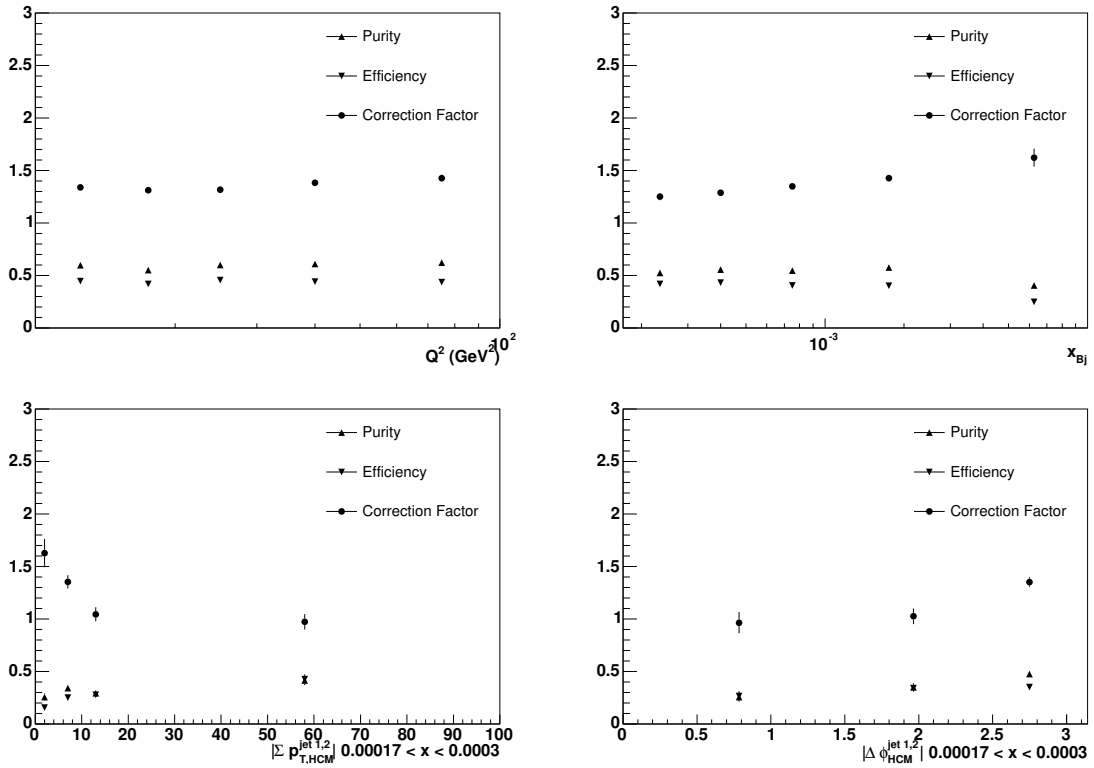

Figure 8.9: Purities, efficiencies, and correction factors for trijet sample as functions of Q^2, x_{Bj}, and $|\Sigma p_{T,\mathrm{HCM}}^{\mathrm{jet1,2}}|$ and $|\Delta\phi_{\mathrm{HCM}}^{\mathrm{jet1,2}}|$ for the lowest bin in x_{Bj}. The correction factors were obtained using ARIADNE.

8.4 QED Corrections

Because the NLOJET calculations account for QED radiation only to leading-order, whereas the data contain QED effects to all orders, the measured cross sections were corrected to the QED Born level by applying an additional correction obtained from a special sample of the LEPTO MC with the radiative QED effects turned off. The correction factors applied to each bin of the cross sections are given by $N_{\mathrm{BORN}}/N_{\mathrm{RAD}}$, where N_{RAD} is the number of events in the bin with the QED radiative effects included, and N_{BORN} is the number of events in the bin without the QED effects included. The QED radiative effects, which are included in the tabulated results, were typically $2-4\%$.

8.5 Hadronization Corrections

In order to make a meaningful comparison with the measurements that have been corrected to the hadron-level, an extra correction factor is applied to the parton-level predictions from NLOJET for the hadronization effects. The NLOJET calculations were corrected using a bin-by-bin procedure using the hadron-level and parton-level samples from the LEPTO sample used for the QED corrections:

$$C_{\mathrm{HAD}} = \frac{N_{\mathrm{HAD}}}{N_{\mathrm{PAR}}} \tag{8.13}$$

The hadronization correction factors, also included in the tabulated results, were typically $0.7-1.0$.

Chapter 9

Results

9.1 Systematic Uncertainty Estimates

A detailed study of the sources contributing to the systematic uncertainties of the measurements has been performed. The main sources contributing to the systematic uncertainties are listed below:

- the data were corrected using LEPTO instead of ARIADNE. This systematic uncertainty was typically $5 - 10\%$ for the single-differential cross sections, and $5 - 30\%$ for the cross sections as functions of jet correlations. This systematic uncertainty accounts for the treatment of the parton shower approach, where for a certain kinematic and jet phase space, the predictions from ARIADNE (CDM), which i includes some BFKL-like effects, might differ greatly from those from LEPTO (MEPS), which is DGLAP-based. In this phase space, the ignorance of how the parton cascade proceeds should be the largest systematic uncertainty.

- the jet energies in the data were scaled up and down by 3% for jets with transverse energy less than 10 GeV and 1% for jets with transverse energy above 10

GeV, according to the estimated jet energy scale uncertainty [66]. The systematic uncertainty from the jet energy scale was approximately $5 - 15\%$.

- the cut on $E_{T,\mathrm{HCM}}^{\mathrm{jet}}$ for each jet was raised and lowered by 1 GeV, corresponding to the E_T resolution, which resulted in a systematic uncertainty of $5 - 10\%$ for the cross sections as functions of jet correlations. Additionally, the cut on $E_{T,\mathrm{HCM}}^{\mathrm{jet3}}$ had a systematic uncertainty of $5 - 10\%$ for the trijet cross sections.

- the upper and lower cuts on $\eta_{\mathrm{LAB}}^{\mathrm{jet1,2(,3)}}$ were each changed by ± 0.1, corresponding to the η resolution, which produced a systematic uncertainty of up to 10% for the cross sections as functions of jet correlations;

- the uncertainties due to the selection cuts was estimated by varying the cuts within the resolution of each variable. These systematic uncertainties were typically similar to or smaller than the statistical uncertainties.

The systematic uncertainties not associated with the absolute energy scale of the jets were added in quadrature to the statistical uncertainties and are shown as error bars. The uncertainty due to the absolute energy scale of the jets is shown separately as a shaded band in each figure in this chapter, due to the large bin-to-bin correlation. In addition, there is an overall normalization uncertainty of 2.2% from the luminosity determination, which is not included in the overall uncertainty. The systematic uncertainties for the measured cross sections are shown in Appendix C.

The theoretical uncertainty was estimated by varying the renormalization and factorization scales simultaneously up and down by a factor of two, which estimates the contribution from higher-order terms not included in the calculations. The un-

certainties in the proton PDFs were estimated in the previous ZEUS multijets analysis [12] by repeating NLOJET calculations using 40 additional sets from CTEQ6M, which resulted in a 2.5% contribution to the theoretical uncertainty and was therefore neglected.

9.2 Single-differential Cross Sections $d\sigma/dQ^2$, $d\sigma/dx_{\mathrm{Bj}}$ and Trijet-to-dijet Cross Section Ratios

To examine the low-x_{Bj} limits of DGLAP applicability, the first test of the NLOJET calculations was to compare its predictions of the kinematic variables Q^2 and x_{Bj} to the measured distributions. The single-differential cross-sections $d\sigma/dQ^2$ and $d\sigma/dx_{\mathrm{Bj}}$ for dijet and trijet production are presented in Figs. 9.1(a) and (c), and Tables A.1–A.14. The ratio $\sigma_{\mathrm{trijet}}/\sigma_{\mathrm{dijet}}$ of the trijet cross section to the dijet cross section, as a function of Q^2 and of x_{Bj} are presented in Figs. 9.1(b) and 9.1(d), respectively. The ratio $\sigma_{\mathrm{trijet}}/\sigma_{\mathrm{dijet}}$ is almost Q^2 independent, as shown in Fig. 9.1(b), and falls steeply with increasing x_{Bj}, as shown in Fig. 9.1(d). In the cross-section ratios, the experimental and theoretical uncertainties partially cancel, providing a possibility to test the pQCD calculations more precisely than can be done with the individual cross sections. Both the cross sections and the cross-section ratios are well described by the NLOJET calculations.

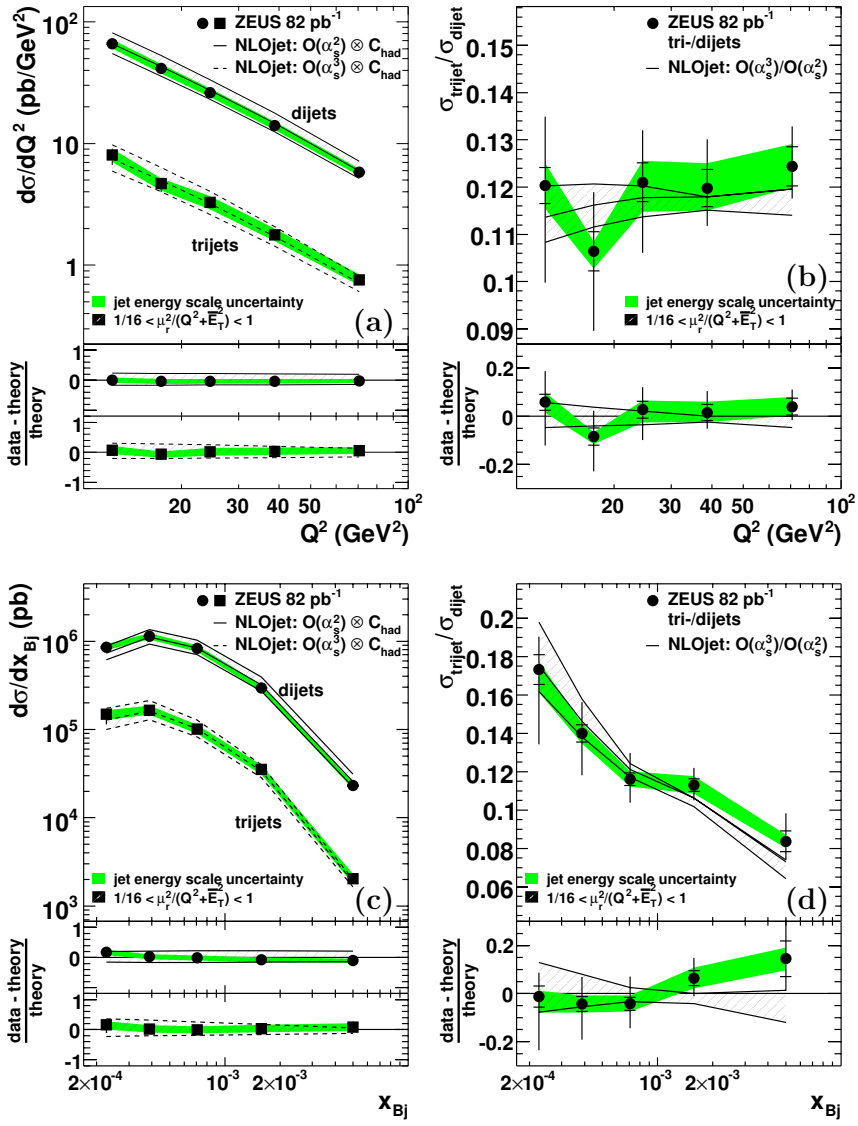

Figure 9.1: Inclusive dijet and trijet cross sections as functions of (a) Q^2 and (c) x_{Bj}. Figures (b) and (d) show the ratios of the trijet to dijet cross sections. The bin-averaged differential cross sections are plotted at the bin centers. The inner error bars represent the statistical uncertainties. The outer error bars represent the quadratic sum of statistical and systematic uncertainties not associated with the jet energy scale. The shaded band indicates the jet energy scale uncertainty. The predictions of perturbative QCD at NLO, corrected for hadronization effects and using the CTEQ6 parameterizations of the proton PDFs, are compared to data. The lower parts of the plots show the relative difference between the data and the corresponding theoretical prediction. The hatched band represents the renormalization-scale uncertainty of the QCD calculation.

9.3 Transverse Energy and Pseudorapidity Dependencies of Cross Sections

The focus of this analysis is using jet correlations to test the accuracy of the DGLAP approach. To ensure that the jets themselves are well-understood in this kinematic region, the cross sections as a function of the jet variables are studied. The single-differential cross-sections $d\sigma/dE^{\rm jet}_{T,\rm HCM}$ for two (three) jet events are presented in Fig. 9.2. The single-differential cross sections $d\sigma/d\eta^{\rm jet}_{\rm LAB}$ for dijet and trijet production are presented in Figs. 9.3(a) and 9.3(c). For this figure, the two (three) jets with highest $E^{\rm jet}_{T,\rm HCM}$ were ordered in $\eta^{\rm jet}_{\rm LAB}$. The measured cross sections are well described by the NLOJET calculations over the whole range in $E^{\rm jet}_{T,\rm HCM}$ and $\eta^{\rm jet}_{\rm LAB}$ considered.

Also shown in Figure 9.3 are the measurements of the single-differential cross-sections $d\sigma/d|\Delta\eta^{\rm jet1,2}_{\rm HCM}|$, where $|\Delta\eta^{\rm jet1,2}_{\rm HCM}|$ is the absolute difference in pseudorapidity of the two jets with highest $E^{\rm jet}_{T,\rm HCM}$ (see Figs. 9.3(b) and 9.3(d)). The measurement of $|\Delta\eta^{\rm jet1,2}_{\rm HCM}|$ is a direct test of the correlation in polar angle of the two hardest jets, which might be sensitive to the parton evolution scheme. The NLOJET predictions describe the measurements well over the entire kinematic range considered, as shown in the figure, and also when separated into bins of $x_{\rm Bj}$ given in A.2 (not shown).

9.4 Jet transverse energy and momentum correlations

Correlations in jet transverse energy are perhaps more sensitive to low-$x_{\rm Bj}$ effects than correlations in jet pseudorapidity, as the transverse energy $E^{\rm jet}_{T,\rm HCM}$ is more directly related to the jet transverse momentum. Correlations in transverse energy of the jets have been investigated by measuring the double-differential cross-sections

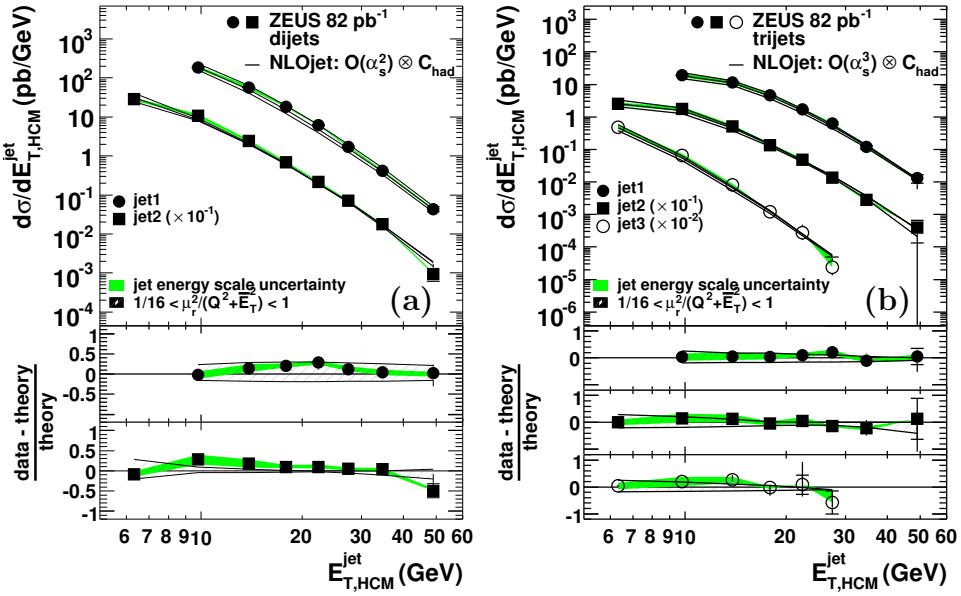

Figure 9.2: Inclusive dijet (a) and trijet (b) cross sections as functions of $E^{\rm jet}_{T,\rm HCM}$ with the jets ordered in $E^{\rm jet}_{T,\rm HCM}$. The cross sections of the second and third jet were scaled for readability. Other details as in the caption to Fig. 9.1.

$d^2\sigma/dx_{\rm Bj}d\Delta E^{\rm jet1,2}_{T,\rm HCM}$, where $\Delta E^{\rm jet1,2}_{T,\rm HCM}$ is the difference in transverse energy between the two jets with the highest $E^{\rm jet}_{T,\rm HCM}$. The measurement was performed in $x_{\rm Bj}$ bins, which are defined in Table A.2, for dijet and trijet production. Figures 9.4 and 9.5 show the cross-sections $d^2\sigma/dx_{\rm Bj}d\Delta E^{\rm jet1,2}_{T,\rm HCM}$ for all bins in $x_{\rm Bj}$ for the dijet and trijet samples, respectively.

The NLOJET calculations at $\mathcal{O}(\alpha_s^2)$ do not describe the high-$\Delta E^{\rm jet1,2}_{T,\rm HCM}$ tail of the dijet sample at low $x_{\rm Bj}$, where the calculations fall below the data. Since these calculations give the lowest-order non-trivial contribution to the cross section in the region $\Delta E^{\rm jet1,2}_{T,\rm HCM} > 0$, they are affected by large uncertainties from the higher-order

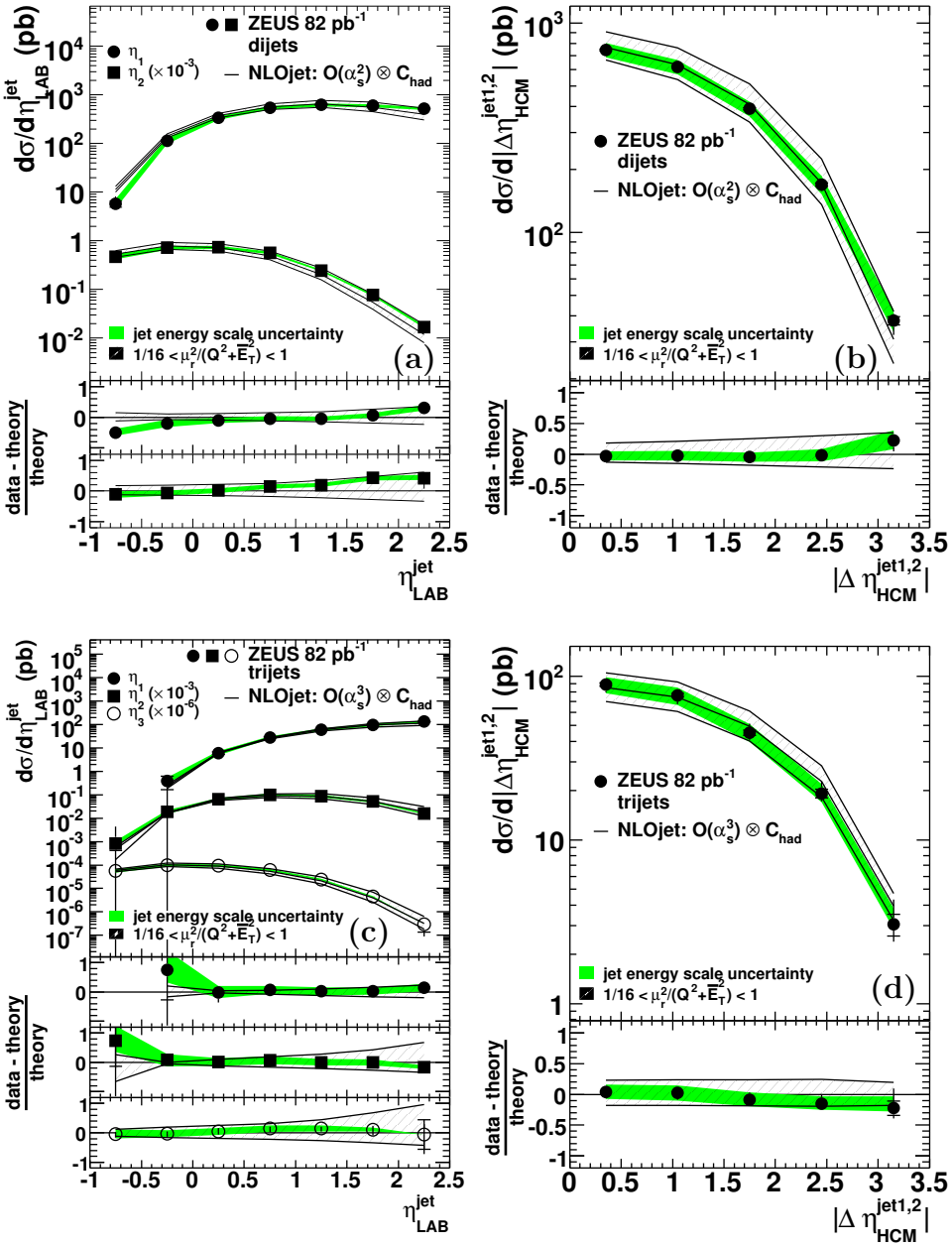

Figure 9.3: The inclusive dijet (a) and trijet (c) cross sections as functions of $\eta^{\rm jet}_{\rm LAB}$ with the jets ordered in $\eta^{\rm jet}_{\rm LAB}$: $\eta^{\rm jet1}_{\rm LAB} > \eta^{\rm jet2}_{\rm LAB} > \eta^{\rm jet3}_{\rm LAB}$. The cross sections of the second and third jet were scaled for readability. Figures (b) and (d) show the dijet and trijet cross sections as functions of $|\Delta\eta^{\rm jet1,2}_{\rm HCM}|$ between the two jets with highest $E^{\rm jet}_{T,\rm HCM}$. Other details as in the caption in Fig. 9.1.

terms in α_s. A higher-order calculation for the dijet sample is possible with NLOJET if the region $\Delta E_{T,\mathrm{HCM}}^{\mathrm{jet1,2}}$ near zero is avoided. NLOJET calculations at $\mathcal{O}(\alpha_s^3)$ for the dijet sample have been obtained for the region $\Delta E_{T,\mathrm{HCM}}^{\mathrm{jet1,2}} > 4$ GeV and are compared to the data in Fig. 9.4. With the inclusion of the next term in the perturbative series in α_s, the NLOJET calculations describe the data within the theoretical uncertainties. The NLOJET calculations at $\mathcal{O}(\alpha_s^3)$ for trijet production are consistent with the measurements.

As a refinement to the studies of the correlations between the transverse energies of the jets, further correlations of the jet transverse momenta have been investigated. The correlations in jet transverse momenta were examined by measuring two sets of double-differential cross sections: $d^2\sigma/dx_{\mathrm{Bj}}d|\Sigma\vec{p}_{T,\mathrm{HCM}}^{\,\mathrm{jet1,2}}|$ and $d^2\sigma/dx_{\mathrm{Bj}}d(|\Delta\vec{p}_{T,\mathrm{HCM}}^{\,\mathrm{jet1,2}}|/(2E_{T,\mathrm{HCM}}^{\mathrm{jet1}}))$. The variable $|\Sigma\vec{p}_{T,\mathrm{HCM}}^{\,\mathrm{jet1,2}}|$ is the transverse component of the vector sum of the jet momenta of the two jets with the highest $E_{T,\mathrm{HCM}}^{\mathrm{jet}}$. For events with only two jets $|\Sigma\vec{p}_{T,\mathrm{HCM}}^{\,\mathrm{jet1,2}}| = 0$, and additional QCD radiation increases this value. The variable $|\Delta\vec{p}_{T,\mathrm{HCM}}^{\,\mathrm{jet1,2}}|/(2E_{T,\mathrm{HCM}}^{\mathrm{jet1}})$ is the magnitude of the vector difference of the transverse momenta of the two jets with the highest $E_{T,\mathrm{HCM}}^{\mathrm{jet}}$ scaled by twice the transverse energy of the hardest jet. For events with only two jets $|\Delta\vec{p}_{T,\mathrm{HCM}}^{\,\mathrm{jet1,2}}|/(2E_{T,\mathrm{HCM}}^{\mathrm{jet1}}) = 1$, and additional QCD radiation decreases this value. Figures 9.6 – 9.9 show the cross-sections $d^2\sigma/dx_{\mathrm{Bj}}d|\Sigma\vec{p}_{T,\mathrm{HCM}}^{\,\mathrm{jet1,2}}|$ and the cross-sections $d^2\sigma/dx_{\mathrm{Bj}}d|\Delta\vec{p}_{T,\mathrm{HCM}}^{\,\mathrm{jet1,2}}|/(2E_{T,\mathrm{HCM}}^{\mathrm{jet1}})$ in bins of x_{Bj} for the dijet and trijet samples.

At low x_{Bj}, the NLOJET calculations at $\mathcal{O}(\alpha_s^2)$ underestimate the dijet cross sections at high values of $|\Sigma\vec{p}_{T,\mathrm{HCM}}^{\,\mathrm{jet1,2}}|$ and low values of $|\Delta\vec{p}_{T,\mathrm{HCM}}^{\,\mathrm{jet1,2}}|/(2E_{T,\mathrm{HCM}}^{\mathrm{jet1}})$. The description of the data by the NLOJET calculations at $\mathcal{O}(\alpha_s^2)$ improves at higher

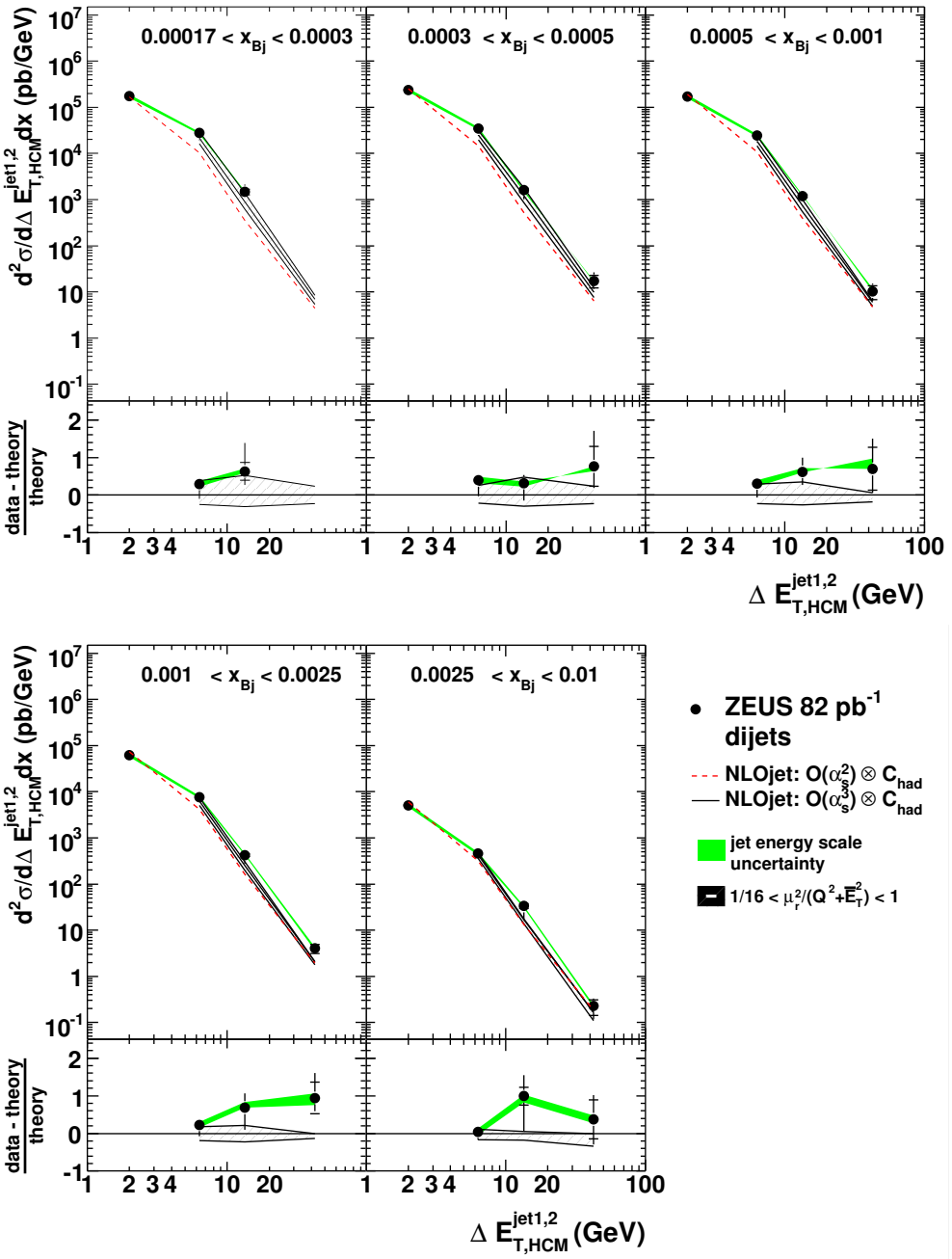

Figure 9.4: Dijet cross sections as functions of $\Delta E^{\mathrm{jet1,2}}_{T,\mathrm{HCM}}$. The NLOJET calculations at $\mathcal{O}(\alpha_s^2)$ ($\mathcal{O}(\alpha_s^3)$) are shown as dashed (solid) lines. The lower parts of the plots show the relative difference between the data and the $\mathcal{O}(\alpha_s^3)$ predictions. Other details as in the caption to Fig. 9.1.

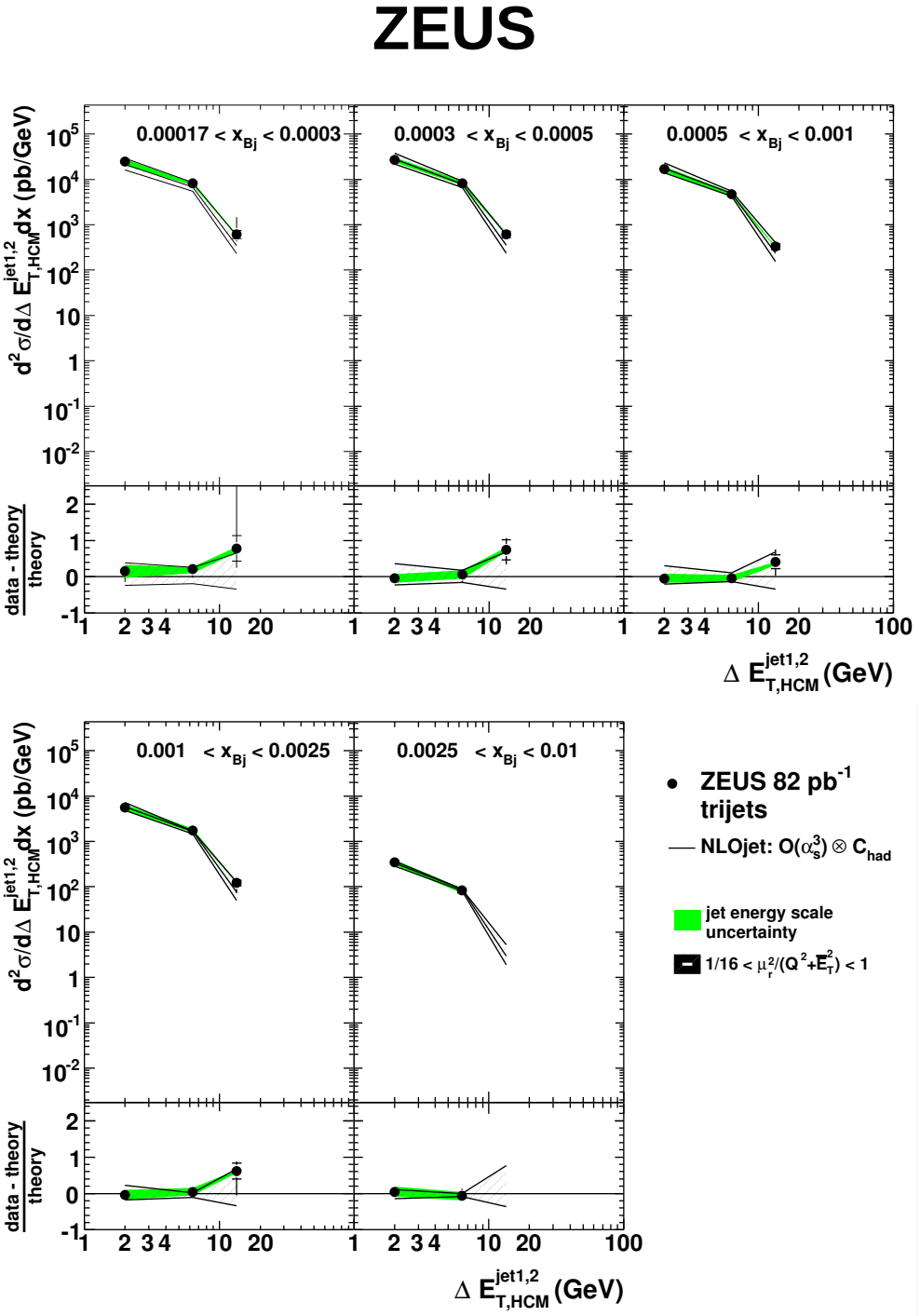

Figure 9.5: Trijet cross sections as functions of $\Delta E_{T,\mathrm{HCM}}^{\mathrm{jet1,2}}$. The measurements are compared to NLOJET calculations at $\mathcal{O}(\alpha_s^3)$. Other details as in the caption to Fig. 9.1.

values of $x_{\rm Bj}$. A higher-order calculation with NLOJET at $\mathcal{O}(\alpha_s^3)$ for the dijet sample has been obtained for the region $|\Sigma\vec{p}_{T,\rm HCM}^{\rm jet1,2}| > 4$ GeV, which is compared to the data in Fig. 9.6; and for the region $|\Delta\vec{p}_{T,\rm HCM}^{\rm jet1,2}|/(2E_{T,\rm HCM}^{\rm jet1}) < 0.85$, which is compared to the data in Fig. 9.8. With the inclusion of the next term in the perturbative series in α_s, the NLOJET calculations describe the data well. The NLOJET calculations at $\mathcal{O}(\alpha_s^3)$ for trijet production are consistent with the measurements.

9.5 Azimuthal distributions of the jets

Measurements of the double-differential cross-section $d^2\sigma/dx_{\rm Bj}d|\Delta\phi_{\rm HCM}^{\rm jet1,2}|$, where $|\Delta\phi_{\rm HCM}^{\rm jet1,2}|$ is the azimuthal separation of the two jets with the largest $E_{T,\rm HCM}^{\rm jet}$, for dijet and trijet production are shown in Figs. 9.10 and 9.11 for all bins in $x_{\rm Bj}$. For dijet and trijet production the cross section falls with $|\Delta\phi_{\rm HCM}^{\rm jet1,2}|$. The NLOJET calculations at $\mathcal{O}(\alpha_S^2)$ for dijet production decrease more rapidly with $|\Delta\phi_{\rm HCM}^{\rm jet1,2}|$ than the data and the calculations disagree with the data at low $|\Delta\phi_{\rm HCM}^{\rm jet1,2}|$. A higher-order NLOJET calculation at $\mathcal{O}(\alpha_S^3)$ for the dijet sample has been obtained for the region $|\Delta\phi_{\rm HCM}^{\rm jet1,2}| < 3\pi/4$ and describes the data well. The measurements for trijet production are reasonably well described by the NLOJET calculations at $\mathcal{O}(\alpha_S^3)$.

A further investigation has been performed by measuring the cross-section $d^2\sigma/dQ^2dx_{\rm Bj}$ for dijet (trijet) events with $|\Delta\phi_{\rm HCM}^{\rm jet1,2}| < 2\pi/3$ as a function of $x_{\rm Bj}$. For the two-jet final states, the presence of two leading jets with $|\Delta\phi_{\rm HCM}^{\rm jet1,2}| < 2\pi/3$ can indicate another high-E_T jet or set of high-E_T jets outside the measured η range. These cross sections are presented in Fig. 9.12. The NLOJET calculations at $\mathcal{O}(\alpha_S^2)$ for dijet production underestimate the data, the difference increasing towards low $x_{\rm Bj}$. The NLOJET calculations at $\mathcal{O}(\alpha_S^3)$ are up to about one order of magnitude

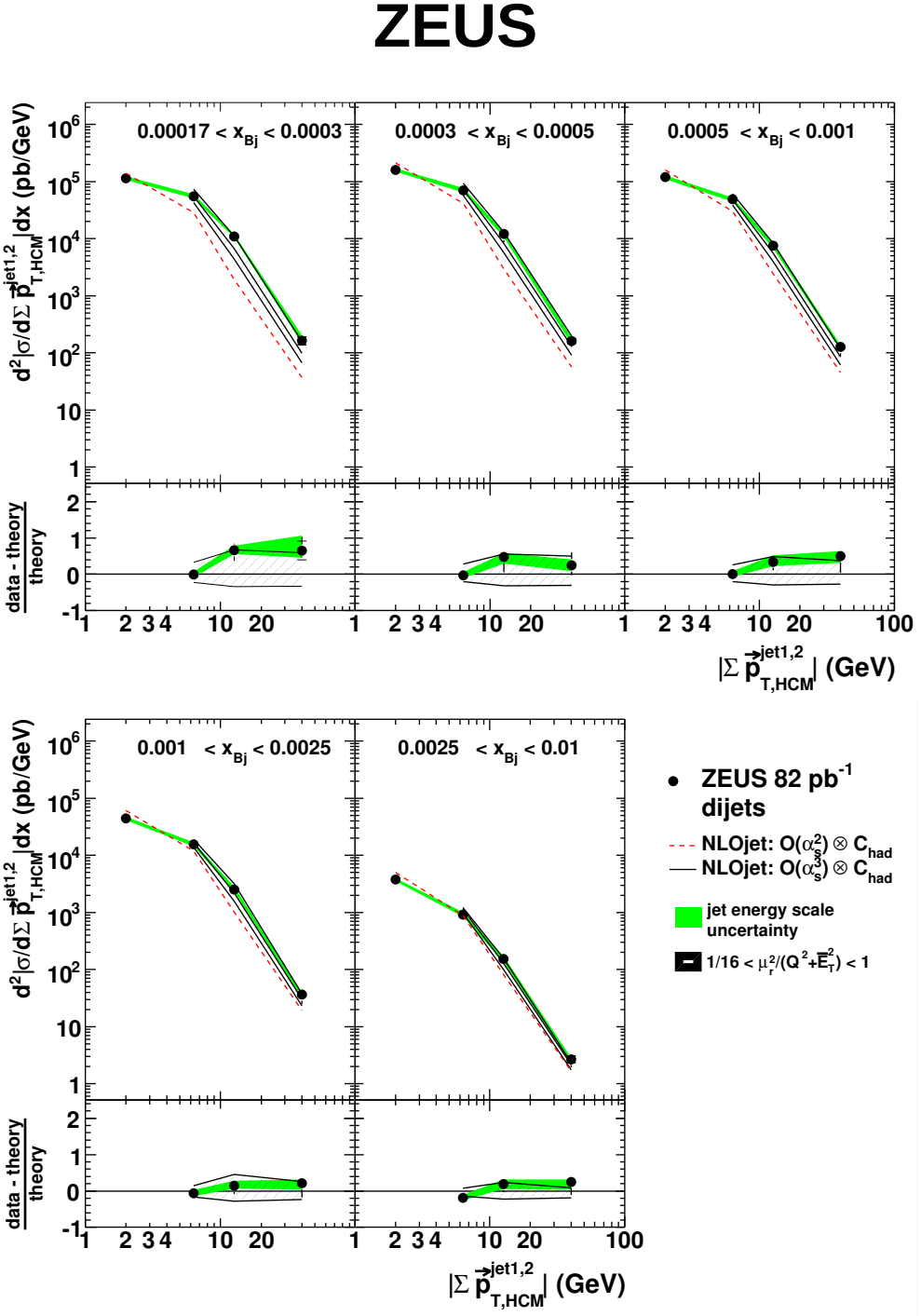

Figure 9.6: Dijet cross sections as functions of $|\Sigma\vec{p}^{\,\mathrm{jet1,2}}_{T,\mathrm{HCM}}|$. The NLOJET calculations at $\mathcal{O}(\alpha_s^2)$ ($\mathcal{O}(\alpha_s^3)$) are shown as dashed (solid) lines. The lower parts of the plots show the relative difference between the data and the $\mathcal{O}(\alpha_s^3)$ predictions. Other details as in the caption to Fig. 9.1.

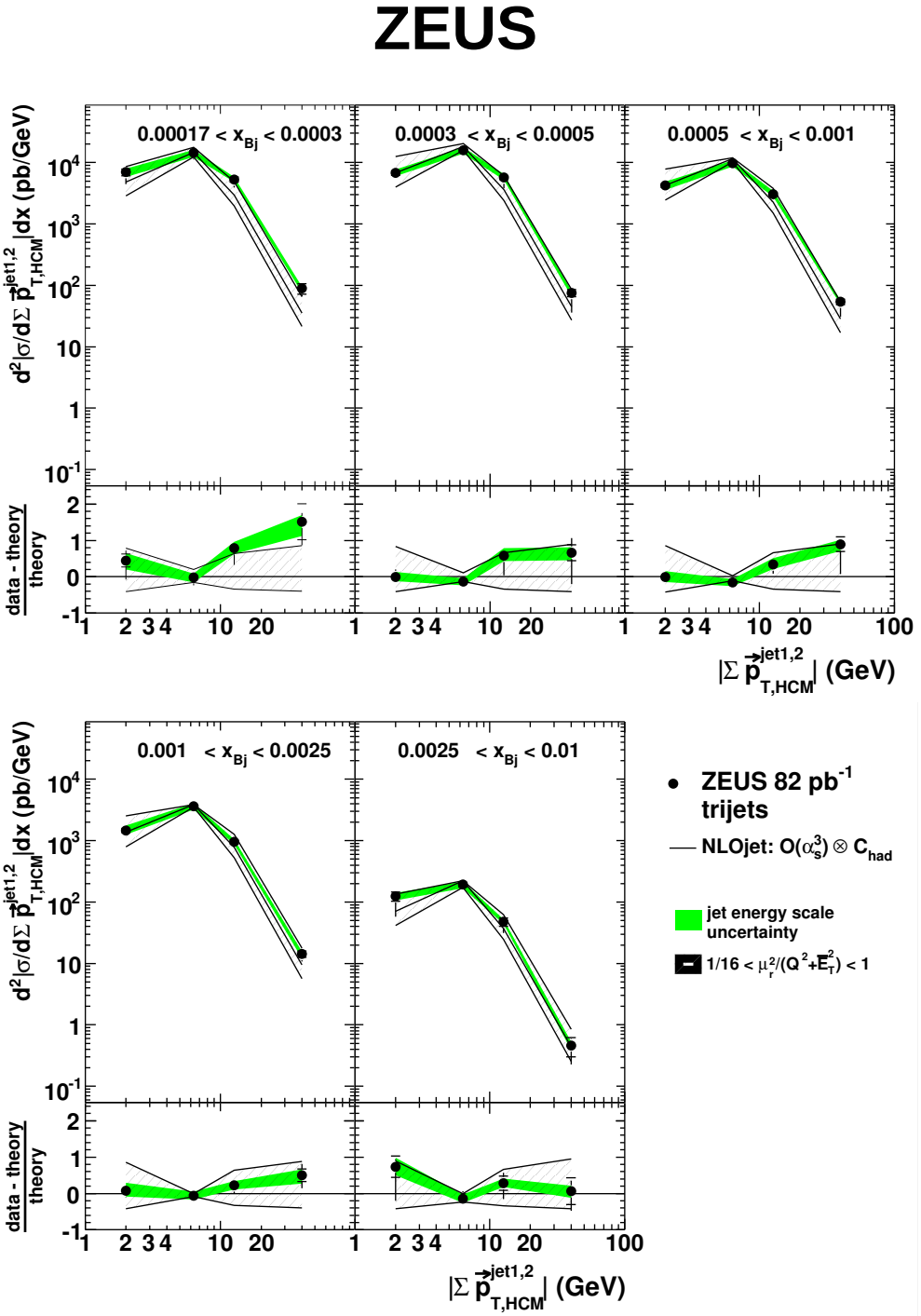

Figure 9.7: Trijet cross sections as functions of $|\Sigma\vec{p}_{T,\mathrm{HCM}}^{\,\mathrm{jet1,2}}|$. The measurements are compared to NLOJET calculations at $\mathcal{O}(\alpha_s^3)$. Other details as in the caption to Fig. 9.1.

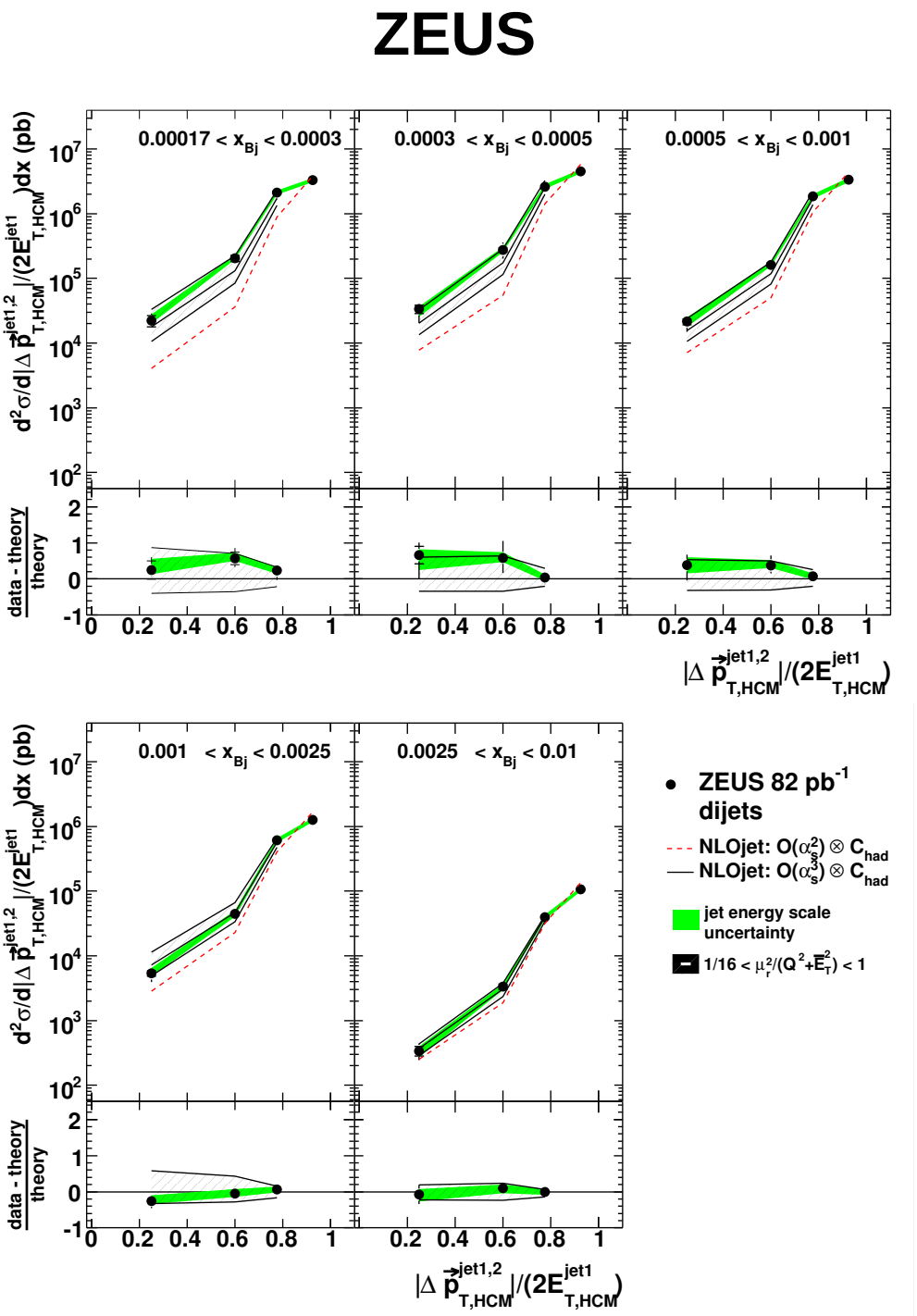

Figure 9.8: Dijet cross sections as functions of $|\Delta\vec{p}^{\,\mathrm{jet1,2}}_{T,\mathrm{HCM}}|/(2E^{\mathrm{jet1}}_{T,\mathrm{HCM}})$. The NLOJET calculations at $\mathcal{O}(\alpha_s^2)$ ($\mathcal{O}(\alpha_s^3)$) are shown as dashed (solid) lines. The lower parts of the plots show the relative difference between the data and the $\mathcal{O}(\alpha_s^3)$ predictions. Other details as in the caption to Fig. 9.1.

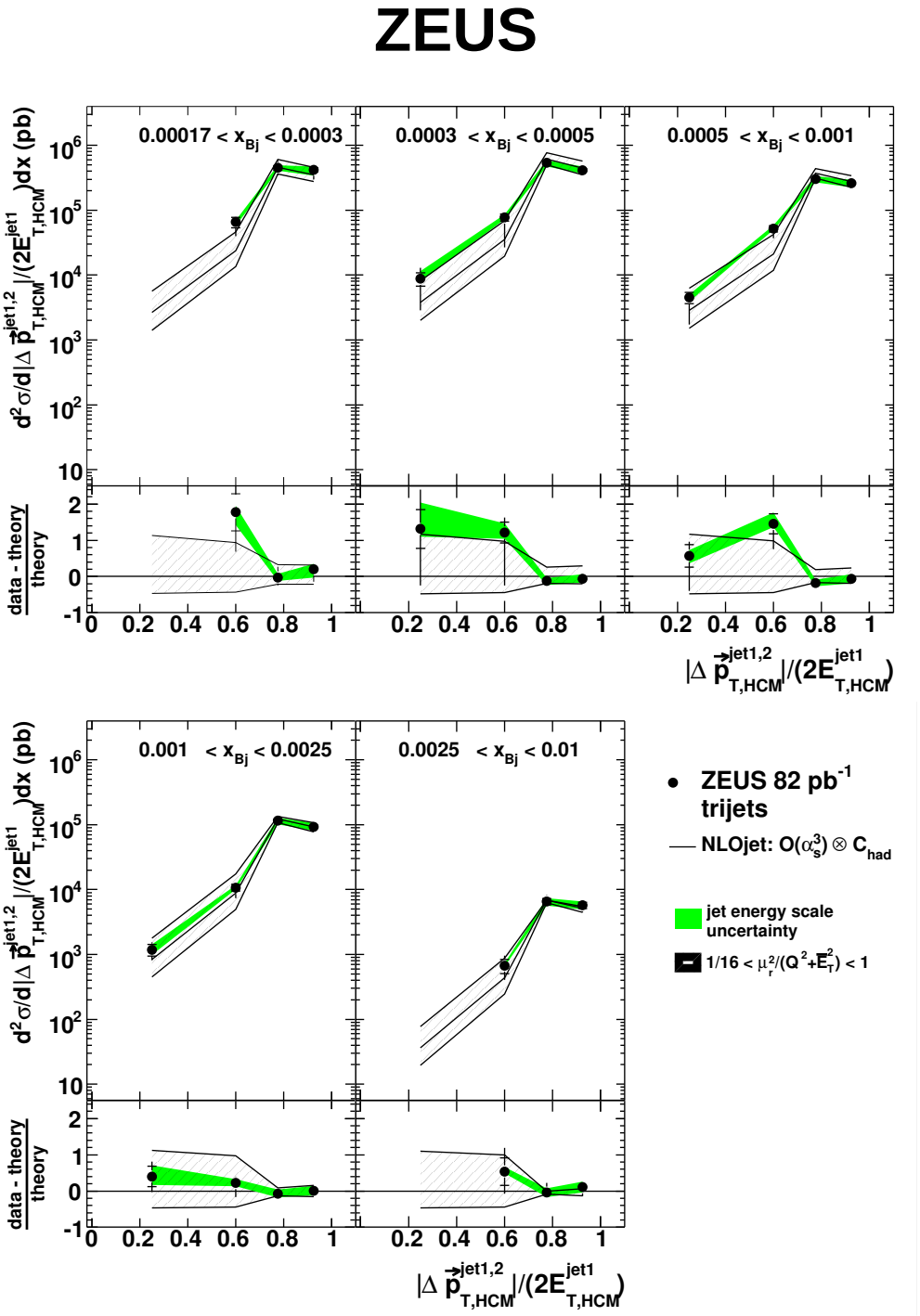

Figure 9.9: Trijet cross sections as functions of $|\Delta\vec{p}^{\,\mathrm{jet1,2}}_{T,\mathrm{HCM}}|/(2E^{\mathrm{jet1}}_{T,\mathrm{HCM}})$. The measurements are compared to NLOJET calculations at $\mathcal{O}(\alpha_s^3)$. Other details as in the caption to Fig. 9.1.

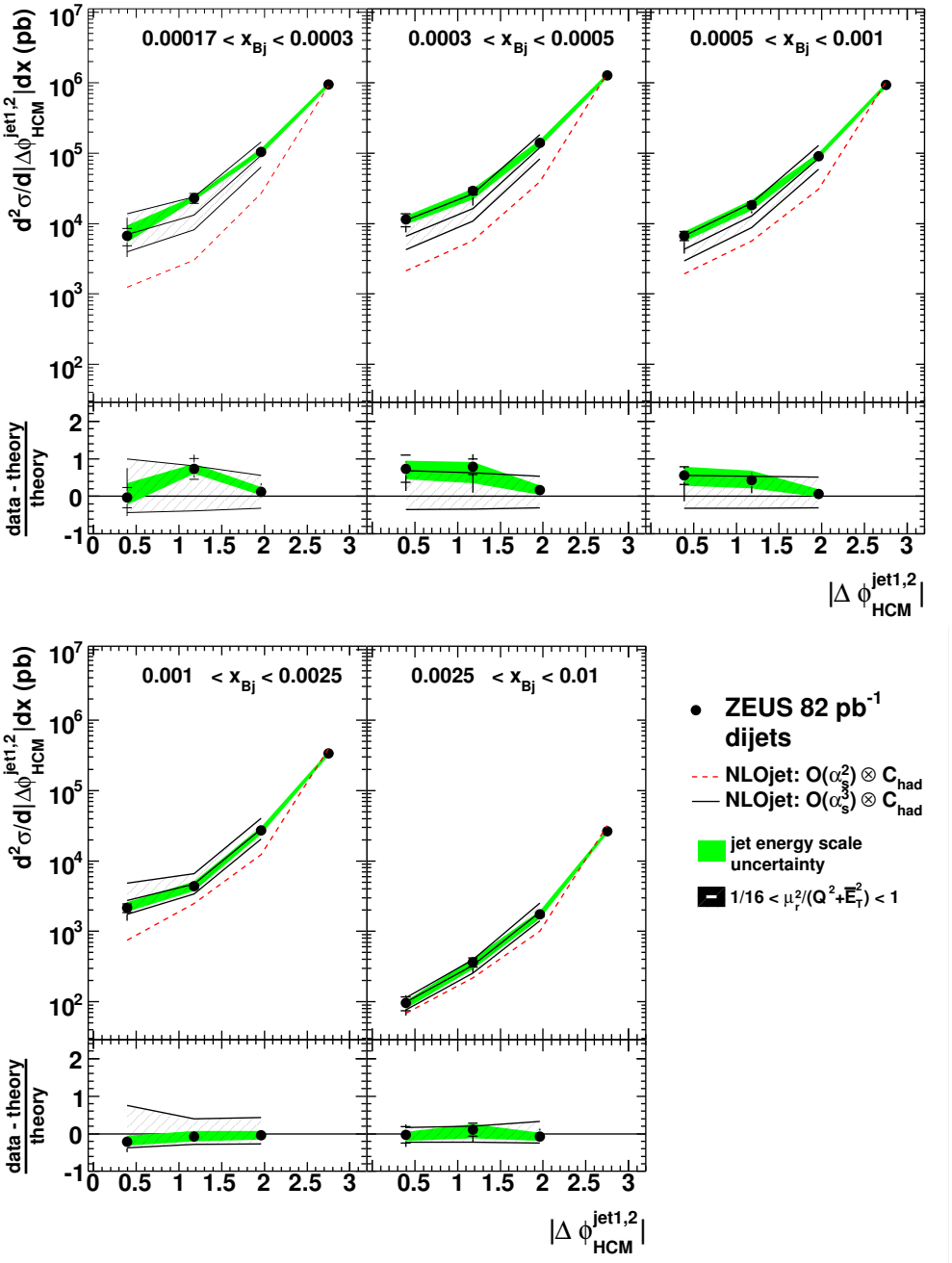

Figure 9.10: Dijet cross sections as functions of $|\Delta\phi^{\rm jet1,2}_{\rm HCM}|$. The NLOJET calculations at $\mathcal{O}(\alpha_s^2)$ ($\mathcal{O}(\alpha_s^3)$) are shown as dashed (solid) lines. The lower parts of the plots show the relative difference between the data and the $\mathcal{O}(\alpha_s^3)$ predictions. Other details as in the caption to Fig. 9.1.

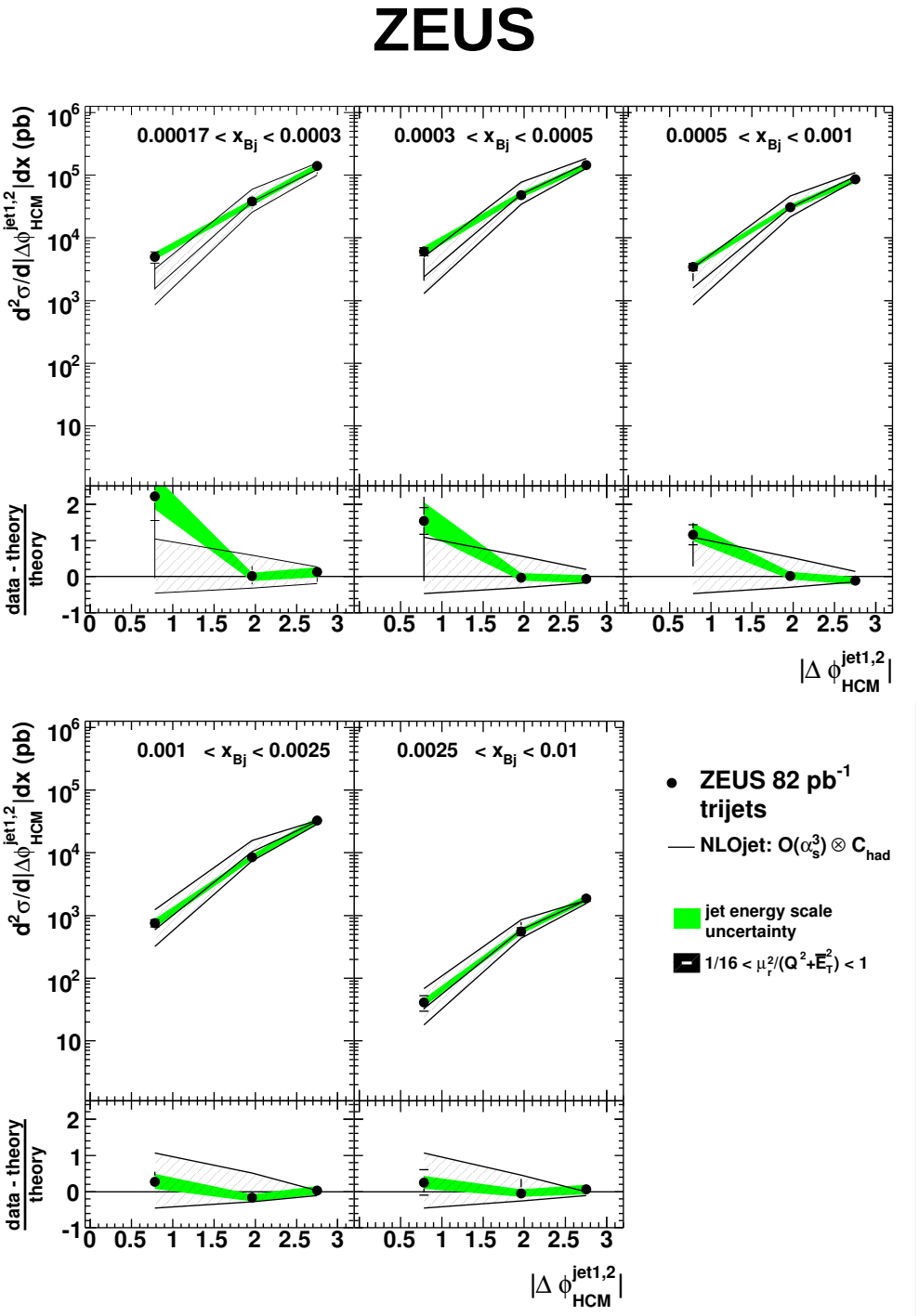

Figure 9.11: Trijet cross sections as functions of $|\Delta\phi^{\mathrm{jet1,2}}_{\mathrm{HCM}}|$. The measurements are compared to NLOJET calculations at $\mathcal{O}(\alpha_s^3)$. Other details as in the caption to Fig. 9.1.

larger than the $\mathcal{O}(\alpha_S^2)$ calculations and are consistent with the data, demonstrating the importance of the higher-order terms in the description of the data especially at low x_{Bj}. The NLOJET calculations at $\mathcal{O}(\alpha_S^3)$ describe the trijet data within the renormalization-scale uncertainties.

9.6 Comparison with Other Results

9.6.1 H1 Dijet Azimuthal Correlations

Dijet azimuthal correlations have also been investigated by the H1 Collaboration [67] by measuring the cross-sections $d^2\sigma/dx_{\mathrm{Bj}}d\Delta\phi^*$, where $\Delta\phi^*$ is the azimuthal separation in the hadronic center-of-mass (HCM) frame between the two selected jets closest to the scattered electron in pseudorapidity. The measurements of $\Delta\phi^*$ are well-described by NLOJET calculations at $\mathcal{O}(\alpha_s^3)$, within theoretical uncertainties similar to those seen in this analysis. To reduce the theoretical uncertainties, the measurements were normalized to the visible cross section for $\Delta\phi^* < 170°$. With a reduced theoretical uncertainty, the calculations are shown to predict a narrower $\Delta\phi^*$ spectrum than is measured, especially at very low x_{Bj} (see Fig. 9.13). The measurements were also compared to predictions from two RAPGAP [68] (DGLAP) samples, with one sample using only direct photons, the other using both direct and resolved photons; LEPTO with CDM instead of MEPS; and two CASCADE [69] (CCFM) samples with different unintegrated PDFs. All models fail to describe $\Delta\phi^*$ over the entire range in x_{Bj} covered.

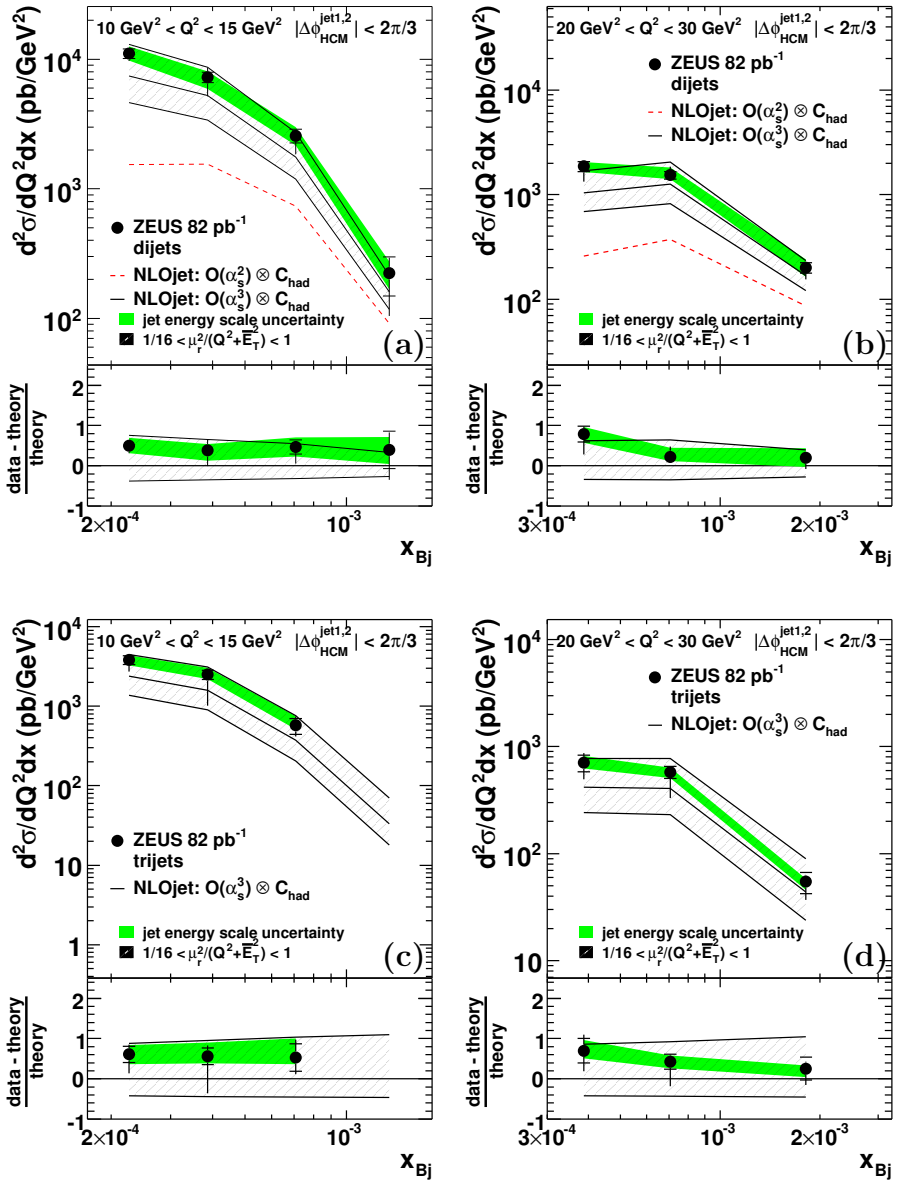

Figure 9.12: The dijet and trijet cross sections for events with $|\Delta\phi^{\mathrm{jet1,2}}_{\mathrm{HCM}}| < 2\pi/3$ as functions of x_{Bj} in two different Q^2-bins. The NLOJET calculations at $\mathcal{O}(\alpha_s^2)$ ($\mathcal{O}(\alpha_s^3)$) are shown as dashed (solid) lines. The trijet measurements are compared to NLOJET calculations at $\mathcal{O}(\alpha_s^3)$. The lower parts of the plots in (a) and (b) show the relative difference between the data and the $\mathcal{O}(\alpha_s^3)$ predictions. Other details as in the caption to Fig. 9.1.

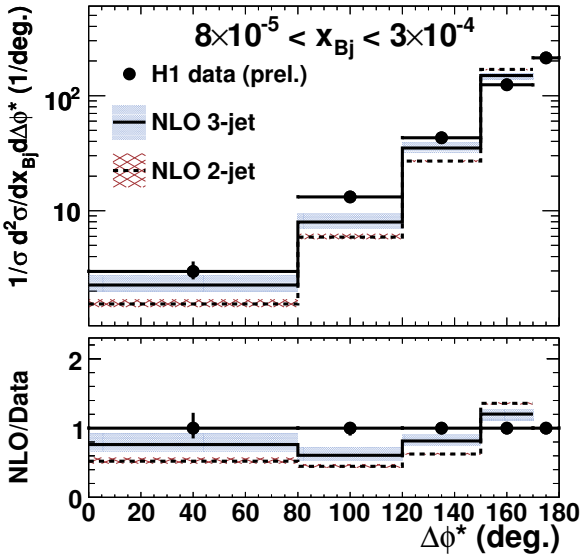

Figure 9.13: Double-differential normalized (see text) cross sections as a function of $\Delta\phi^*$ as measured by H1 compared to NLOJET calculations for $\mathcal{O}(\alpha_s^2)$ and $\mathcal{O}(\alpha_s^3)$. For this measurement, the cross sections were normalized to the visible cross section for $|\Delta\phi^* < 170^\circ$ to reduce the theoretical uncertainty.

9.6.2 ZEUS Forward Jet Production

To examine the sensitivity of parton evolution to forward jet production, the ZEUS collaboration has studied jet production in an extended pseudorapidity range of $2 < \eta^{\text{jet}}_{LAB} < 4.3$ by incorporating the ZEUS Forward Plug Calorimeter (FPC) [70] used during the HERAI running period [71]. Measurements of cross sections as functions of Q^2, x_{Bj}, $E^{\text{jet}}_{T,LAB}$, and η^{jet}_{LAB} are underestimated slightly by calculations from DISENT [46], with large theoretical uncertainties at both low x_{Bj} and high η^{jet}_{LAB}. Predictions from LEPTO (DGLAP); ARIADNE [37] (CDM); and CASCADE, with two sets from the J2003 unintegrated gluon PDF used, were also compared to the measurements. Overall, ARIADNE provides the best description of the measured cross sections; LEPTO consistently underestimates the cross sections, and CASCADE fails to consis-

tently reproduce the shapes of the distributions.

In addition to inclusive forward jet production, the correlations in pseudorapidity for a forward jet + dijet sample were also examined. The jets were ordered in pseudorapidity with $\eta^{\rm jet1}_{\rm LAB} < \eta^{\rm jet2}_{\rm LAB} < \eta^{\rm fjet}_{\rm LAB}$, and the cross sections as functions of $\Delta\eta_1 = \eta^{\rm jet2}_{\rm LAB} - \eta^{\rm jet1}_{\rm LAB}$ and $\Delta\eta_2 = \eta^{\rm fjet}_{\rm LAB} - \eta^{\rm jet2}_{\rm LAB}$. The measurement of $\Delta\eta_2$ was also performed for events with $\Delta\eta_1 > 1$ and for events with $\Delta\eta_1 < 1$. Predictions from NLOJET at $\mathcal{O}(\alpha_s^3)$ underestimate the cross sections for small $\Delta\eta_1$ and $\Delta\eta_2$, a configuration where all three jets are in the forward region, which may not be accurately predicted by DGLAP-based predictions (see Fig. 9.14). Predictions from a tuned version of ARIADNE provide better overall predictions of these cross sections, while CASCADE and LEPTO fail to describe the cross sections.

9.6.3 Trijet Production and Correlations

Trijet cross sections and correlations were measured by the H1 collaboration as a study of parton evolution at low $x_{\rm Bj}$ [72]. Cross sections were measured as functions of $x_{\rm Bj}$, jet pseudorapidity, scaled jet energies, and correlations in the jet angles θ' and ψ'. The variable θ' is defined as the angle between the proton beam and the jet with the highest transverse energy, while ψ' is defined as the angle between the plane defined by the proton beam and the highest E_T jet, and the plane defined by the two jets with the highest E_T. These measurements were made for three separate trijet samples: an inclusive trijet sample, and two trijet samples with one and two forward jets, respectively, with a forward jet having $\theta^{\rm jet}_{LAB} < 20^\circ$ and $x_{jet} = E^{\rm jet}_{HCM}/E_{pbeam} > 0.035$. For the inclusive trijet sample, NLOJET calculations provide a reasonable description of the measured cross sections, but slightly underestimate the measurements in the

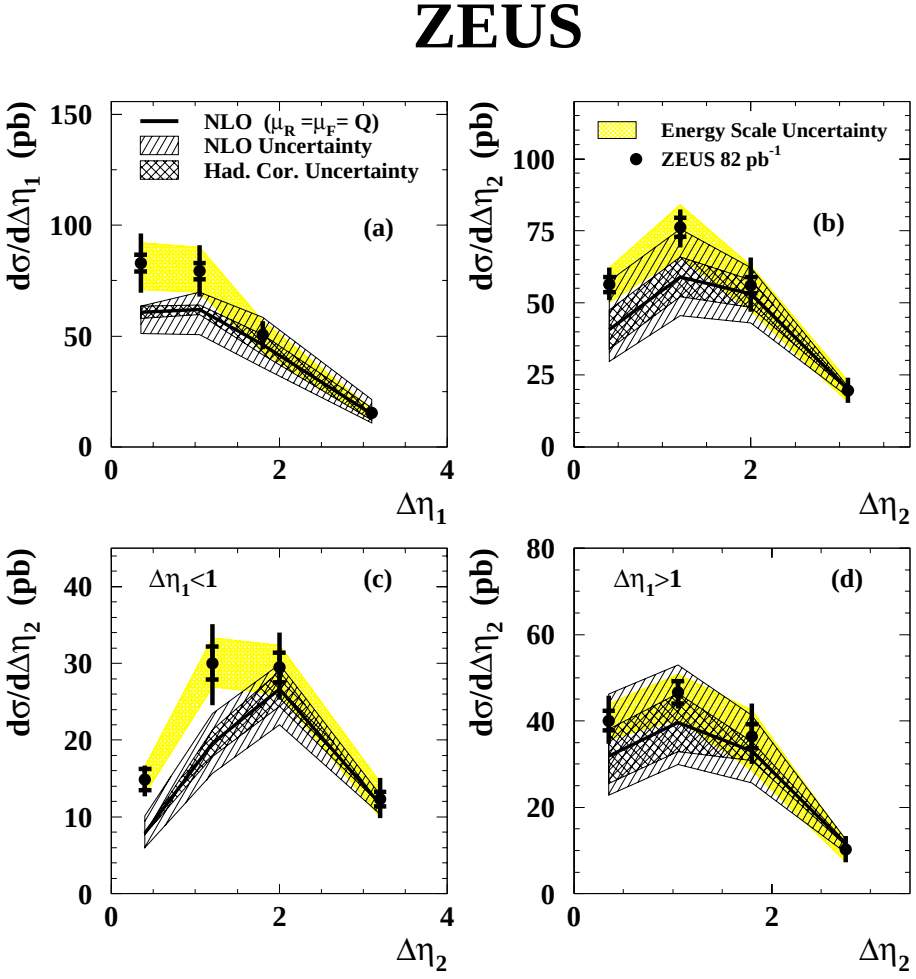

Figure 9.14: Differential cross sections for the ZEUS forward+dijet sample as a function of (a) $\Delta\eta_1$, (b) $\Delta\eta_2$, (c) $\Delta\eta_2$ for $\Delta\eta_1 < 1$ and (d) $\Delta\eta_2$ for $\Delta\eta_1 > 1$. Other details as in the caption to Fig. 9.1.

lowest bin of x_{Bj}. The agreement between the calculations and the measured cross section in x_{Bj} is worse for the trijet sample containing two forward jets, with the most noticeable disagreement observed at lowest x_{Bj}. The selection of two forward jets favors events with forward gluon emission unordered in transverse momentum, which the calculations at $\mathcal{O}(\alpha_s^3)$ do not predict entirely. Also seen in Fig. 9.15 is that the higher-order terms in the NLOJET calculations are important for forward jet emissions. The other cross sections for this sample are well-described by the calculations.

Predictions from DJANGOH (CDM) and RAPGAP LO MC models were also compared to the measured cross sections. The cross sections for the inclusive trijet sample are better described by CDM predictions, but both the CDM and RAPGAP predictions are inconsistent for the jet correlation angles $\theta^{'}$ and $\psi^{'}$; the RAPGAP predictions fail to describe the $\theta^{'}$ distributions, and the CDM predictions fail to describe the $\psi^{'}$ cross sections.

The results from the comparison of the measured cross sections to NLOJET predictions from the ZEUS forward jets analysis, the analysis presented in this thesis, and the two H1 analyses are overall consistent. For the three analyses with trijet samples, some disagreement between the cross sections and the NLOJET predictions is seen, but unlike the case of the dijet sample, the "NNLO" calculations for the trijet sample are currently unavailable, though with the large theoretical uncertainties seen in this kinematic range, the contribution of higher-order terms to the calculations may be non-negligible.

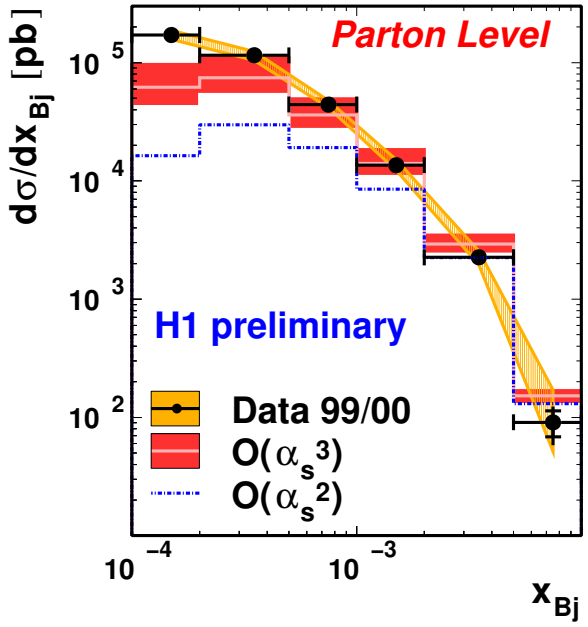

Figure 9.15: H1 trijet cross sections as a function of x_{Bj} for events with two forward jets compared to NLOJET calculations at $\mathcal{O}(\alpha_s^2)$ and $\mathcal{O}(\alpha_s^3)$.

Chapter 10

Conclusions

Dijet and trijet production in deep inelastic ep scattering has been measured in the phase space region $10 < Q^2 < 100$ GeV^2 and $10^{-4} < x_{\mathrm{Bj}} < 10^{-2}$ using an integrated luminosity of 82 pb^{-1} collected by the ZEUS experiment [73]. The statistics available from the 1998-2000 HERA running period have allowed detailed studies of multijet production at low x_{Bj} for comparison to DGLAP-based NLOJET predictions. The dependence of dijet and trijet production on the kinematic variables Q^2 and x_{Bj} and on the jet variables $E^{\mathrm{jet}}_{T,\mathrm{HCM}}$ and $\eta^{\mathrm{jet}}_{\mathrm{LAB}}$ is well described by perturbative QCD calculations which include NLO corrections.

To investigate possible deviations with respect to the collinear factorization approximation used in the standard pQCD approach, measurements of the correlations between the two jets with highest $E^{\mathrm{jet}}_{T,\mathrm{HCM}}$ have been made. At low x_{Bj}, measurements of dijet production with low azimuthal separation are reproduced by the perturbative QCD calculations provided that higher-order terms ($\mathcal{O}(\alpha_s^3)$) are accounted for. Such terms increase the predictions of pQCD calculations by up to one order of magnitude when the two jets with the highest $E^{\mathrm{jet1,2}}_{T,\mathrm{HCM}}$ are not balanced in transverse momentum. This demonstrates the importance of higher-order corrections in the low-x_{Bj} region for

such events. With the higher-order terms taken into consideration, predictions base on the DGLAP double-leading log approach are in agreement with jet correlations for values of x_{Bj} as low as 10^{-4}. Even without the higher-order terms, the DGLAP DLL approach reproduces the cross sections for the kinematic and jet variables over the same kinematic range.

For a complete study of parton evolution schemes in low-x_{Bj} DIS, the measurements presented in this analysis should also be compared to predictions from BFKL and CCFM in this kinematic range. As seen in the discussion of other current results from ZEUS and H1, the predictions from CCFM-based CASCADE program have been shown to depend heavily on the unintegrated PDF used and provide an overall inconsistent description of forward jet data in kinematic range similar to the one used in this analysis. Fixed-order pQCD calculations for the BFKL approach are currently unavailable, as the resummation involves an expansion near the non-perturbative limit. Although the DGLAP DLL approach is still applicable to $x_{\mathrm{Bj}} \sim 10^{-4}$, the predictions from BFKL-based pQCD calculations may be less sensitive to higher-order terms.

Appendix A

Data Tables

Q^2 (GeV^2)	$\frac{d\sigma}{dQ^2}$ (pb/GeV^2)	δ_{stat} (pb/GeV^2)	δ_{syst} (pb/GeV^2)	δ_{ES} (pb/GeV^2)	C_{QED}	C_{had}
10 - 15	66.1	0.8	$^{+3.5}_{-4.4}$	$^{+5.8}_{-5.9}$	0.984	0.866
15 - 20	41.3	0.6	$^{+2.0}_{-2.2}$	$^{+3.5}_{-3.7}$	0.968	0.870
20 - 30	26.2	0.3	$^{+1.0}_{-0.8}$	$^{+2.2}_{-2.1}$	0.965	0.876
30 - 50	14.0	0.1	$^{+0.3}_{-0.4}$	$^{+1.1}_{-1.1}$	0.955	0.884
50 - 100	5.82	0.06	$^{+0.18}_{-0.15}$	$^{+0.41}_{-0.40}$	0.952	0.887

Table A.1: The inclusive dijet cross sections as functions of Q^2. Included are the statistical, systematic, and jet energy scale uncertainties in columns 3, 4, and 5, respectively. Column 6 shows the correction factor from QED radiative effects applied to the measured cross sections, and column 7 shows the hadronization correction applied to the NLOJET calculations shown in the figures.

$x_{\mathrm{Bj}} \times 10^{-4}$	$\frac{d\sigma}{dx_{\mathrm{Bj}}}$ (pb, $\times 10^{-4}$)	δ_{stat} (pb, $\times 10^{-4}$)	δ_{syst} (pb, $\times 10^{-4}$)	δ_{ES} (pb, $\times 10^{-4}$)	C_{QED}	C_{had}
1.7 - 3.0	85.5	1.7	$^{+5.5}_{-7.1}$	$^{+6.9}_{-6.2}$	0.987	0.910
3.0 - 5.0	113.8	1.6	$^{+5.9}_{-6.1}$	$^{+9.1}_{-9.1}$	0.975	0.887
5.0 - 10.0	82.9	0.9	$^{+3.3}_{-3.7}$	$^{+6.8}_{-7.0}$	0.969	0.876
10.0 - 25.0	29.5	0.3	$^{+0.8}_{-0.7}$	$^{+2.4}_{-2.3}$	0.958	0.876
25.0 - 100.0	2.32	0.03	$^{+0.08}_{-0.08}$	$^{+0.19}_{-0.19}$	0.948	0.862

Table A.2: The inclusive dijet cross sections as functions of x_{Bj}. Other details as in the caption to Table A.1.

$E_{T,HCM}^{jet,1}$ (GeV)	$\frac{d\sigma}{dE_{T,HCM}^{jet,1}}$ (pb/ GeV)	δ_{stat} (pb/ GeV)	δ_{syst} (pb/ GeV)	δ_{ES} (pb/ GeV)	C_{QED}	C_{had}
8 - 12	184	2	$^{+4}_{-3}$	$^{+17}_{-18}$	0.965	0.884
12 - 16	57.3	0.7	$^{+1.1}_{-4.2}$	$^{+5.3}_{-4.5}$	0.963	0.924
16 - 20	18.27	0.34	$^{+0.36}_{-0.76}$	$^{+0.88}_{-0.69}$	0.956	0.936
20 - 25	6.22	0.16	$^{+0.21}_{-0.85}$	$^{+0.26}_{-0.25}$	0.965	0.939
25 - 30	1.72	0.08	$^{+0.06}_{-0.08}$	$^{+0.11}_{-0.07}$	0.96	0.930
30 - 40	0.415	0.027	$^{+0.020}_{-0.034}$	$^{+0.024}_{-0.028}$	0.96	0.93
40 - 60	0.043	0.007	$^{+0.009}_{-0.014}$	$^{+0.002}_{-0.003}$	1.01	0.93

Table A.3: The inclusive dijet cross sections as functions of $E_{T,HCM}^{jet,1}$. Other details as in the caption to Table A.1.

$E_{T,HCM}^{jet,2}$ (GeV)	$\frac{d\sigma}{dE_{T,HCM}^{jet,2}}$ (pb/ GeV)	δ_{stat} (pb/ GeV)	δ_{syst} (pb/ GeV)	δ_{ES} (pb/ GeV)	C_{QED}	C_{had}
5 - 8	278	2	$^{+6}_{-8}$	$^{+20}_{-20}$	0.964	0.864
8 - 12	104	1	$^{+1}_{-2}$	$^{+10}_{-11}$	0.965	0.879
12 - 16	23.3	0.4	$^{+0.4}_{-0.3}$	$^{+2.1}_{-1.8}$	0.965	0.926
16 - 20	6.57	0.19	$^{+0.67}_{-0.20}$	$^{+0.33}_{-0.22}$	0.958	0.953
20 - 25	2.08	0.09	$^{+0.26}_{-0.08}$	$^{+0.12}_{-0.06}$	0.97	0.937
25 - 30	0.662	0.053	$^{+0.072}_{-0.024}$	$^{+0.022}_{-0.027}$	0.93	0.97
30 - 40	0.173	0.018	$^{+0.016}_{-0.023}$	$^{+0.004}_{-0.013}$	0.97	0.95
40 - 60	0.0100	0.0035	$^{+0.0083}_{-0.0028}$	$^{+0.0011}_{-0.0000}$	1.07	0.93

Table A.4: The inclusive dijet cross sections as functions of $E_{T,HCM}^{jet,2}$. Other details as in the caption to Table A.1.

$\eta_{LAB}^{jet,1}$	$\frac{d\sigma}{d\eta_{LAB}^{jet,1}}$ (pb)	δ_{stat} (pb)	δ_{syst} (pb)	δ_{ES} (pb)	C_{QED}	C_{had}
-1.0 - -0.5	5.7	0.8	$^{+2.4}_{-0.7}$	$^{+1.5}_{-1.1}$	0.94	0.424
-0.5 - 0.0	114	3	$^{+6}_{-2}$	$^{+19}_{-16}$	0.977	0.742
0.0 - 0.5	337	5	$^{+10}_{-11}$	$^{+31}_{-32}$	0.968	0.855
0.5 - 1.0	546	7	$^{+21}_{-22}$	$^{+48}_{-47}$	0.964	0.885
1.0 - 1.5	629	7	$^{+28}_{-23}$	$^{+44}_{-48}$	0.963	0.910
1.5 - 2.0	599	7	$^{+20}_{-27}$	$^{+41}_{-44}$	0.959	0.915
2.0 - 2.5	521	8	$^{+33}_{-37}$	$^{+38}_{-34}$	0.967	0.849

Table A.5: The inclusive dijet cross sections as functions of $\eta_{LAB}^{jet,1}$. Other details as in the caption to Table A.1.

$\eta^{jet,2}_{LAB}$	$\frac{d\sigma}{d\eta^{jet,2}_{LAB}}$ (pb)	δ_{stat} (pb)	δ_{syst} (pb)	δ_{ES} (pb)	C_{QED}	C_{had}
-1.0 - -0.5	456	7	$^{+14}_{-26}$	$^{+55}_{-53}$	0.968	0.767
-0.5 - 0.0	702	8	$^{+27}_{-26}$	$^{+67}_{-65}$	0.968	0.873
0.0 - 0.5	708	7	$^{+32}_{-28}$	$^{+52}_{-54}$	0.963	0.899
0.5 - 1.0	543	6	$^{+20}_{-28}$	$^{+32}_{-35}$	0.960	0.933
1.0 - 1.5	233	4	$^{+14}_{-9}$	$^{+13}_{-11}$	0.960	0.992
1.5 - 2.0	74.1	2.3	$^{+5.2}_{-6.2}$	$^{+3.4}_{-4.3}$	0.954	0.910
2.0 - 2.5	15.9	1.3	$^{+1.4}_{-3.8}$	$^{+1.1}_{-0.7}$	0.94	0.87

Table A.6: The inclusive dijet cross sections as functions of $\eta^{jet,2}_{LAB}$. Other details as in the caption to Table A.1.

$\Delta\eta^{\mathrm{jet1,2}}_{HCM}$	$\frac{d\sigma}{d\Delta\eta^{\mathrm{jet1,2}}_{HCM}}$ (pb)	δ_{stat} (pb)	δ_{syst} (pb)	δ_{ES} (pb)	C_{QED}	C_{had}
0.0 - 0.7	744	6	$^{+25}_{-25}$	$^{+57}_{-58}$	0.964	0.890
0.7 - 1.4	616	6	$^{+20}_{-21}$	$^{+49}_{-48}$	0.962	0.905
1.4 - 2.1	390	5	$^{+27}_{-20}$	$^{+31}_{-31}$	0.966	0.878
2.1 - 2.8	169	3	$^{+9}_{-13}$	$^{+17}_{-17}$	0.966	0.793
2.8 - 3.5	37.8	1.8	$^{+3.0}_{-5.5}$	$^{+4.9}_{-4.4}$	0.977	0.623

Table A.7: The inclusive dijet cross sections as functions of $\Delta\eta^{\mathrm{jet1,2}}_{HCM}$. Other details as in the caption to Table A.1.

$x_{\mathrm{Bj}} \times 10^4$	$\Delta E_{T,HCM}^{\mathrm{jet1,2}}$ (GeV)	$\frac{d^2\sigma}{d(\Delta E_{T,HCM}^{\mathrm{jet1,2}})dx_{\mathrm{Bj}}}$ (pb/ GeV)	δ_{stat} (pb/ GeV)	δ_{syst} (pb/ GeV)	δ_{ES} (pb/ GeV)	C_{QED}	C_{had}
1.7 - 3.0	0.0 - 4.0	1.75×10^5	4.4×10^3	$^{+1.0\times10^4}_{-1.2\times10^4}$	$^{+1.6\times10^4}_{-1.4\times10^4}$	0.984	0.908
	4.0 - 10.0	2.77×10^4	1.2×10^3	$^{+3.6\times10^3}_{-8.5\times10^3}$	$^{+1.6\times10^3}_{-1.7\times10^3}$	1.00	0.920
	10.0 - 18.0	1.47×10^3	2.1×10^2	$^{+6.8\times10^2}_{-3.2\times10^2}$	$^{+7.1\times10^1}_{-3.3\times10^1}$	1.04	0.89
3.0 - 5.0	0.0 - 4.0	2.36×10^5	4.0×10^3	$^{+1.3\times10^4}_{-6.7\times10^3}$	$^{+2.0\times10^4}_{-2.1\times10^4}$	0.975	0.883
	4.0 - 10.0	3.5×10^4	1.0×10^3	$^{+3.9\times10^3}_{-1.1\times10^4}$	$^{+2.4\times10^3}_{-1.9\times10^3}$	0.976	0.918
	10.0 - 18.0	1.60×10^3	1.5×10^2	$^{+2.5\times10^2}_{-5.7\times10^2}$	$^{+4.7\times10^1}_{-1.2\times10^2}$	0.97	0.88
	18.0 - 100.0	17.3	5.2	$^{+9.2}_{-5.7}$	$^{-1.2}_{-0.0}$	1.1	0.81
5.0 - 10	0.0 - 4.0	1.73×10^5	2.2×10^3	$^{+3.7\times10^3}_{-5.1\times10^3}$	$^{+1.5\times10^4}_{-1.6\times10^4}$	0.970	0.872
	4.0 - 10.0	2.44×10^4	5.8×10^2	$^{+2.4\times10^3}_{-7.0\times10^3}$	$^{+1.7\times10^3}_{-1.5\times10^3}$	0.964	0.905
	10.0 - 18.0	1.19×10^3	8.3×10^1	$^{+2.8\times10^2}_{-2.6\times10^2}$	$^{+7.4\times10^1}_{-8.6\times10^0}$	0.99	0.86
	18.0 - 100.0	10.2	3.4	$^{+4.8}_{-3.8}$	$^{-0.0}_{-1.6}$	0.96	0.80
10 - 25	0.0 - 4.0	6.25×10^4	6.9×10^2	$^{+1.9\times10^3}_{-1.6\times10^3}$	$^{+5.4\times10^3}_{-5.4\times10^3}$	0.959	0.874
	4.0 - 10.0	7.7×10^3	1.7×10^2	$^{+3.2\times10^2}_{-1.9\times10^3}$	$^{+5.0\times10^2}_{-4.9\times10^2}$	0.959	0.896
	10.0 - 18.0	423	27	$^{+96}_{-149}$	$^{+36}_{-2}$	0.94	0.82
	18.0 - 100.0	4.0	0.9	$^{+1.4}_{-0.7}$	$^{+0.3}_{-0.4}$	1.00	0.78
25 - 100	0.0 - 4.0	5.10×10^3	9.2×10^1	$^{+1.6\times10^2}_{-1.4\times10^2}$	$^{+4.2\times10^2}_{-4.2\times10^2}$	0.949	0.860
	4.0 - 10.0	455	18	$^{+23}_{-94}$	$^{+36}_{-38}$	0.941	0.885
	10.0 - 18.0	33	4	$^{+9}_{-16}$	$^{+1}_{-3}$	1.05	0.78
	18.0 - 100.0	0.23	0.09	$^{+0.11}_{-0.11}$	$^{+0.02}_{-0.02}$	0.7	1.0

Table A.8: The dijet double-differential cross sections as functions of $\Delta E_{T,HCM}^{jet1,2}$. Included are the statistical, systematic, and jet energy scale uncertainties in columns 4, 5, and 6, respectively. Column 7 shows the correction factor from QED radiative effects applied to the measured cross sections, and column 8 shows the hadronization correction applied to the NLOJET calculations shown in the figures.

$x_{\rm Bj} \times 10^4$	$\lvert\Sigma\vec{p}_{T,HCM}^{\,\rm jet1,2}\rvert$ (GeV)	$\frac{d^2\sigma}{d\left(\lvert\Sigma\vec{p}_{T,HCM}^{\,\rm jet1,2}\rvert\right)dx_{\rm Bj}}$ (pb/ GeV)	δ_{stat} (pb/ GeV)	δ_{syst} (pb/ GeV)	δ_{ES} (pb/ GeV)	C_{QED}	C_{had}
1.7 - 3.0	0.0 - 4.0	1.146×10^5	3.7×10^3	$^{+7.9\times10^3}_{-8.6\times10^3}$	$^{+8.7\times10^3}_{-7.9\times10^3}$	0.978	0.934
	4.0 - 10.0	5.50×10^4	1.8×10^3	$^{+3.0\times10^3}_{-6.1\times10^3}$	$^{+4.4\times10^3}_{-4.2\times10^3}$	0.995	0.878
	10.0 - 16.0	1.10×10^4	7.6×10^2	$^{+1.3\times10^3}_{-1.8\times10^3}$	$^{+8.5\times10^2}_{-6.4\times10^2}$	1.02	0.88
	16.0 - 100.0	164	26	$^{+37}_{-19}$	$^{+41}_{-19}$	1.02	0.85
3.0 - 5.0	0.0 - 4.0	1.59×10^5	3.4×10^3	$^{+7.2\times10^3}_{-4.4\times10^3}$	$^{+1.1\times10^4}_{-1.1\times10^4}$	0.973	0.898
	4.0 - 10.0	7.02×10^4	1.6×10^3	$^{+4.7\times10^3}_{-4.2\times10^3}$	$^{+6.4\times10^3}_{-5.7\times10^3}$	0.977	0.873
	10.0 - 16.0	1.21×10^4	6.0×10^2	$^{+1.1\times10^3}_{-3.4\times10^3}$	$^{+8.9\times10^2}_{-1.5\times10^3}$	0.98	0.86
	16.0 - 100.0	162	16	$^{+46}_{-36}$	$^{+22}_{-21}$	1.03	0.85
5.0 - 10	0.0 - 4.0	1.192×10^5	1.9×10^3	$^{+3.8\times10^3}_{-3.9\times10^3}$	$^{+8.6\times10^3}_{-1.0\times10^4}$	0.973	0.885
	4.0 - 10.0	4.86×10^4	8.4×10^2	$^{+2.2\times10^3}_{-3.8\times10^3}$	$^{+4.1\times10^3}_{-4.1\times10^3}$	0.967	0.859
	10.0 - 16.0	7.5×10^3	3.0×10^2	$^{+9.1\times10^2}_{-1.3\times10^3}$	$^{+1.0\times10^3}_{-6.6\times10^2}$	0.94	0.865
	16.0 - 100.0	127	10	$^{+10}_{-39}$	$^{+12}_{-15}$	0.94	0.84
10 - 25	0.0 - 4.0	4.43×10^4	6.1×10^2	$^{+2.0\times10^3}_{-1.5\times10^3}$	$^{+3.1\times10^3}_{-3.3\times10^3}$	0.959	0.883
	4.0 - 10.0	1.55×10^4	2.5×10^2	$^{+4.7\times10^2}_{-5.6\times10^2}$	$^{+1.4\times10^3}_{-1.3\times10^3}$	0.960	0.864
	10.0 - 16.0	2.53×10^3	9.7×10^1	$^{+1.8\times10^2}_{-5.0\times10^2}$	$^{+2.9\times10^2}_{-1.7\times10^2}$	0.939	0.855
	16.0 - 100.0	37	3	$^{+5}_{-12}$	$^{+3}_{-5}$	0.94	0.83
25 - 100	0.0 - 4.0	3.75×10^3	8.3×10^1	$^{+1.1\times10^2}_{-1.4\times10^2}$	$^{+2.2\times10^2}_{-2.5\times10^2}$	0.949	0.870
	4.0 - 10.0	921	26	$^{+92}_{-41}$	$^{+90}_{-80}$	0.947	0.847
	10.0 - 16.0	154	11	$^{+16}_{-28}$	$^{+17}_{-18}$	0.95	0.81
	16.0 - 100.0	2.69	0.36	$^{+0.33}_{-0.77}$	$^{+0.16}_{-0.45}$	0.93	0.82

Table A.9: The dijet double-differential cross sections as functions of $|\Sigma\vec{p}_{T,HCM}^{\,\rm jet1,2}|$. Other details as in the caption to Table A.8.

$x_{\rm Bj} \times 10^4$	$\frac{\lvert\Delta\vec{p}^{\,\rm jet1,2}_{T,HCM}\rvert}{2E^{\rm jet1}_{T,HCM}}$	$\frac{d^2\sigma}{d\left(\frac{\lvert\Delta\vec{p}^{\,\rm jet1,2}_{T,HCM}\rvert}{2E^{\rm jet1}_{T,HCM}}\right)dx_{\rm Bj}}$ (pb)	δ_{stat} (pb)	δ_{syst} (pb)	δ_{ES} (pb)	C_{QED}	C_{had}
1.7 - 3.0	0.0 - 0.5	2.21×10^4	4.4×10^3	$^{+6.4\times10^3}_{-3.3\times10^3}$	$^{+5.5\times10^3}_{-2.2\times10^3}$	0.86	0.95
	0.5 - 0.7	2.05×10^5	2.3×10^4	$^{+3.7\times10^4}_{-3.2\times10^4}$	$^{+2.0\times10^4}_{-9.2\times10^3}$	0.98	0.89
	0.7 - 0.9	2.13×10^6	1.0×10^5	$^{+1.7\times10^5}_{-4.5\times10^5}$	$^{+1.5\times10^5}_{-1.6\times10^5}$	1.00	0.82
	0.9 - 1.0	3.30×10^6	9.2×10^4	$^{+2.6\times10^5}_{-1.8\times10^5}$	$^{+2.6\times10^5}_{-2.4\times10^5}$	0.987	0.912
3.0 - 5.0	0.0 - 0.5	3.4×10^4	4.9×10^3	$^{+6.9\times10^3}_{-1.3\times10^4}$	$^{+3.1\times10^3}_{-8.4\times10^3}$	1.01	0.88
	0.5 - 0.7	2.76×10^5	2.1×10^4	$^{+8.2\times10^4}_{-7.3\times10^4}$	$^{+2.7\times10^4}_{-2.0\times10^4}$	1.12	0.79
	0.7 - 0.9	2.62×10^6	8.3×10^4	$^{+1.9\times10^5}_{-4.7\times10^5}$	$^{+2.1\times10^5}_{-2.1\times10^5}$	0.96	0.86
	0.9 - 1.0	4.54×10^6	8.5×10^4	$^{+3.8\times10^5}_{-1.1\times10^5}$	$^{+3.5\times10^5}_{-3.5\times10^5}$	0.975	0.889
5.0 - 10	0.0 - 0.5	2.14×10^4	2.3×10^3	$^{+4.5\times10^3}_{-6.6\times10^3}$	$^{+3.4\times10^3}_{-3.6\times10^3}$	0.95	0.85
	0.5 - 0.7	1.63×10^5	9.4×10^3	$^{+3.2\times10^4}_{-2.5\times10^4}$	$^{+1.8\times10^4}_{-8.1\times10^3}$	0.97	0.83
	0.7 - 0.9	1.86×10^6	4.4×10^4	$^{+8.5\times10^4}_{-2.8\times10^5}$	$^{+1.4\times10^5}_{-1.6\times10^5}$	0.95	0.831
	0.9 - 1.0	3.36×10^6	4.7×10^4	$^{+8.4\times10^4}_{-6.8\times10^4}$	$^{+2.7\times10^5}_{-2.8\times10^5}$	0.970	0.877
10 - 25	0.0 - 0.5	5.4×10^3	5.2×10^2	$^{+1.1\times10^3}_{-1.4\times10^3}$	$^{+1.2\times10^3}_{-5.7\times10^2}$	0.98	0.78
	0.5 - 0.7	4.43×10^4	2.4×10^3	$^{+5.4\times10^3}_{-4.0\times10^3}$	$^{+5.9\times10^3}_{-4.1\times10^3}$	0.89	0.87
	0.7 - 0.9	6.10×10^5	1.3×10^4	$^{+1.2\times10^4}_{-5.3\times10^4}$	$^{+4.6\times10^4}_{-4.6\times10^4}$	0.96	0.825
	0.9 - 1.0	1.27×10^6	1.6×10^4	$^{+3.7\times10^4}_{-2.7\times10^4}$	$^{+9.7\times10^4}_{-1.0\times10^5}$	0.959	0.878
25 - 100	0.0 - 0.5	340	55	$^{+99}_{-95}$	$^{+57}_{-70}$	0.91	0.71
	0.5 - 0.7	3.35×10^3	3.2×10^2	$^{+3.1\times10^2}_{-3.5\times10^2}$	$^{+3.2\times10^2}_{-3.9\times10^2}$	0.99	0.77
	0.7 - 0.9	3.98×10^4	1.4×10^3	$^{+1.6\times10^3}_{-2.7\times10^3}$	$^{+3.3\times10^3}_{-3.3\times10^3}$	0.97	0.82
	0.9 - 1.0	1.063×10^5	2.2×10^3	$^{+3.4\times10^3}_{-3.0\times10^3}$	$^{+7.9\times10^3}_{-7.7\times10^3}$	0.948	0.864

Table A.10: The dijet double-differential cross sections as functions of $|\Delta\vec{p}^{\,\rm jet1,2}_{T,HCM}|/(2E^{\rm jet1}_{T,HCM})$. Other details as in the caption to Table A.8.

$x_{\rm Bj} \times 10^4$	$\Delta\phi^{\rm jet1,2}_{HCM}$	$\frac{d^2\sigma}{d(\Delta\phi^{\rm jet1,2}_{HCM})dx_{\rm Bj}}$ (pb)	δ_{stat} (pb)	δ_{syst} (pb)	δ_{ES} (pb)	C_{QED}	C_{had}
1.7 - 3.0	0.0 - $\pi/4$	6.7×10^3	1.8×10^3	$^{+5.4\times10^3}_{-3.4\times10^3}$	$^{+2.6\times10^3}_{-1.3\times10^3}$	0.78	1.1
	$\pi/4$ - $\pi/2$	2.30×10^4	3.7×10^3	$^{+4.9\times10^3}_{-3.0\times10^3}$	$^{+1.7\times10^3}_{-1.7\times10^3}$	1.00	0.83
	$\pi/2$ - $3\pi/4$	1.04×10^5	7.5×10^3	$^{+2.1\times10^4}_{-6.6\times10^3}$	$^{+1.1\times10^4}_{-8.8\times10^3}$	0.98	0.85
	$3\pi/4$ - π	9.45×10^5	2.1×10^4	$^{+5.6\times10^4}_{-8.1\times10^4}$	$^{+7.0\times10^4}_{-6.5\times10^4}$	0.988	0.916
3.0 - 5.0	0.0 - $\pi/4$	1.14×10^4	2.4×10^3	$^{+1.3\times10^3}_{-3.9\times10^3}$	$^{+1.4\times10^3}_{-1.8\times10^3}$	1.00	0.87
	$\pi/4$ - $\pi/2$	2.9×10^4	3.4×10^3	$^{+5.5\times10^3}_{-1.1\times10^4}$	$^{+2.1\times10^3}_{-7.0\times10^3}$	1.10	0.80
	$\pi/2$ - $3\pi/4$	1.39×10^5	6.9×10^3	$^{+1.5\times10^4}_{-1.4\times10^4}$	$^{+1.5\times10^4}_{-1.6\times10^4}$	0.98	0.839
	$3\pi/4$ - π	1.265×10^6	1.9×10^4	$^{+5.6\times10^4}_{-5.1\times10^4}$	$^{+9.6\times10^4}_{-9.0\times10^4}$	0.974	0.893
5.0 - 10	0.0 - $\pi/4$	6.7×10^3	1.0×10^3	$^{+9.9\times10^2}_{-3.0\times10^3}$	$^{+1.0\times10^3}_{-1.2\times10^3}$	0.91	0.81
	$\pi/4$ - $\pi/2$	1.84×10^4	1.7×10^3	$^{+2.4\times10^3}_{-4.5\times10^3}$	$^{+3.2\times10^3}_{-2.9\times10^3}$	0.95	0.84
	$\pi/2$ - $3\pi/4$	9.0×10^4	3.6×10^3	$^{+3.5\times10^3}_{-6.3\times10^3}$	$^{+1.1\times10^4}_{-6.9\times10^3}$	0.961	0.828
	$3\pi/4$ - π	9.32×10^5	1.0×10^4	$^{+2.9\times10^4}_{-3.0\times10^4}$	$^{+7.0\times10^4}_{-7.7\times10^4}$	0.970	0.881
10 - 25	0.0 - $\pi/4$	2.16×10^3	3.0×10^2	$^{+3.9\times10^2}_{-7.5\times10^2}$	$^{+4.4\times10^2}_{-2.7\times10^2}$	1.04	0.73
	$\pi/4$ - $\pi/2$	4.37×10^3	3.5×10^2	$^{+7.5\times10^2}_{-6.9\times10^2}$	$^{+7.1\times10^2}_{-6.2\times10^2}$	0.89	0.86
	$\pi/2$ - $3\pi/4$	2.71×10^4	1.1×10^3	$^{+1.7\times10^3}_{-4.5\times10^2}$	$^{+3.3\times10^3}_{-3.2\times10^3}$	0.945	0.822
	$3\pi/4$ - π	3.38×10^5	3.3×10^3	$^{+6.8\times10^3}_{-7.0\times10^3}$	$^{+2.5\times10^4}_{-2.5\times10^4}$	0.960	0.881
25 - 100	0.0 - $\pi/4$	96	21	$^{+27}_{-32}$	$^{+8}_{-16}$	0.85	0.70
	$\pi/4$ - $\pi/2$	365	56	$^{+45}_{-111}$	$^{+47}_{-76}$	0.97	0.79
	$\pi/2$ - $3\pi/4$	1.74×10^3	1.2×10^2	$^{+4.0\times10^2}_{-1.8\times10^2}$	$^{+2.1\times10^2}_{-2.2\times10^2}$	0.94	0.808
	$3\pi/4$ - π	2.63×10^4	4.2×10^2	$^{+1.0\times10^3}_{-5.9\times10^2}$	$^{+1.9\times10^3}_{-1.9\times10^3}$	0.949	0.867

Table A.11: The dijet double-differential cross sections as functions of $|\Delta\phi^{\rm jet1,2}_{HCM}|$. Other details as in the caption to Table A.8.

Q^2(GeV^2)	$x_{\rm Bj} \times 10^4$ (GeV^2)	$\frac{d^2\sigma}{d(Q^2)dx_{\rm Bj}}$ (pb/ GeV^2)	δ_{stat} (pb/ GeV^2)	δ_{syst} (pb/ GeV^2)	δ_{ES} (pb/ GeV^2)	C_{QED}	C_{had}
10 - 15	1.7 - 3.0	1.11×10^4	9.5×10^2	$^{+1.1\times10^3}_{-1.4\times10^3}$	$^{+1.5\times10^3}_{-1.3\times10^3}$	1.00	0.84
	3.0 - 5.0	7.3×10^3	6.7×10^2	$^{+1.3\times10^3}_{-2.1\times10^3}$	$^{+8.2\times10^2}_{-1.4\times10^3}$	1.01	0.83
	5.0 - 10.0	2.57×10^3	3.0×10^2	$^{+2.0\times10^2}_{-7.3\times10^2}$	$^{+4.1\times10^2}_{-4.1\times10^2}$	0.99	0.77
	10.0 - 18.0	224	74	$^{+70}_{-119}$	$^{+51}_{-57}$	0.93	0.69
15 - 20	3.0 - 5.0	4.5×10^3	4.6×10^2	$^{+5.7\times10^2}_{-1.1\times10^3}$	$^{+3.4\times10^2}_{-9.6\times10^2}$	0.98	0.87
	5.0 - 10.0	2.08×10^3	2.5×10^2	$^{+2.8\times10^2}_{-8.1\times10^2}$	$^{+2.7\times10^2}_{-2.9\times10^2}$	0.96	0.81
	10.0 - 22.0	268	62	$^{+77}_{-103}$	$^{+46}_{-22}$	0.92	0.75
20 - 30	3.0 - 5.0	1.87×10^3	2.1×10^2	$^{+1.9\times10^2}_{-5.3\times10^2}$	$^{+1.8\times10^2}_{-2.3\times10^2}$	0.93	0.88
	5.0 - 10.0	1.54×10^3	1.2×10^2	$^{+3.2\times10^2}_{-1.2\times10^2}$	$^{+2.8\times10^2}_{-1.3\times10^2}$	0.95	0.87
	10.0 - 33.0	201	23	$^{+22}_{-46}$	$^{+40}_{-38}$	0.97	0.78
30 - 50	5.0 - 10.0	526	43	$^{+64}_{-90}$	$^{+72}_{-54}$	0.91	0.89
	10.0 - 55.0	92	6	$^{+9}_{-11}$	$^{+12}_{-14}$	0.94	0.82
50 - 100	10.0 - 25.0	108	7	$^{+13}_{-14}$	$^{+14}_{-11}$	0.95	0.86
	25.0 - 100.0	18.9	1.8	$^{+0.7}_{-5.3}$	$^{+2.4}_{-2.3}$	0.95	0.81

Table A.12: The dijet double-differential cross sections as functions of $x_{\rm Bj}$ for events with $|\Delta\phi^{\rm jet1,2}_{HCM}| < 2\pi/3$. Other details as in the caption to Table A.8.

Q^2 (GeV^2)	$\frac{d\sigma}{dQ^2}$ (pb/ GeV^2)	δ_{stat} (pb/ GeV^2)	δ_{syst} (pb/ GeV^2)	δ_{ES} (pb/ GeV^2)	C_{QED}	C_{had}
10 - 15	8.0	0.3	$^{+1.1}_{-1.4}$	$^{+1.0}_{-1.0}$	0.991	0.759
15 - 20	4.42	0.17	$^{+0.46}_{-0.66}$	$^{+0.47}_{-0.53}$	0.946	0.776
20 - 30	3.19	0.11	$^{+0.28}_{-0.37}$	$^{+0.39}_{-0.40}$	0.969	0.786
30 - 50	1.69	0.06	$^{+0.12}_{-0.11}$	$^{+0.21}_{-0.20}$	0.949	0.794
50 - 100	0.724	0.024	$^{+0.046}_{-0.031}$	$^{+0.081}_{-0.073}$	0.956	0.795

Table A.13: The inclusive trijet cross sections as functions of Q^2. Other details as in the caption to Table A.1.

$x_{\mathrm{Bj}} \times 10^{-4}$	$\frac{d\sigma}{dx_{\mathrm{Bj}}}$ (pb, $\times 10^{-4}$)	δ_{stat} (pb, $\times 10^{-4}$)	δ_{syst} (pb, $\times 10^{-4}$)	δ_{ES} (pb, $\times 10^{-4}$)	C_{QED}	C_{had}
1.7 - 3.0	14.9	0.7	$^{+1.6}_{-3.4}$	$^{+1.6}_{-2.0}$	1.00	0.811
3.0 - 5.0	16.1	0.5	$^{+1.9}_{-2.4}$	$^{+1.9}_{-1.8}$	0.968	0.796
5.0 - 10.0	9.7	0.3	$^{+0.9}_{-0.9}$	$^{+1.2}_{-1.1}$	0.961	0.780
10.0 - 25.0	3.35	0.10	$^{+0.22}_{-0.20}$	$^{+0.42}_{-0.39}$	0.954	0.785
25.0 - 100.0	0.194	0.013	$^{+0.033}_{-0.021}$	$^{+0.024}_{-0.024}$	0.95	0.739

Table A.14: The inclusive trijet cross sections as functions of x_{Bj}. Other details as in the caption to Table A.1.

$E_{T,HCM}^{jet,1}$ (GeV)	$\frac{d\sigma}{dE_{T,HCM}^{jet,1}}$ (pb/ GeV)	δ_{stat} (pb/ GeV)	δ_{syst} (pb/ GeV)	δ_{ES} (pb/ GeV)	C_{QED}	C_{had}
8 - 12	19.2	0.5	$^{+1.3}_{-0.9}$	$^{+2.4}_{-2.7}$	0.965	0.764
12 - 16	11.6	0.4	$^{+0.1}_{-0.6}$	$^{+1.7}_{-1.5}$	0.965	0.799
16 - 20	4.58	0.19	$^{+0.24}_{-0.25}$	$^{+0.41}_{-0.40}$	0.96	0.823
20 - 25	1.69	0.09	$^{+0.07}_{-0.20}$	$^{+0.15}_{-0.10}$	0.96	0.83
25 - 30	0.630	0.054	$^{+0.022}_{-0.050}$	$^{+0.049}_{-0.057}$	0.98	0.81
30 - 40	0.118	0.014	$^{+0.036}_{-0.017}$	$^{+0.006}_{-0.008}$	0.97	0.83
40 - 60	0.0130	0.0038	$^{+0.0032}_{-0.0070}$	$^{+0.0009}_{-0.0019}$	1.03	0.78

Table A.15: The inclusive trijet cross sections as functions of $E_{T,HCM}^{jet,1}$. Other details as in the caption to Table A.1.

$E_{T,HCM}^{jet,2}$ (GeV)	$\frac{d\sigma}{dE_{T,HCM}^{jet,2}}$ (pb/ GeV)	δ_{stat} (pb/ GeV)	δ_{syst} (pb/ GeV)	δ_{ES} (pb/ GeV)	C_{QED}	C_{had}
5 - 8	24.1	0.7	$^{+1.3}_{-1.1}$	$^{+2.2}_{-2.5}$	0.951	0.774
8 - 12	17.3	0.4	$^{+0.3}_{-0.5}$	$^{+2.5}_{-2.4}$	0.975	0.773
12 - 16	4.87	0.19	$^{+0.14}_{-0.28}$	$^{+0.68}_{-0.55}$	0.96	0.816
16 - 20	1.31	0.09	$^{+0.10}_{-0.10}$	$^{+0.11}_{-0.08}$	0.96	0.84
20 - 25	0.471	0.046	$^{+0.067}_{-0.052}$	$^{+0.067}_{-0.050}$	0.98	0.82
25 - 30	0.121	0.021	$^{+0.016}_{-0.012}$	$^{+0.000}_{-0.007}$	0.90	0.84
30 - 40	0.030	0.007	$^{+0.012}_{-0.010}$	$^{+0.003}_{-0.003}$	1.06	0.77
40 - 60	0.0050	0.0034	$^{+0.0012}_{-0.0054}$	$^{-0.0000}_{-0.0000}$	1.3	0.78

Table A.16: The inclusive trijet cross sections as functions of $E_{T,HCM}^{jet,2}$. Other details as in the caption to Table A.1.

$E_{T,HCM}^{jet,3}$ (GeV)	$\frac{d\sigma}{dE_{T,HCM}^{jet,3}}$ (pb/ GeV)	δ_{stat} (pb/ GeV)	δ_{syst} (pb/ GeV)	δ_{ES} (pb/ GeV)	C_{QED}	C_{had}
5 - 8	46.6	0.9	$^{+1.8}_{-2.1}$	$^{+5.3}_{-5.4}$	0.964	0.777
8 - 12	6.18	0.21	$^{+0.12}_{-0.22}$	$^{+0.96}_{-0.84}$	0.956	0.801
12 - 16	0.78	0.06	$^{+0.11}_{-0.02}$	$^{+0.07}_{-0.06}$	0.95	0.82
16 - 20	0.122	0.023	$^{+0.010}_{-0.039}$	$^{+0.003}_{-0.006}$	1.00	0.88
20 - 25	0.026	0.009	$^{+0.021}_{-0.011}$	$^{-0.000}_{-0.000}$	0.96	0.90
25 - 30	0.0019	0.0020	$^{+0.0017}_{-0.0009}$	$^{+0.0019}_{-0.0000}$	0.8	1.1

Table A.17: The inclusive trijet cross sections as functions of $E_{T,HCM}^{jet,3}$. Other details as in the caption to Table A.1.

$\eta_{LAB}^{jet,1}$	$\frac{d\sigma}{d\eta_{LAB}^{jet,1}}$ (pb)	δ_{stat} (pb)	δ_{syst} (pb)	δ_{ES} (pb)	C_{QED}	C_{had}
-0.5 - 0.0	0.39	0.23	$^{+0.28}_{-0.43}$	$^{+0.15}_{-0.10}$	1.2	0.42
0.0 - 0.5	6.0	0.7	$^{+0.9}_{-2.1}$	$^{+1.4}_{-1.2}$	0.95	0.62
0.5 - 1.0	28.2	1.6	$^{+0.2}_{-2.0}$	$^{+3.7}_{-3.5}$	0.97	0.731
1.0 - 1.5	61.2	2.2	$^{+5.4}_{-4.7}$	$^{+7.8}_{-8.4}$	0.963	0.779
1.5 - 2.0	97	3	$^{+10}_{-11}$	$^{+11}_{-11}$	0.963	0.789
2.0 - 2.5	132	3	$^{+15}_{-14}$	$^{+15}_{-13}$	0.960	0.799

Table A.18: The inclusive trijet cross sections as functions of $\eta_{LAB}^{jet,1}$. Other details as in the caption to Table A.1.

$\eta^{jet,2}_{LAB}$	$\frac{d\sigma}{d\eta^{jet,2}_{LAB}}$ (pb)	δ_{stat} (pb)	δ_{syst} (pb)	δ_{ES} (pb)	C_{QED}	C_{had}
-1.0 - -0.5	0.8	0.4	$^{+3.5}_{-0.9}$	$^{+0.2}_{-0.2}$	0.99	0.33
-0.5 - 0.0	18.4	1.4	$^{+2.2}_{-2.3}$	$^{+3.3}_{-3.6}$	0.97	0.606
0.0 - 0.5	62.4	2.3	$^{+2.3}_{-4.5}$	$^{+8.4}_{-8.3}$	0.963	0.746
0.5 - 1.0	96	3	$^{+12}_{-9}$	$^{+12}_{-11}$	0.970	0.799
1.0 - 1.5	84.2	2.4	$^{+5.9}_{-8.4}$	$^{+9.2}_{-9.5}$	0.963	0.826
1.5 - 2.0	48.9	1.8	$^{+5.6}_{-4.8}$	$^{+5.1}_{-4.8}$	0.943	0.835
2.0 - 2.5	14.9	1.3	$^{+1.0}_{-3.0}$	$^{+1.1}_{-1.1}$	0.96	0.86

Table A.19: The inclusive trijet cross sections as functions of $\eta^{jet,2}_{LAB}$. Other details as in the caption to Table A.1.

$\eta^{jet,3}_{LAB}$	$\frac{d\sigma}{d\eta^{jet,3}_{LAB}}$ (pb)	δ_{stat} (pb)	δ_{syst} (pb)	δ_{ES} (pb)	C_{QED}	C_{had}
-1.0 - -0.5	53.9	2.3	$^{+4.2}_{-6.9}$	$^{+9.1}_{-8.7}$	0.960	0.681
-0.5 - 0.0	96	3	$^{+7}_{-10}$	$^{+12}_{-12}$	0.972	0.785
0.0 - 0.5	91	3	$^{+10}_{-10}$	$^{+10}_{-11}$	0.960	0.823
0.5 - 1.0	58.4	2.1	$^{+3.6}_{-5.7}$	$^{+5.6}_{-5.7}$	0.956	0.828
1.0 - 1.5	23.0	1.3	$^{+1.2}_{-2.1}$	$^{+2.0}_{-2.1}$	0.96	0.86
1.5 - 2.0	4.20	0.54	$^{+0.47}_{-0.73}$	$^{+0.30}_{-0.21}$	0.94	0.87
2.0 - 2.5	0.31	0.18	$^{+0.12}_{-0.22}$	$^{-0.00}_{-0.00}$	1.1	0.8

Table A.20: The inclusive trijet cross sections as functions of $\eta^{jet,3}_{LAB}$. Other details as in the caption to Table A.1.

$\Delta\eta^{\mathrm{jet1,2}}_{HCM}$	$\frac{d\sigma}{d\Delta\eta^{\mathrm{jet1,2}}_{HCM}}$ (pb)	δ_{stat} (pb)	δ_{syst} (pb)	δ_{ES} (pb)	C_{QED}	C_{had}
0.0 - 0.7	88.8	2.1	$^{+5.5}_{-9.1}$	$^{+9.8}_{-9.9}$	0.963	0.784
0.7 - 1.4	76.6	2.2	$^{+3.1}_{-8.9}$	$^{+8.9}_{-9.8}$	0.956	0.800
1.4 - 2.1	45.1	1.7	$^{+6.1}_{-4.4}$	$^{+5.9}_{-5.4}$	0.962	0.784
2.1 - 2.8	19.3	1.2	$^{+3.5}_{-2.1}$	$^{+2.8}_{-2.2}$	0.98	0.756
2.8 - 3.5	3.1	0.5	$^{+1.3}_{-0.7}$	$^{+0.8}_{-0.2}$	0.95	0.66

Table A.21: The inclusive trijet cross sections as functions of $\Delta\eta^{\mathrm{jet1,2}}_{HCM}$. Other details as in the caption to Table A.1.

$x_{\rm Bj} \times 10^4$	$\Delta E^{\rm jet1,2}_{T,HCM}$ (GeV)	$\frac{d^2\sigma}{d(\Delta E^{\rm jet1,2}_{T,HCM})dx_{\rm Bj}}$ (pb/ GeV)	δ_{stat} (pb/ GeV)	δ_{syst} (pb/ GeV)	δ_{ES} (pb/ GeV)	C_{QED}	C_{had}
1.7 - 3.0	0.0 - 4.0	2.46×10^4	1.5×10^3	$^{+2.3\times10^3}_{-6.3\times10^3}$	$^{+3.6\times10^3}_{-4.0\times10^3}$	0.99	0.801
	4.0 - 10.0	8.1×10^3	6.8×10^2	$^{+4.7\times10^2}_{-1.6\times10^3}$	$^{+4.2\times10^2}_{-7.7\times10^2}$	1.02	0.83
	10.0 - 18.0	617	121	$^{+863}_{-186}$	$^{+13}_{-40}$	1.04	0.87
3.0 - 5.0	0.0 - 4.0	2.69×10^4	1.2×10^3	$^{+3.3\times10^3}_{-3.0\times10^3}$	$^{+3.5\times10^3}_{-3.3\times10^3}$	0.97	0.788
	4.0 - 10.0	8.2×10^3	5.0×10^2	$^{+1.2\times10^3}_{-1.8\times10^3}$	$^{+9.3\times10^2}_{-8.8\times10^2}$	0.96	0.82
	10.0 - 18.0	620	98	$^{+116}_{-142}$	$^{+28}_{-19}$	1.08	0.77
5.0 - 10	0.0 - 4.0	1.67×10^4	6.3×10^2	$^{+1.2\times10^3}_{-1.4\times10^3}$	$^{+2.3\times10^3}_{-2.1\times10^3}$	0.966	0.766
	4.0 - 10.0	4.72×10^3	2.5×10^2	$^{+5.6\times10^2}_{-4.2\times10^2}$	$^{+4.6\times10^2}_{-4.9\times10^2}$	0.95	0.815
	10.0 - 18.0	333	44	$^{+80}_{-90}$	$^{-0}_{-23}$	0.97	0.85
10 - 25	0.0 - 4.0	5.64×10^3	2.2×10^2	$^{+5.2\times10^2}_{-2.5\times10^2}$	$^{+7.9\times10^2}_{-7.6\times10^2}$	0.952	0.775
	4.0 - 10.0	1.73×10^3	9.7×10^1	$^{+4.0\times10^1}_{-1.6\times10^2}$	$^{+2.0\times10^2}_{-1.6\times10^2}$	0.96	0.813
	10.0 - 18.0	123	17	$^{+20}_{-50}$	$^{+2}_{-4}$	0.97	0.77
25 - 100	0.0 - 4.0	348	30	$^{+53}_{-36}$	$^{+47}_{-42}$	0.95	0.731
	4.0 - 10.0	83	10	$^{+18}_{-11}$	$^{+9}_{-11}$	0.95	0.76

Table A.22: The trijet double-differential cross sections as functions of $\Delta E^{\rm jet1,2}_{T,HCM}$. Other details as in the caption to Table A.8.

$x_{\rm Bj} \times 10^4$	$\lvert\Sigma\vec{p}^{\,\rm jet1,2}_{T,HCM}\rvert$ (GeV)	$\frac{d^2\sigma}{d\left(\lvert\Sigma\vec{p}^{\,\rm jet1,2}_{T,HCM}\rvert\right)dx_{\rm Bj}}$ (pb/ GeV)	δ_{stat} (pb/ GeV)	δ_{syst} (pb/ GeV)	δ_{ES} (pb/ GeV)	C_{QED}	C_{had}
1.7 - 3.0	0.0 - 4.0	7.0×10^3	8.6×10^2	$^{+1.3\times10^3}_{-2.5\times10^3}$	$^{+1.0\times10^3}_{-1.2\times10^3}$	0.98	0.85
	4.0 - 10.0	1.45×10^4	9.7×10^2	$^{+2.0\times10^3}_{-3.3\times10^3}$	$^{+1.5\times10^3}_{-2.1\times10^3}$	1.00	0.798
	10.0 - 16.0	5.3×10^3	5.0×10^2	$^{+3.3\times10^2}_{-1.4\times10^3}$	$^{+5.1\times10^2}_{-4.7\times10^2}$	1.04	0.85
	16.0 - 100.0	89	18	$^{+9}_{-23}$	$^{+7}_{-14}$	1.01	0.79
3.0 - 5.0	0.0 - 4.0	6.8×10^3	6.2×10^2	$^{+1.4\times10^3}_{-9.6\times10^2}$	$^{+9.3\times10^2}_{-7.7\times10^2}$	0.96	0.86
	4.0 - 10.0	1.59×10^4	7.6×10^2	$^{+2.7\times10^3}_{-2.8\times10^3}$	$^{+1.8\times10^3}_{-1.9\times10^3}$	0.97	0.778
	10.0 - 16.0	5.7×10^3	4.2×10^2	$^{+4.2\times10^2}_{-1.9\times10^3}$	$^{+7.5\times10^2}_{-5.3\times10^2}$	0.98	0.83
	16.0 - 100.0	75	10	$^{+19}_{-39}$	$^{+7}_{-9}$	0.93	0.81
5.0 - 10	0.0 - 4.0	4.22×10^3	3.1×10^2	$^{+5.1\times10^2}_{-4.5\times10^2}$	$^{+6.8\times10^2}_{-6.2\times10^2}$	0.96	0.84
	4.0 - 10.0	9.7×10^3	4.0×10^2	$^{+1.6\times10^3}_{-8.9\times10^2}$	$^{+1.1\times10^3}_{-1.1\times10^3}$	0.966	0.761
	10.0 - 16.0	3.05×10^3	2.0×10^2	$^{+2.0\times10^2}_{-5.7\times10^2}$	$^{+4.0\times10^2}_{-2.8\times10^2}$	0.93	0.83
	16.0 - 100.0	54	6	$^{+4}_{-23}$	$^{+4}_{-5}$	0.92	0.82
10 - 25	0.0 - 4.0	1.47×10^3	1.2×10^2	$^{+1.6\times10^2}_{-2.5\times10^2}$	$^{+2.9\times10^2}_{-2.2\times10^2}$	0.97	0.81
	4.0 - 10.0	3.62×10^3	1.5×10^2	$^{+2.1\times10^2}_{-1.7\times10^2}$	$^{+4.4\times10^2}_{-4.1\times10^2}$	0.955	0.772
	10.0 - 16.0	952	67	$^{+48}_{-172}$	$^{+94}_{-87}$	0.93	0.84
	16.0 - 100.0	14.2	1.6	$^{+2.9}_{-3.4}$	$^{+1.4}_{-2.2}$	0.94	0.77
25 - 100	0.0 - 4.0	124	21	$^{+15}_{-66}$	$^{+18}_{-17}$	0.93	0.74
	4.0 - 10.0	192	18	$^{+45}_{-16}$	$^{+24}_{-25}$	0.96	0.734
	10.0 - 16.0	48	7	$^{+11}_{-16}$	$^{+5}_{-4}$	0.93	0.77
	16.0 - 100.0	0.46	0.16	$^{+0.13}_{-0.24}$	$^{+0.07}_{-0.08}$	0.90	0.76

Table A.23: The trijet double-differential cross sections as functions of $|\Sigma\vec{p}^{\,\rm jet1,2}_{T,HCM}|$. Other details as in the caption to Table A.8.

$x_{\rm Bj} \times 10^4$	$\frac{\lvert\Delta\vec{p}_{T,HCM}^{\rm jet1,2}\rvert}{2E_{T,HCM}^{\rm jet1}}$	$\frac{d^2\sigma}{d\left(\frac{\lvert\Delta\vec{p}_{T,HCM}^{\rm jet1,2}\rvert}{2E_{T,HCM}^{\rm jet1}}\right)dx_{\rm Bj}}$ (pb)	δ_{stat} (pb)	δ_{syst} (pb)	δ_{ES} (pb)	C_{QED}	C_{had}
1.7 - 3.0	0.5 - 0.7	6.6×10^4	1.3×10^4	$^{+3.3\times10^3}_{-2.6\times10^4}$	$^{+4.3\times10^3}_{-8.4\times10^3}$	1.0	0.70
	0.7 - 0.9	4.5×10^5	4.0×10^4	$^{+1.3\times10^5}_{-1.0\times10^5}$	$^{+4.7\times10^4}_{-4.3\times10^4}$	0.99	0.81
	0.9 - 1.0	4.2×10^5	3.4×10^4	$^{+2.6\times10^4}_{-1.2\times10^5}$	$^{+5.2\times10^4}_{-8.0\times10^4}$	1.00	0.812
3.0 - 5.0	0.0 - 0.5	8.8×10^3	2.1×10^3	$^{+4.1\times10^3}_{-5.9\times10^3}$	$^{+2.8\times10^3}_{-8.0\times10^2}$	1.0	0.81
	0.5 - 0.7	7.8×10^4	1.1×10^4	$^{+1.5\times10^4}_{-5.1\times10^4}$	$^{+8.8\times10^3}_{-6.1\times10^3}$	1.04	0.76
	0.7 - 0.9	5.38×10^5	3.6×10^4	$^{+5.5\times10^4}_{-9.4\times10^4}$	$^{+5.1\times10^4}_{-6.8\times10^4}$	0.98	0.85
	0.9 - 1.0	4.15×10^5	2.5×10^4	$^{+7.6\times10^4}_{-4.6\times10^4}$	$^{+5.7\times10^4}_{-4.6\times10^4}$	0.967	0.794
5.0 - 10	0.0 - 0.5	4.5×10^3	9.3×10^2	$^{+1.1\times10^3}_{-2.8\times10^3}$	$^{+4.6\times10^2}_{-6.0\times10^2}$	0.9	0.96
	0.5 - 0.7	5.2×10^4	6.2×10^3	$^{+3.3\times10^3}_{-1.5\times10^4}$	$^{+6.4\times10^3}_{-2.0\times10^3}$	1.05	0.70
	0.7 - 0.9	3.03×10^5	1.7×10^4	$^{+4.9\times10^4}_{-2.8\times10^4}$	$^{+3.4\times10^4}_{-3.4\times10^4}$	0.95	0.80
	0.9 - 1.0	2.60×10^5	1.3×10^4	$^{+1.8\times10^4}_{-2.3\times10^4}$	$^{+3.4\times10^4}_{-3.6\times10^4}$	0.961	0.780
10 - 25	0.0 - 0.5	1.18×10^3	2.5×10^2	$^{+3.5\times10^2}_{-3.6\times10^2}$	$^{+2.5\times10^2}_{-1.9\times10^2}$	1.0	0.78
	0.5 - 0.7	1.07×10^4	1.3×10^3	$^{+1.5\times10^3}_{-3.4\times10^3}$	$^{+9.3\times10^2}_{-7.2\times10^2}$	0.84	0.85
	0.7 - 0.9	1.15×10^5	6.6×10^3	$^{+5.1\times10^3}_{-1.1\times10^4}$	$^{+1.3\times10^4}_{-1.3\times10^4}$	0.97	0.81
	0.9 - 1.0	9.3×10^4	5.0×10^3	$^{+7.4\times10^3}_{-4.5\times10^3}$	$^{+1.3\times10^4}_{-1.2\times10^4}$	0.955	0.783
25 - 100	0.5 - 0.7	675	170	$^{+286}_{-269}$	$^{+54}_{-25}$	1.0	0.71
	0.7 - 0.9	6.5×10^3	7.7×10^2	$^{+1.8\times10^3}_{-6.6\times10^2}$	$^{+8.0\times10^2}_{-8.7\times10^2}$	0.94	0.76
	0.9 - 1.0	5.7×10^3	6.9×10^2	$^{+7.3\times10^2}_{-1.3\times10^3}$	$^{+8.1\times10^2}_{-7.5\times10^2}$	0.95	0.739

Table A.24: The trijet double-differential cross sections as functions of $|\Delta\vec{p}_{T,HCM}^{\rm jet1,2}|/(2E_{T,HCM}^{\rm jet1})$. Other details as in the caption to Table A.8.

$x_{\rm Bj} \times 10^4$	$\Delta\phi^{\rm jet1,2}_{HCM}$	$\frac{d^2\sigma}{d(\Delta\phi^{\rm jet1,2}_{HCM})dx_{\rm Bj}}$ (pb)	δ_{stat} (pb)	δ_{syst} (pb)	δ_{ES} (pb)	C_{QED}	C_{had}
1.7 - 3.0	0.0 - $\pi/2$	5.0×10^3	1.0×10^3	$^{+6.3\times10^2}_{-3.5\times10^3}$	$^{+8.9\times10^2}_{-5.4\times10^2}$	0.92	0.75
	$\pi/2$ - $3\pi/4$	3.8×10^4	4.0×10^3	$^{+1.0\times10^4}_{-8.2\times10^3}$	$^{+3.5\times10^3}_{-5.2\times10^3}$	0.97	0.82
	$3\pi/4$ - π	1.40×10^5	7.4×10^3	$^{+1.4\times10^4}_{-3.4\times10^4}$	$^{+1.5\times10^4}_{-1.9\times10^4}$	1.01	0.811
3.0 - 5.0	0.0 - $\pi/2$	6.0×10^3	8.7×10^2	$^{+1.6\times10^3}_{-4.0\times10^3}$	$^{+1.2\times10^3}_{-7.8\times10^2}$	1.04	0.77
	$\pi/2$ - $3\pi/4$	4.79×10^4	3.7×10^3	$^{+4.6\times10^3}_{-5.8\times10^3}$	$^{+6.0\times10^3}_{-4.3\times10^3}$	0.97	0.79
	$3\pi/4$ - π	1.43×10^5	5.6×10^3	$^{+2.0\times10^4}_{-2.2\times10^4}$	$^{+1.6\times10^4}_{-1.8\times10^4}$	0.966	0.798
5.0 - 10	0.0 - $\pi/2$	3.4×10^3	4.4×10^2	$^{+5.2\times10^2}_{-1.4\times10^3}$	$^{+5.1\times10^2}_{-2.7\times10^2}$	0.95	0.79
	$\pi/2$ - $3\pi/4$	3.08×10^4	2.0×10^3	$^{+1.5\times10^3}_{-5.2\times10^3}$	$^{+3.6\times10^3}_{-2.6\times10^3}$	0.95	0.780
	$3\pi/4$ - π	8.6×10^4	2.9×10^3	$^{+1.4\times10^4}_{-7.3\times10^3}$	$^{+1.0\times10^4}_{-1.1\times10^4}$	0.964	0.780
10 - 25	0.0 - $\pi/2$	752	98	$^{+162}_{-65}$	$^{+130}_{-112}$	0.87	0.82
	$\pi/2$ - $3\pi/4$	8.5×10^3	6.0×10^2	$^{+1.1\times10^3}_{-4.3\times10^2}$	$^{+9.7\times10^2}_{-9.6\times10^2}$	0.94	0.778
	$3\pi/4$ - π	3.27×10^4	1.1×10^3	$^{+1.3\times10^3}_{-2.5\times10^3}$	$^{+4.1\times10^3}_{-3.7\times10^3}$	0.960	0.786
25 - 100	0.0 - $\pi/2$	41	12	$^{+6}_{-9}$	$^{+6}_{-6}$	0.99	0.73
	$\pi/2$ - $3\pi/4$	558	83	$^{+233}_{-72}$	$^{+67}_{-53}$	0.95	0.73
	$3\pi/4$ - π	1.86×10^3	1.5×10^2	$^{+2.9\times10^2}_{-2.2\times10^2}$	$^{+2.3\times10^2}_{-2.4\times10^2}$	0.95	0.740

Table A.25: The trijet double-differential cross sections as functions of $\Delta\phi^{\rm jet1,2}_{HCM}$. Other details as in the caption to Table A.8.

$Q^2(\,\mathrm{GeV}^2)$	$x_{\mathrm{Bj}} \times 10^4$ $(\,\mathrm{GeV}^2)$	$\frac{d^2\sigma}{d(Q^2)dx_{\mathrm{Bj}}}$ $(\mathrm{pb}/\,\mathrm{GeV}^2)$	δ_{stat} $(\mathrm{pb}/\,\mathrm{GeV}^2)$	δ_{syst} $(\mathrm{pb}/\,\mathrm{GeV}^2)$	δ_{ES} $(\mathrm{pb}/\,\mathrm{GeV}^2)$	C_{QED}	C_{had}
10 - 15	1.7 - 3.0	3.8×10^3	4.8×10^2	$^{+5.6\times10^2}_{-1.1\times10^3}$	$^{+5.5\times10^2}_{-5.8\times10^2}$	0.95	0.82
	3.0 - 5.0	2.5×10^3	3.3×10^2	$^{+4.2\times10^2}_{-1.5\times10^3}$	$^{+5.4\times10^2}_{-2.8\times10^2}$	1.00	0.81
	5.0 - 10.0	572	129	$^{+165}_{-154}$	$^{+178}_{-63}$	0.91	0.74
15 - 20	3.0 - 5.0	1.36×10^3	2.0×10^2	$^{+3.2\times10^2}_{-4.1\times10^2}$	$^{+1.7\times10^2}_{-1.9\times10^2}$	0.98	0.85
	5.0 - 10.0	520	93	$^{+117}_{-200}$	$^{+66}_{-48}$	1.00	0.73
20 - 30	3.0 - 5.0	706	127	$^{+167}_{-213}$	$^{+108}_{-79}$	0.91	0.91
	5.0 - 10.0	578	74	$^{+73}_{-246}$	$^{+61}_{-68}$	0.94	0.84
	10.0 - 33.0	55	12	$^{+8}_{-18}$	$^{+4}_{-9}$	1.03	0.76
30 - 50	5.0 - 10.0	211	29	$^{+27}_{-50}$	$^{+27}_{-15}$	0.97	0.86
	10.0 - 55.0	27.3	3.5	$^{+2.9}_{-3.5}$	$^{+4.0}_{-3.4}$	0.93	0.79
50 - 100	10.0 - 25.0	34.1	4.0	$^{+7.0}_{-4.3}$	$^{+4.4}_{-3.7}$	0.94	0.85
	25.0 - 100.0	4.6	0.9	$^{+1.7}_{-1.8}$	$^{+0.6}_{-0.5}$	0.98	0.74

Table A.26: The dijet double-differential cross sections as functions of x_{Bj} for events with $|\Delta\phi^{\mathrm{jet1,2}}_{HCM}| < 2\pi/3$. Other details as in the caption to Table A.8.

Appendix B

Purities, Efficiencies, and Correction Factors

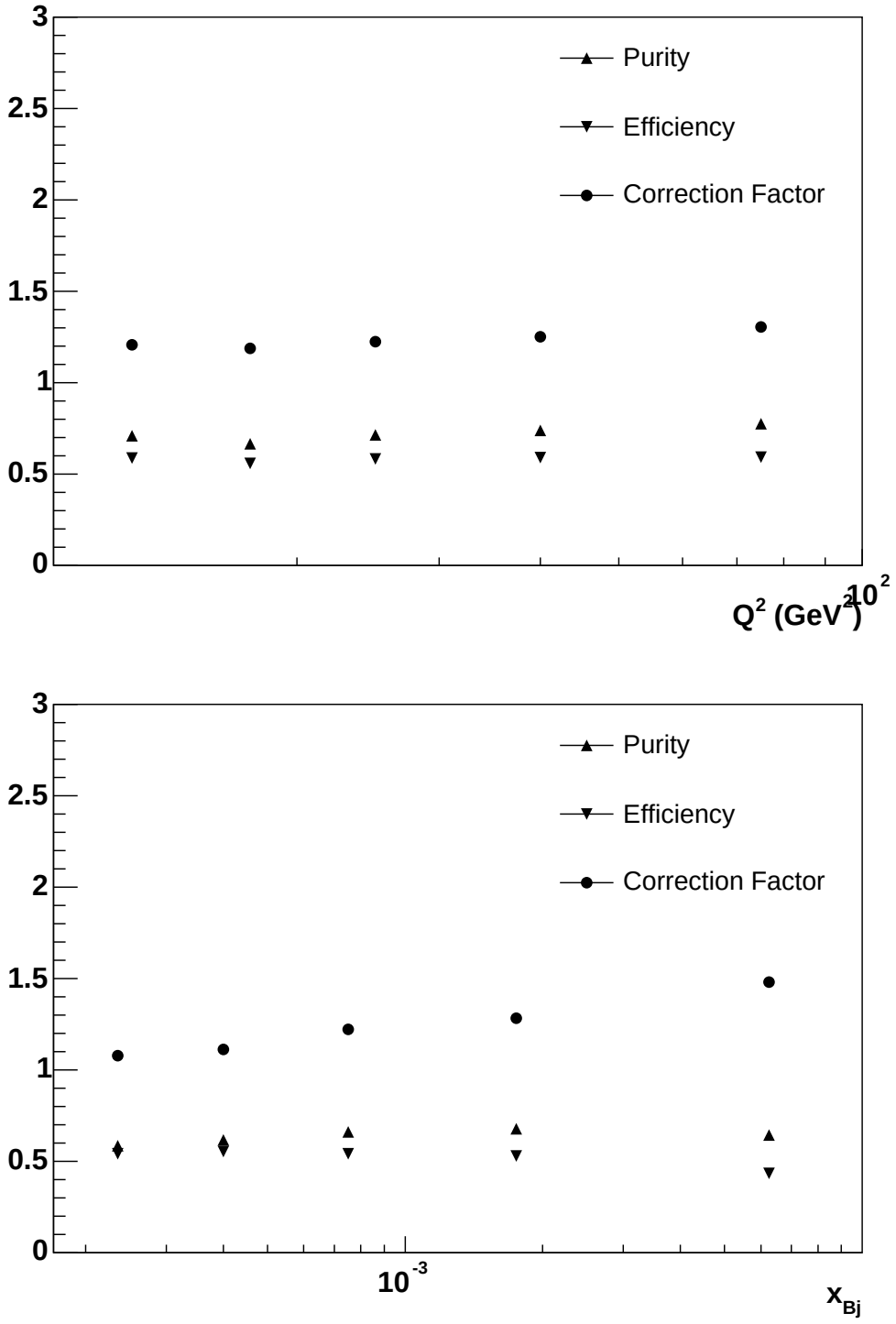

Figure B.1: Purities, efficiencies, and correction factors for Q^2 and x_{Bj} for the dijet sample.

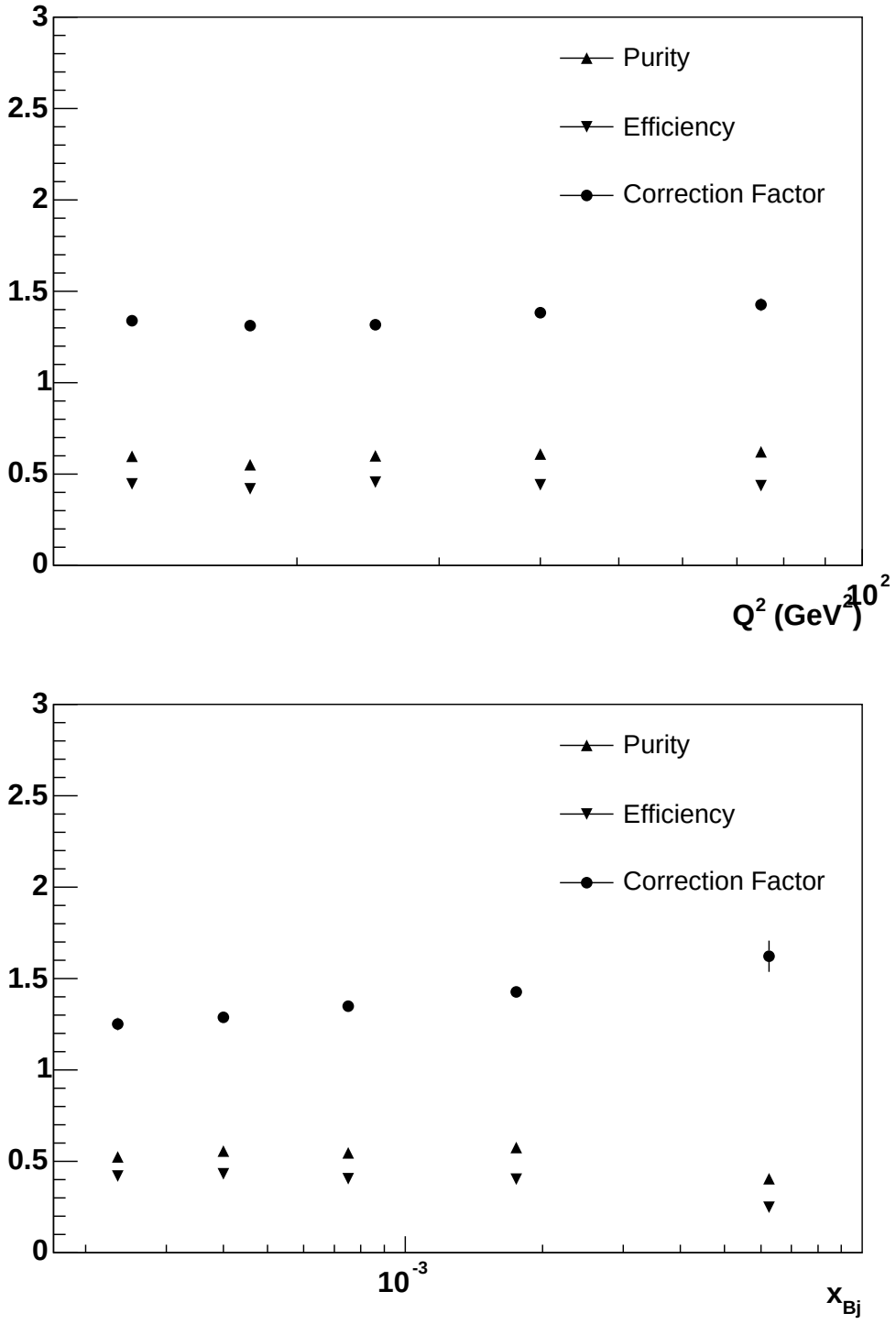

Figure B.2: Purities, efficiencies, and correction factors for the Q^2 and x_{Bj} cross sections for the trijet sample.

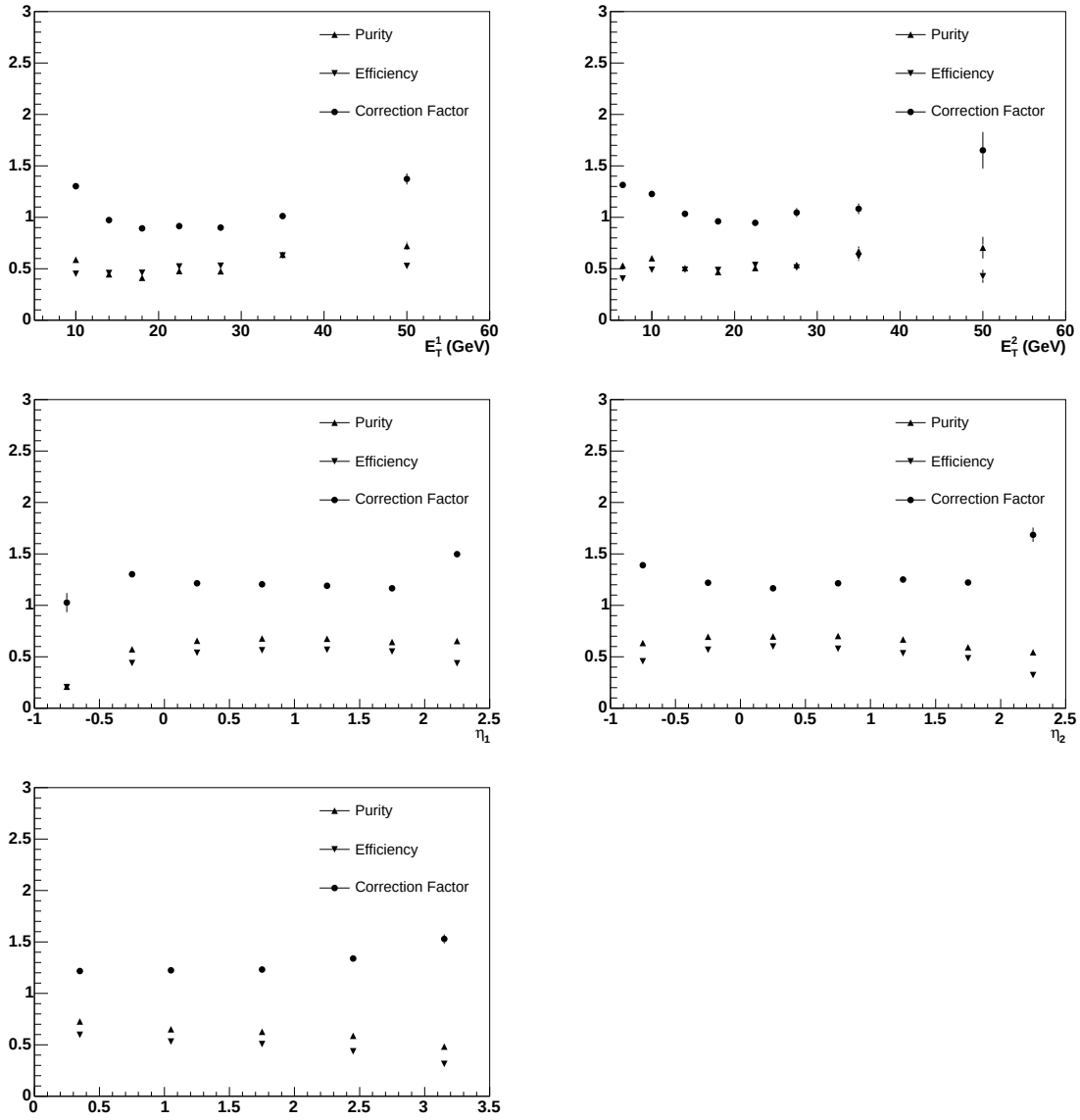

Figure B.3: Purities, efficiencies, and correction factors for the $E_{T,\mathrm{HCM}}^{\mathrm{jet1}}$, $E_{T,\mathrm{HCM}}^{\mathrm{jet2}}$, $\eta_{\mathrm{LAB}}^{\mathrm{jet1}}$, $\eta_{\mathrm{LAB}}^{\mathrm{jet2}}$, and $|\Delta\eta_{\mathrm{HCM}}^{\mathrm{jet1,2}}$ cross sections for the dijet sample.

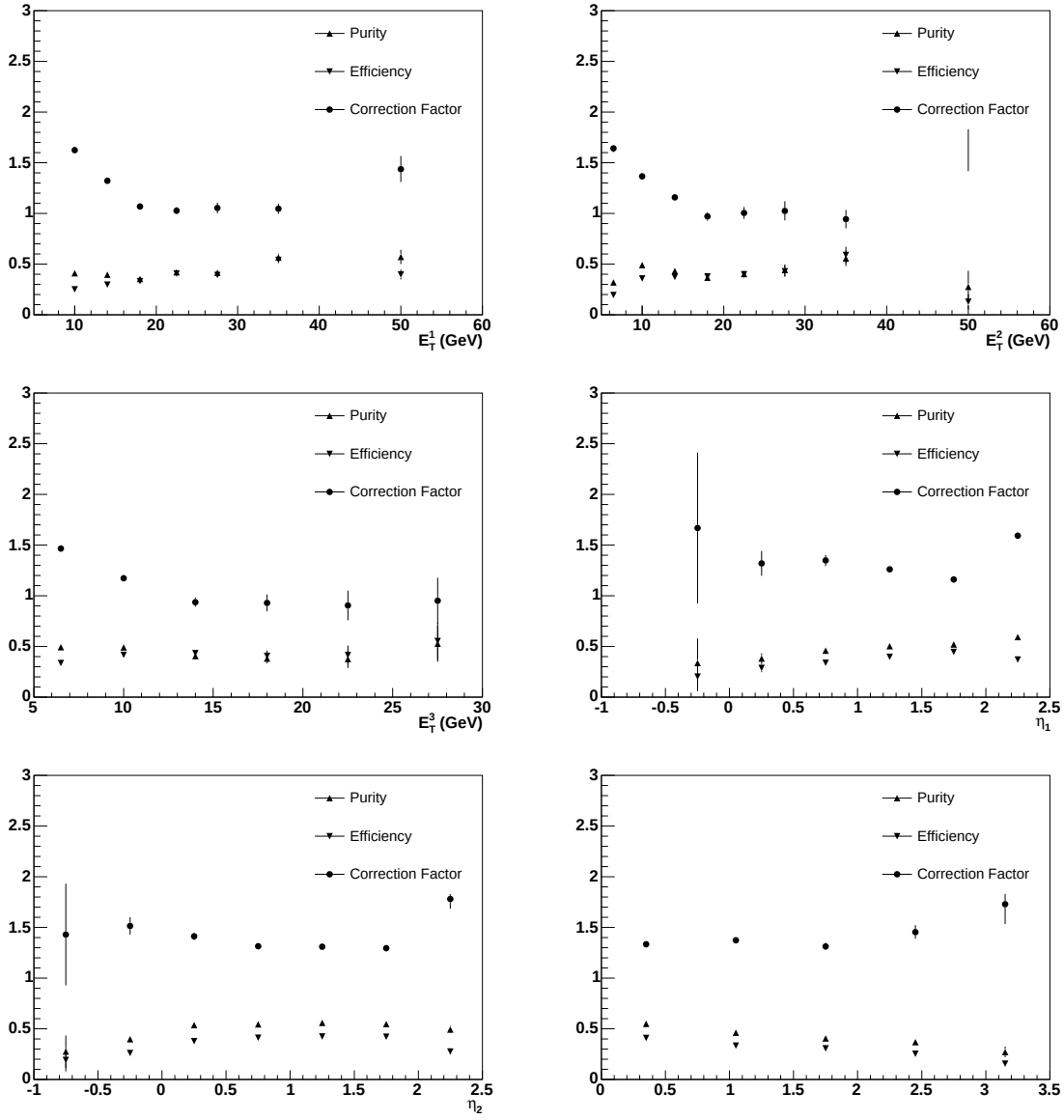

Figure B.4: Purities, efficiencies, and correction factors for the $E_{T,\mathrm{HCM}}^{\mathrm{jet1}}$, $E_{T,\mathrm{HCM}}^{\mathrm{jet2}}$, $E_{T,\mathrm{HCM}}^{\mathrm{jet3}}$, $\eta_{\mathrm{LAB}}^{\mathrm{jet1}}$, $\eta_{\mathrm{LAB}}^{\mathrm{jet2}}$, and $|\Delta\eta_{\mathrm{HCM}}^{\mathrm{jet1,2}}$ cross sections for the trijet sample.

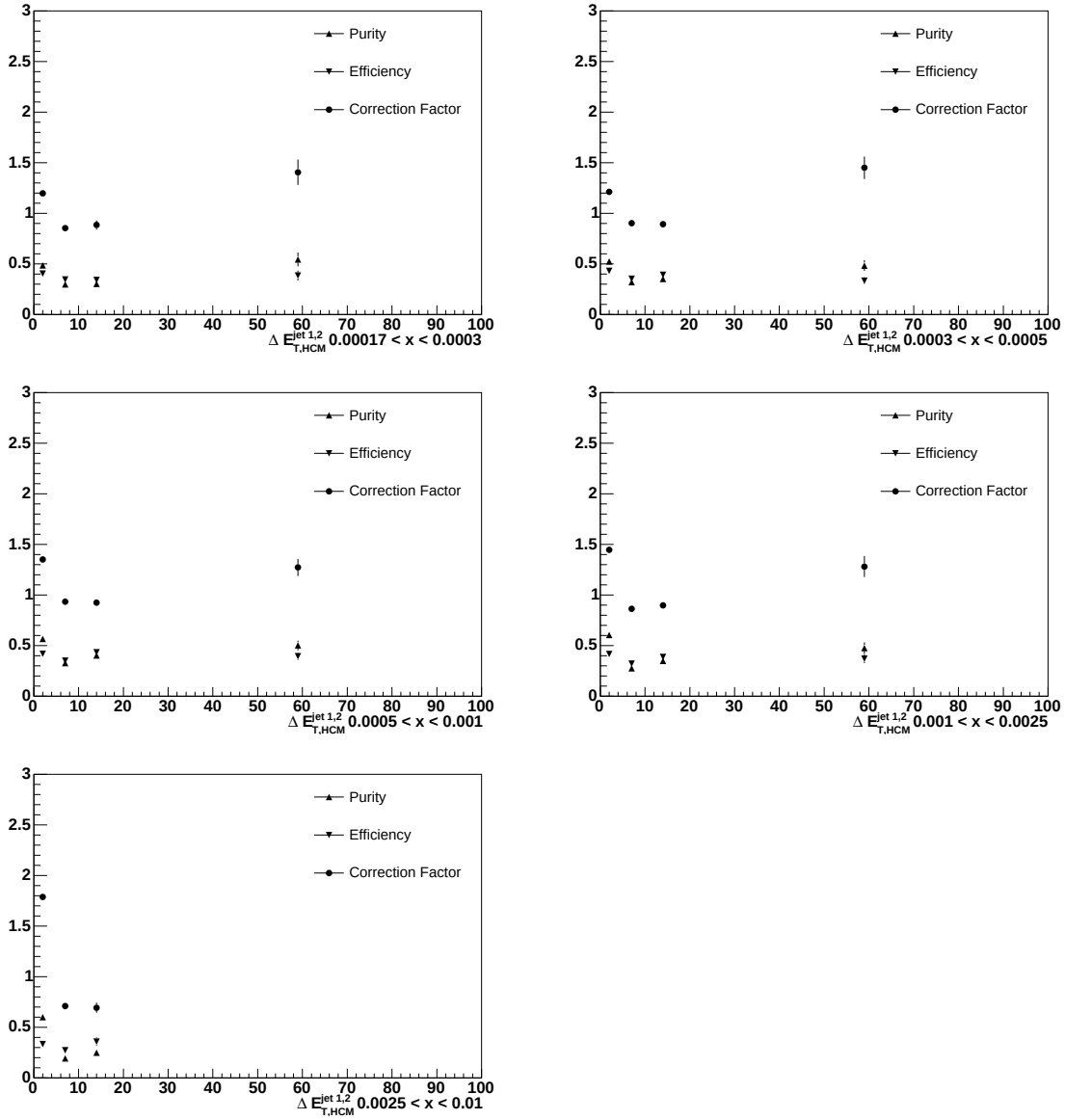

Figure B.5: Purities, efficiencies, and correction factors for the $\Delta E_{T,\mathrm{HCM}}^{\mathrm{jet1,2}}$ cross sections for the dijet sample in ascending bins of x_{Bj}.

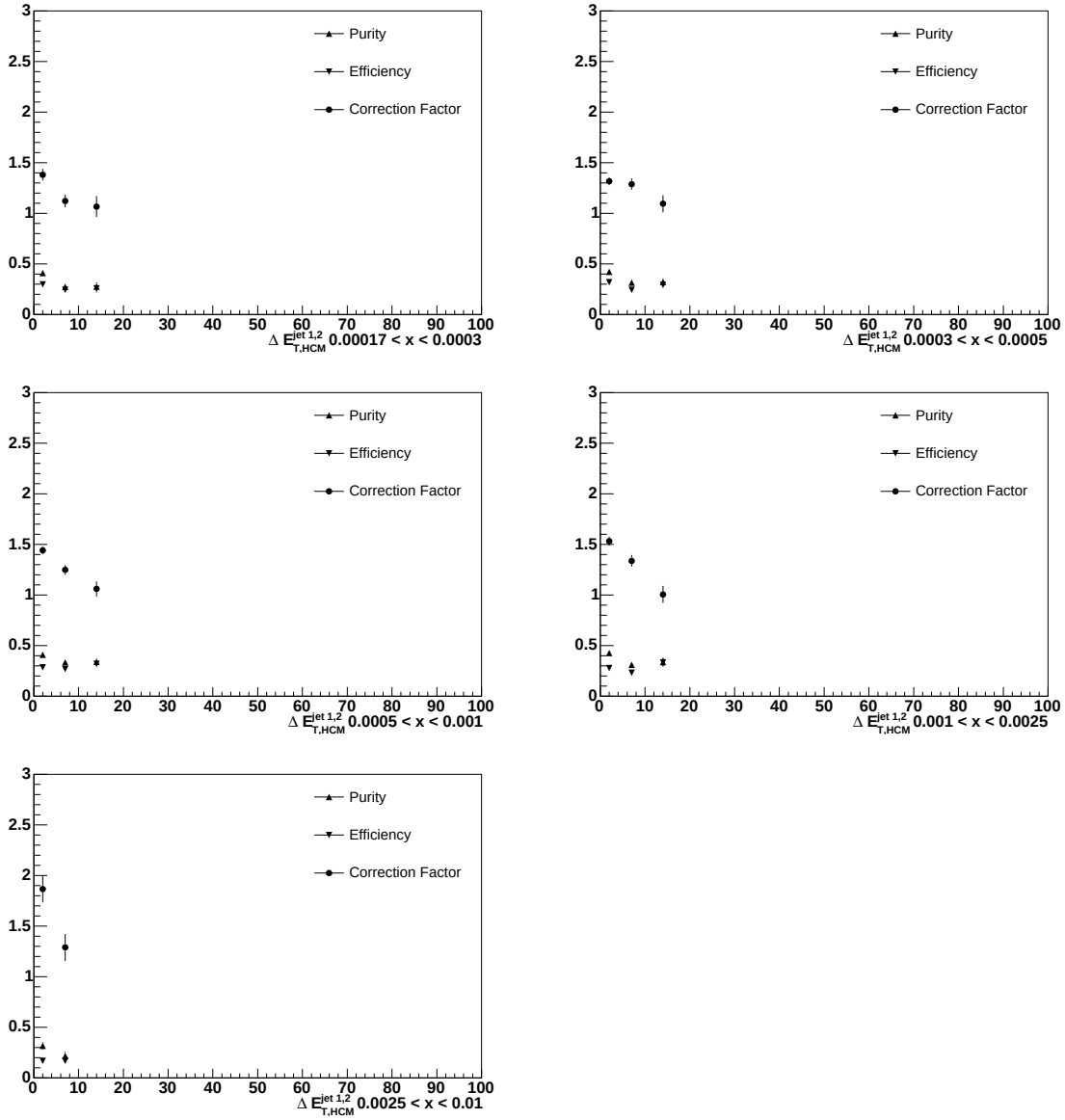

Figure B.6: Purities, efficiencies, and correction factors for the $\Delta E_{T,\mathrm{HCM}}^{\mathrm{jet1,2}}$ cross sections for the trijet sample in ascending bins of x_{Bj}.

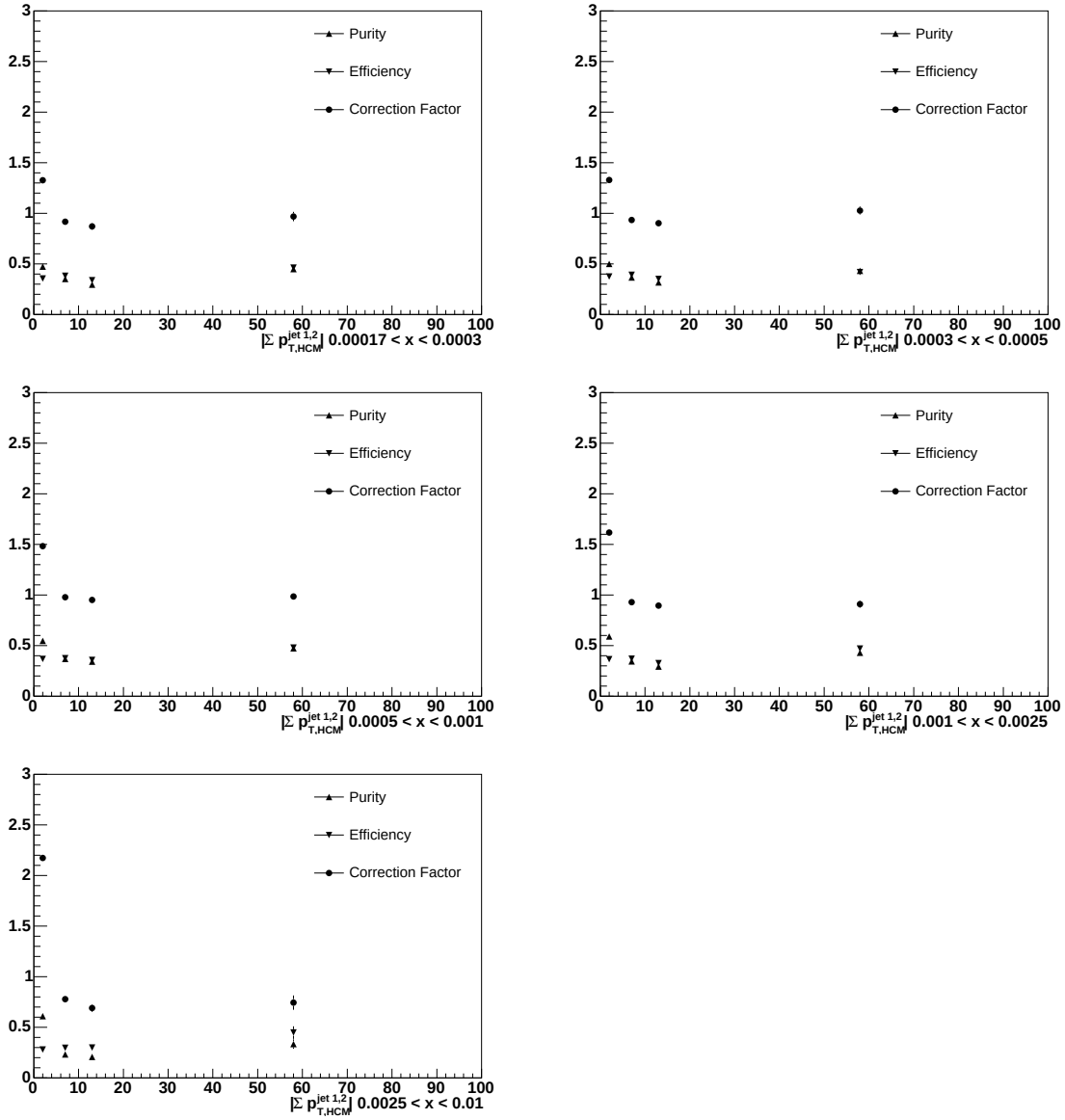

Figure B.7: Purities, efficiencies, and correction factors for the $|\Delta\vec{p}_{T,\mathrm{HCM}}^{\mathrm{jet1,2}}|/(2E_{T,\mathrm{HCM}}^{\mathrm{jet1}})$ cross sections for the dijet sample in ascending bins of x_{Bj}.

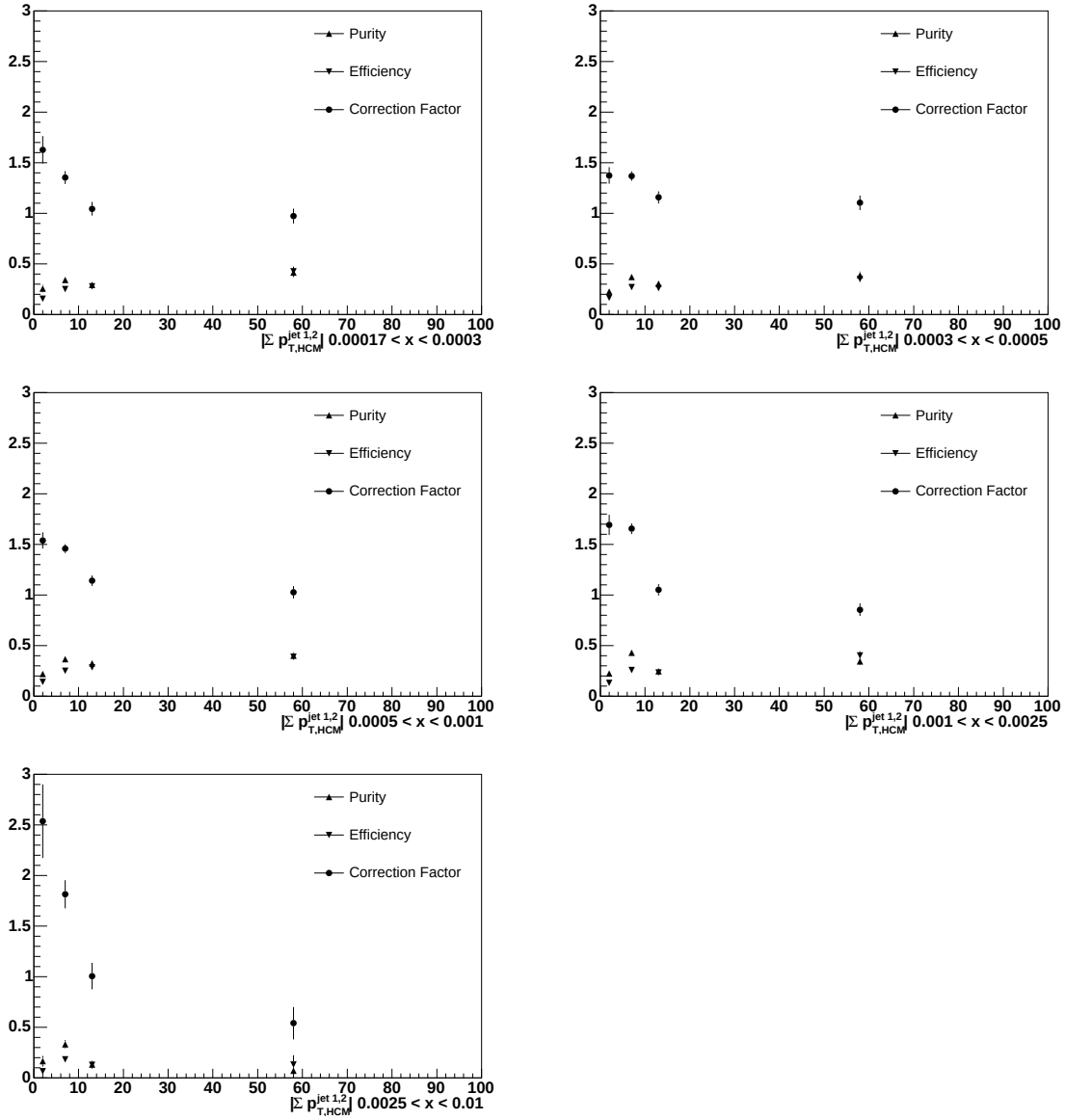

Figure B.8: Purities, efficiencies, and correction factors for the $|\Delta\vec{p}_{T,\mathrm{HCM}}^{\,\mathrm{jet1,2}}|/(2E_{T,\mathrm{HCM}}^{\mathrm{jet1}})$ cross sections for the trijet sample in ascending bins of x_{Bj}.

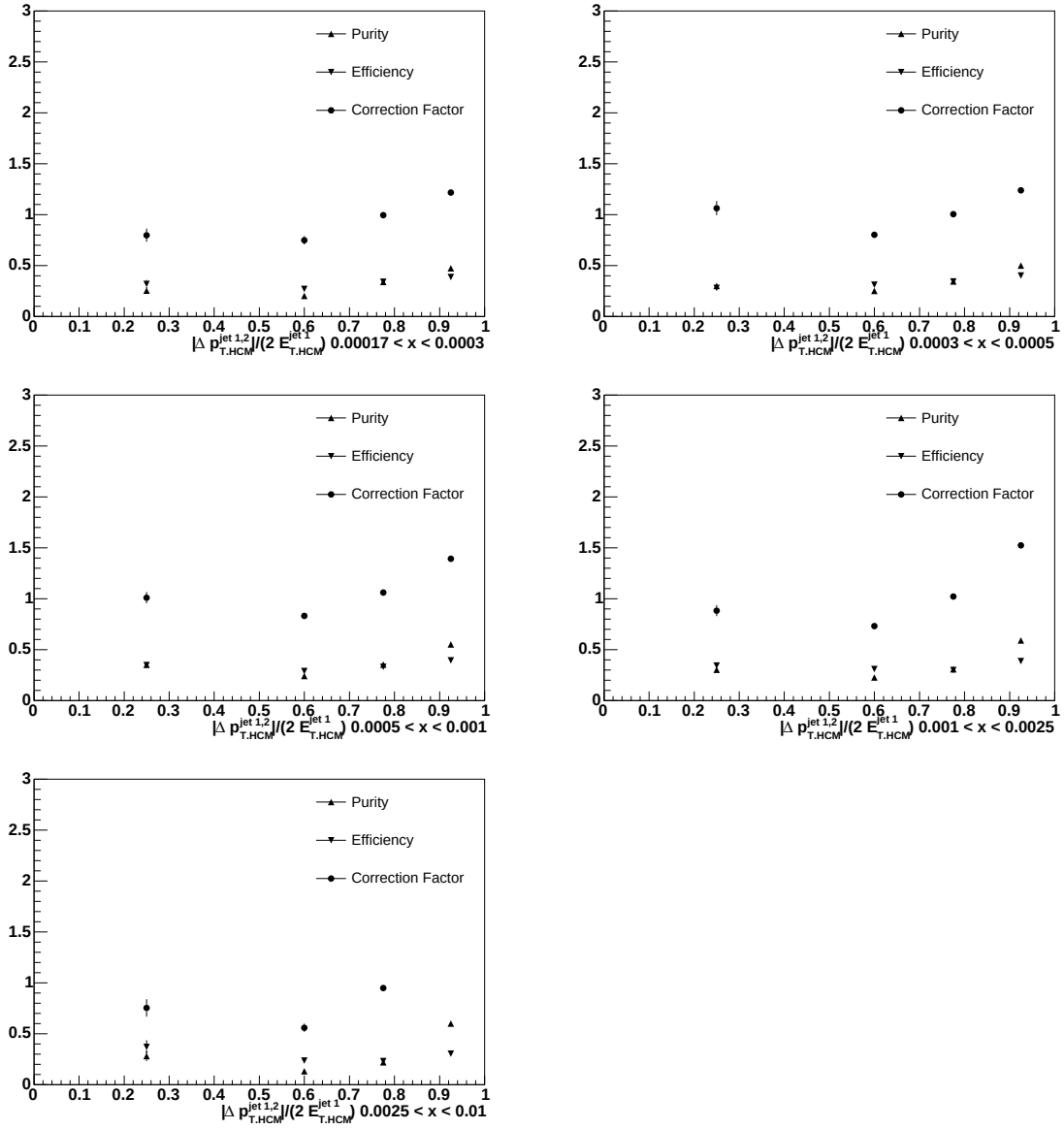

Figure B.9: Purities, efficiencies, and correction factors for the $|\Delta\vec{p}_{T,\mathrm{HCM}}^{\mathrm{jet1,2}}|/(2E_{T,\mathrm{HCM}}^{\mathrm{jet1}})$ cross sections for the dijet sample in ascending bins of x_{Bj}.

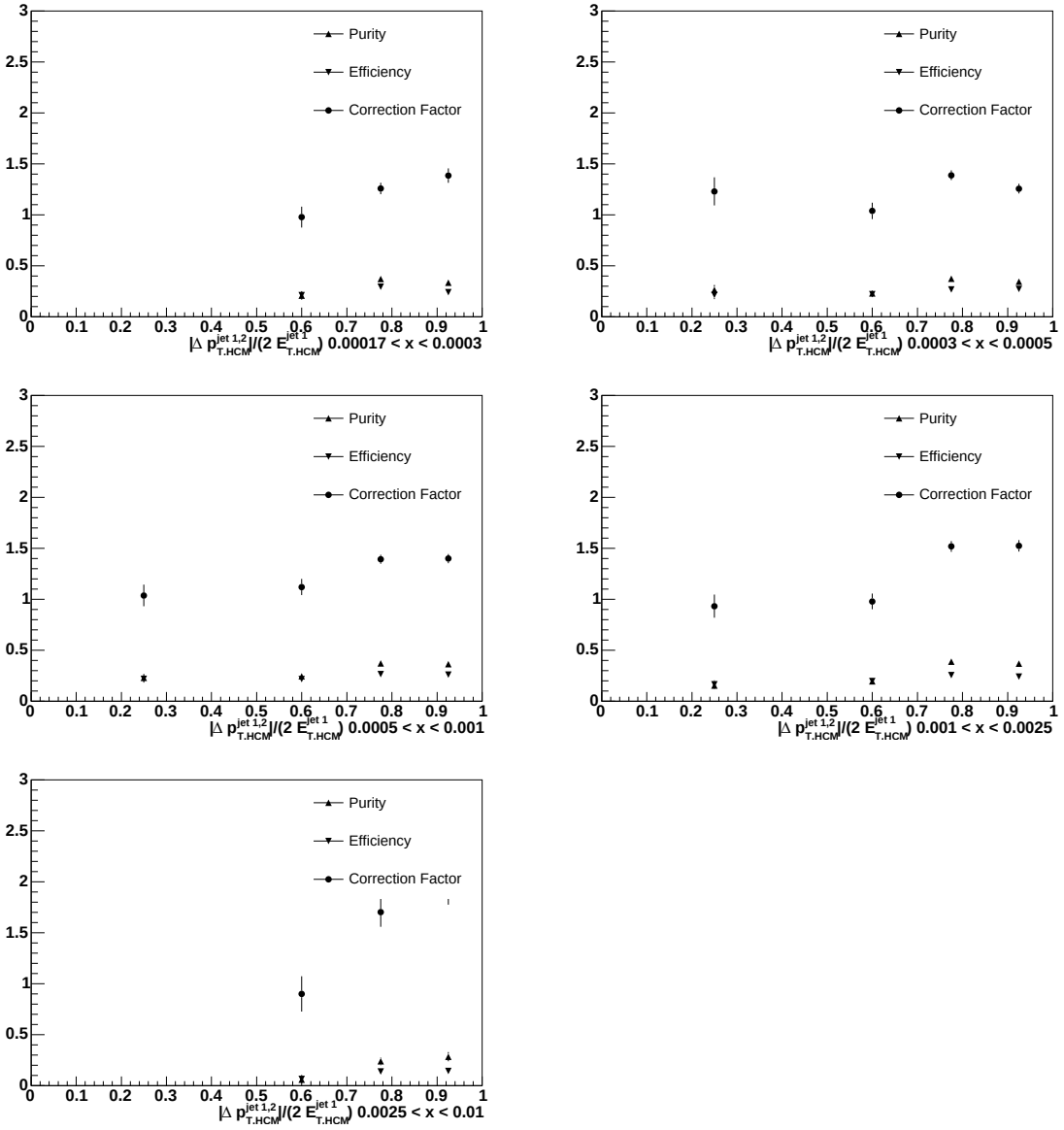

Figure B.10: Purities, efficiencies, and correction factors for the $|\Delta\vec{p}_{T,\mathrm{HCM}}^{\mathrm{jet1,2}}|/(2E_{T,\mathrm{HCM}}^{\mathrm{jet1}})$ cross sections for the trijet sample in ascending bins of x_{Bj}.

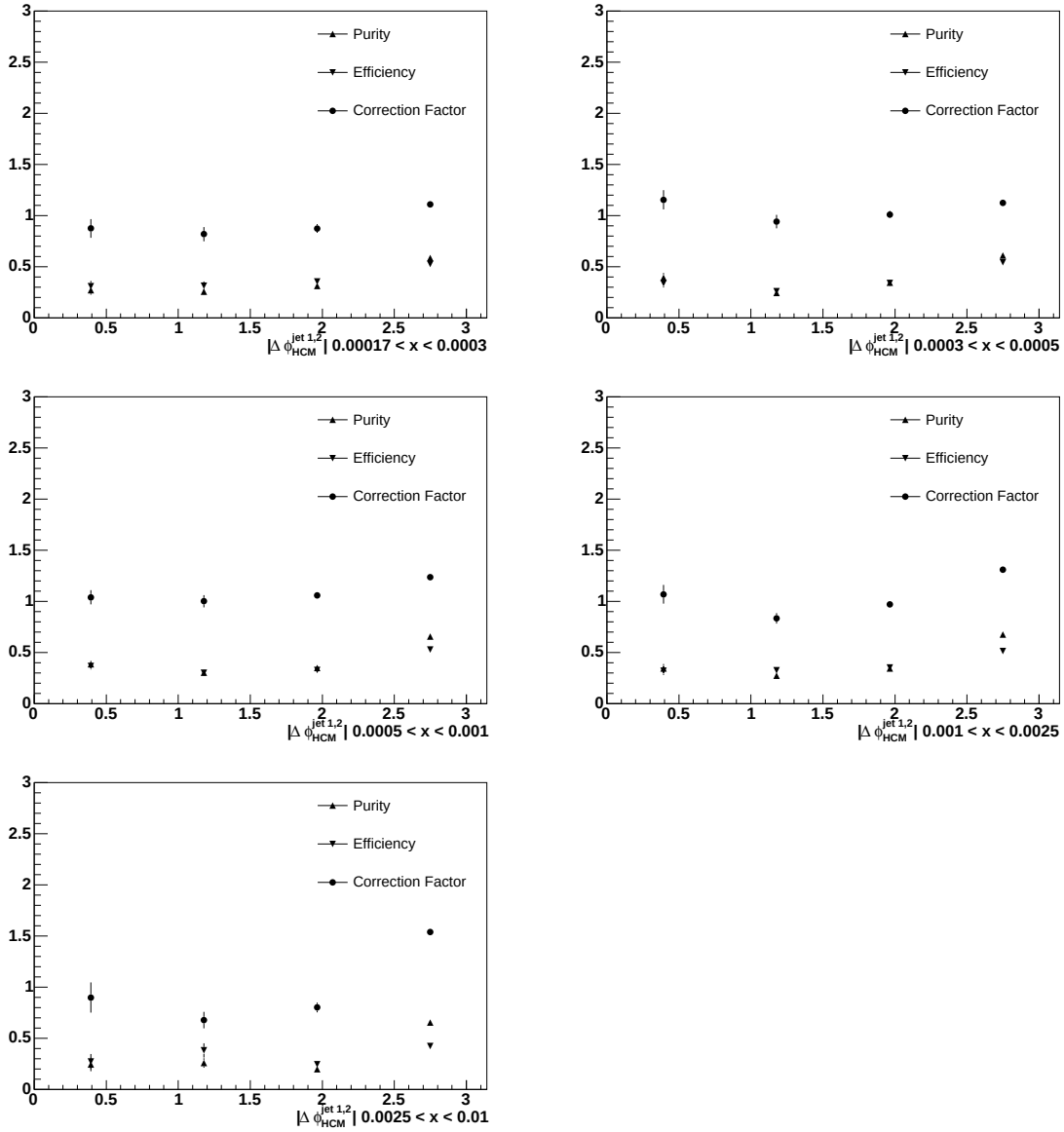

Figure B.11: Purities, efficiencies, and correction factors for the $|\Delta\phi^{\mathrm{jet1,2}}_{\mathrm{HCM}}|$ cross sections for the dijet sample in ascending bins of x_{Bj}.

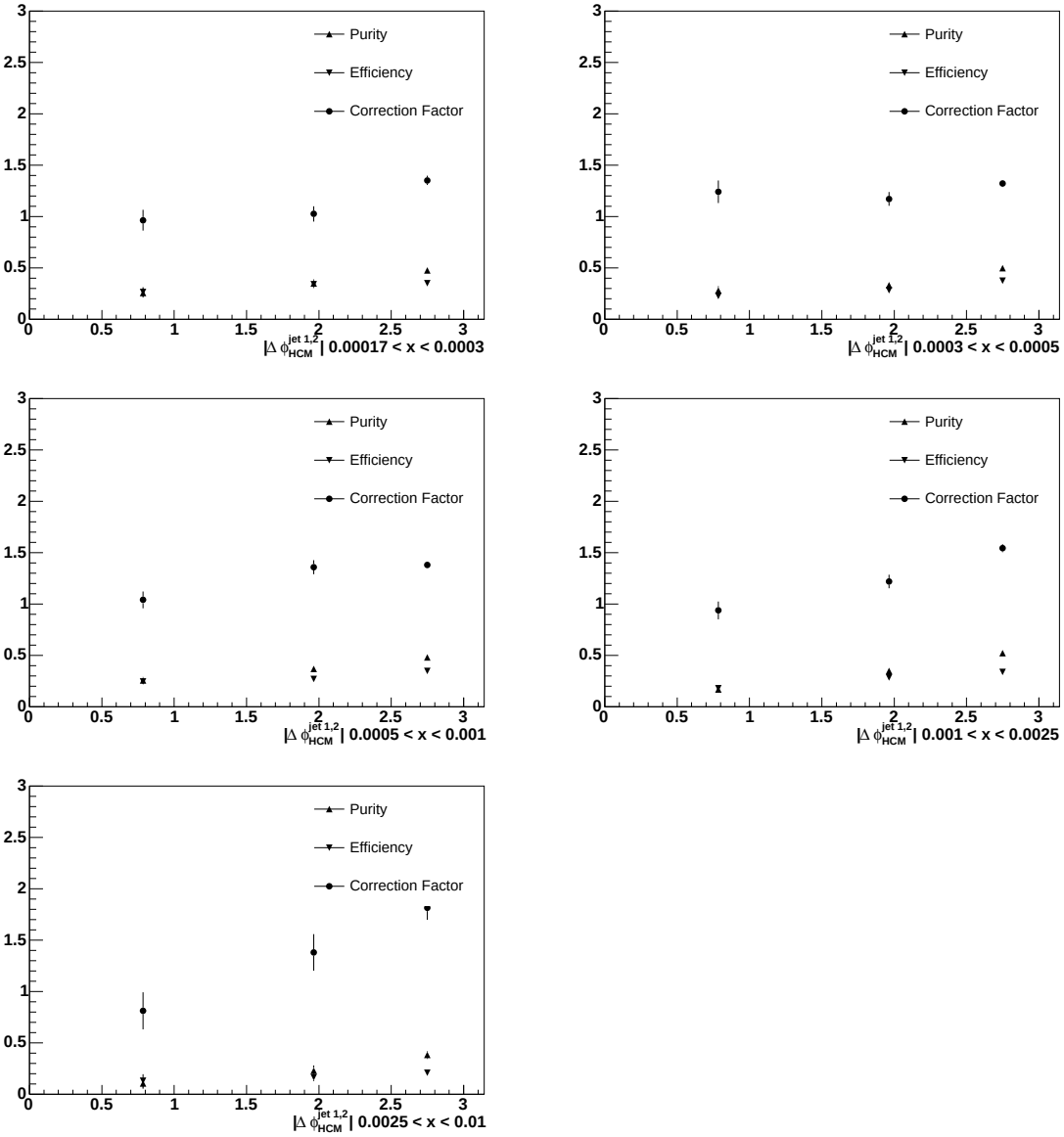

Figure B.12: Purities, efficiencies, and correction factors for the $|\Delta\phi^{\mathrm{jet1,2}}_{\mathrm{HCM}}|$ cross sections for the trijet sample in ascending bins of x_{Bj}.

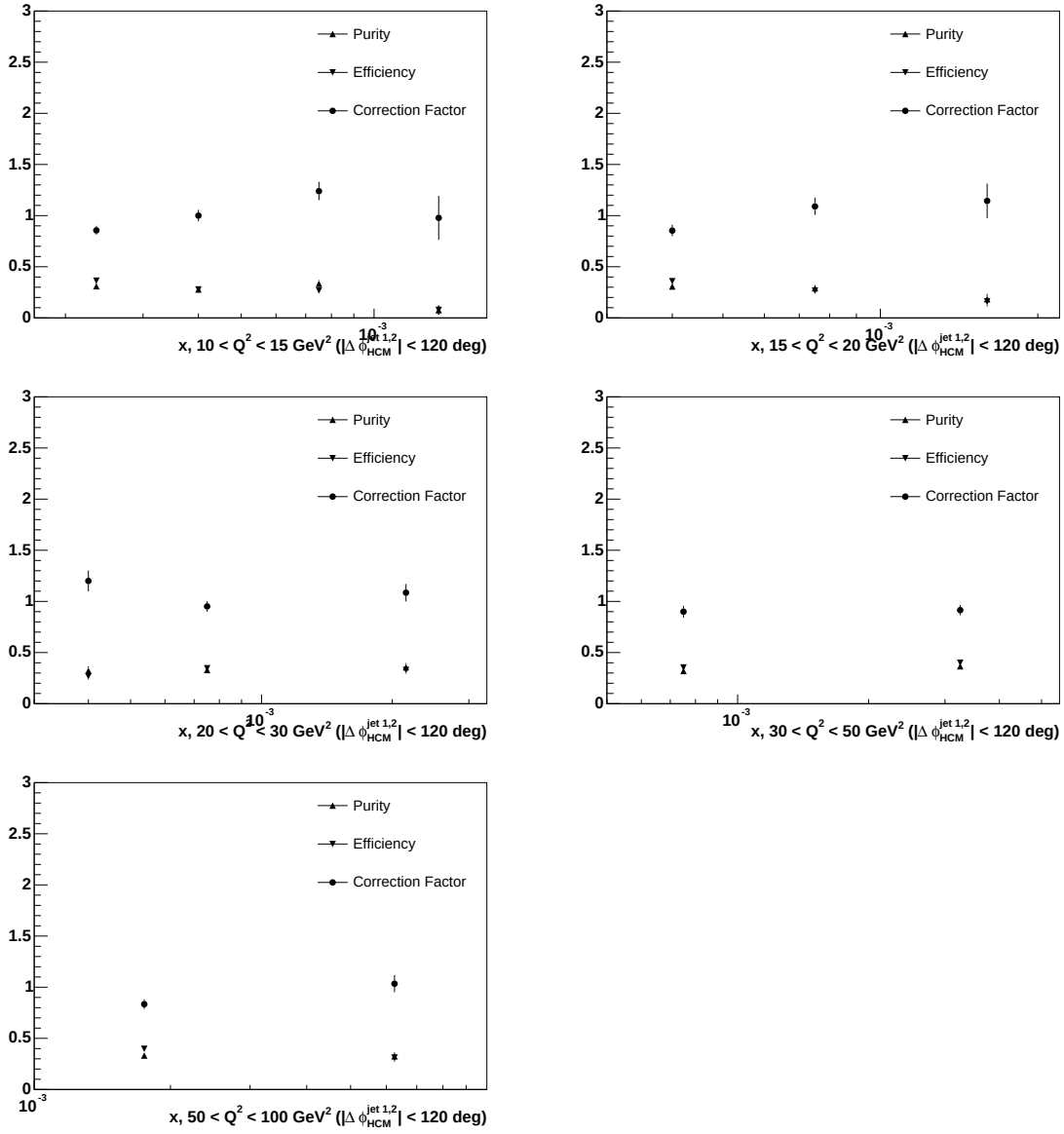

Figure B.13: Purities, efficiencies, and correction factors for the cross sections in Q^2 and x_{Bj} with $|\Delta\phi^{\mathrm{jet1,2}}_{\mathrm{HCM}}| < 2\pi/3$ for the dijet sample in ascending bins of Q^2.

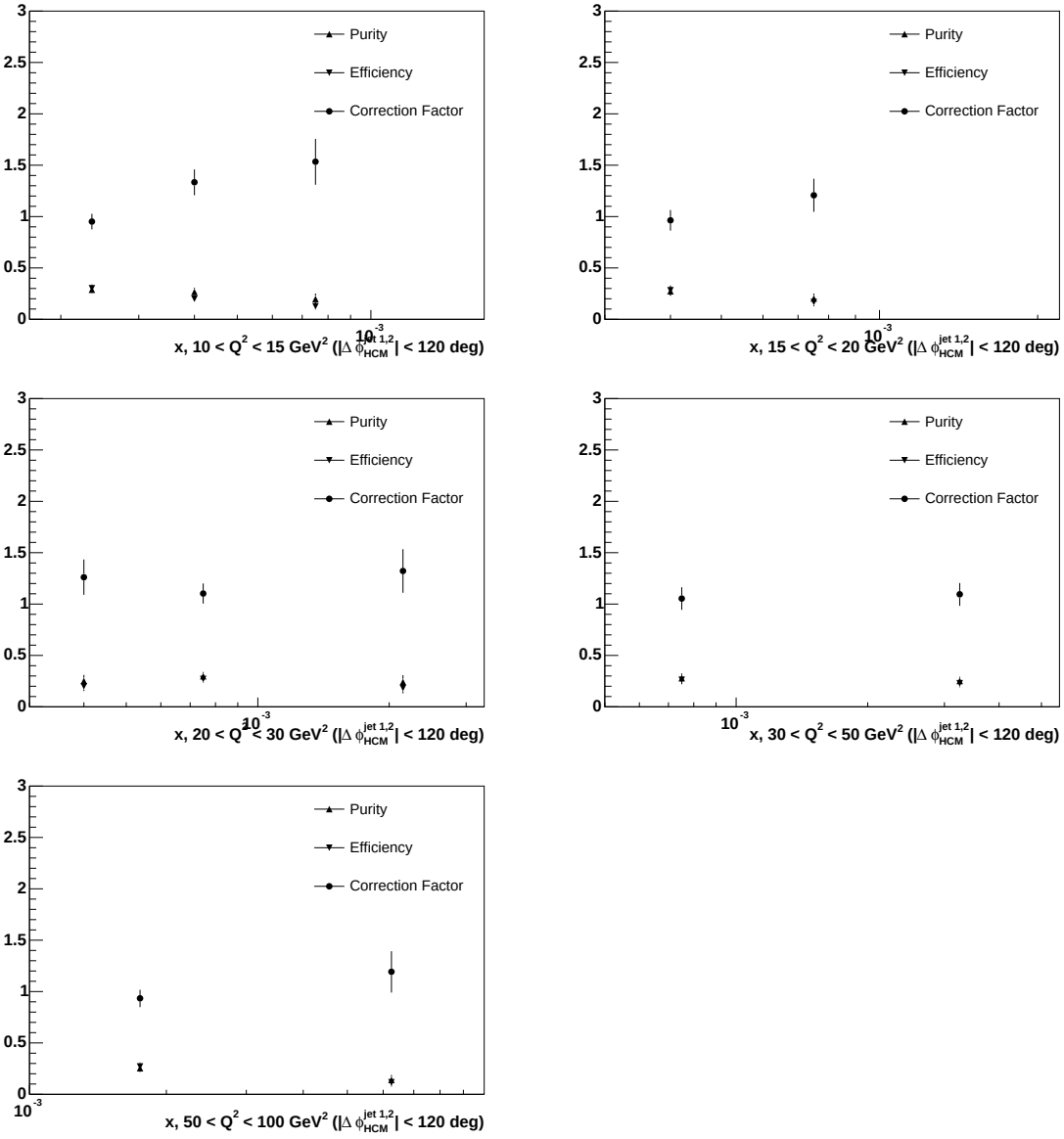

Figure B.14: Purities, efficiencies, and correction factors for the cross sections in Q^2 and x_{Bj} with $|\Delta\phi^{\mathrm{jet1,2}}_{\mathrm{HCM}}| < 2\pi/3$ for the dijet sample in ascending bins of Q^2.

Appendix C

Systematic Uncertainties

The points representing the systematic uncertainties in the following figures are numbered in ascending order from left to right. Table C lists all the systematics considered in this analysis. The uncertainties associated with the cuts on Q^2 and x_{Bj} were determined by scaling those variables by their resolutions to preserve the binning for the mult-differential cross sections. The points representing the systematic uncertainties in the following figures are numbered in ascending order from left to right.

Systematic Number	Variation
1	Q^2 scaled +
2	Q^2 scaled −
3	x_{Bj} scaled +
4	x_{Bj} scaled −
5	y_{JB} cut −
6	y_{JB} cut +
7	y_{el} cut −
8	y_{el} cut +
9	$E - p_z$ lower cut −
10	$E - p_z$ lower cut +
11	$E - p_z$ upper cut −
12	$E - p_z$ upper cut +
13	E_e cut −
14	E_e cut +
15	$E_{T,\mathrm{HCM}}^{\mathrm{jet1}}$ cut −
16	$E_{T,\mathrm{HCM}}^{\mathrm{jet1}}$ cut +
17	$E_{T,\mathrm{HCM}}^{\mathrm{jet2}}$ cut −
18	$E_{T,\mathrm{HCM}}^{\mathrm{jet2}}$ cut +
19	$\eta_{\mathrm{LAB}}^{\mathrm{jet}}$ lower cut −
20	$\eta_{\mathrm{LAB}}^{\mathrm{jet}}$ lower cut +
21	$\eta_{\mathrm{LAB}}^{\mathrm{jet}}$ upper cut −
22	$\eta_{\mathrm{LAB}}^{\mathrm{jet}}$ upper cut +
23	$E_{T,\mathrm{HCM}}^{\mathrm{jet3}}$ cut − (trijet sample only)
24	$E_{T,\mathrm{HCM}}^{\mathrm{jet3}}$ cut + (trijet sample only)
25	LEPTO systematic (23 for dijet sample)

Table C.1: The systematic uncertainties considered in this analysis. Also considered, but not appearing in the following figures is the uncertainty from the jet energy scale.

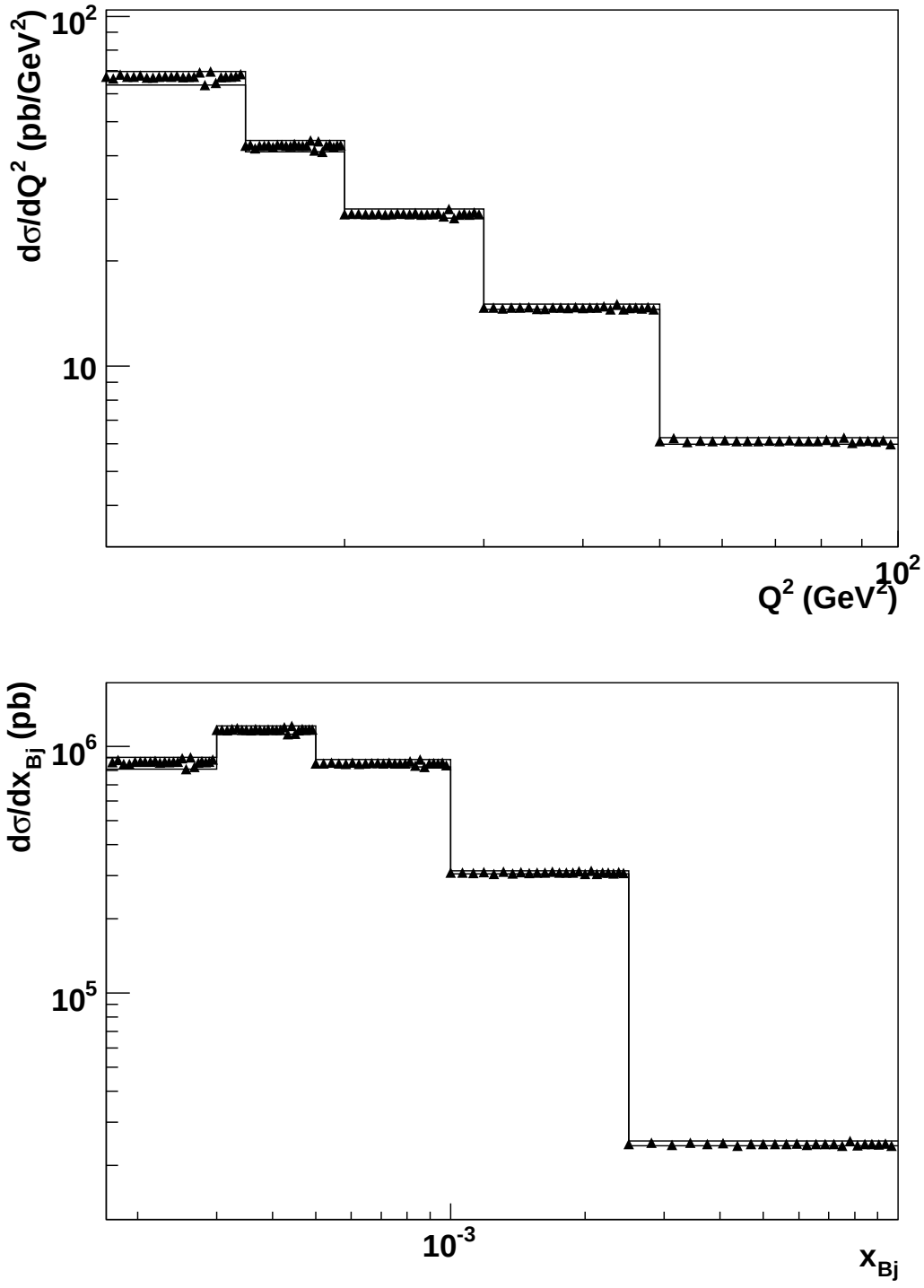

Figure C.1: Systematic uncertainties for Q^2 and x_{Bj} for the dijet sample.

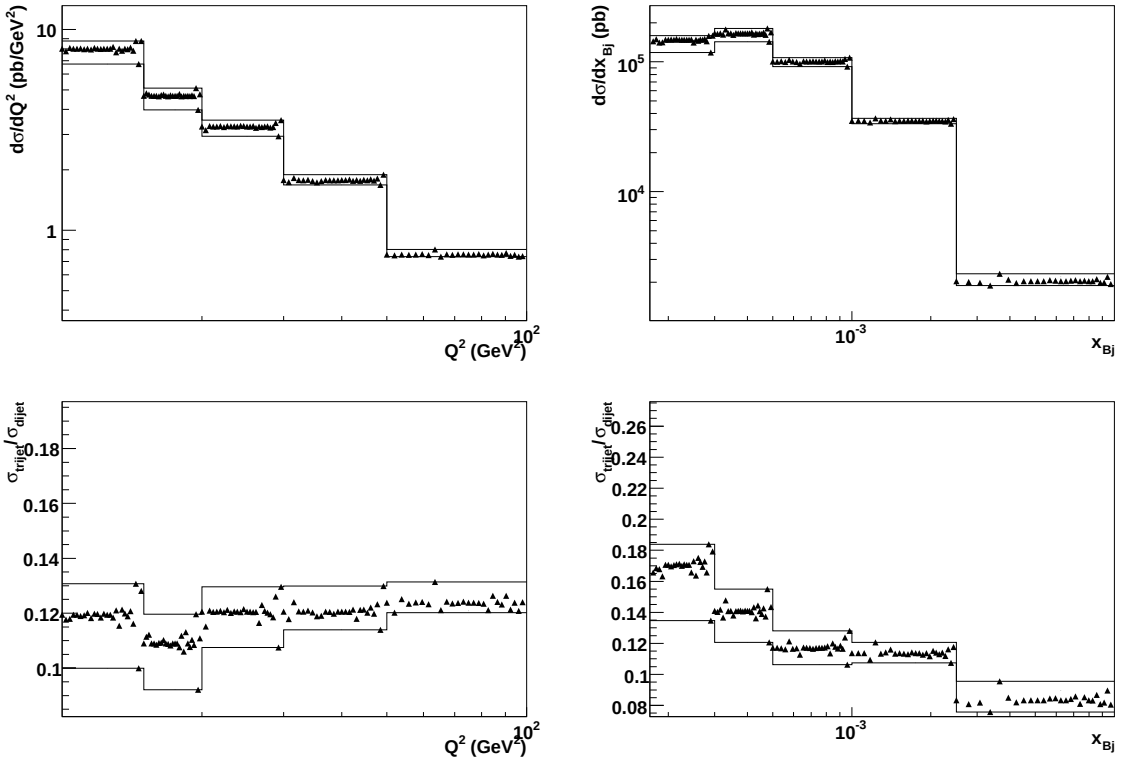

Figure C.2: Systematic uncertainties for the Q^2 and x_{Bj} cross sections for the trijet sample, and the ratio $\sigma_{trijet}/\sigma_{dijet}$.

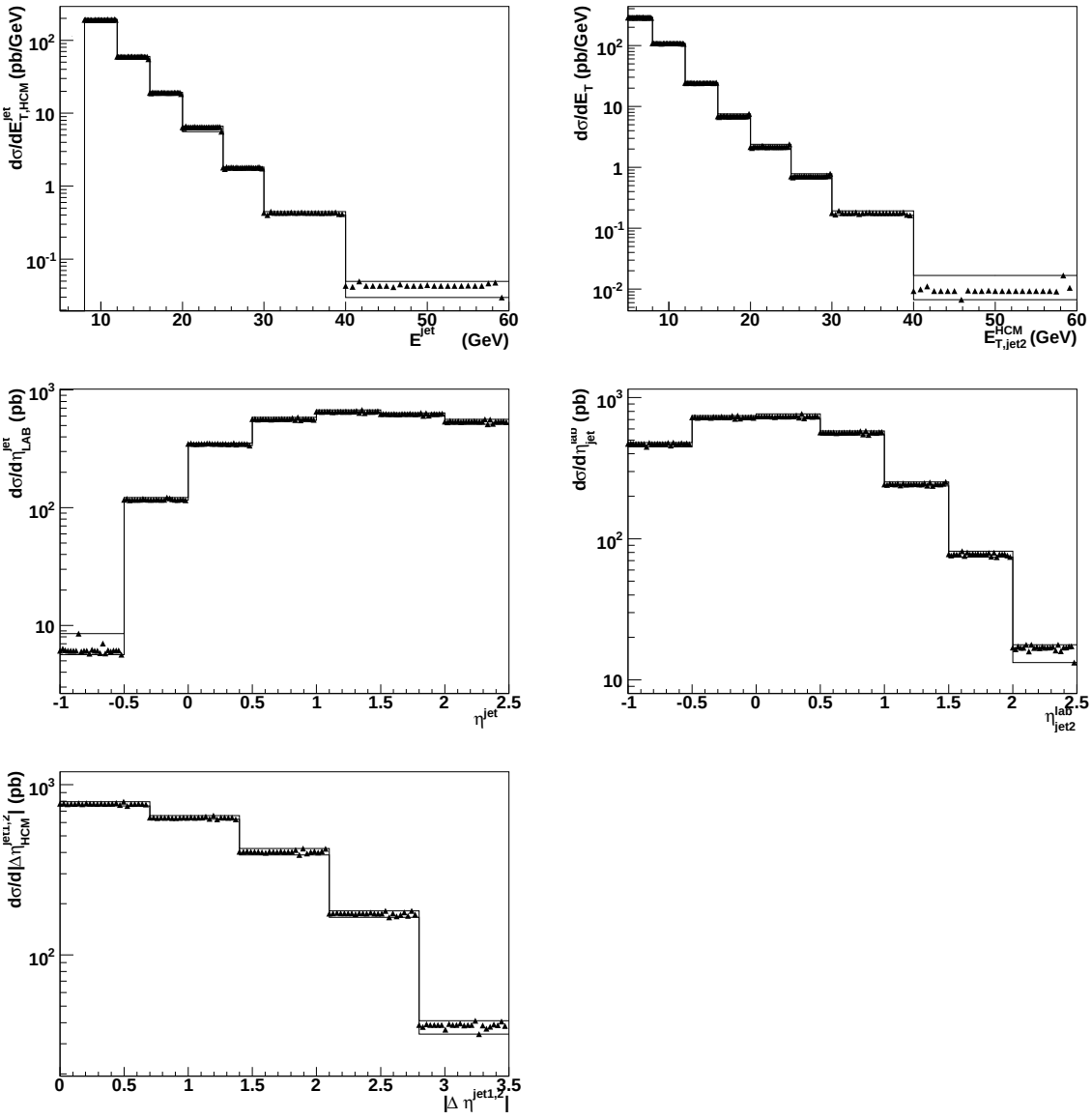

Figure C.3: Systematic uncertainties for the $E_{T,\mathrm{HCM}}^{\mathrm{jet1}}$, $E_{T,\mathrm{HCM}}^{\mathrm{jet2}}$, $\eta_{\mathrm{LAB}}^{\mathrm{jet1}}$, $\eta_{\mathrm{LAB}}^{\mathrm{jet2}}$, and $|\Delta\eta_{\mathrm{HCM}}^{\mathrm{jet1,2}}$ cross sections for the dijet sample.

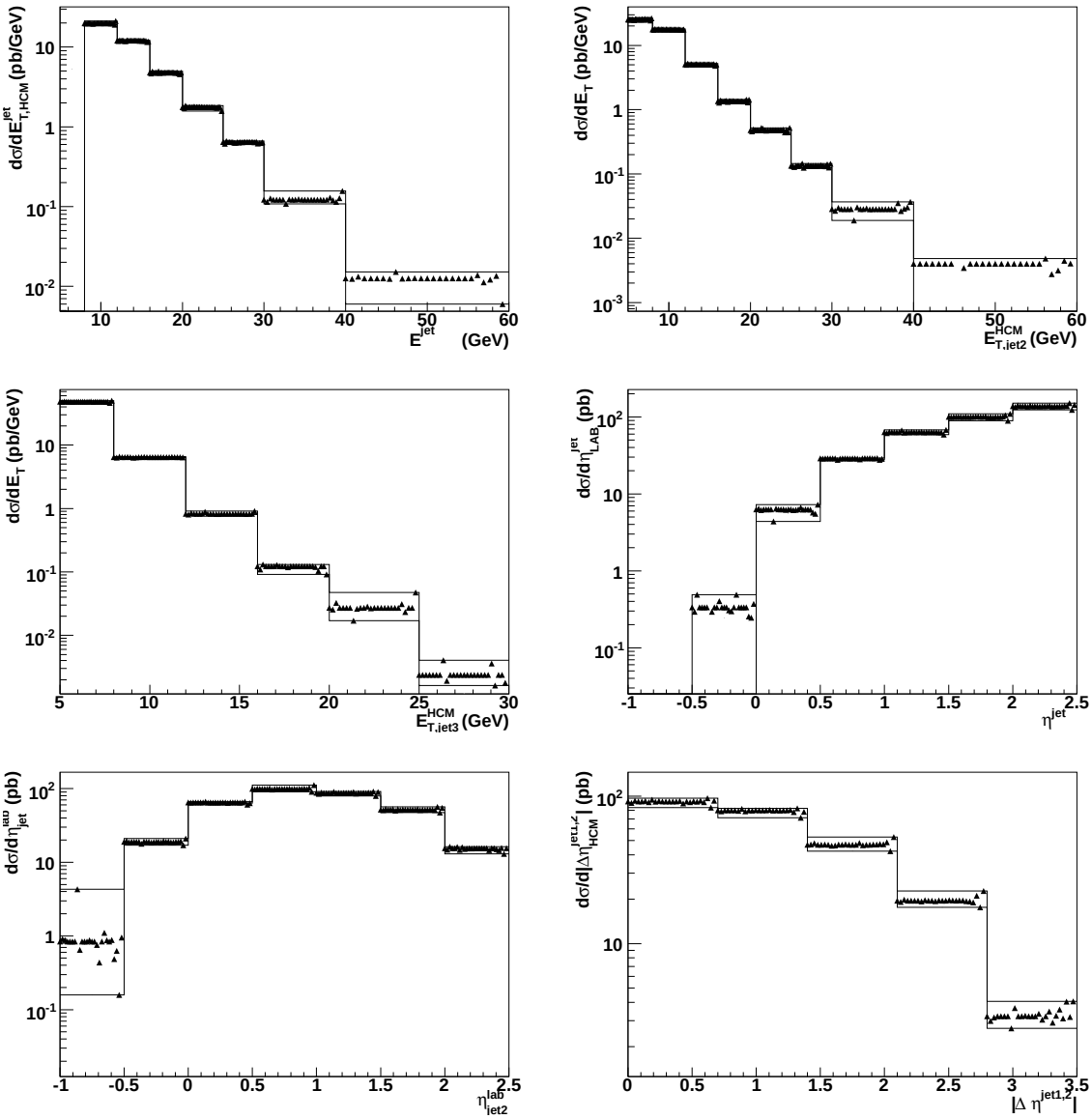

Figure C.4: Systematic uncertainties for the $E_{T,\mathrm{HCM}}^{\mathrm{jet1}}$, $E_{T,\mathrm{HCM}}^{\mathrm{jet2}}$, $E_{T,\mathrm{HCM}}^{\mathrm{jet3}}$, $\eta_{\mathrm{LAB}}^{\mathrm{jet1}}$, $\eta_{\mathrm{LAB}}^{\mathrm{jet2}}$, and $|\Delta\eta_{\mathrm{HCM}}^{\mathrm{jet1,2}}$ cross sections for the trijet sample.

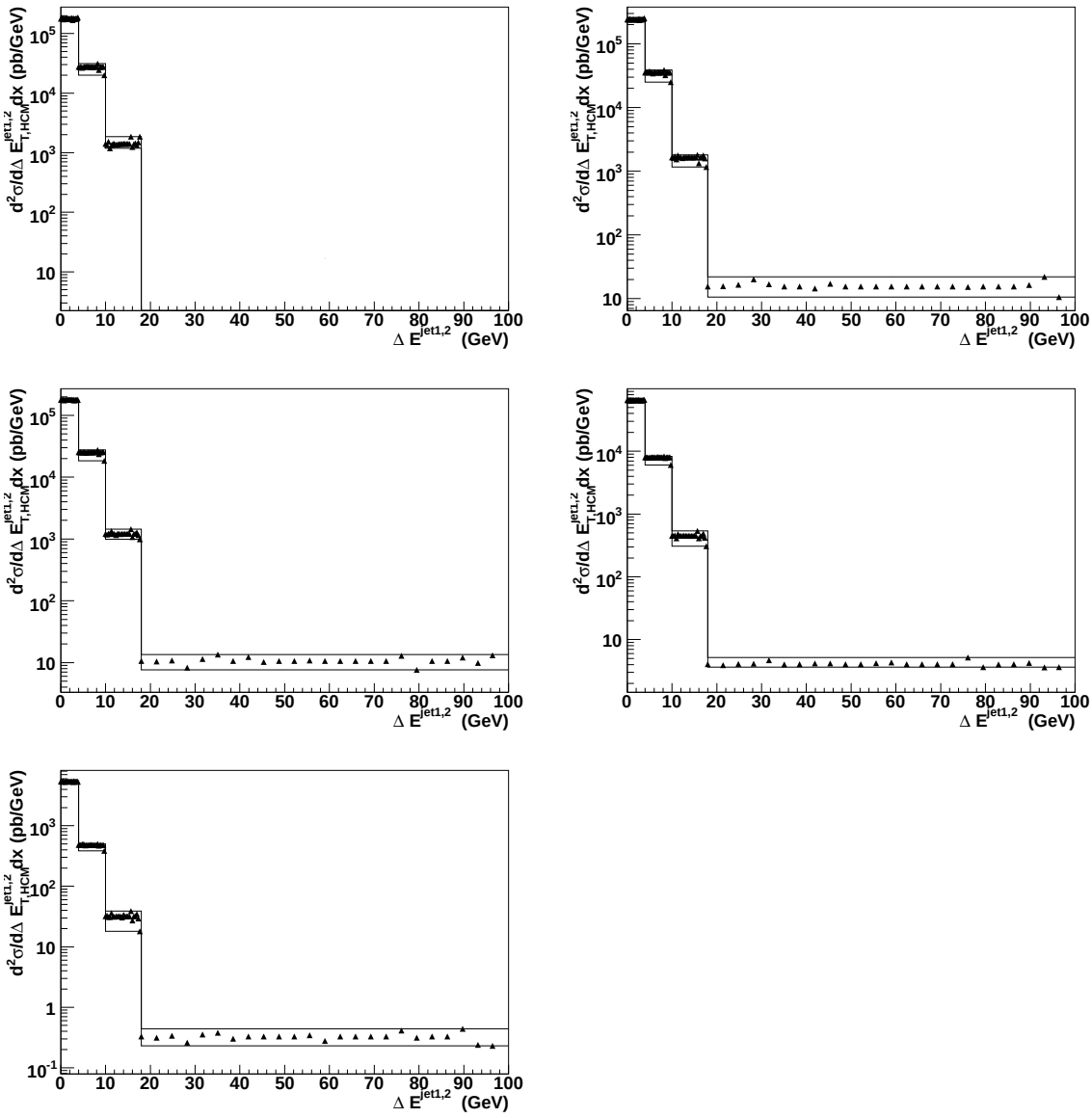

Figure C.5: Systematic uncertainties for the $\Delta E_{T,\mathrm{HCM}}^{\mathrm{jet1,2}}$ cross sections for the dijet sample in ascending bins of x_{Bj}.

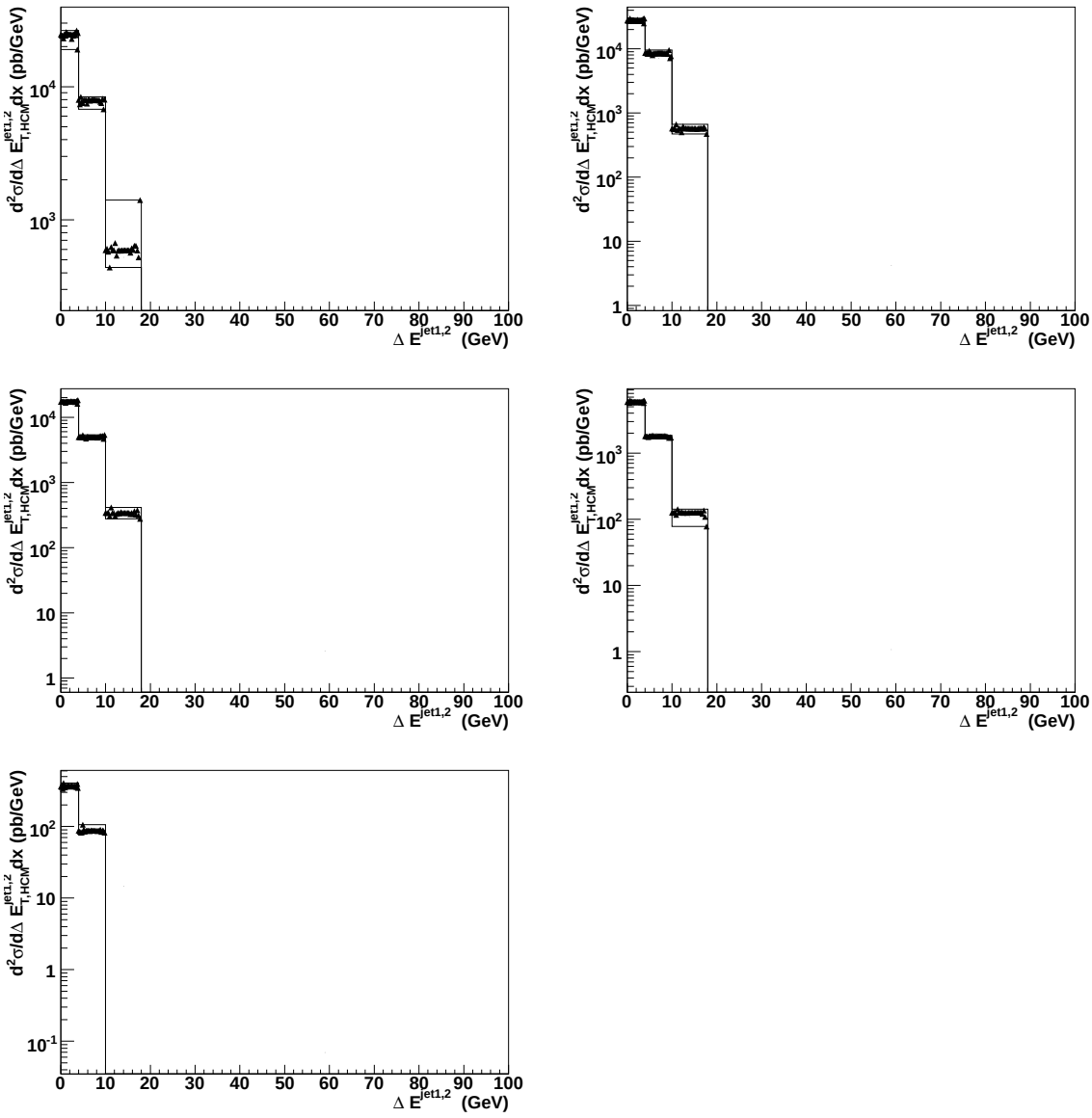

Figure C.6: Systematic uncertainties for the $\Delta E_{T,\mathrm{HCM}}^{\mathrm{jet1,2}}$ cross sections for the trijet sample in ascending bins of x_{Bj}.

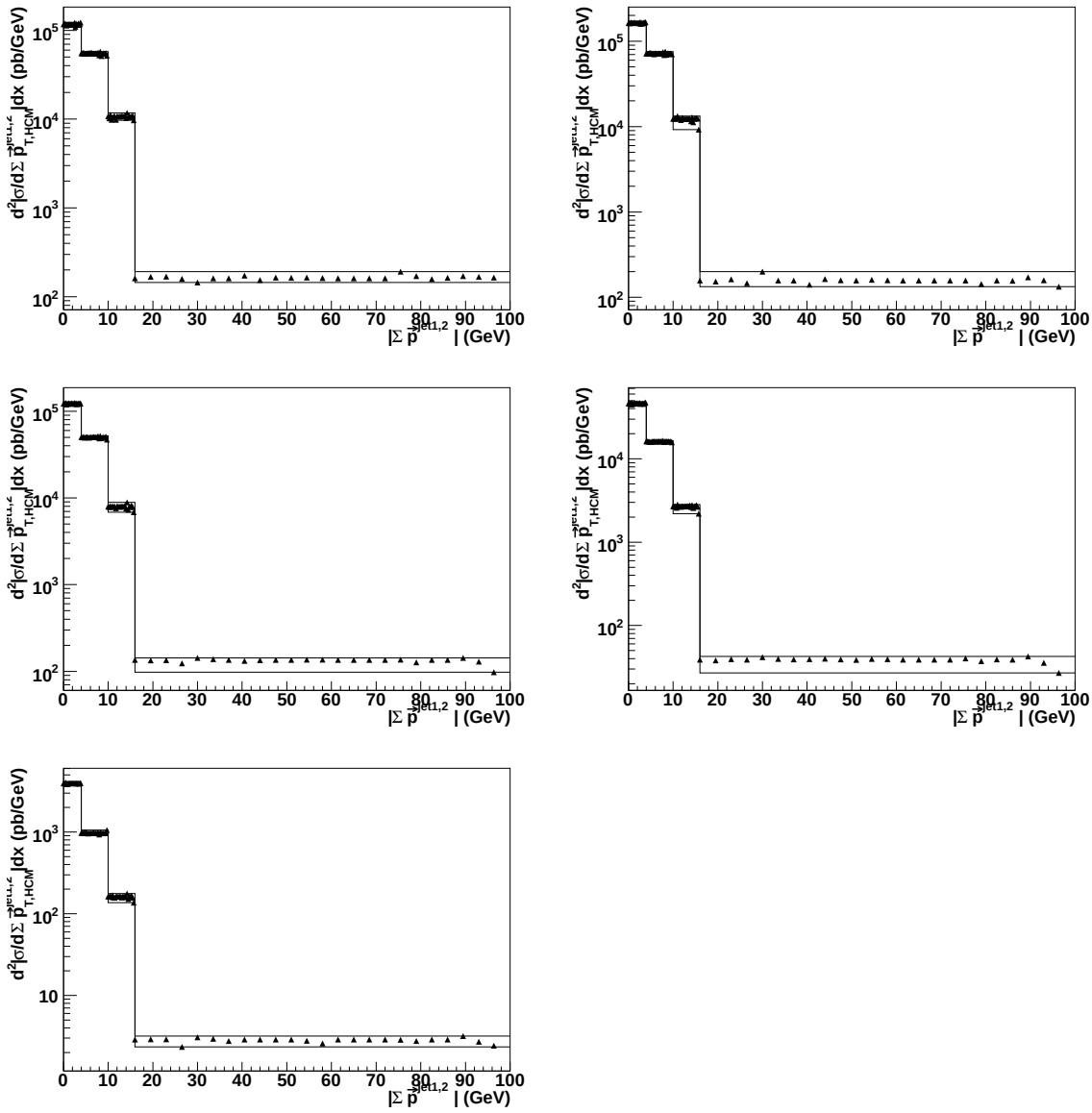

Figure C.7: Systematic uncertainties for the $|\Delta\vec{p}_{T,\mathrm{HCM}}^{\,\mathrm{jet1,2}}|/(2E_{T,\mathrm{HCM}}^{\mathrm{jet1}})$ cross sections for the dijet sample in ascending bins of x_{Bj}.

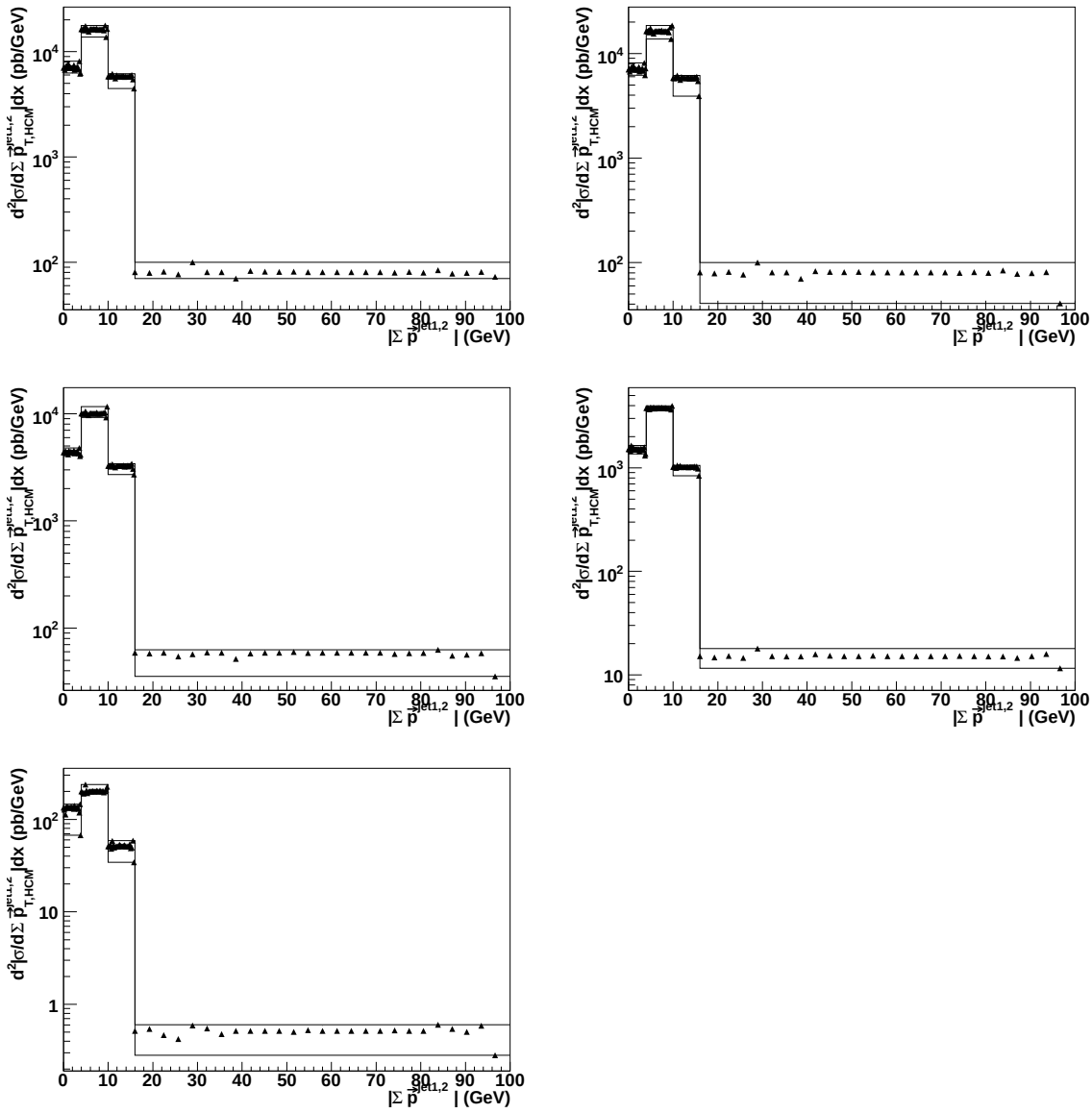

Figure C.8: Systematic uncertainties for the $|\Delta\vec{p}_{T,\mathrm{HCM}}^{\,\mathrm{jet1,2}}|/(2E_{T,\mathrm{HCM}}^{\mathrm{jet1}})$ cross sections for the trijet sample in ascending bins of x_{Bj}.

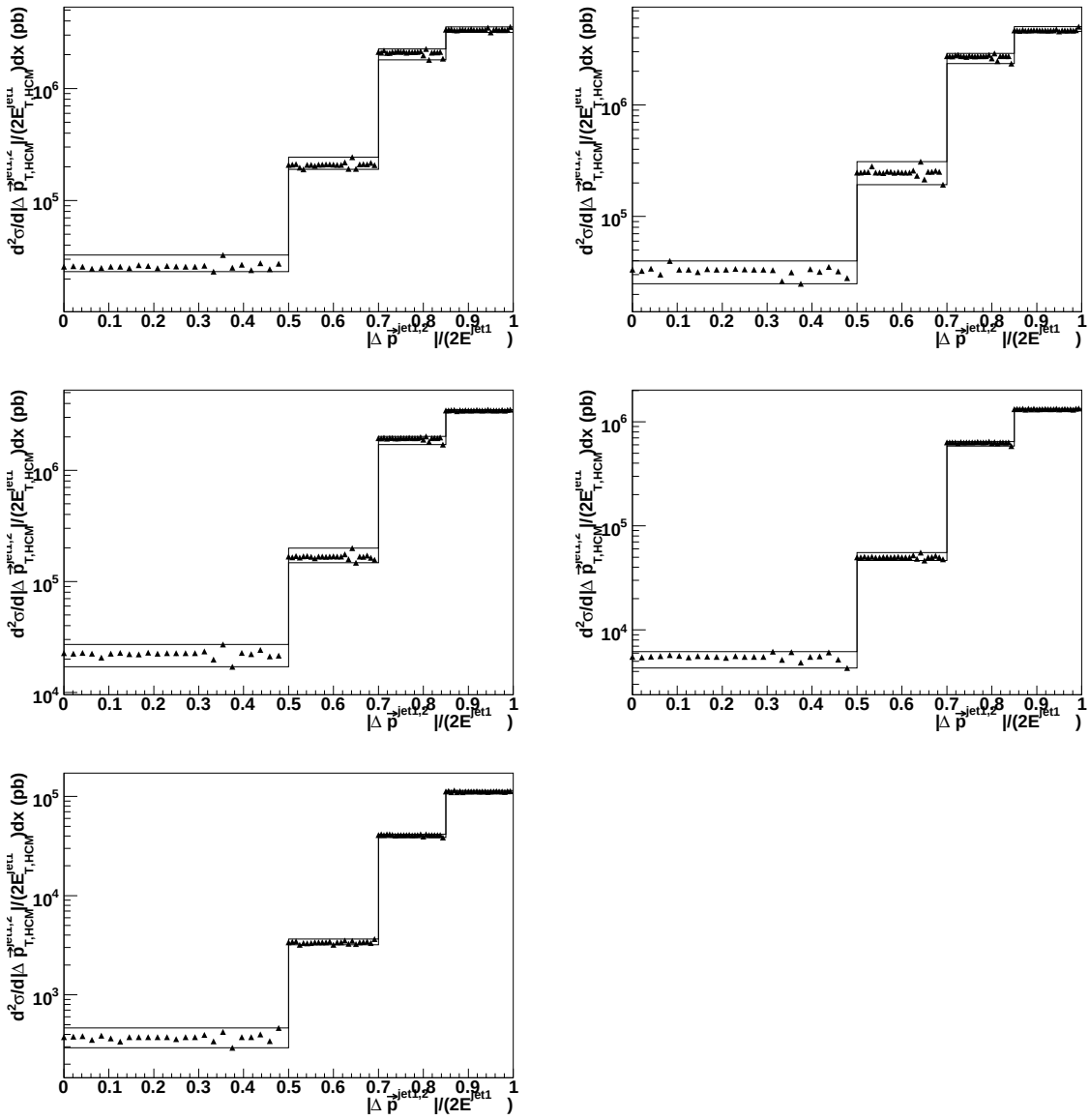

Figure C.9: Systematic uncertainties for the $|\Delta\vec{p}_{T,\mathrm{HCM}}^{\,\mathrm{jet1,2}}|/(2E_{T,\mathrm{HCM}}^{\mathrm{jet1}})$ cross sections for the dijet sample in ascending bins of x_{Bj}.

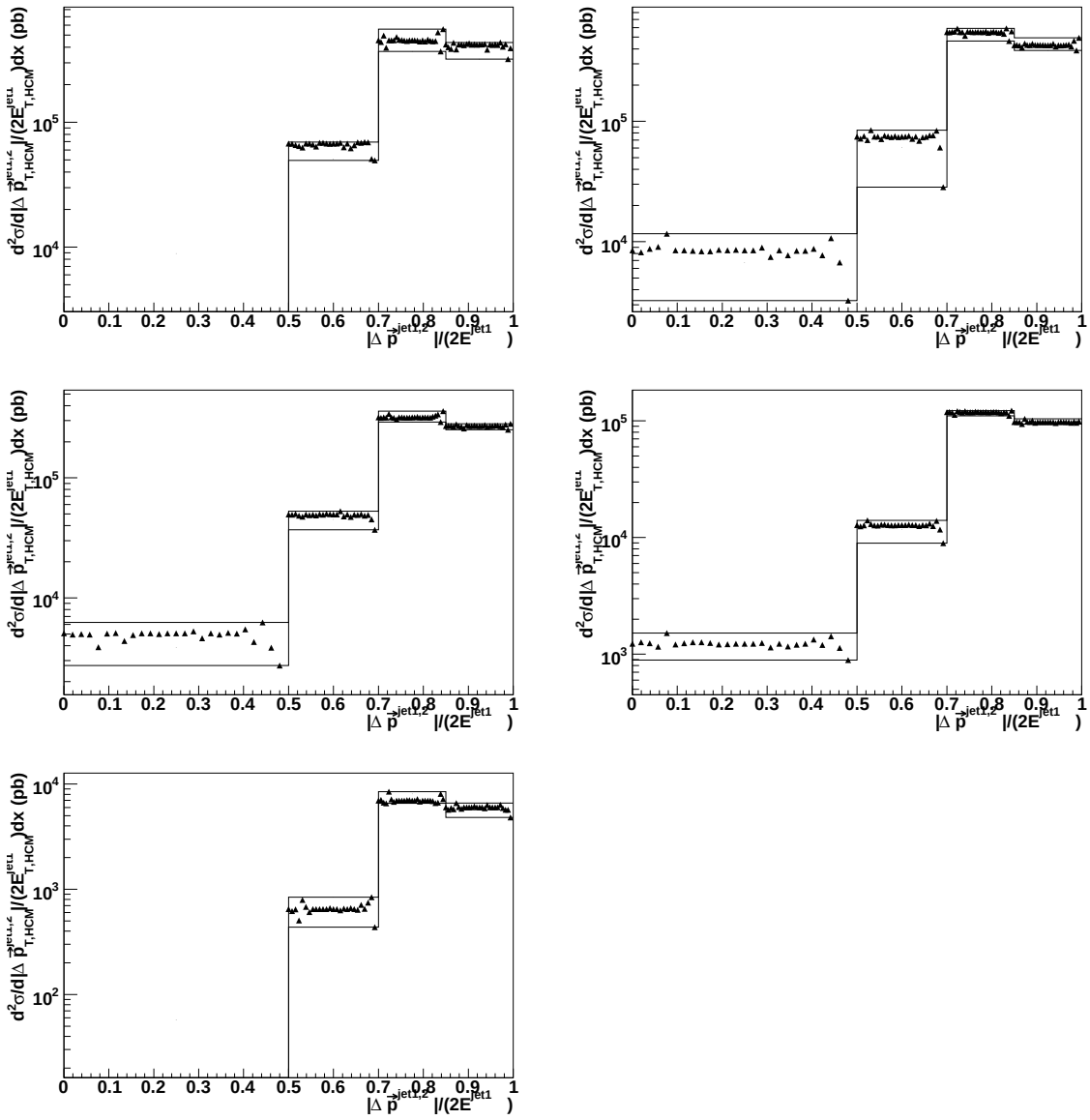

Figure C.10: Systematic uncertainties for the $|\Delta\vec{p}_{T,\mathrm{HCM}}^{\,\mathrm{jet1,2}}|/(2E_{T,\mathrm{HCM}}^{\mathrm{jet1}})$ cross sections for the trijet sample in ascending bins of x_{Bj}.

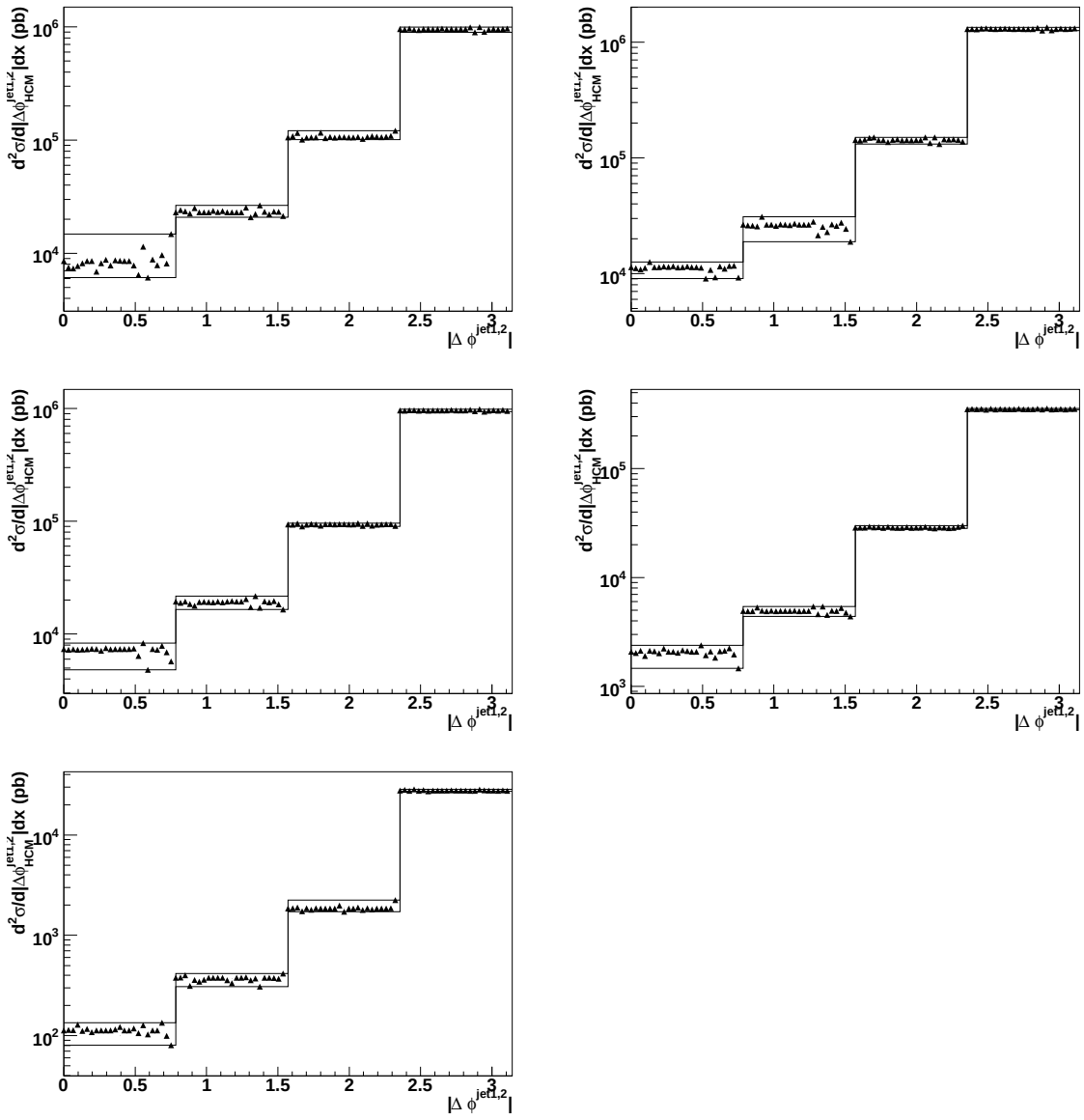

Figure C.11: Systematic uncertainties for the $|\Delta\phi^{\mathrm{jet1,2}}_{\mathrm{HCM}}|$ cross sections for the dijet sample in ascending bins of x_{Bj}.

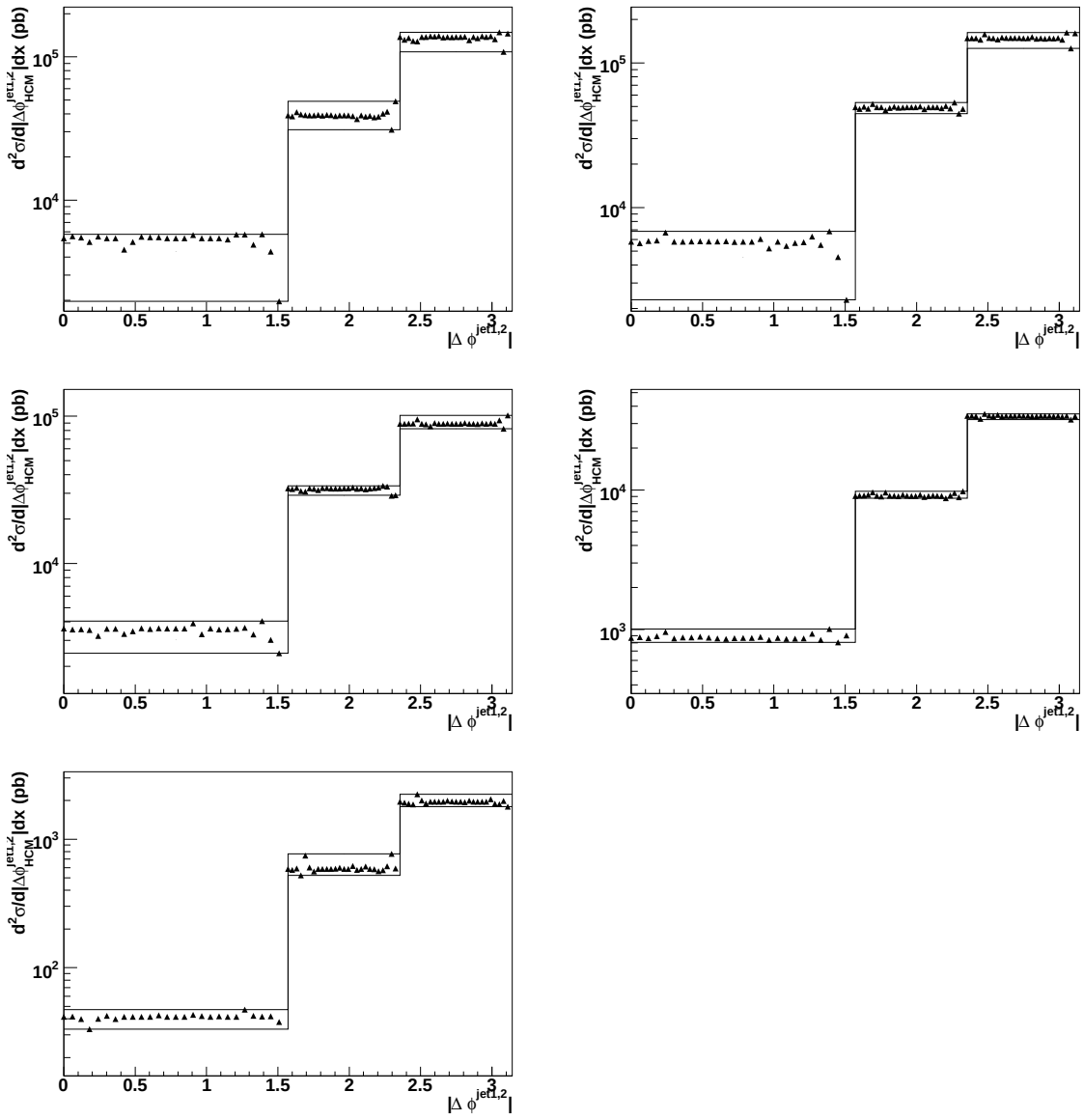

Figure C.12: Systematic uncertainties for the $|\Delta\phi^{\mathrm{jet1,2}}_{\mathrm{HCM}}|$ cross sections for the trijet sample in ascending bins of x_{Bj}.

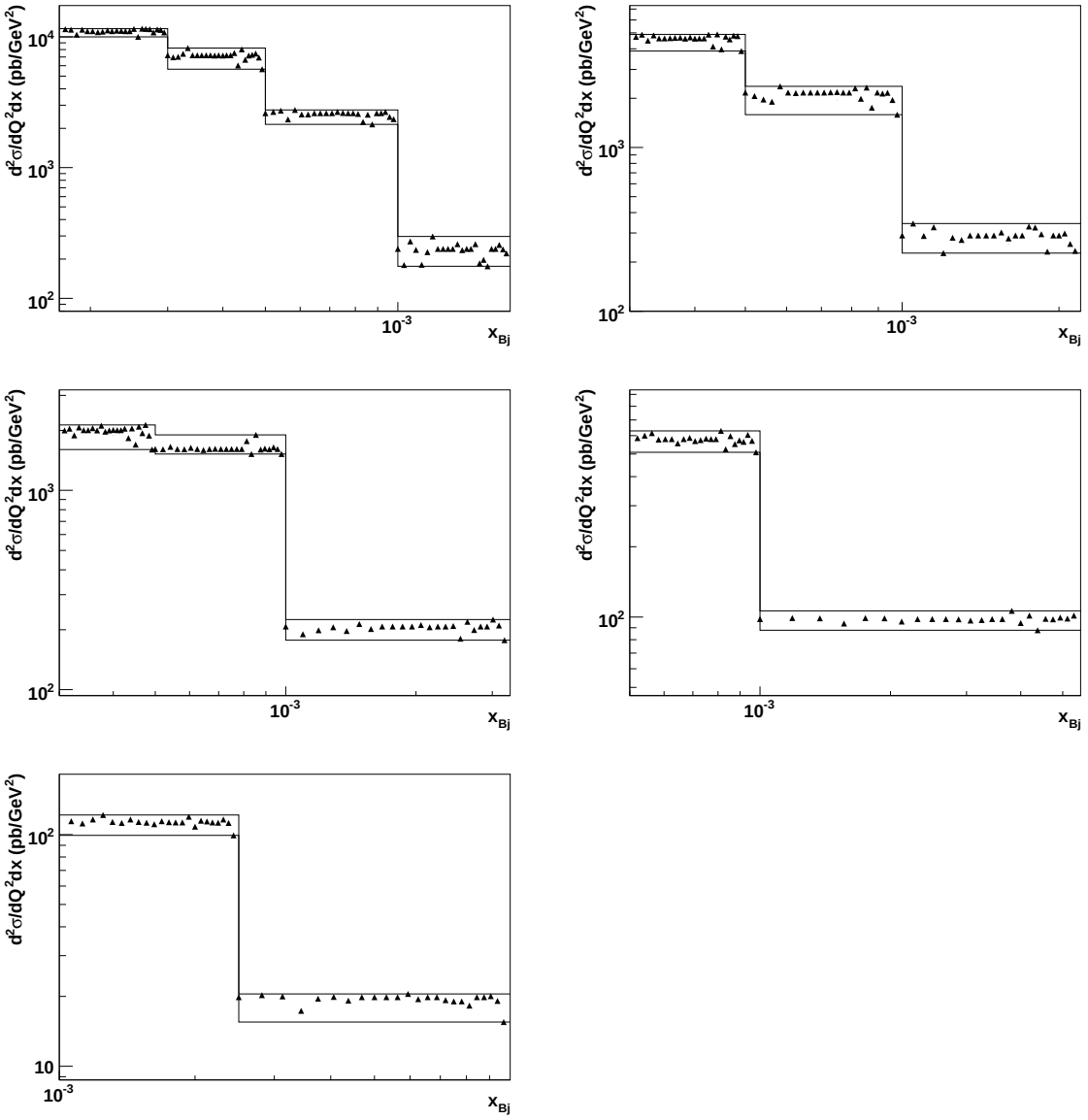

Figure C.13: Systematic uncertainties for the cross sections in Q^2 and x_{Bj} with $|\Delta\phi^{\mathrm{jet1,2}}_{\mathrm{HCM}}| < 2\pi/3$ for the dijet sample in ascending bins of Q^2.

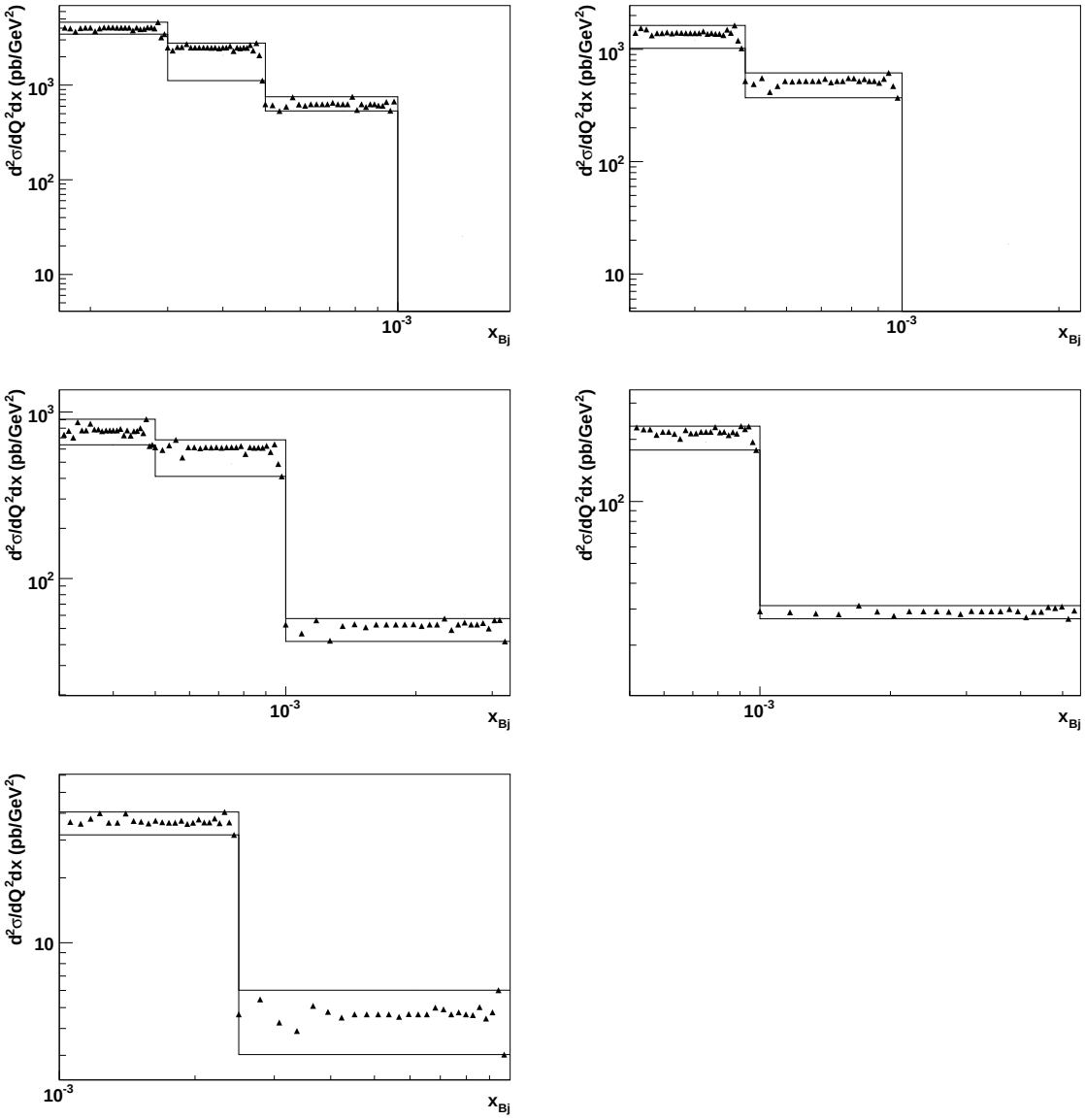

Figure C.14: Systematic uncertainties for the cross sections in Q^2 and x_{Bj} with $|\Delta\phi^{\mathrm{jet1,2}}_{\mathrm{HCM}}| < 2\pi/3$ for the dijet sample in ascending bins of Q^2.

Bibliography

[1] F. Halzen and A.D. Martin, *Quarks and Leptons: An Introductory Course in Modern Particle Physics*. John Wiley & Sons, Inc, 1984.

[2] *Particle Physics Timeline*, available on `http://http://www.particleadventure.org/other/history/index.html`. Accessed 3 Sept. 2007.

[3] Glashow, Sheldon L. and Weinberg, Steven, Phys. Rev. D **15**, 1958 (1977).

[4] W.A. Bardeen et al., Phys. Rev. **D 18**, 3998 (1978).

[5] *HERA Graphics*, available on `http://http://zms.desy.de/e548/e550/e6944/e76/index_eng.html`. Accessed 10 Sept. 2007.

[6] J.D. Bjorken, Phys. Rev. **179**, 1547 (1969).

[7] V.N. Gribov and L.N. Lipatov, Sov. J. Nucl. Phys. **15**, 438 (1972);
G. Altarelli and G. Parisi, Nucl. Phys. **B 126**, 298 (1977);
L.N. Lipatov, Sov. J. Nucl. Phys. **20**, 94 (1975);
Yu.L. Dokshitzer, JETP **46**, 641 (1977).

[8] Jung, H., *QCD and collider physics Lecture WS 2005/2006 University Hamburg*, available on `https://www.desy.de/~jung/qcd_collider_physics_2005/`. Accessed 12 Sept. 2007.

[9] Sudakov, V. V., Sov. Phys. JETP **3**, 65 (1956).

[10] H1 Coll., C. Adloff et al., Eur. Phys. J. **C 21**, 33 (2001).

[11] ZEUS Coll., S. Chekanov et al., Phys. Rev. **D 67**, 012007 (2003).

[12] ZEUS Coll., S. Chekanov et al., Eur. Phys. J. **C 44**, 183 (2005).

[13] H1 Coll., Adloff, C. et al., Phys. Lett. **B515**, 17 (2001).

[14] ZEUS Coll., S. Chekanov et al., Eur. Phys. J. **C 23**, 13 (2002);
ZEUS Coll., S. Chekanov et al., Phys. Lett. **B 547**, 164 (2002);
ZEUS Coll., S. Chekanov et al., Eur. Phys. J. **C 21**, 443 (2001).

[15] H1 Coll., C. Adloff et al., Eur. Phys. J. **C 19**, 289 (2001);
H1 Coll., C. Adloff et al., Phys. Lett. **B 515**, 17 (2001);
H1 Coll., S. Aid et al., Nucl. Phys. **B 470**, 3 (1996).

[16] E.A. Kuraev, L.N. Lipatov and V.S. Fadin, JETP **45**, 199 (1977);
Ya.Ya. Balitskiĭ and L.N. Lipatov, Sov. J. Nucl. Phys. **28**, 822 (1978).

[17] Jalilian-Marian, Jamal and Kovner, Alex and Leonidov, Andrei and Weigert, Heribert, Nucl. Phys. **B504**, 415 (1997).

[18] R.K. Ellis, W.J. Stirling and B.R. Webber, *QCD and Collider Physics*, Cambridge Monographs on Particle Physics, Nuclear Physics and Cosmology, Vol. 8. Cambridge University Press, 1996.

[19] S. Catani, F. Fiorani and G. Marchesini, Nucl. Phys. **B 336**, 18 (1990);
M. Ciafaloni, Nucl. Phys. **B 296**, 49 (1988).

[20] Catani, S. and Ciafaloni, M. and Hautmann, F., Nucl. Phys. **B366**, 135 (1991);
L.V. Gribov, E.M. Levin and M.G. Ryskin, Phys. Rep. **100**, 1 (1983);
Collins, John C. and Ellis, R. Keith, Nucl. Phys. **B360**, 3 (1991).

[21] R.P. Feynman, *Photon-Hadron Interactions*. Benjamin, New York, 1972;
K.H. Streng, T.F. Walsh, P.M. Zerwas, Z. Phys. **C**, 237 (1979).

[22] N. Harnew et al., Nucl. Inst. Meth. **A 279**, 290 (1989);
B. Foster et al., Nucl. Phys. Proc. Suppl. **B 32**, 181 (1993);
B. Foster et al., Nucl. Inst. Meth. **A 338**, 254 (1994).

[23] M. Derrick et al., Nucl. Inst. Meth. **A 309**, 77 (1991);
A. Andresen et al., Nucl. Inst. Meth. **A 309**, 101 (1991);
A. Caldwell et al., Nucl. Inst. Meth. **A 321**, 356 (1992);
A. Bernstein et al., Nucl. Inst. Meth. **A 336**, 23 (1993).

[24] ZEUS Coll., U. Holm (ed.), *The ZEUS Detector*. Status Report (unpublished), DESY (1993), available on `http://www-zeus.desy.de/bluebook/bluebook.html`.

[25] R. Hall-Wilton et al., *The CTD Tracking Resolution* (unpublished). ZEUS-99-024, internal ZEUS-note, 1999.

[26] D.S. Bailey et al., Nucl. Inst. Meth. **A 396**, 320 (1997).

[27] Wigmans, Richard, Ann. Rev. Nucl. Part. Sci. **41**, 133 (1991).

[28] H. Bethe and W. Heitler, Proc. Roy. Soc. Lond. **A146**, 83 (1934).

[29] H.L. Lai et al., Phys. Rev. **D 51**, 4763 (1995).

[30] A.D. Martin, R.G. Roberts and W.J. Stirling, Phys. Rev. **D 50**, 6734 (1994).

[31] M. Bengtsson, G. Ingelman and T. Sjöstrand, *Proc. HERA Workshop*, R.D. Peccei (ed.), Vol. 1, pp. 149–165. DESY, Hamburg, Germany (1987).

[32] G. Gustafson and U. Pettersson, Nucl. Phys. **B 306**, 746 (1988).

[33] B. Andersson et al., Phys. Rep. **97**, 31 (1983).

[34] A. Kwiatkowski, H. Spiesberger and H.-J. Möhring, Comp. Phys. Comm. **69**, 155 (1992). Also in *Proc. Workshop Physics at HERA*, 1991, DESY, Hamburg.

[35] K. Charchula, G.A. Schuler and H. Spiesberger, Comp. Phys. Comm. **81**, 381 (1994).

[36] *Geant v3.13 modules GMOLI.FPP & GMOLS.FPP*, available on `http://wwwinfo.cern.ch/adsoc/geant_html3/node247.html`.

[37] L. Lönnblad, Comp. Phys. Comm. **71**, 15 (1992).

[38] G. Ingelman, A. Edin and J. Rathsman, Comp. Phys. Comm. **101**, 108 (1997).

[39] H.L. Lai et al., Phys. Rev. **D 55**, 1280 (1997).

[40] M. Bengtsson and T. Sjöstrand, Comp. Phys. Comm. **46**, 43 (1987).

[41] T. Sjöstrand, Comp. Phys. Comm. **82**, 74 (1994).

[42] Z. Nagy and Z Trocsanyi, Phys. Rev. Lett. **87**, 082001 (2001).

[43] E. Mirkes and D. Zeppenfeld, Phys. Lett. **B**, 205 (1996).

[44] Fabricius, K. and Schmitt, I. and Kramer, G. and Schierholz, G., Zeit. Phys. **C11**, 315 (1981).

[45] Ellis, R. Keith and Ross, D. A. and Terrano, A. E., Nucl. Phys. **B178**, 421 (1981).

[46] S. Catani and M. H. Seymour, Nucl. Phys. **B 485**, 291 (1997).

[47] N. Krumnack, *Three Jet Events in Deep Inelastic Scattering*. Ph.D. Thesis, University of Hamburg, 2004.

[48] L. Li. Ph.D. Thesis, University of Wisconsin-Madison, 2004.

[49] Chekanov, S. and others, Phys. Lett. **B632**, 13 (2006).

[50] J. Pumplin et al., Preprint hep-ph/0201195, 2002.

[51] G. F. Hartner, *VCTRAK Briefing: Program and Math* (unpublished). Zeus-98-058, internal ZEUS-note, 1998.

[52] A. Savin, *Study of Calorimeter Noise in the 1996 Data* (unpublished). ZEUS-98-007, internal ZEUS-note, 1998.

[53] Ch. Amelung, *Electron Position Reconstruction in ZEUS: Further Update of the ELECPO Package (Based on 1995 Data)* (unpublished). ZEUS-96-093, internal ZEUS note, 1996.

[54] Abramowicz, Halina and Caldwell, Allen and Sinkus, Ralph, Nucl. Instrum. Meth. **A365**, 508 (1995).

[55] M. Wodarczyk, *Measurement of the F_2 Structure Function of the Proton at HERA from 1996 and 1997 ZEUS Data.* Ph.D. Thesis, University of Wisconsin, 1999.

[56] N. Tuning, *ZUFOs: Hadronic Final State Reconstruction with Calorimeter, Tracking and Backsplash Correction* (unpublished). ZEUS-Note-01-021, 2001.

[57] D. Chapin, *A Measurement of Dijet Production in Neutral Current Deep Inelastic Scattering with ZEUS at HERA.* Ph.D. Thesis, Univeristy of Wisconsin, Madison, 2001. Unpublished.

[58] S. Bentvelsen, J. Engelen and P. Kooijman, *Proc. Workshop on Physics at HERA*, W. Buchmüller and G. Ingelman (eds.), Vol. 1, p. 23. Hamburg, Germany, DESY (1992);
K.C. Höger, *Proc. Workshop on Physics at HERA*, W. Buchmüller and G. Ingelman (eds.), Vol. 1, p. 43. Hamburg, Germany, DESY (1992).

[59] J. Repond, *Jet Energy Corrections* (unpublished). ZEUS Note96-104.

[60] N. Tuning and M. Wodarczyk, *rcalcor.fpp, Calorimeter correction routine, PHANTOM Users Library.*

[61] F. Jacquet and A. Blondel, *Proceedings of the Study for an ep Facility for Europe*, U. Amaldi (ed.), p. 391. Hamburg, Germany (1979). Also in preprint DESY 79/48.

[62] P.J. Bussey, *EUCELL.* ZEUS Phantom Library.

[63] J.E. Huth et al., *Research Directions for the Decade. Proceedings of Summer Study on High Energy Physics, 1990*, E.L. Berger (ed.), p. 134. World Scientific (1992). Also in preprint FERMILAB-CONF-90-249-E.

[64] S.Catani et al., Nucl. Phys. **B406**, 187 (1993).

[65] Gonzalez Lopez, O., *Precise determinations of the strong coupling constant at HERA*. Thesis, Universidad Autonoma de Madrid, 2002. DESY-THESIS-2002-020.

[66] ZEUS Coll., S. Chekanov et al., Eur. Phys. J. **C 27**, 531 (2003);
ZEUS Coll., S. Chekanov et al., Eur. Phys. J. **C 23**, 615 (2002);
Wing, M. (on behalf of the ZEUS Coll.). Proc. of the 10th International Conference on Calorimetry in High Energy Physics, R. Zhu (ed.), p. 767. Pasadena, USA (2002). Also in preprint hep-ex/0206036.

[67] H1 Coll., A. Aktas et al. H1prelim-06-032, 2006.

[68] H. Jung, Comp. Phys. Comm. **86**, 147 (1995).

[69] H. Jung and G. P. Salam, Eur. Phys. J. **C 19** (2001).

[70] ZEUS Coll., FPC group, A. Bamberger et al., Nucl. Inst. Meth. **A 450**, 235 (2000).

[71] Chekanov, S. and others (2007). Accepted by Eur. Phys. Journal C.

[72] H1 Coll., A. Aktas et al. H1prelim-06-034, 2006.

[73] Chekanov, S. and others (2007). Accepted by Nucl. Phys. B.